Doctoral theses at NTNU, 2017:101

Vegard Aune

Behaviour and Modelling of Flexible Structures Subjected to Blast Loading

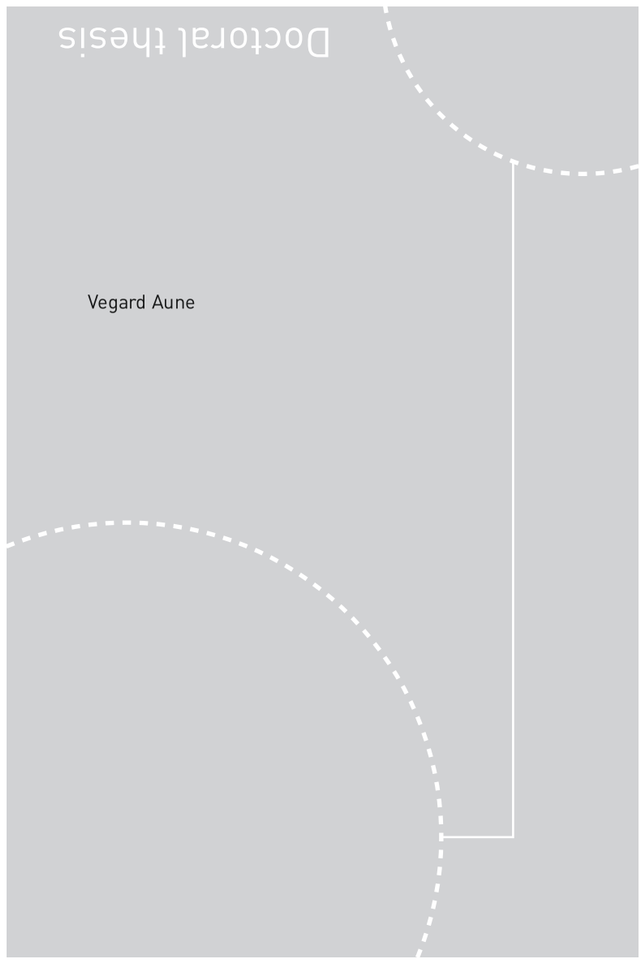

ISBN 978-82-326-2274-0 (printed ver.)
ISBN 978-82-326-2275-7 (electronic ver.)
ISSN 1503-8181

NTNU
Norwegian University of
Science and Technology

NTNU
Norwegian University of Science and Technology
Thesis for the Degree of
Philosophiae Doctor
Faculty of Engineering
Department of Structural Engineering

Doctoral theses at NTNU, 2017:101

NTNU
Norwegian University of
Science and Technology

Vegard Aune

Behaviour and Modelling of Flexible Structures Subjected to Blast Loading

Thesis for the Degree of Philosophiae Doctor

Trondheim, May 2017

Norwegian University of Science and Technology
Faculty of Engineering
Department of Structural Engineering

NTNU
Norwegian University of
Science and Technology

NTNU
Norwegian University of Science and Technology

Thesis for the Degree of Philosophiae Doctor

Faculty of Engineering
Department of Structural Engineering

ISBN 978-82-326-2274-0 (printed ver.)
ISBN 978-82-326-2275-7 (electronic ver.)
ISSN 1503-8181

Doctoral theses at NTNU, 2017:101

Printed by NTNU Grafisk senter

Preface

This thesis is submitted in partial fulfillment of the requirements for the degree of Philosophiae Doctor in Structural Engineering at the Norwegian University of Science and Technology. The work has been carried out at the Structural Impact Laboratory (SIMLab), Centre for Research-based Innovation, housed at the Department of Structural Engineering, under the supervision of Professor Tore Børvik and Professor Magnus Langseth.

The thesis consists of four parts. **Part I** gives the background and motivation, a brief review of previous work, objectives and scope, and the contributions of this thesis. **Part II** focuses on thin steel and aluminium plates exposed to free-field airblast loading, where the numerical simulations are performed using an uncoupled approach during the blast-structure interaction. **Part III** presents the shock tube technique as an alternative to explosive detonations and the design of a new shock tube facility established at SIMLab. Experimental and numerical studies on the dynamic response of blast-loaded plates are also presented in **Part III**, where the numerical simulations are performed using both uncoupled and coupled approaches during the blast-structure interaction. **Part IV** summarize this work by giving some general conclusions and suggestions for further work.

The reader should be aware that a wide range of topics related to the behaviour and modelling of blast-loaded structures are covered in this work. It is therefore chosen to include some basic theory in the beginning of **Parts II** and **III** for the completeness of this thesis. Moreover, it is emphasized that this thesis is written from a structural engineering point of view where the main focus is on the dynamic response of blast-loaded plates. The shock physics and thermodynamics necessary to understand compressible fluid flow in **Part III** are therefore kept at a basic level. Compressible fluid flow is an active field of research and detailed studies within this topic is beyond the scope of this thesis.

Vegard Aune
Trondheim, Norway
April 3, 2017

Abstract

The last two decades have seen a significant increase in the research activity on blast-loaded structures. This is to a large extent related to the increased threat of deliberate use of high explosives against civilian targets. Blast events in urban environments introduce new materials, lightweight and flexible structures to the scope of protective design. Historically, the blast-resistant design mostly involved conflict areas and hardened structures. It is therefore a need to review the capabilities of the current computational methods in predicting the response of flexible structures subjected to blast loading. This thesis presents both experimental and numerical investigations on the dynamic response of thin aluminium and steel plates exposed to blast loading, where the experimental data serve as a basis of comparison for the numerical simulations. The numerical simulations are mainly performed in the finite element code EUROPLEXUS. Material tests are also performed to determine the materials' behaviour at large plastic strains and for calibration of an energy-based failure criterion.

The dynamic response of the blast-loaded plates is first studied using free-field airblast testing. The blast loading was varied by detonating spherical charges of plastic explosives at various stand-off distances relative to the centre point of the plates. The tests covered the entire range of response from complete failure at the support to a more counter-intuitive behaviour (CIB) where the permanent mid-point deflection was in the opposite direction to the incident blast wave due to reversed snap buckling (RSB). The trend in all tests was that the maximum response is driven by the positive impulse from the airblast, as it occurred after the positive duration of the pressure pulse. However, depending on the blast intensity and the structural properties, the response of the plates may become significantly different. RSB attracted special attention since this is an unstable configuration sensitive to small changes in the loading and in structural properties. The dynamic response of the plates was therefore studied numerically, where the loading was represented using parameters for the positive and negative phase recommended in traditional design manuals. The numerical results were in good agreement with the tests and predicted the entire range of experimental observations. The negative phase of the blast load is usually neglected in blast-resistant design. However, the numerical simulations showed that the negative overpressure dominated the response and led to RSB at some loading and structural conditions. Two distinctive types of CIB were identified and both were found to depend on the timing and magnitude of the peak negative overpressure relative to the dynamic response of the plates. The partial and complete failure along the boundaries observed in some of the tests was also successfully recreated in the simulations by using element erosion.

Then, the development of a new shock tube facility to produce controlled, repeatable blast loading in laboratory environments is presented. The facility was found to generate a planar shock wave over the tube cross-section by measuring the pressure distribution on a massive steel plate located at the end of the tube. The properties of the shock wave proved to be a function of driver length and driver pressure, and the positive phase of the measured pressure histories was similar as those generated from actual far-field explosive detonations. This shock tube therefore allows for the evaluation of fluid-structure interaction (FSI) effects without the need to consider the inherent complexity in close-in and near-field detonations. Shock tube experiments were therefore carried out to investigate the influence of FSI effects and pre-formed holes on the response of blast-loaded plates. Both massive and flexible plates were located at the tube end during testing, where the massive plate tests served as a basis for comparison with respect to FSI effects. Both the plates with and without holes resulted in a reduced reflected overpressure, where the reduction was more distinct in the plates with pre-formed holes. The introduction of holes in the plates resulted in increased mid-point deflections and failure at the largest blast intensities. Finally, numerical simulations were performed to study the wave patterns and FSI effects during the shock tube experiments. The wave patterns were studied using a purely Eulerian analysis to evaluate the capabilities of the idealized gas theory in predicting the pressure histories obtained in the massive plate tests. Even though the numerical simulations of the wave propagation captured most of the events occurring in the experiments, the pressure histories were overestimated at larger magnitudes of pressure. The investigation of FSI effects was therefore studied qualitatively by comparing the results from fully coupled simulations to those obtained with an uncoupled approach, where the uncoupled approach used the loading from the purely Eulerian simulations. The reduction of the reflected pressure was also observed in the fully coupled simulations, and increasing magnitudes of pressure resulted in reduced deformation of the plates compared to those in the uncoupled approach. Moreover, the experimental observations of crack growth along the diagonals were successfully recreated in both the uncoupled and coupled simulations by using adaptive mesh refinement and element erosion. The mesh refinement was driven by the damage parameter in the material model and occurred at user-defined levels of this parameter.

The experiments and simulations presented herein provide valuable insight to the behaviour and modelling of flexible structures subjected to blast loading. Parameters influencing the dynamic response have been investigated and identified, and the experimental data may therefore be used in the evaluation of computational methods used in blast-resistant design. It is emphasized that an accurate description of the loading is necessary for quantitative investigations of the dynamic response and failure mechanisms in flexible structures.

Depending on the blast intensity, the response of the structure may become significantly different. Moreover, the reduction in reflected pressure in the vicinity of the plate and corresponding decrease in deformation during FSI are interesting in view of blast mitigation. Provided that the structural member can sustain the deformation that arise without experiencing failure, this implies that ductile materials may be utilized in the design of flexible structures by allowing for finite deformations. The FSI may then reduce the transmitted impulse and serve as alternative load paths. However, this requires a thorough understanding of the governing physics in the problem.

Acknowledgements

I wish to thank Professor Tore Børvik and Professor Magnus Langseth for giving me the opportunity to study this topic. Professor Tore Børvik served as the main supervisor and Professor Magnus Langseth as the co-supervisor. Their guidance and continuous support throughout the course of this work are deeply acknowledged. In particular, their experience, understanding and encouragement during the process of establishing a test facility have been invaluable during the past four years. I could not have asked for a better team of supervisors.

The work has been financed by the Structural Impact Laboratory (SIMLab), Centre for Research-based Innovation (CRI), and the Faculty of Engineering Science and Technology at the Norwegian University of Science and Technology (NTNU).

It is a pleasure to extend my gratitude to all who have participated during the preparation of this thesis. I would like to thank my colleagues and friends at the department, and especially at SIMLab, who makes this a great place to work, both educationally and socially. A special thank you goes to my office neighbour Jens Kristian Holmen for our many work- and non-work-related discussions. The SIMLab Shock Tube Facility (SSTF) was designed in cooperation with Mr. Olav Fismen and his contribution in performing the construction drawings, continuous effort and discussions during the final design are gratefully acknowledged. I also want to thank Mr. Arnfinn Jenssen (1930-2016) for sharing his experience and motivation during the preliminary design and establishment of the SSTF. The construction of the SSTF was carried out by Heimdal Industriservice AS and made possible by financial support from CRI-SIMLab, NTNU and the Norwegian National Security Authority. I am very grateful to Mr. Trond Auestad and Mr. Tore Wisth for their contributions during the establishment of the SSTF and for always helping me during the experimental work. Acknowledgements are given to the Norwegian Defence Estate Agency and Mr. Knut Ove Hauge for their assistance during the free-field airblast testing. Dr. Egil Fagerholt has been very helpful and made significant contributions through his assistance with the digital image correlation analyses. Working with Dr. Folco Casadei, Dr. Georgios Valsamos and Dr. Martin Larcher at the Joint Research Centre (EC-JRC) in Ispra, Italy has been both enjoyable and beneficial. Their valuable input and assistance during the numerical simulations in EUROPLEXUS are highly appreciated. A special thank you goes to Dr. Folco Casadei for his support, continuous implementations of new features, willingness to share knowledge and patient guidance during the numerical work. Contributions from each of the master

students who dedicated their final semester to work with topics related to this thesis are greatly acknowledged. Their assistance in the laboratory, curiosity, discussions and questions made this a better thesis.

Finally, I want to express my gratitude to my family and friends. Thank you for your encouragement and support throughout this work. A *special* thank you goes to Lena. You are my best friend and partner in life. I know that it has been anything but amusing to live with someone who was either working or thinking on how to write this thesis. Your love and patience during the last four years have been crucial. You have given us our daughter Iben. She always makes me laugh and both of you remind me that there is more to life than working. I would also like to give a special gratitude to my mother Agnes Bente for her unconditional love and support, my father Rolf Bjarne for providing important moral support and for introducing me to the field of structural engineering, and finally my sister Kristin and brother Sigurd for always believing in their big brother.

Contents

Part I

Description of Thesis

1

Introduction

The first chapter presents the background and motivation for this thesis, a brief review of previous research within the field of blast-loaded structures, as well as the objectives, scope and contributions of this work.

1.1 Background and motivation

Protection of civilian infrastructure against blast loading has received a lot of attention in recent years. Explosions can be either intentional or accidental and occur in a large variety of circumstances, both in conflict areas as well as in various industrial applications such as petrochemical, chemical or nuclear industries. Unfortunately, explosive devices have also become the weapon of choice for the majority of terrorist attacks. The readily available information on the construction and manufacturing of improvised explosive devices (IEDs), their mobility and portability coupled with their huge potential for damage, are responsible for the significant increase in deliberate use of high explosives against civilian targets all over the world [1]. It is therefore an increased need to be able to design structural components to resist the effect of blast loading. Today's design of civilian infrastructure also extend the scope of traditional blast-resistant design by introducing new materials and lightweight structures.

The first of the two terrorist attacks on the 22 July 2011 in Norway is an example of this trend. A large vehicle-borne IED (VBIED) exploded in the Executive Government District in Oslo. The bomb was assumed to comprise a mixture of 950 kg ammonium nitrate and fuel oil (ANFO), and was later estimated to be a trinitrotoluene (TNT) equivalent somewhere between 400 and 700 kg. The shock wave from the explosion caused severe damage on the surrounding buildings, especially the buildings inside a distance of 100 m (see Figure 1.1a). Eight people were killed and at least 209 were injured, twelve of them seriously [2]. The dominant effects of such an explosive detonation are typically the blast overpressure (Figure 1.1b), fragments generated by the

explosion itself (Figure 1.1b) and the shock loads produced by the shock wave transmitted through the air or the ground (Figure 1.1d). Of these three effects, the blast overpressure are usually the governing factor in the determination of the structural response and the main consequence of the blast wave in urban areas is the breaking of windows and the creation of large quantities of hazardous secondary fragments of glass (Figure 1.1c). Another consequence of the shattering windows is that the blast pressure enters the building at these locations (Figure 1.1e). This may cause additional injuries to the occupants. Although the secondary fragments will have relatively low velocities compared to primary fragments, they are created throughout the zone around the explosion, wherever windows are broken, and may completely permeate the blast-affected area. A car bomb may break windows of up to 400 m away and therefore affect a zone of approximately half a square kilometer.

The most appealing alternative for blast wave mitigation is increased distance between the explosive charge and the target. However, this is not always feasible in urban areas because at some point the cost of increased distance becomes questionable. Hence, there is a need for innovative and optimized solutions considering safety as well as architectural requirements. Figure 1.1 illustrates that a successful assessment of blast-loaded structures requires a thorough understanding of the governing physics in such scenarios. Not only should the design prevent a total structural collapse, but it should also protect the people inside the building so that the building itself does not pose an added threat to the occupants (Figure 1.1e). This requires structural members that are able to withstand the extreme loading conditions occuring during blast events. Such structures often consist of thin steel or aluminium plates. Steel is often preferred due to its combination of high strength, high ductility and good formability, resulting in an effective load carrying capability at a relatively low cost compared to many other materials. During the last decades aluminium alloys have become increasingly more attractive for structural applications, particularly due to its relatively high strength to weight ratio.

Due to the complexity in both the loading and the resulting response, numerical methods are often required for sufficient insight in the structural component optimization. Before using such computational methods their performance should be evaluated in terms of reliability, robustness and effectiveness in predicting both the loading and the response. Experimental validation is ideal since it represents the actual physics of the problem, and controlled small-scale experiments could therefore be used to evaluate the current computational methods and improve the understanding of the dynamic response during blast events. This thesis will therefore perform experimental investigations of thin aluminium and steel plates before using this data to evaluate the performance of typical computational methods in predicting the experimental observations.

(a)

(b)

(c)

(d)

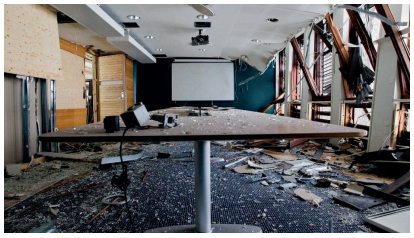

(e)

Figure 1.1: Pictures from the terror attack against the Executive Government Quarter in Norway 22 July 2011 [2]: (a) Executive Government Building after the explosion, (b) detonation of the car bomb, (c) shattering windows from adjacent building, (d) location of the car bomb and (e) inside the building.

1.2 Previous work

The response of blast-loaded structures is an active field of research and considerable work already exists on the subject. A brief overview of previous work related to this thesis is therefore presented. The review is limited to the representation of airblast loading, response of blast-loaded plates, fluid-structure interaction and experimental techniques.

1.2.1 Representation of blast loading

To study the response of blast-loaded structures, it is essential with an accurate description of the blast loading. A typical pressure-time history experienced by a fixed point in space after an exposure to a blast wave is shown in Figure 1.2. The positive phase of the blast wave is characterized by an almost instantaneous rise (within the timescale of nanoseconds) from atmospheric pressure p_1 to a peak incident overpressure $p_{\mathrm{so,max}}$ followed by an exponential decay in pressure back to the ambient pressure p_1 (see Figure 1.2). The positive phase has short time duration $t_{\mathrm{d}+}$ (typically milliseconds). When the blast wave interacts with a structure that is not parallel to the direction of the wave, it is reflected and reinforced. This is known as the peak reflected overpressure $p_{\mathrm{r,max}}$ and the reflected blast wave has the same general shape as the incident wave. The magnitude, duration and distribution of the blast load are a function of the explosive properties (i.e., the explosive material, weight W and shape), the location of the detonation relative to the structure (i.e., the stand-off distance R), potential objects located between the detonation and the structure, and finally the amplification of the pressure during its interaction with the surroundings or the structure itself.

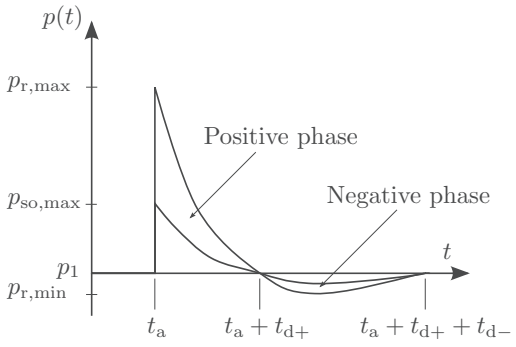

Figure 1.2: Typical incident and reflected pressure profiles after reflecting on an infinite and planar surface.

Some well-established references for the properties of the positive phase from an ideal airblast are the works by Baker et al. [3], Kingery and Bulmash [4] and Kinney and Graham [5]. Kingery and Bulmash [4] and Kinney and Graham [5] used a large range of experimental data from spherical and hemispherical charges [6–13] which were curve-fitted to high-order polynomials representing the necessary blast parameters of a TNT equivalent charge using Hopkinson-Cranz scaling ($Z = R/W^{1/3}$) [14]. A comparison of the properties predicted for free airbursts by Kingery and Bulmash [4] with those of Kinney and Graham [5] is performed in [15], where the peak reflected overpressures are found to be in good agreement while the impulses in the work by Kinney and Graham are slightly lower than the corresponding impulses reported by Kingery and Bulmash. In view of these references [3–5], it seems that the blast properties suggested by Kingery and Bulmash [4] are most widely used in the literature (see e.g. [16]). However, these empirical equations are only valid in the experimental range in which they were obtained. In particular, the data in [4] were limited to blast wave interactions with plane and infinite reflecting surfaces and contained limited data for blast parameters at scaled distances beyond the range of 0.40 m/kg$^{1/3}$ $< Z <$ 40 m/kg$^{1/3}$. Some of the parameters were therefore extrapolated to smaller distances using the available data and theoretical considerations. These experiments and empirical equations form the basis for various simplified tools to predict blast loading from a given explosive weight W at a known distance R from the target, where the most commonly used tool is known as the Conventional Weapons Effects Program (ConWep) [17]. When the parameters governing the positive phase are known, the modified Friedlander equation [18–20] with an exponential decay coefficient is typically used to represent the pressure-time history. Karlos et al. [21] reviewed several approaches for calculating the exponential decay parameter and suggested new polynomial equations in determining this parameter for spherical and hemispherical charge conditions.

As the blast wave expands, the pressure decays back to ambient pressure p_1 and a negative phase occurs (where the pressure is below p_1) which typically has a longer duration $t_{\mathrm{d}-}$ than the positive phase. The negative phase results from the momentum of air which generates an overexpansion so that the absolute pressure at the tail of the blast wave falls below atmospheric pressure (see Figure 1.2). This underpressure slows down the surrounding gas molecules, producing a reversed flow back towards the explosion centre. The most commonly used negative phase parameters seem to be those given in the traditional diagrams in the U.S. Army Technical Manual [16]. However, there still seems to be some uncertainty regarding the modelling and treatment of the negative phase of the pressure-time history. The literature reveals three basic representations of the pressure-time history when modelling this phase, i.e., a bilinear approximation [16, 22, 23], an extended Friedlander equation based on

the waveform of the positive phase [24–26] and a cubic representation [27–31]. Rigby et al. [30] reviewed the existing methods in representing the negative phase and evaluated these methods using pressure measurements of a blast wave from a hemispherical charge acting on a rigid target. It was found that bilinear and cubic representations of the negative phase resulted in the best agreement with experimental data.

The blast loading from high-explosive detonations is typically categorized based on the stand-off distance R and the equivalent mass W of TNT by using the scaled distance $Z = R/W^{1/3}$, where it is commonly referred to close-in ($Z < 0.5$ m/kg$^{1/3}$), near-field ($0.5 \leq Z \leq 2.0$ m/kg$^{1/3}$) and far-field ($Z > 2.0$ m/kg$^{1/3}$) detonations as distinct loading domains [32]. As the loading becomes increasingly near-field ($Z \leq 2.0$), the use of the empirical equations requires that the non-uniform spatial distribution of the loading is included in the calculation. This can be done by considering both the incident overpressure $p_{\mathrm{so,max}}$ and the angle of incidence α when determining the reflected pressure acting on the structure. The use of the empirical methods are found to provide good estimates of the blast properties within the underlying range of experimental data (see e.g. [33–37]), i.e., for scaled distances in the range of 0.40 m/kg$^{1/3}$ $< Z <$ 40 m/kg$^{1/3}$. However, the use of these simplified methods is questionable at close-in detonations and numerical simulations are often necessary for an adequate representation of the loading in these environments [36, 38]. This is due to the inherent complexity in such blast environments where the target is often located inside the fireball and there is an interaction between the expanding detonation products and the blast overpressure [37, 39].

1.2.2 Response of blast-loaded plates

In blast-resistant design of protective structures the focus is usually on the structural response due to the positive phase of the blast loading (see e.g. [15–17, 40–42]). This is particularly the case for small values of the scaled distance Z, resulting in high magnitudes of overpressure. In such events the structure is expected to deform in the same direction as the incoming blast wave, i.e., in the intuitive direction. Nurick and Martin [43, 44] presented a comprehensive literature review of thin plates subjected to blast loading. These studies included theoretical considerations, experimental techniques and experimental results for relatively large permanent displacements. Nurick and Martin [44] also suggested a non-dimensional empirical analysis in an attempt to compare experimental results from various studies using different loading parameters, plate dimensions and materials. This approach has proven to be a useful guideline to predict the maximum deflection of impulsively loaded plates.

The dynamic elasto-plastic structural response under pulse loading may be

divided into three categories depending on the intensity of the loading and the permanent mid-point deflection (see Figure 1.3 and [45, 46]). If the structural component oscillates on both sides of its original configuration with a positive permanent deflection this is called Type I. However, if the pulse is more intense the structural component will oscillate only on the positive side of the original configuration (Type II). Finally, the structural component may first deform in the positive direction and then rebound to the negative side of the original configuration (Type III). The two first types of response are intuitive as the final deflection is positive (i.e., in the same direction as the external loading), while the latter type confounds intuition as the permanent deflection is negative (i.e., in the direction opposite to the external loading). This phenomenon was first reported during numerical studies by Symonds and Yu [47] and called counter-intuitive behaviour (CIB). They noted that this behaviour was extremely sensitive to the structural and loading parameters, and concluded that the response pattern was strongly dependent on the peak deflection and the corresponding rotation in the plastic hinges at which reverse motion starts. Thus, CIB only occurred within a narrow range of structural and loading conditions during the transition from elastic to moderate plastic deformations and is frequently referred to as reversed snap buckling (RSB). The unexpected nature of this behaviour has received much attention during the years [48–50], and is still a topic of interest in the literature [51]. Theoretical and numerical investigations have managed to associate the phenomenon with chaotic and complex vibrations [50, 52], and this insight has motivated experiments to evaluate both theoretical and numerical investigations [46,53,54]. The experiments found in the literature observing CIB due to RSB mainly consider projectile impacts where there is no negative loading phase [46–48] or blast events where only the positive phase is considered [51].

While the effect of the positive phase on blast-loaded structures seems to be well understood, the current literature indicates that the research on the influence of the negative phase is rather sparse. The U.S. Army Technical Manual [16] states that the negative phase may influence the response of flexible structures in some blast loading situations, without going into any details of the governing parameters in such events. After reviewing the existing methods in representing the negative phase, Rigby et al. [30] discussed the consequences of choosing an inappropriate model by using an elastic SDOF system. It was shown that the dynamic response was highly dependent on an accurate description of the negative part of the pressure-time history. Bryant et al. [31] used a cubic representation of the negative phase and investigated its influence on the response of blast-loaded reinforced concrete panels and flexible metal wall systems. The negative phase was found to either mitigate or dominate the structural response depending on the timing and pressure magnitude relative to the dynamic response of the structure. Krauthammer and Altenberg [22]

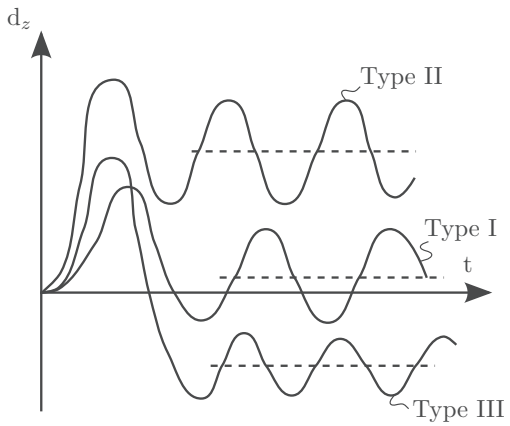

Figure 1.3: Typical response of blast-loaded plates in terms of mid-point deflection-time histories. Dashed lines illustrates the permanent deflections for each type of response.

followed the recommendations in [16] and used a piecewise linear representation of the pressure-time history to investigate the influence of the negative phase on glass panels. Their numerical study indicated that the negative phase dominated the dynamic response for relatively small pressures, i.e., when the peak reflected overpressure was of similar magnitude to the peak negative overpressure. The influence of the negative phase was also found to depend on the dynamic characteristics of the flexible panel relative to the explosive load. In particular, the negative phase was found to dominate the response if it occurred during the elastic rebound. Enhancement of the elastic rebound after maximum deflection was also observed experimentally by Galiev [54] for blast-loaded aluminium plates.

It is evident that depending on the blast intensity the dynamic response of flexible structures may become significantly different. Menkes and Opat [55] reported failure modes on clamped aluminium beams subjected to blast loading using sheet explosives (see Figure 1.4). By monotonically increasing the impulse they identified three different damage modes, i.e., large inelastic deformation (Mode I in Figure 1.4a), tensile tearing at supports (Mode II in Figure 1.4b) and transverse shear at supports (Mode III in Figure 1.4c). Teeling-Smith and Nurick [56] found the same failure modes for clamped circular plates subjected to impulsive loading, and reported that the magnitude and shape of the deformed plates depend on the intensity of the loading. These failure modes were also observed for square plates by Olson et al. [57]. However, a slight change in the interpretation was needed to account for tensile tearing at the supports as failure was first observed at the centre of the boundary before progressing towards the corners with increasing impulse. Subsequent work by

Nurick et al. [58, 59] extended these failure modes by including necking at the boundary for Mode I, and some geometric additions to Mode II by including the amount of tearing at the boundary (called Mode II* in the literature). Experimental evidence was used to show a significant effect of the boundary conditions when predicting tearing. Similar results were also reported by Wierzbicki and Nurick [60].

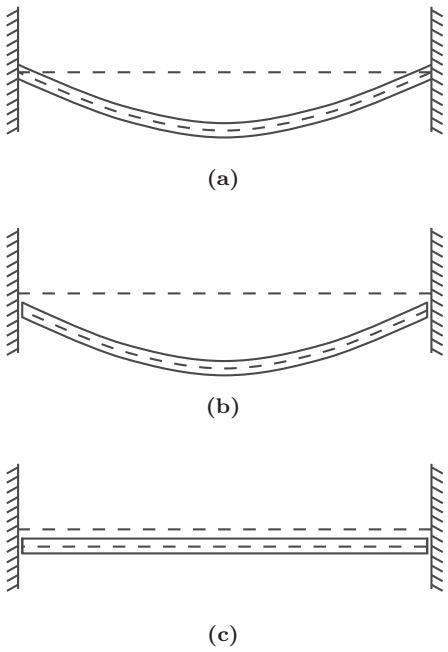

Figure 1.4: Failure modes for impulsively loaded beams and plates [55, 59]: (a) Mode I - Large inelastic deformation, (b) Mode II - Tensile tearing at supports and (c) Mode III - Shear failure at supports.

It is observed that the Type I and Type II responses in Figure 1.3 resemble the Mode I response in Figure 1.4a, and that the plate will respond in a ductile manner and experience a permanently deformed shape (see Figure 1.4a) when subjected to imposed velocities less than a certain value (see Jones [61]). However, when the imposed velocities are equal to this critical value, the plate will fail due to tearing at the supports (see Figure 1.4b). If the impulsive velocities are further increased beyond this critical value, failure will occur and the plastic deformation of the plate will become more localized near the supports until another critical velocity is reached. At this second critical velocity transverse shear failure will occur at the supports (see Figure 1.4c). Thus, as the blast intensity increases and the loading becomes increasingly

impulsive, structural elements exposed to intensive blast loading must have adequate shear capacity to ensure that they do not fail in Mode III if Mode I or Mode II failure is required.

Even though blast events often involve plated structures with holes, the current literature indicates that there is limited research on the influence of holes on the dynamic response of these types of structures. Holes may be induced in plated structures for various applications and reasons, e.g. due to perforations in combined blast and fragmentation events [62] and pre-formed holes in façade systems or passive mitigation systems [63,64]. Rakvåg et al. [65] investigated the response of medium-strength steel plates exposed to pressure pulse loading and the influence of pre-formed holes with different geometries. Although the plates experienced large deformations, there were no signs of failure other than some localization of plastic strain in the extremities of the holes. Schleyer et al. [66] also studied the inelastic deformation of mild steel plates with pre-formed holes subjected to a pressure pulse loading, and evaluated the capabilities of energy-based analytical solutions in predicting the experimental observations. The predictions by the approximate methods were found to be in acceptable agreement with the experimental data, which indicated that such methods may provide design guidelines for blast-loaded plates. Veldman et al. [67] studied the response of pre-pressurized aluminium plates subjected to blast loading. The test panels were reinforced with aluminium extrusions attached to the plates using rivet joints. Consistent failure of the rivet joints motivated tests without reinforcement and only the drilled holes at the rivet locations. It was found that the crack initiation emerged from these holes due to stress concentrations. Complex failure patterns were also observed for thin steel sheets supported on a cellular metal foundation [68], where the cracks originated at laser welded joints.

1.2.3 Fluid-structure interaction

Blast-loaded structures may experience severe blast-structure interaction and considerable work already exists on this subject (see e.g. [69–73]). As discussed in Section 1.2.1, blast-structure interaction occurs when the blast wave encounters a structural surface that is not parallel to the direction of the wave. The blast wave is then reflected and reinforced. Depending on the blast and structural properties, the structure typically behaves as either a rigid or a deformable surface. Fluid-structure interaction (FSI) takes place if the structural surface is allowed to move or deform.

Taylor [74] is considered to be one of the pioneers in the field of FSI in blast environments, suggesting that lightweight structures undertake less momentum compared to heavier structures when exposed to the same blast intensity. That is, the motion of the reflecting surface reduces the pressure acting on

it. Recent years have seen a significant increase in the amount of research investigating the influence of FSI effects on the response of blast-loaded plates. Much of this research was focused on plated structures in underwater blast environments [75–79]. These investigations typically assumed an acoustic medium characterized by an incompressible fluid and linear superposition of weak shock waves. Although the need to account for a compressible fluid behaviour was recognized [73, 76, 80, 81], this was not taken into account during FSI in airblast environments until the works of Kambouchev et al. [70, 82–84] and Hutchinson et al. [85, 86]. The acoustic assumption holds for underwater explosions, but compressibility effects are significant in air even for small magnitudes of blast overpressures. The compressible behaviour of air may results in a significant increase in the magnitude of the stagnation pressure experienced by the structure during the blast-structure interaction, since the reflected overpressure increases with the incident pressure in a highly non-linear manner. A basic understanding of the influence of FSI when the blast wave (in a compressible fluid) interacts with a movable or deformable surface is given in the works of Courant and Friedrichs [87], Toro [88] and Subramaniam et al. [72]. If the structure starts to move, the motion alters the pressure at its surface. Previous research has shown that FSI effects can mitigate the blast load acting on the structure [83–85, 89], especially in situations involving large deformations [70–72]. The blast mitigation has been related to both the induced velocity [71, 72] and to the deformed shape of the structure [89–91]. This is interesting in view of lightweight and flexible structures. Lightweight structures will experience a higher induced velocity after impact and a reduction in the transmitted impulse, while flexible structures will experience the Mode I deformation (see Figure 1.4) and a possible overlapping of the dynamic response and the positive phase duration. This implies that large deformations and energy absorption in structural members are favourable, since the blast wave is partially absorbed through various deformation mechanisms in the structure. Provided that the structural member can sustain the deformation that arise without experiencing failure, this indicates that ductile materials may be utilized in the design of flexible structures by allowing for finite deformations. The FSI may then reduce the transmitted impulse and serve as alternative load paths. However, this requires a thorough understanding of the governing physics in the problem.

A large variety of methods have been proposed during the years to predict the response of blast-loaded structures. These methods range from equivalent static loads based on conventional static design methods, to simplified dynamic solutions based on single-degree-of-freedom (SDOF) methods accounting for the dynamic properties and ductility of the structural component, and finally to more advanced methods like the finite element (FE) method. Thus, the methods and procedures used in blast-resistant design can vary considerably in

complexity, accuracy, computational cost and efficiency. Although approximate methods may provide design guidance, these methods are often based on several assumptions regarding the spatial and temporal distribution of the loading. Advanced numerical techniques are therefore often required for a sufficient insight in both the loading and the resulting dynamic response. A widely used design tool for this class of problems is the explicit non-linear FE method [92]. The uncoupled approach is often the preferred procedure in today's blast-resistant design. The loading is then obtained using either empirical relations from the literature or numerical simulations of the blast wave propagation in an Eulerian (fixed) reference frame. The underlying assumption in this approach is rigid boundary conditions and no deformation of the structure, where the numerical simulations are typically performed in a computational fluid dynamics (CFD) code. These types of codes compute the spatial and temporal pressure distribution along the fluid boundary. Then the obtained pressure history is applied in a computational structural dynamics (CSD) code to determine the corresponding dynamic response. The uncoupled approach therefore makes the inherent assumption that the blast properties are unaltered by the structural motion and vice versa. Since the response of blast-loaded plates is highly non-linear (both in geometry and in material behaviour), this may not be an adequate approach and could result in a non-physical response. Both the pressure distribution and the dynamic response may be significantly influenced due to FSI effects. This was illustrated by Casadei et al. [69] and Børvik et al. [71] by comparing uncoupled and fully coupled FSI simulations for typically industrial applications. Børvik et al. [71] observed considerable variations in the predicted results from uncoupled and coupled methods and emphasized the importance of an accurate quantification of the loading. Recent advancements [93, 94] in the field of FE methods make it now possible to study the FSI effects in blast events involving complex geometries, large deformations, failure and fragmentation. In particular, adaptive mesh refinement (AMR) [95–98] in both the fluid and structural sub-domains allows for a sufficiently fine mesh size to represent the near instantaneous rise in pressure over the blast wave and to predict crack propagation in the structure without too much loss of mass when using element erosion. This can be used to investigate the effect of FSI on the dynamic response of plated structures, both with and without holes.

1.2.4 Experimental techniques

As discussed in Section 1.2.3, numerical methods are often required for sufficient insight during blast-structure interaction. Before using such computational methods their performance should be validated in terms of reliability, robustness and effectiveness in predicting both the loading and the response. Experimental validation is ideal since it represents the actual physics of the problem. Full-scale

testing of realistic blast scenarios is normally too expensive and time consuming. This requires explosive charges in the range of 100-30,000 kg TNT and large outdoor areas [99, 100]. Even medium-scale detonations (1-100 kg TNT at stand-off distances of several meters [101,102]) are challenging to perform in non-military laboratory settings. At these scales instrumentation becomes difficult which often results in a qualitative rather than a quantitative assessment of the experimental observations. Controlled small-scale experiments in laboratory environments should therefore be used to evaluate current computational methods and improve the understanding of the underlying physics during blast events.

Research on blast-loaded plates using small-scale explosive detonations typically involves plate dimensions up to 0.5 m, explosive charges are less than 100 g and detonated at distances up to 0.5 m from the test specimen [44, 103, 104]. This is often carried out in controlled laboratory environments at scaled distances corresponding to close-in or near-field detonations ($Z < 2.0$ m/kg$^{1/3}$) using either the ballistic pendulum approach (see e.g. [44, 104–109]), or free-field airblast experiments using an explosive charge at a given stand-off distance from the plate (see e.g. [54, 68, 103, 110]). In the latter setup, the plate is typically installed in a mounting frame which is fixed to the ground. All setups are in general interested in an accurate quantification of the loading and on the resulting structural response. The ballistic pendulum approach uses the maximum angle reached by the pendulum to determine the impulse imparted to the plate, while pressure sensors positioned in the vicinity of the plate may be used to indicate the loading in free airblast tests. The spatial and temporal distribution of the blast loading are controlled by varying the explosive material, charge geometry, explosive mass and stand-off distance. The structural response are often reported in terms of the permanent deflection and deformed shape of the plate.

Experimentation involving small-scale detonations have many benefits and are necessary to investigate the inherent complexity in such blast environments (e.g. highly non-uniform spatial and temporal pressure distributions and the interaction between the fireball and the blast overpressure in the vicinity of the target). However, such experiments also introduce some challenges (e.g. ground reflections, light flashes and fireballs) and special care must be taken to ensure accurate geometries and alignments of the charge relative to the structure. Small geometric imperfections and deviations in the alignment may lead to non-symmetric spatial and temporal distributions of the pressure and variations in blast parameters between each test at the same configuration [111]. Moreover, high-explosives may be hazardous and involves legal restrictions which often make such experiments less available for research purposes.

Due to these challenges, alternative techniques have been developed to generate

a blast loading similar to those from actual free-field detonations. Examples of such techniques are the pressure blow down apparatus [65, 66, 112] and shock tube facilities [113–121]. These alternative techniques and scaled explosive detonations cover distinct loading regimes. Scaled explosive detonations are ideal for close-in and near-field testing, while the pressure blow down apparatus and shock tubes produce a blast environment resembling that of far-field detonations. Briefly stated, scaled explosive detonations typically result in peak reflected overpressures above 1 MPa and durations shorter than 1 ms, while the pressure blow down apparatus and shock tubes are characterized by peak reflected overpressures below 1 MPa and durations greater than 1 ms. In the pressure blow down apparatus, the transient loading is generated by using a pressure vessel where the test component is clamped between the centre flanges. The test component then divides the pressure vessel in two pressure chambers and a rapid evacuation of the pressure in one of the chambers will produce a uniform pulse pressure loading on the test specimen. The shock tube technique is well-known within the field of gas dynamics using well-defined and easily controllable initial conditions [122–125]. It typically consists of a gas-filled tube in which a high-pressure chamber is separated from a low-pressure chamber using multiple diaphragms. A sudden opening of the diaphragms generates a shock wave propagating downstream the diaphragms and into the low-pressure chamber, while rarefaction waves expand into the high-pressure chamber. Using a relatively small ratio between the lengths of the two pressure chambers, this experimental setup differs from traditional shock tubes in the way that the reflected rarefaction waves catch up with the shock wave resulting in pressure profiles similar to that from an explosive detonation. It should be noted that the blast wave may also be generated using explosive-driven shock tubes where the pressurized air is replaced by an explosive detonation in the high-pressure chamber [118]. The interaction between a planar blast wave and a structure may then be studied by placing a test object inside or at the end of the tube. Pressure blow down apparatuses and shock tube facilities therefore allow for the evaluation of blast-structure interaction without the need to considering the inherent complexity in close-in and near-field detonations.

Finally, it is emphasized that measurement techniques are equally important as the experimental setup since they determine the usefulness, reliability and validity of the experimental data. Until recently it was difficult to measure the deflection-time history of plates exposed to blast loading. However, the recent development of three-dimensional digital image correlation (3D-DIC) techniques has enabled such measurements of the complete deformation history during blast experiments [103, 126, 127]. The two most common techniques are the subset-based local DIC [128] and the finite element-based global DIC [129]. Tiwari et al. [126] and Zhao et al. [127] used subset-based local 3D-DIC to obtain transient deformations of thin aluminium plates during buried blast

events to simulate realistic ground conditions and to validate a dimensional analysis, respectively. Spranghers et al. [103] used a similar subset-based DIC technique for measurements of aluminium plates under free airblast loading conditions.

1.3 Objectives

The increased demand for computer-aided design of safer and more cost-effective protective structures introduces a need to evaluate the performance of current computational methods in predicting both the loading and the response in blast events involving flexible structures. The objective of this thesis is therefore to develop an improved understanding of the behaviour and modelling of flexible structures subjected to blast loading.

The overall research objectives are as following:

- Obtain knowledge and understanding of the current state-of-the-art in testing, behaviour and modelling of blast-loaded structures.
- Establish test setups to produce controlled, repeatable blast loading in laboratory environments. Special focus is placed on the establishment of a shock tube facility capable of producing a loading similar to that from actual explosive detonations.
- Use the test setups to obtain experimental data covering a wide range of dynamic responses of thin aluminium and steel plates.
- Evaluate the capabilities of computational methods typically used in protective design in predicting the experimental observations, i.e., both the loading and the resulting response.
- Identify parameters influencing the dynamic response of thin aluminium and steel plates in the experimental and numerical studies.

This type of knowledge, understanding and investigations are important to meet the current demand for innovative and optimized solutions considering safety as well as architectural requirements in blast-resistant design.

1.4 Scope

Due to the wide range of topics related to the behaviour and modelling of flexible structures subjected to blast loading, it is necessary to impose some limitations on the present work:

- The test setups are limited to small-scale free-field airblasts and shock tube tests in controlled environments.
- The blast environments are limited to those from non-contact and unconfined explosive detonations external to the target where the dominant effect is considered to be the blast overpressure.
- The material modelling in the numerical simulations of the blast-loaded plates are limited to isotropic behaviour and ductile materials.
- The shock physics and thermodynamics necessary to understand compressible fluid flow are limited to the idealized gas theory. Compressible fluid flow is an active field of research and detailed studies within this topic are not considered in this work.
- Numerical simulations are restricted to the finite element software EUROPLEXUS [130].

Other, more detailed restrictions, are presented where needed.

1.5 Contributions of this work

This thesis contributes to an improved understanding of the behaviour and modelling of flexible structures subjected to blast loading. The works of this thesis have been presented at international conferences and published in international peer-reviewed journals and in the form of EC-JRC Technical reports. The main publications from this thesis are:

Journal publications

I V. Aune, E. Fagerholt, K. O. Hauge, M. Langseth, T. Børvik. *Experimental study on the response of thin aluminium and steel plates subjected to airblast loading.* International Journal of Impact Engineering **90** (2016), p. 106-121. DOI: 10.1016/j.ijimpeng.2015.11.017.

II V. Aune, E. Fagerholt, M. Langseth, T. Børvik. *A shock tube facility to generate blast loading on structures.* International Journal of Protective Structures **7(3)** (2016), p. 340-366. DOI: 10.1177/2041419616666236.

III V. Aune, G. Valsamos, F. Casadei, M. Larcher, M. Langseth, T. Børvik. *Numerical study on the structural response of blast-loaded thin aluminium and steel plates.* International Journal of Impact Engineering **99** (2017), p. 131-144. DOI: 10.1016/j.ijimpeng.2016.08.010.

Conference proceedings and contributions

IV V. Aune, T. Børvik, M. Langseth. *Behaviour of plated structures subjected to blast loading*. European Physical Journal - Web of Conference **94** (2015), 01015. DOI: 10.1051/epjconf/20159401015.

V V. Aune, T. Børvik, M. Langseth. *On the fluid-structure interaction effects of plated structures subjected to blast loading – An experimental and numerical investigation*. In: B. Skallerud & H. I. Andersson (eds.). Proceedings of the 8th National Conference on Computational Mechanics (MekIT'15), Trondheim, Norway, 18-19 May 2015, pages 59-83. ISBN 978-84-944244-9-6.

VI V. Aune, G. Valsamos, F. Casadei, M. Larcher, M. Langseth, T. Børvik. *Inelastic response of thin aluminium plates exposed to blast loading*. In: 1st International Conference on Impact Loading of Structures and Materials (ICILSM), Turin, Italy, 22-26 May 2016.

Books/Compendiums/Technical reports

VII V. Aune, T. Børvik, M. Langseth. *Lecture Notes in TKT4128 Impact Mechanics: An introduction to blast mechanics*. Norwegian University of Science and Technology, Department of Structural Engineering, SIMLab (2015).

VIII V. Aune, F. Casadei, G. Valsamos, T. Børvik. *Formulation and implementation of the VPJC material model in EUROPLEXUS*. Technical Report EUR 27982 EN. European Commission, Luxembourg (2016). DOI: 10.2788/609529. ISBN: 978-92-79-59746-6.

Other publications related to this work, but not explicitly covered in this thesis, are:

Conference proceedings and contributions

IX M. Kristoffersen, K. Osnes, S.R. Haug, V. Aune, T. Børvik. *Shock tube testing and numerical simulations of concrete slabs*. In: 1st International Conference on Impact Loading of Structures and Materials (ICILSM), Turin, Italy, 22-26 May 2016.

Technical reports

X F. Casadei, V. Aune, G. Valsamos, M. Larcher. *Description of the elasto-plastic material routine SGDI*. Technical Report EUR 27434 EN. European Commission, Luxembourg (2015). DOI: 10.2788/403240. ISBN: 978-92-79-51226-1.

XI F. Casadei, G. Valsamos, M. Larcher, V. Aune. *Some notes on the organization of routines for solid materials in EUROPLEXUS*. Technical Report EUR 27683 EN. European Commission, Luxembourg (2015). DOI: 10.2788/98573. ISBN: 978-92-79-54259-6.

XII F. Casadei, V. Aune, G. Valsamos, M. Larcher. *Testing of the Johnson-Cook material model VPJC in EUROPLEXUS*. Technical Report EUR 27594 EN. European Commission, Luxembourg (2015). DOI: 10.2788/02760. ISBN: 978-92-79-53999-2.

XIII F. Casadei, V. Aune, G. Valsamos, M. Larcher. *Accounting for large membrane strains in Q4GS and T3GS elements in EUROPLEXUS*. Technical Report EUR 27836 EN. European Commission, Luxembourg (2016). DOI: 10.2788/888282. ISBN: 978-92-79-57731-4.

XIV F. Casadei, V. Aune, G. Valsamos, M. Larcher. *Generalization of the pinball contact/impact model for use with mesh adaptivity in EUROPLEXUS*. Technical Report EUR 27888 EN. European Commission, Luxembourg (2016). DOI: 10.2788/333017. ISBN: 978-92-79-57972-1.

XV F. Casadei, V. Aune, F. Daude, P. Galon, G. Valsamos, M. Larcher. *Shock tube tests with coupled 1D-3D models in EUROPLEXUS*. Technical Report EUR 27890 EN. European Commission, Luxembourg (2016). DOI: 10.2788/702507. ISBN: 978-92-79-57976-9.

In addition, several master's theses at NTNU [131–137] have been produced related to this work. All of these master's theses have contributed positively in writing this thesis.

Part II

Free-field Airblast Loading

2

Blast loading

The typical protection scenario in blast-resistant design of civilian infrastructure is a high-explosive (HE) detonation (see e.g. [16, 100–102, 138–140]), where the dominant effect of the HE detonation is the blast overpressure. **Part II** of this thesis is therefore limited to the blast overpressure origination from an HE detonation and the resulting dynamic response of flexible structures. The objective of this chapter is to introduce the definitions and phenomena that are essential to model and understand the loading generated by an explosive detonation. Although the fundamental aspects of these topics are well established in the literature [3, 15, 16, 32, 141–143], such a presentation is necessary for the understanding and discussion of the results later in this thesis.

2.1 Blast phenomena

Solid explosives must detonate to produce any explosive effect other than a fire. The term detonation refers to a very rapid and stable chemical reaction which proceeds through the explosive material at a speed (called the detonation velocity) which is supersonic in the unreacted explosive. Detonation velocities range from 1900 to 9000 m/s for most high explosives. The detonation wave rapidly converts the solid or liquid explosive into a very hot, dense, high-pressure gas, and the volume of this gas which initially was the explosive material is then the source of a blast wave propagating into the surrounding air. Pressures immediately behind the detonation front range from approximately 10 GPa to 30 GPa and temperatures of about 3000 - 4000 °C [143]. Only about one-third of the total chemical energy available in most high explosives is released in the detonation process. The remaining two-thirds are released more slowly as the detonation products mix with air and burn. This afterburning process is much slower than the detonation and its influence on the blast wave properties diminishes with the distance. However, close to the point of detonation or at later stages of the process the blast wave can be affected by the afterburning, particularly for explosions in confined spaces.

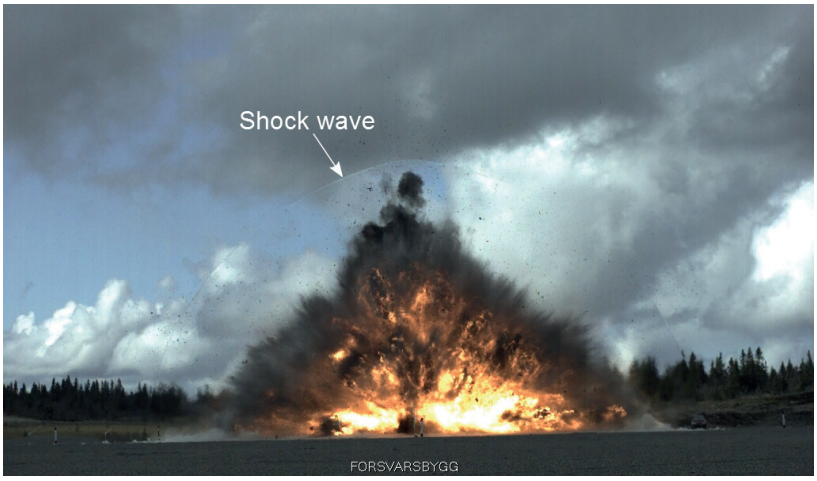

Figure 2.1: Detonation of a VBIED comprising a mixture of 950 kg ANFO. The copyright of this picture is the property of the Norwegian Defence Estate Agency.

Figure 2.1 illustrates the events occurring during a typical HE detonation. This is a photo taken immediately after the detonation of a vehicle-born improvised explosive device (VBIED), where the bomb comprised a mixture of 950 kg ammonium nitrate and fuel oil (ANFO). The bomb is estimated to explode with an energy similar to that of approximately 400 to 700 kg trinitrotoluene (TNT). It is observed that the energy (i.e., high-pressure gas) expands radially and compresses the surrounding air to produce an incident shock (or blast) wave. The blast wave is visible in Figure 2.1 due to the jump in density across the shock wave and, since the explosion takes place at the surface and in free air, it expands hemispherically. The high-temperature gases arising from the detonation form a fireball. This fireball is lagging behind the blast wave, and may last for a considerable time radiating heat and may cause thermal damage or fires close to the point of detonation. It is also noticed hazardous fragments accelerated by the blast wave. These types of fragments are often categorized as primary and secondary fragments. Primary fragments are defined as parts initially contained in the explosive device (e.g. ball bearings or nails) or parts from the fractured casing (or container) of the explosive (e.g. the vehicle). Secondary fragments are a result of objects external to the explosive device that are accelerated by the blast wave and corresponding pressures. Typical examples of secondary fragments are building debris caused by the blast wave (e.g. shattering windows) or loose items (e.g. gravel and sand). Thus, if the explosive device is close to the target, the target may experience the combined effect of fragmentation and blast loading. This is a complex loading situation outside the scope of this thesis.

As the distance from the point of detonation increases, the dominant effect of an explosion is mainly the blast wave itself. This is composed of a high-intensity shock front which expands outward from the surface of the explosive into the surrounding air (Figure 2.1). This is due to the fact that the compressed layer (i.e., the shock wave) conserves most of the energy released by the explosion as pressure energy. The shock wave (or blast wave) therefore propagates outwards from the centre of the explosion due to the disequilibrium between the highly compressed air in the blast wave and the undisturbed air in front of it. As the wave expands, it decays in strength, increases in duration, and decreases in velocity (Figure 2.2). The pressure decreases rapidly (with the cube of the distance) due to geometrical (i.e., spherical) divergence and the dissipation of energy in heating the air. At this stage the chemical reaction is completed, except from some afterburning associated with the hot explosion products mixing with the surrounding atmosphere. Thus, an explosion can be visualized as a sphere of highly compressed air that expands until reaching equilibrium with the surrounding air.

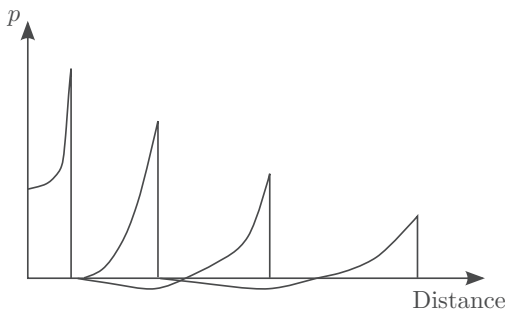

Figure 2.2: Influence of the distance from the explosion on the blast pressure (inspired by [15]).

This expanding sphere is called the incident blast wave and is characterized by an almost instantaneous rise (within a timescale of nanoseconds) from ambient pressure p_1 to a peak incident overpressure $p_{so,max}$ (see Figure 2.3). The pressure decays exponentially back to the ambient condition p_1 within a very short duration t_{d+} in time (i.e., typically in milliseconds). This is known as the positive (overpressure) phase. As the shock front expands, a negative phase occurs (where the pressure is below p_1) which typically has a longer duration t_{d-} than the positive phase. The negative phase results from the momentum of air which generates an overexpansion so that the absolute pressure at the tail of the blast wave falls below the ambient pressure (Figure 2.3). This underpressure slows down the surrounding gas molecules, producing a reversal of flow back towards the point of detonation.

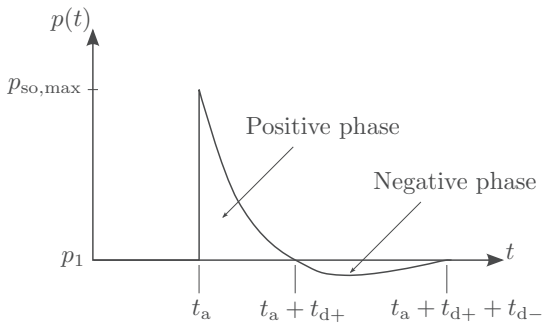

Figure 2.3: Typical pressure-time history for the incident blast wave.

As the wave expands, it impinges on structures located within its path and then the structure is loaded by the blast pressure (Figure 2.4). The magnitude, duration and distribution of the blast load are a function of the explosive properties (i.e., the explosive material, weight and shape), the location of the detonation relative to the structure (i.e., the stand-off distance R), potential objects located between the detonation and the structure, and finally the magnitude and amplification of the pressure by its interaction with the ground or the structure itself.

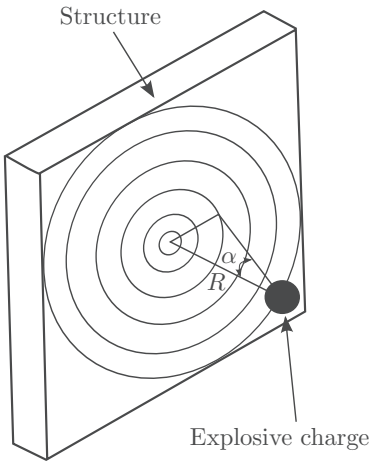

Figure 2.4: Distribution of reflected pressure depending on the angle of incidence α. The angle of incidence is defined as the angle between the normal vector and the direct vector between the charge and point of interest on the structure. The normal vector is also known as the stand-off distance R and is the shortest distance from the explosive charge to the structure [144].

Thus, when the blast wave interacts with a structure that is not parallel to

the direction of the wave, it is reflected and reinforced. This is known as the reflected overpressure p_{r} and the reflected blast wave has the same general shape as the incident wave (Figure 2.5). The reflected overpressure is also the actual loading to be used in the blast-resistant design, and may be represented as a pressure-time history described by exponential functions such as the modified Friedlander equation [18, 143], i.e.,

$$p_{\mathrm{r}}(t) = p_{\mathrm{r,max}} \left(1 - \frac{t - t_{\mathrm{a}}}{t_{\mathrm{d+}}}\right) \exp\left(\frac{-b(t - t_{\mathrm{a}})}{t_{\mathrm{d+}}}\right) \tag{2.1}$$

where $p_{\mathrm{r,max}}$ is the peak reflected overpressure and b is the exponential decay coefficient. It can be shown that the peak reflected overpressure is a function of the peak incident overpressure $p_{\mathrm{so,max}}$ through the well-known relation (see e.g. [143, 145])

$$p_{\mathrm{r,max}} = 2p_{\mathrm{so,max}} \left(\frac{7p_1 + 4p_{\mathrm{so,max}}}{7p_1 + p_{\mathrm{so,max}}}\right) \tag{2.2}$$

where it is assumed an ideal gas behaviour of the gas and the Rankine-Hugoniot relations [146–149]. Eq. (2.2) also proves that the peak reflected overpressure $p_{\mathrm{r,max}}$ is always greater than the peak incident overpressure $p_{\mathrm{so,max}}$ for the same explosive properties and at the same distance from the explosion. It is seen that small magnitudes of the incident overpressure ($p_{\mathrm{so,max}} \to 0$) result in a reflected overpressure twice the incident overpressure, while strong shocks ($p_{\mathrm{so,max}} \to \infty$) result in an upper limit of $p_{\mathrm{r,max}}/p_{\mathrm{so,max}} = 8$.

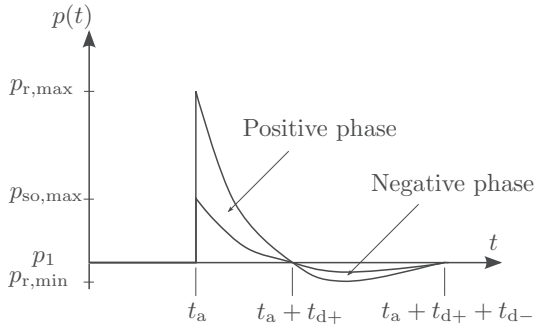

Figure 2.5: Typical incident and reflected pressure profiles after reflecting on an infinite and planar surface.

The integrated area under the pressure-time history is defined as the specific impulse i, where both the positive and negative phase contributes to the total specific impulse. The specific impulse of the positive phase $i_{\mathrm{r+}}$ may be expressed

using Eq. (2.1) as

$$\begin{aligned} i_{\mathrm{r}+} &= \int_{t_\mathrm{a}}^{t_\mathrm{a}+t_{\mathrm{d}+}} p_{\mathrm{r,max}} \left(1 - \frac{t - t_\mathrm{a}}{t_{\mathrm{d}+}}\right) \exp\left(\frac{-b(t - t_\mathrm{a})}{t_{\mathrm{d}+}}\right) dt \\ &= \frac{p_{\mathrm{r,max}} t_{\mathrm{d}+}}{b^2} \left[b - 1 + \exp(-b)\right] \end{aligned} \tag{2.3}$$

This non-linear equation can also be solved iteratively to determine the value of the decay parameter b which produces the impulse $i_{\mathrm{r}+}$ when the parameters $p_{\mathrm{r,max}}$, $t_{\mathrm{d}+}$ and $i_{\mathrm{r}+}$ are known. Also note that the same expressions are valid for the incident blast wave when substituting $p_{\mathrm{r,max}}$ with $p_{\mathrm{so,max}}$ in Eqs. (2.1) and (2.3).

The magnitude of the peak reflected overpressure is dependent on both the angle of incidence α and the peak incident overpressure $p_{\mathrm{so,max}}$, where the latter is a function of the explosive weight and distance from the point of detonation (Figure 2.4). The point of impact on the structure will experience the maximum reflected pressure when the blast wave encounters a surface that is perpendicular to the direction of propagation (see Figure 2.6a), while the structure will only experience the incident pressure when the surface is parallel to the incoming blast wave (see Figure 2.6b).

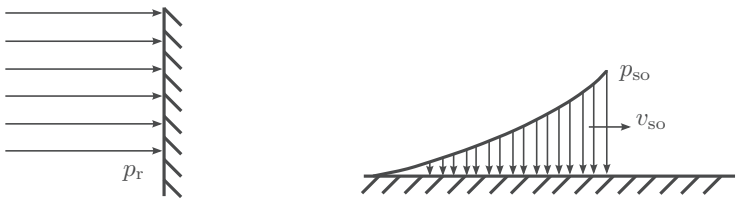

Figure 2.6: Illustration of side-on and head-on pressure loading (inspired by [143]): (a) head-on loading ($\alpha = 0°$) and (b) side-on loading ($\alpha = 90°$).

Figure 2.7 shows the reflected pressure coefficient $C_{\mathrm{r}\alpha} = p_{\mathrm{r}\alpha}/p_{\mathrm{so,max}}$ for typical angles of incidence. These data are based on measurements from experiments using TNT and Pentolite where the shock wave impacts the structure at an oblique angle [16, 150].

It is observed that the peak reflected overpressure $p_{\mathrm{r}\alpha}$ can be almost 13 times greater than the peak incident overpressure, and the reflected pressure coefficient are significantly greater at smaller stand-off distances (i.e., for larger incident pressures). Also note that the upper limit predicted by the Rankine-Hugoniot relations and Eq. (2.2) is clearly exceeded at higher values of the incident

overpressure $p_{so,max}$. This is due to the fact that air ionizes and dissociates as the shock strength increases and γ is no longer constant. In fact, the real upper limit ratio may be as high as 20 [3]. This pressure amplification is explained by the propagation of the blast wave. As the wave travels, it accelerates air particles that collide with the structural surface upon impact. In an ideal linear elastic case the particles would be able to bounce back freely resulting in a reflected pressure equal to the incident pressure. The structure would then experience a doubling of the acting pressure. In a strong blast wave, as for a shock wave which is a non-linear phenomenon, the reflection of these particles is obstructed by subsequent air particles arriving at the reflecting surface. Thus, the air molecules adjacent to the structure are unable to move freely which again result in compression and heating of the shock wave and the structure would experience a pressure significantly larger than the incident pressure. This is called gas ionization and dissociation effects, and is often related to strong shocks and close range detonations [3, 143].

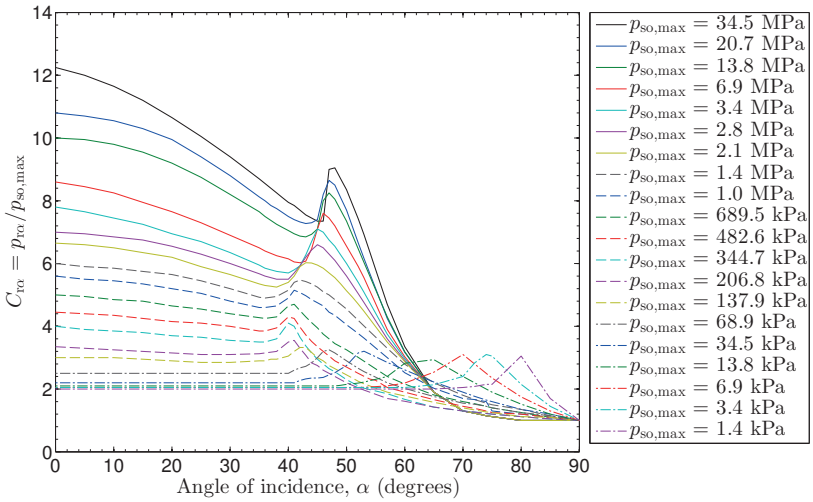

Figure 2.7: Reflected pressure coefficient $C_{r\alpha}$ versus angle of incidence α [16]. Note that $\alpha = 0°$ means that the shock wave is perpendicular to the surface (head-on), while $\alpha = 90°$ implies that the propagation of the wave is parallel to the surface (side-on).

Thus, when considering the reflection of a blast wave from a surface, the angle of incidence α and the peak incident overpressure $p_{so,max}$ must be defined. Moreover, oblique reflection is classified as either regular or Mach reflection. Regular reflections occur at angles of incidence from 0° up to approximately 40° in air (Figure 2.8a). For this particular type of reflection the incident shock wave travels through still air (i.e., region 1 in Figure 2.8a) at velocity v_{so} where the front is oriented with α relative to the structural surface. Properties behind

this front (i.e., region 2 in Figure 2.8a) are those for a free airburst blast wave and at contact with the surface the flow behind the incident shock is reversed. This is due to the component of the flow normal to the surface which has to be zero at impact. Thus, the shock is reflected from the structure at a reflection angle α_r that is different from α and the conditions in region 3 in Figure 2.8a represent the reflected shock properties. From a physical point of view, a pressure sensor flush mounted at the structural surface would record only the ambient pressure p_1 and the reflected overpressure $p_{r\alpha}$ (i.e., a direct jump from region 1 to region 3) as the wave propagate along the wall. However, a sensor mounted at a short distance from the surface would record p_1, then p_{so}, and finally p_r. The Mach reflection process occurs when α exceeds some critical angle, depending on the shock strength. This critical angle is about 40° in air. Mach reflection is a complex process and is sometimes described as a burst-of-pressure-type effect where the incident wave graze the reflecting surface (see Figure 2.8b) rather than bouncing back as is the case at lower values of α. The result is that the reflected wave catch up and coalesces with the incident wave at some point above the reflected surface to produce a third wave front called the Mach stem (or Mach front). The point of coalescence of the three waves is called the triple point. A slipstream region occurs at the boundary behind the Mach stem and reflected waves where different densities and particle velocities exist (i.e., a contact discontinuity). However, the pressure is constant over this region. Thus, when the Mach wave is formed at the structural surface (or due to reflections from the ground), it grows with the locus of the triple point as the shock systems move along the surface (Figure 2.8b). Mach reflection is also evident in Figure 2.7 for angles of incidence above 40°. Note that although head-on loading (i.e., normal reflection) usually provides upper limits for blast loads on structures, smaller values of the peak incident overpressure $p_{so,max}$ at larger angles of incident may result in a larger reflected pressure coefficient.

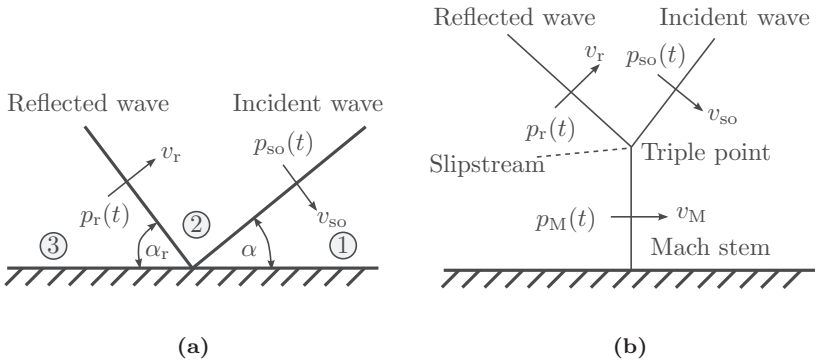

Figure 2.8: Illustration of oblique reflection (inspired by [3, 143]): (a) regular reflection ($0 < \alpha \lesssim 40°$) and (b) Mach reflection ($\alpha \gtrsim 40°$).

Typical examples of scenarios where the formation of the Mach stem is important is when an explosive device detonates at a height H above the ground that is smaller than the distance to the structure ($H < R$ in Figure 2.9), and also when a device is detonated inside a structure where the angles of incidence on the internal surfaces can vary over a wide range. The former example is illustrated in Figure 2.9 for an airburst detonation. It is seen that the reflection from the ground (i.e., an enhanced shock) interacts with the incident shock wave and produces the Mach front. For design purposes, it is assumed that the Mach front is a plane wave with a uniform pressure distribution, and that the pressure magnitude is about the same as that of the incident overpressure p_{so} (it is also sometimes larger) [142]. If the triple point is above the structure (i.e., the Mach front is taller than the structure), it can be further assumed that the entire structure is loaded by a uniform pressure distribution.

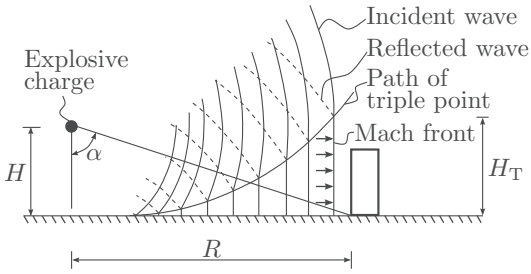

Figure 2.9: Illustration of a blast environment from an airburst (inspired by [16]).

However, if the triple point is below the structure's full height, the pressure distribution must be adjusted accordingly (i.e., a uniform pressure distribution up to the triple point and the oblique incident pressure above it). The calculation of the pressure acting on the structure is then performed by first determining the distance between the explosive charge and the respective points of interest (see Figure 2.4). Then, the blast parameters are computed according to a suitable method (e.g. the empirical equations by Kingery and Bulmash [4]), and finally, the pressure-time history $p_{\mathrm{r}}(t)$ at the structural surface is computed as a function of α according to Figure 2.7. Diagrams for the estimation of the height of the triple point H_T as a function of stand-off distance R and explosive weight W may be found in [16]. Finally, the corresponding reflected impulse $i_{\mathrm{r}\alpha+}$ for the positive phase as a function of α can be found in Figure 2.10. Note that the impulse in Figure 2.10 is scaled with respect to the cube root of the explosive mass ($\bar{i}_{\mathrm{r}\alpha+} = i_{\mathrm{r}\alpha+}/W^{1/3}$), and that if the incident $i_{\mathrm{so}+}$ and reflected $i_{\mathrm{r}+}$ impulses are known the oblique impulse $i_{\mathrm{r}\alpha+}$ can be found by the following interpolation equation [143]

$$i_{\mathrm{r}\alpha+} = i_{\mathrm{so}+}\left(1 + \cos\alpha - 2\cos^2\alpha\right) + i_{\mathrm{r}+}\cos^2\alpha \tag{2.4}$$

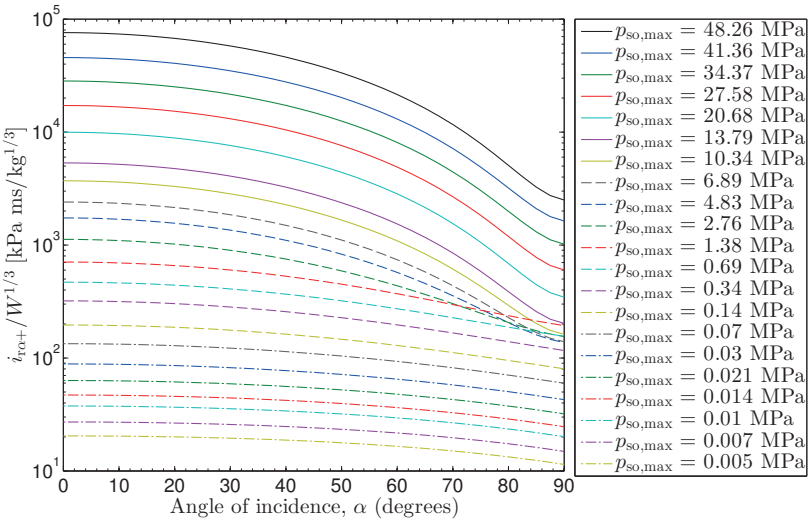

Figure 2.10: Reflected scaled impulse $i_{r\alpha+}$ versus angle of incidence α [16].

2.2 Blast environments

The explosion may be categorized into three distinct airblast environments depending on the position of the charge relative to the target (see e.g. [16]). The differentiation is typically based on the height above the ground H and the shortest distance R from the point of detonation to the target (i.e., the stand-off distance). In the particular case of a free airburst detonation (see Figure 2.11), the charge is detonated in the air and the blast wave expands spherically and impact the target before encountering any other obstacles or surfaces (i.e., $H > R$).

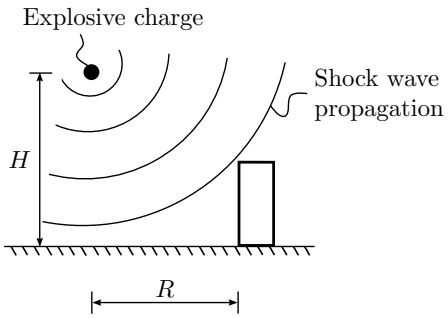

Figure 2.11: Illustration of a free airburst blast environment.

If the charge is detonated closer to the ground than the target (i.e., $H < R$), the explosion is called an airburst detonation (Figure 2.12). The blast wave will then impact the target after being reflected from the ground. Depending on the height of the triple point, the target will be partly or entirely loaded by the Mach front (see also Figure 2.9).

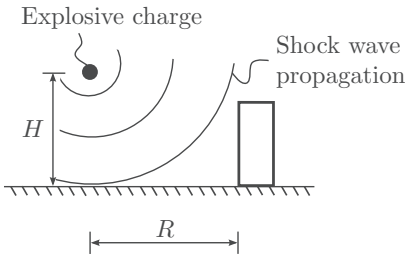

Figure 2.12: Illustration of an airburst blast environment.

The Mach front is typical for airbursts since the reflected wave (dotted line in Figure 2.13) catch up with and coalesces with the incident wave (solid line in Figure 2.13), forming the path of the triple point (see dashed-dotted line in Figure 2.13).

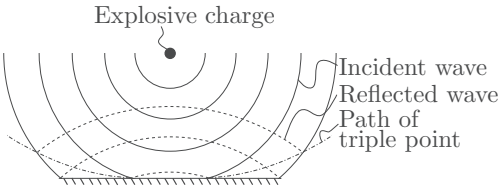

Figure 2.13: Illustration of shock wave reflection and path of the triple point in an airburst (inspired by [15]).

Finally, if the explosive charge is detonated at or very close to the ground, the blast wave immediately interacts with the ground before expanding hemispherically towards the target (Figure 2.14). As already illustrated in Figure 2.1, this is the typical loading scenario for a VBIED and is defined as a surface burst. Note that instead of producing a Mach front, the incident blast wave is reflected immediately from the ground resulting in higher pressures.

If the ground was a rigid surface, the resulting pressure would be twice that produced by the same charge under free airburst conditions. This implies that the pressure relations developed for free airbursts may be applicable also in the

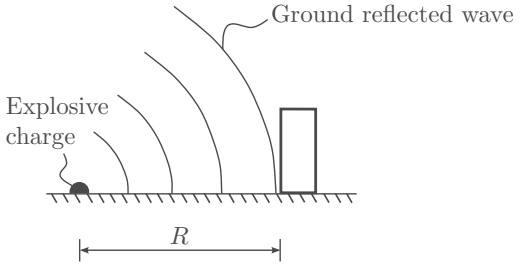

Figure 2.14: Illustration of a surface burst environment.

case of surface bursts by using twice the explosive weight. However, depending on the soil and type of explosive, some of the energy will be absorbed by the ground due to cratering (i.e., through displacement and fragmentation of material from the ground surface) and experience indicates that a multiplying factor between 1.7 and 1.8 should be applied (see e.g. [151] and Figure 1.1d). Moreover, the characteristics of the blast wave generated from a surface burst are similar to that of the Mach front. That is, for a sufficiently large stand-off distance R (i.e., far-field loading), the blast wave can be assumed to be plane and uniformly distributed over the target (see Figure 2.15).

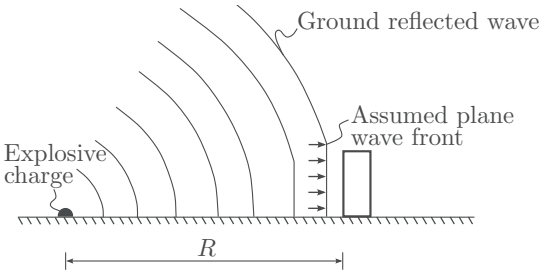

Figure 2.15: Assumed plane wave front in surface burst blast environment (inspired by [16]).

This shows that the magnitude and pressure distribution of a blast-loaded structure are not only dependent on the properties of the explosives, but also the location of the detonation relative to the structure which may result in reinforcement of the pressure through interactions with the ground or other surrounding surfaces.

2.3 Explosives and TNT equivalence

Explosive materials are commonly distinguished based on their sensitivity to detonation. An explosive is classified as a primary explosive if it is easily detonated by a simple ignition, such as a spark, flame or impact. Examples of such materials are mercury fulminate, lead and silver azide, and lead styphnate [143]. Secondary explosives are detonated less easily than primary explosives. To detonate a secondary explosive it is necessary to use a detonator (typically a primary explosive). The high-velocity shock wave produced by the detonator travels at the detonation velocity through the secondary explosive charge, compresses it and causes it to undergo adiabatic heating. A well-known and much used secondary explosive is Composition C-4 (hereafter denoted C-4), which is a member of the Composition C family consisting primarily of RDX. C-4 can easily be moulded into any desired shape, it can be pressed into any gaps, cracks, holes and voids, and it is extremely stable. Other examples of these materials are TNT and RDX.

Of all explosives available today (far too many to be mentioned), TNT holds a special position. As well as being a very effective explosive, TNT is widely accepted as the basis for comparison with other high-explosive materials. This is known as the free air equivalent weight of TNT (or TNT equivalent) [16]. This is the weight of TNT required to produce a particular blast parameter of equal magnitude as that produced by a unit weight of the explosive of interest [142]. The TNT equivalent is typically determined based on thermodynamic calculations and the energy released during the detonation. Thus, first the chemical equations have to be balanced. As an example, and without going into any details, TNT has the chemical formula $C_6H_2\left(NO_2\right)_3CH_3$, which gives the molecular formula $C_7H_5N_3O_6$ (or $7C + 5H + 3N + 6O$). The balanced equation, showing the products of reaction resulting from the detonation of TNT, is given as [141]

$$C_6H_2\left(NO_2\right)_3CH_3 \quad \rightarrow \quad 1.5N_2 + 2.5H_2O + 3.5CO + 3.5C \tag{2.5}$$

Thermodynamic calculations can then be conducted from Eq. (2.5), but this is outside the scope of this thesis and the reader is referred to [141, 142] for a more detailed presentation.

The result of such calculations and some characteristic properties of typical explosives are given in Table 2.1. It is observed that 1 kg of TNT typically releases 4100 - 4900 kJ upon detonation.

The TNT equivalent is a universal quantity and is commonly used in the estimation of blast parameters. An equivalent weight of TNT W_{TNT} may

Table 2.1: Some characteristic properties of typical explosives [142].

Explosive type	Explosive density ρ_{exp} [g/cm^3]	Detonation velocity v_{exp} [km/s]	Heat of detonation E_{exp} [kJ/kg]
Nitroglycerin	1.60	7.58	6300
PETN	1.77	8.40	6120-6320
RDX	1.82	8.75	5130-6190
HMX	1.91	9.10	5130
TNT	1.64	6.90	4100-4900
C-4	1.59	8.04	5860-6057
ANFO*	1.30	3.20	1590

* The properties are dependent on the particular mixture of solid ammonium nitrate and fuel oil.

therefore be calculated for any explosive with a given weight W_{exp} by using the ratio of the heat produced during the detonation, i.e.,

$$W_{\text{TNT}} = W_{\text{exp}} \frac{E_{\text{exp}}}{E_{\text{TNT}}} \tag{2.6}$$

A measure of the detonation energy E_{TNT} is found to be 4520 kJ/kg in the literature [19]. As an example, the TNT equivalent for C-4 can then be found using Table 2.1 and is estimated to be $E_{\text{C}-4}/E_{\text{TNT}} = 6057/4520 = 1.34$. This implies that 1 kg of C-4 is equivalent to 1.34 kg of TNT. Table 2.2 presents TNT equivalents for typical explosives found in the literature. These factors result from Eq. (2.6) and can be used to determine the weight of TNT that generates the same blast properties as that from another type of explosive of a given weight. It is observed that the blast properties may be compared either in terms of the peak pressure or impulse. Thus, the blast properties will not only depend on the explosive material but also on the nature of the loading.

2.4 Blast scaling laws

Scaling of the blast properties from an explosive detonation is common practice, and with the basic understanding of blast engineering these scaling laws may be used to predict the blast properties from large-scale explosions based on experiments at much smaller scales (or vice versa). Since the blast properties are usually normalized to sea level ambient conditions, such results may also be used to predict the blast properties from detonations at high-altitude conditions [144]. The scalability of blast waves is therefore an important characteristic within the field of blast engineering.

A comprehensive review and derivation of the various scaling laws are given by Baker et al. [14]. The most common approach of blast scaling is the so-called Hopkinson-Cranz (or cube-root) scaling. This law states that two explosive

Table 2.2: TNT equivalents for typical explosive materials [19, 32, 142, 152].

Explosive type	TNT equivalent mass factor	
	Peak pressure	Impulse
TNT	1.00	1.00
Composition B	1.11	0.98
Composition C-3	1.08	1.01
Composition C-4	1.34-1.38	1.19
HMX	1.02	1.03
Octol 75/25	1.06	1.06
PETN	1.27	1.11
RDX	1.14	1.09
RDX/TNT 60/40 (Cyclotol)	1.14	1.09
Tetryl	1.07	1.05
Tritonal	1.07	0.96
Amatol	0.99	0.98
ANFO*	0.82	-
Pentolite	1.42	1.00
Nitroglycerine	1.48	-

* The properties are dependent on the particular mixture of solid ammonium nitrate and fuel oil.

charges of similar geometry and the same material, but of different mass, will produce self-similar blast waves at identical scaled distances and times if detonated in the same atmosphere. If R is the stand-off distance from the reference explosive charge, E is the total heat of detonation of the explosive, and W is the total weight of the reference explosive source (typically TNT), then the blast properties of the reference explosion can be related to those arising from another charge W_1 with a total energy E_1 and located at a distance R_1 as follows

$$\frac{R}{R_1} = \left(\frac{E}{E_1}\right)^{1/3} = \left(\frac{W}{W_1}\right)^{1/3} \tag{2.7}$$

If W_1 and E_1 are chosen as a unit of mass (e.g. 1 kg) or energy (e.g. 1 kJ), it is convenient to introduce the scaled distance Z as [14]

$$Z = R_1 = \frac{R}{E^{1/3}} = \Lambda R \tag{2.8}$$

or

$$Z = R_1 = \frac{R}{W^{1/3}} = \Lambda R \tag{2.9}$$

where also the parameter Λ is introduce as the scaling factor. The application of either Eq. (2.8) or Eq. (2.9) will depend on the particular problem. However, Eq. (2.9) is often used when considering chemical explosives. Since chemical explosives are the aim of **Part II**, the definition in Eq. (2.9) is used in the following.

The implications of the Hopkinson-Cranz scaling are shown schematically in

Figure 2.16. That is, a sensor located at a distance R from the centre of the explosive charge with characteristic dimension d will experience a blast wave of magnitude p, duration $t_{\mathrm{d}+}$, where the integral of the corresponding pressure-time history is the specific impulse i_+. Then, according to the Hopkinson-Cranz scaling law, a sensor positioned at a distance ΛR from the centre of a similar explosive charge of dimension Λd detonated in the same atmosphere would experience a blast wave of similar form with magnitude p, duration $\Lambda t_{\mathrm{d}+}$ and specific impulse Λi_+.

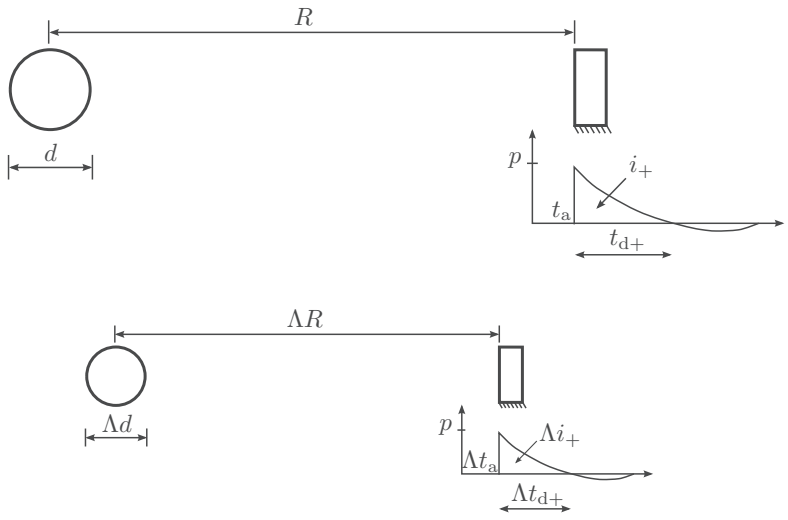

Figure 2.16: Hopkinson-Cranz blast wave scaling (inspired by [14]).

Following the argumentation of Eq. (2.9), an appropriate value of Λ would be

$$\Lambda = \frac{1}{W^{1/3}} \tag{2.10}$$

resulting in a scaled specific impulse $\bar{i}$ and time of arrival $\bar{t}_{\mathrm{a}}$ given by [14]

$$\bar{i} = \Lambda i = \frac{i}{W^{1/3}} \tag{2.11a}$$

$$\bar{t}_{\mathrm{a}} = \Lambda t_{\mathrm{a}} = \frac{t_{\mathrm{a}}}{W^{1/3}} \tag{2.11b}$$

Thus, the cube-root scaling implies that all physical quantities with dimensions of pressure and velocity remain unchanged in the scaling. The scaling relationships also assume that the charge-to-surface geometries are identical (i.e., similar blast environments). Under other conditions, the same scaling laws may be used to obtain approximate blast properties. However, in such cases the relationships should be used with caution. Even though the Hopkinson-Cranz scaling laws has been thoroughly validated experimentally over a large

range of explosive charges, the lack of experimental data at very small scaled distances (i.e., $Z < 0.32$ m/kg$^{1/3}$) make validation in this area difficult (see e.g. [142, 144]).

It is noticed that the basic principles of cube-root scaling follows the same principles introduced earlier for the blast phenomenon. That is, the energy released from an explosion results in a shock wave propagating as an expanding sphere. The blast properties will therefore be proportional to the energy per unit volume (i.e., the specific energy). Since the volume of a sphere is proportional to R^3, the scaling will involve the cube root. An important result of this argumentation is that the scaling is dependent on the geometry of the explosive charge and that the scaling laws in Eqs. (2.7)-(2.11) may change for other geometries than spherical charges. As an example, square-root scaling may be a better choice for the scaling of an explosive line or cylindrical charge since the energy will propagate with the expanding cylindrical shock front. These differences are important in the case of close-in detonations, in which the charge shape is essential in defining the shock front. However, for explosions farther away from the target, the blast wave will eventually take on the form of a plane shock wave and the scaling laws based on a spherical charge (i.e., a point detonation) is reasonable and cube-root scaling should be used [142].

The scaled distance Z in Eq. (2.9) is also commonly used to distinguish between various loading scenarios. A differentiation in loading categories is convenient because the structural response depends on both the distribution and magnitude of the loading, in which the stand-off distance is the governing parameter. Three loading categories are found in the literature, i.e., contact (or close-in), near-field and far-field detonations (see e.g. [32]). Close-in detonations are characterized through high pressure magnitudes (typically in the order of 10 to 30 GPa) within the timescale of microseconds and include both detonation products (e.g. fireballs) and compressed air. Although the duration of the loading is very short, the reflection coefficient can be as high as 13 resulting in very large impulses (see Figures 2.7 and 2.10). Due to the small distances between the explosive charge and the target, these types of detonations involve highly localized effects on the structure and also fragments (both primary and secondary) can be an issue. Typically, the failure modes of the structure are categorized by shear, spalling, punching or petalling, depending on the thickness and material properties of the structure. Both near-field and far-field detonations are characterized by a more distant blast wave that mainly involves the compression of ambient air. Near-field loading is characterized by a non-uniform spatial distribution of the pressure on the structural surface and may involve both global and local effects in the structural response. A common assumption at far-field loading is a uniform and plane shock wave over the entire structural surface resulting in a global response (see Figures 2.9

and 2.15). The following categories are often given in the literature [32]

$$\begin{aligned} Z &\leq 0.5 && \text{(Close-in)} \\ 0.5 < Z &\leq 2.0 && \text{(Near-field)} \\ Z &> 2.0 && \text{(Far-field)} \end{aligned} \tag{2.12}$$

This classification is convenient in the blast-resistant design and may provide an important indication of the necessary complexity in the computational method. However, one should be aware that when discussing the local or global effects on the structural response this categorization could be somewhat misleading. Eq. (2.9) implies that a small charge exploding near the structure may result in the same values for Z as that from a large charge detonating farther away from the structure. Only considering Eq. (2.12) may result in the same category although the behaviour of a structure exposed to a relatively small detonation near the structure could be totally different from its behaviour under a large explosion far away from it. Depending on the blast intensity the structural behaviour may become significantly different.

2.5 Prediction of blast loads

The objective of this section is to briefly review the basic approaches used to predict the blast parameters required in blast-resistant design. These approaches are often divided into empirical, semi-empirical and numerical (or computational) methods [143]. Empirical methods are basically correlations with experimental data, which implies that this approach is limited by the extent of the underlying experimental database. The accuracy of all empirical methods diminishes as the blast becomes increasingly near-field and approaches close-in detonations. Semi-empirical methods are based on simplified models of physical phenomena. They attempt to model the underlying physics in a simplified way. These methods rely on extensive data and case studies and their accuracy is generally better than that provided by the empirical methods. Numerical (or computational) methods are based on the mathematical equations that describe the basic laws of physics governing a problem. These principles typically include conservation of mass, momentum and energy. In addition, the material behaviour of the air is described by constitutive relations (known as equations of state). These models are commonly called computational fluid dynamic (CFD) models. Note that semi-empirical methods are developed primarily by defence-related agencies and the distribution are therefore restricted to the government and its contractors (see e.g. [153, 154]). This thesis is therefore limited to empirical and CFD methods which are readily available to the public. The empirical method are presented in **Part II** of this thesis, while the CFD method are discussed in more detail in **Part III**.

Of the many available references in the literature (see e.g. [3, 5, 15, 142, 143, 150]) the most reliable and referenced works dates back to a few U.S. Army publications. That is, the technical report by Kingery and Bulmash [4] and the Army Technical Manual TM 5-1300 [16]. The latter was updated and replaced by UFC 3-340-02 in recent years and provides detailed information and procedures for the design of structures to resist the effects of explosions. However, many of the blast properties predicted by this manual also dates back to the former publication. The most common reference in predicting blast loading is therefore the work by Kingery and Bulmash [4], in which experimental data from idealized conditions (i.e., spherical and hemispherical high-explosive detonations) were gathered and curve-fitted to higher-order polynomial equations for the necessary blast parameters using the Hopkinson-Cranz scaling laws for a large range of TNT equivalent charges ($1 \text{ kg} < W_{\text{TNT}} < 400,000 \text{ kg}$). As already mentioned in Section 1.2.1, the data used by Kingery and Bulmash [4] contained limited data for blast parameters at scaled distances less than 0.40 $\text{m/kg}^{1/3}$, and some of the parameters were therefore extrapolated at smaller distances using the available data and theoretical considerations. These experiments and empirical equations, together with the Friedlander equation in Eq. (2.1), form the basis for various simplified tools to predict blast loading from a given explosive weight at a known distance from the target. The most common and widely used tool is known as the Conventional Weapons Effects Program (ConWep, formerly TM 5-855-1) [17]. These simplified tools are often called empirical methods in the literature and present an idealized representation of blast loads for design purposes. Due to the idealized nature, these methods have significant advantages compared to other methods in terms of time consumption and are therefore frequently used in so-called quick assessments. This is a typical starting point of a blast-load analysis, providing useful insight in the performance of structures and may be used for a first optimization before more elaborate analyses and methods may be considered.

The empirical equations by Kingery and Bulmash [4] are given for spherical free airbursts in Figure 2.17a and hemispherical surface bursts in Figure 2.17b. It is observed that the blast properties in Figure 2.17b are similar to those in Figure 2.17a. However, in a surface burst the parameters will be larger in magnitude due to the instantaneous reflection from the ground (see Figure 2.14). Note that the parameters in terms of specific impulses i, positive duration $t_{\text{d}+}$ and time-of-arrival t_{a} are scaled using Hopkinson-Cranz scaling [14]. That is, scaled by the cube-root of the charge mass. Also note that Figures 2.17a and 2.17b do not provide a value for the exponential decay coefficient b in Eq. (2.1). This may be found by solving the implicit non-linear equation in Eq. (2.3) since the value of the reflected specific impulse $\bar{i}_{\text{r}+}$, peak reflected overpressure $p_{\text{r,max}}$ and duration $\bar{t}_{\text{d}+}$ of the positive phase is known. As the loading becomes increasingly near-field ($Z \leq 2.0$), the use of the empirical

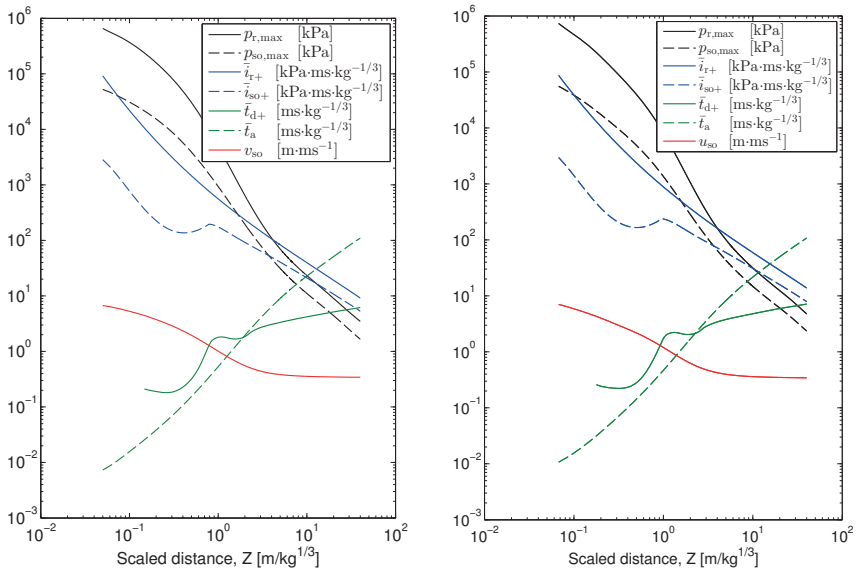

(a) Spherical charge **(b)** Hemispherical charge

Figure 2.17: Blast parameters for a charge of TNT, detonated in free air at sea level, given by Kingery and Bulmash [4].

equations requires that the non-uniform spatial distribution of the loading is included in the calculation. This can be done by considering both the incident overpressure $p_{so,max}$ and the angle of incidence α when determining the reflected pressure acting on the structure (see Section 2.1 and Figures 2.4, 2.7 and 2.10). Intermediate values of the peak incident overpressure $p_{so,max}$ in Figure 2.7 may be found by interpolation between adjacent curves. If the charge shape is spherical or hemispherical, the reflecting surface is considered plane and of infinite size, and the scaled distance is defined as a near- or far-field detonation ($Z \geq 0.5$), the simplified methods based on Figures 2.17a and 2.17b are in general found to provide good estimates of the blast properties [33].

However, at scaled distances defined as a close-in detonation ($Z \leq 0.5$), the use of simplified methods is questionable due to the increasing complexity of the load in the vicinity of the structure [38, 39]. That is, the empirical methods do not consider potential interactions between the fireball and the blast overpressure. Moreover, these methods are not valid for blast environments involving complex geometries. Complex geometries and structures of finite surfaces involves clearing, shielding and confinement between neighboring buildings. This introduces the need for more elaborate methods (e.g. semi-empirical or numerical methods), since the reflected pressure will be relieved by a rarefaction wave generated during the diffraction of the reflected shock around

the boundary of the reflecting surface (see e.g. [16,155]). This requires advanced numerical methods based on computational fluid dynamics (CFD) to estimate the loading for contact detonations or complicated geometries [38]. Thus, when using the empirical methods, it is necessary with a proper understanding of the blast phenomenon and underlying limitations of the method to ensure that the blast properties are valid estimates.

Finally, although the effects of the negative phase are usually neglected in the design of hardened structures (e.g. reinforced concrete or similar), this phase may be of importance when considering the response of flexible structures where the overall motion will be affected by the timing of the negative phase. The most commonly used negative phase parameters seem to be those given in [16, 27]. These parameters are presented in Figures 2.18a and 2.18b for spherical and hemispherical charges, respectively. Note that $p_{\mathrm{r,max}}$, $\bar{t}_{\mathrm{d}+}$ and $\bar{i}_{\mathrm{r}+}$ from Figures 2.17a and 2.17b are included for comparison to the corresponding negative phase parameters ($p_{\mathrm{r,min}}$, $\bar{t}_{\mathrm{d}-}$ and $\bar{i}_{\mathrm{r}-}$). It is observed that although there is a relatively large difference between peak reflected pressure $p_{\mathrm{r,max}}$ and peak negative pressure $p_{\mathrm{r,min}}$, the corresponding impulses ($\bar{i}_{\mathrm{r}+}$ and $\bar{i}_{\mathrm{r}-}$) approaches the same order of magnitude for $Z > 1$. Studies by Rigby et al. [30] also suggest that the angle of incidence α has limited influence of the negative phase parameters ($p_{\mathrm{r,min}}$, $\bar{t}_{\mathrm{d}-}$ and $\bar{i}_{\mathrm{r}-}$).

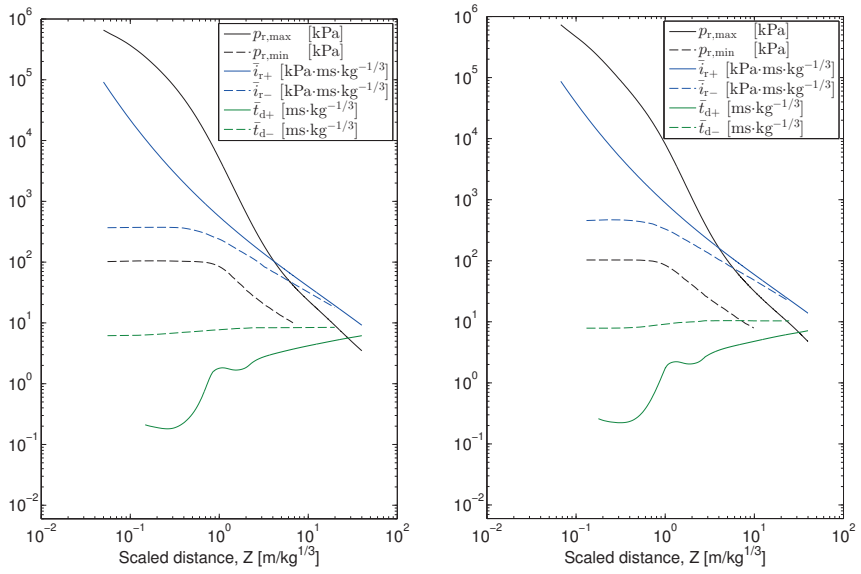

(a) Spherical charge **(b)** Hemispherical charge

Figure 2.18: Parameters for the positive and negative phase from a charge of TNT detonated in free air at sea level [4, 16].

3

Airblast experiments

This chapter is mainly based on the first paper published in International Journal of Impact Engineering [156]. It presents an experimental investigation on the influence of stand-off distance on the dynamic response of thin aluminium and steel plates subjected to airblast loading and covers the experimental work related to **Part II** of this thesis. The experimental results provide a set of data which can be used to evaluate the performance of current computational methods in predicting the structural response of thin ductile plates exposed to blast loading.

3.1 Introduction

As discussed in Section 1.2.4, experiments involving high-explosive detonations are necessary to investigate the inherent complexity in such blast environments (e.g. highly non-uniform spatial and temporal pressure distributions and the interaction between the fireball and the blast overpressure in the vicinity of the target). A series of airburst detonations was therefore carried out to obtain knowledge and an improved understanding of near-field blast events. The experimental results presented in this chapter will also serve as a basis of comparison for the numerical simulations in Chapter 5.

The blast intensity and pressure distribution were varied by detonating small-scale spherical charges of plastic explosive at various stand-off distances relative to the centre of the plates. Piezoelectric pressure sensors were used for pressure recordings and synchronized with two high-speed cameras in a stereovision setup to capture the dynamic response using a finite element-based three-dimensional digital image correlation (3D-DIC) technique. Material tests were also performed to determine the materials' behaviour at large plastic strains.

3.2 Experimental study

This section starts with a presentation of the experimental setup and programme before presenting the material tests and the procedure used in the three-dimensional digital image correlation analyses.

3.2.1 Experimental setup and programme

All tests were performed at an indoor test facility possessed by the Research and Development Section at the Norwegian Defence Estates Agency. The experimental setup is shown in Figures 3.1a and 3.1b and was inspired by Spranghers et al. [103]. The setup consisted of a steel mounting frame fixed to the concrete floor with outer dimensions 1.0 m × 1.0 m × 0.015 m and a square opening of 0.3 m × 0.3 m in the centre. The square plate specimens with dimensions of 0.4 m × 0.4 m × 0.0008 m were clamped to the rigid frame using bolted connections and a clamping frame in an attempt to achieve fixed boundary conditions. The 16 bolts were tightened using a wrench with a torque M_t of 200 Nm, which is equivalent to a pre-tensioning force F_p of 92.6 kN [157] for the M12 bolts used in this study.

Two high-speed cameras in a stereoscopic setup were used to capture the response of the thin plates with a framing rate of 21,000 fps. The plates were painted with a speckle pattern to measure the transient deformation fields using a three-dimensional digital image correlation (3D-DIC) technique (Figure 3.1c). It was necessary with additional lighting for the speckle pattern to have enough contrast to calculate the transient deformation fields using DIC. The cameras were triggered manually and the trigger mode was centred such that an equal number of frames before and after the explosion were stored. A blast pencil was used to determine when the shock wave arrived at the cameras (see Figures 3.1a and 3.1b). From this point on the correlation of the images had reduced accuracy due to possible oscillations of the cameras, resulting in a loss of calibration of the system.

The explosive mass W was positioned at various stand-off distances R relative to the centre point of the plate depending on the material, and the test matrix is given in Table 3.1. The explosive material was Composition C-4 with a spherical shape, a mass of 30 g (equivalent to 40.2 g of TNT) and a diameter of approximately 34.5 mm. The blast was initiated by an electric detonator of type RP-83 exploding bridgewire (EBW) with a TNT equivalent of 1 g. The explosive charge and detonator were held together using a black electrical insulation tape (Figure 3.1d).

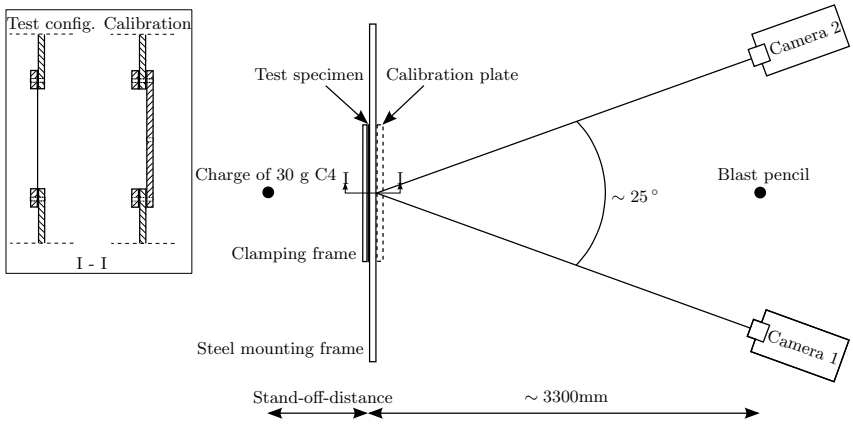

(a)

(b)

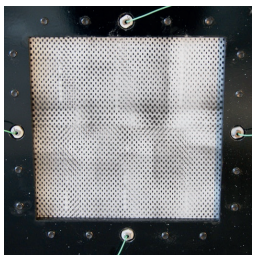

(c)

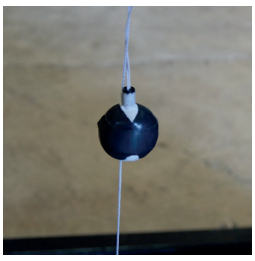

(d)

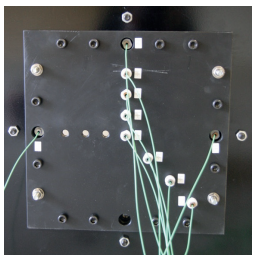

(e)

Figure 3.1: Experimental setup: (a) sketch of the setup, (b) picture of the setup, (c) DIC speckle pattern, (d) spherical charge and (e) calibration plate. Both the speckle pattern in (c) and the calibration plate in (e) are seen from the cameras.

Table 3.1: Test matrix.

Plate thickness [mm]	Stand-off distance R [m]	Test number*				
		1	2	3	4	5
15 (rigid steel plate)	0.250	R11	R12	R13	-	-
	0.375	R21	R22	R23	-	-
	0.500	R31	R32	R33	-	-
0.8 (steel plate)	0.125	S11	S12	S13	S14	S15
	0.250	S21	S22	S23	-	-
	0.375	S31	S32	S33	-	-
0.8 (aluminium plate)	0.250	A01	-	-	-	-
	0.375	A11	A12	A13	-	-
	0.500	A21	A22	A23	-	-
	0.625	A31	A32	A33	-	-

*The tests are numbered XYZ in which X denotes the rigid steel (R), deformable steel (S) or aluminium (A) test specimens, Y is the subsequent stand-off distance (0, 1, 2 and 3) and Z is the test number.

Piezoelectric pressure sensors (Kistler 603B), corresponding charge amplifiers (Kistler 5064) and data acquisition systems from National Instruments (NI USB-6356) and Yokogawa (DL850E ScopeCorder) were used to measure the pressure at selected locations during the experiments (see sensors in Figures 3.1c and 3.1e). These sensors are designed to measure fluctuations of high frequency with short rise time, and are capable of measuring pressures up to 20 MPa at temperatures up to 200 °C [158]. The pressure sensors were positioned in threaded adapters which were fastened at the desirable locations. The pressure was recorded using two independently operating acquisition systems and sampling frequencies, i.e., 10 MHz and 21 kHz. The first frequency enabled the recording of the steep gradient and short rise time of the blast wave, while the second frequency was the same as for the high-speed cameras enabling a synchronization of the pressure and the 3D-DIC measurements. No low-pass filtering was used in the pressure measurements.

Before testing the thin steel and aluminium plates, similar tests were performed on a massive steel plate with a thickness of 15 mm. The main objective with these experiments was to investigate the pressure distribution on a rigid calibration plate, and to use these measurements as a basis to investigate potential fluid-structure interaction (FSI) effects in the thin-plate tests. To enable the investigation of the FSI effects the clamping frame had to be positioned at the same location for both the pressure measurements and the subsequent thin-plate tests. The calibration plate was therefore placed on the same side as the high-speed cameras, i.e., on the opposite side of the steel mounting frame compared to the clamping frame (see Figure 3.1a). This resulted in a slightly different stand-off distance for the loading of the calibration plate compared to the steel and aluminium plates (Figures 3.1c and 3.1e).

The calibration tests were performed using three different stand-off distances

and with a sufficient amount of pressure sensors to determine the pressure distribution along the vertical and diagonal of the calibration plate. The position of the 10 sensors used in these tests are shown in Figure 3.2a. To reduce the risk of damaging the sensors, the calibration tests were not performed at a stand-off distance of 0.125 m (see Table 3.1). Sensors 1-4 and 8-10 were mounted on the calibration plate, while 5-7 were located on the clamping frame. Sensor 1 was moved to the remaining position (lower centre part) in the clamping frame for the thin-plate experiments and renamed sensor 11 (Figure 3.2b). A break wire was synchronized with the pressure measurements and used to determine the time of detonation. This is an analog device with an electric circuit which registers the time of a potential break in the wire as a change in the signal. As soon as the explosive charge detonates, the wire will break and thus define the time of detonation.

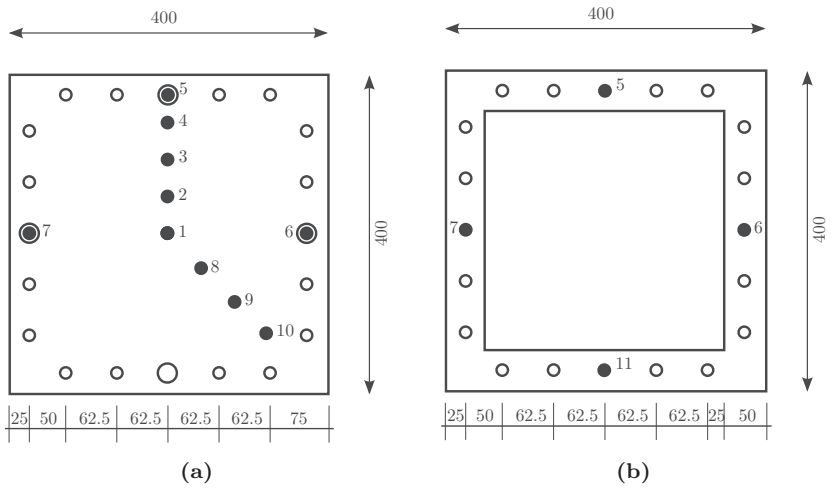

Figure 3.2: Position of pressure sensors (seen from the cameras) in the calibration plate (a) and clamping frame (b). All measurements are in mm.

3.2.2 Materials

The 0.8-mm-thick steel plates used in these tests were manufactured from medium-strength, high-hardening and cold-rolled sheets of type Docol 600DL produced by Swedish Steel Ltd. (SSAB). Heat treatment is used to produce a two-phase structure of ferrite and martensite, where the ferrite gives the forming properties and the martensite gives the strength. This material is often used in the automotive industry. Table 3.2 gives the nominal chemical composition of the material [159]. The nominal yield stress was reported by the manufacturer to be in the range from 280 MPa to 360 MPa, while the nominal tensile strength was stated to be between 600 MPa and 700 MPa.

Table 3.2: Chemical composition of Docol 600DL (in wt.%).

C	Si	Mn	P	S	Al
0.10	0.40	1.50	0.010	0.002	0.040

Gruben et al. [160, 161] investigated the mechanical properties of Docol 600DL steel by performing a comprehensive experimental study on 2 mm thick plates, while Rakvåg et al. [65] and Holmen et al. [162] performed material tests on respectively 0.7 mm and 0.8 mm thick plates of the same material. These studies compared the material behaviour in three different directions (0°, 45° and 90°) regarding the rolling direction of the plate, and concluded that the material is isotropic with a small variation in failure strain. The material was also found to be moderately strain rate sensitive at elevated strain rates [65]. It should further be noted that the material specimens used by Holmen et al. [162] were taken from the same plates as those used in this study. Thus, the material data provided in [162] also apply in this study, and no additional material tests were performed for the steel sheets.

The 0.8-mm-thick aluminium plates were manufactured from low-strength, strain-hardened and cold-rolled sheets of the alloy EN AW 1050A-H14 produced by Norsk Hydro ASA. This is 99.5 % pure aluminium subjected to annealing before work hardened by rolling until a yield stress which is approximately half of the ultimate tensile strength is achieved. The material is often used for sheet metal work where high mechanical properties are not required. The nominal chemical composition is provided in Table 3.3, while the nominal yield and ultimate tensile strengths were given by the producer to be about 75 MPa and 105-145 MPa, respectively.

Table 3.3: Chemical composition of EN AW 1050A-H14 (in wt.%).

Si	Fe	Cu	Mn	Mg	Zn	Ti	Al
0.030	0.360	0.001	0.002	0.000	0.003	0.010	Rest

Uniaxial tensile tests were carried out on dog-bone specimens cut from the aluminium plates using the same geometry as in [162] (see Figure 3.3). The tests were performed in a Zwick/Roell Z030 testing machine at a constant deformation rate of 2.1 mm/min. This corresponds to an initial strain rate of $\dot{\varepsilon} = 5 \times 10^{-4}$ s^{-1} for a gauge length of 70 mm. Three parallel tests were performed in three different directions (0°, 45° and 90°) with respect to the rolling direction of the plate. The force and displacement were measured by the hydraulic test machine at 4 Hz for all tests, and the displacement field was measured using DIC. In addition, the first test in each series was instrumented with an extensometer to measure the displacement of the gauge length for comparison with the DIC measurements. The DIC measurements

were validated by using a vector at the same location and of the same length as the extensometer. The DIC measurements and the extensometer showed excellent agreement, and only the DIC recordings are therefore used in the following.

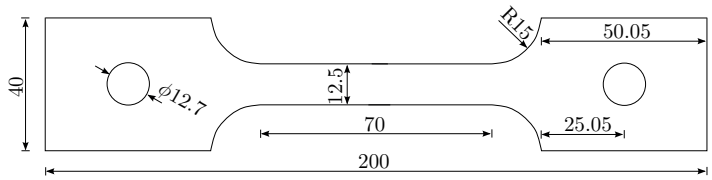

Figure 3.3: Geometry of the uniaxial tension tests. All measurements are in mm.

Nominal stress-strain curves from quasi-static uniaxial tensile tests of both materials are shown in Figure 3.4. It is observed that the aluminium is slightly anisotropic both in flow stress and failure strain (Figure 3.4b). Diffuse necking occurs at very small plastic strains (approximately 0.7 %) in all three directions, which indicates that the deformation before necking is very low for this alloy. This can be explained by the manufacturing process since these sheets were formed and work-hardened by cold-rolling until half hard, i.e., to a yield stress approximately half the ultimate tensile strength [163]. It is well known that increasing the yield stress by cold-working may reduce the ductility before necking.

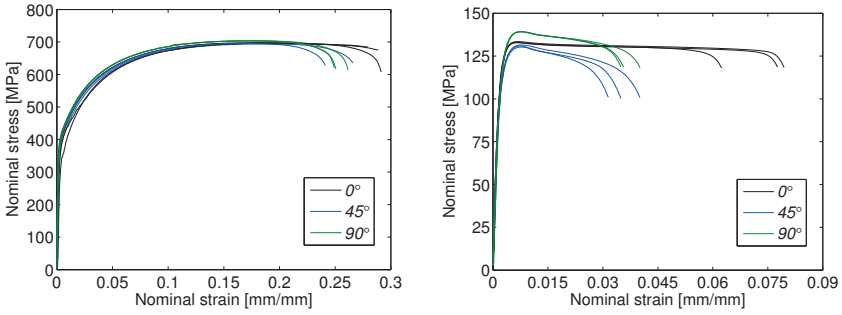

Figure 3.4: Nominal stress-strain curves from uniaxial tensile tests at three different loading directions for (a) Docol 600DL [162] and (b) EN AW 1050A-H14.

Diffuse necking in the tensile test indicates the end of the uniform deformation in the gauge area and a triaxial stress state will increase the value of the longitudinal stress. Usually this is seen on the nominal stress-strain curve as a rapid decrease in the stress until failure (as e.g. seen for the Docol 600DL steel in Figure 3.4a). However, for the EN AW 1050A-H14 aluminium alloy only a

small and rapid decrease in stress before a long-lasting stagnation in stress level before failure is observed (see Figure 3.4b). This behaviour was most evident in the specimens taken from the rolling direction of the sheet. From a physical point of view this indicates that the load-carrying capacity of the material is noticeably increased immediately after the onset of diffuse necking, which may be explained by the high rate-sensitivity of the material [164–167]. As the neck develops, this instability will increase the strain rate in the localised area of the neck which for this material seems to result in a severe increase in the load-carrying capacity of the specimen.

3.2.3 3D-DIC measurements

Three-dimensional digital image correlation (3D-DIC) analyses were conducted for all blast tests using a stereovision setup with two Phantom v1610 high-speed cameras. The separation angle between the optical axes of the cameras was approximately 25° (Figure 3.1a). The recording rate was chosen to 21,000 fps in all tests with an image resolution of 896×800 pixels and 12-bit grey level digitization. The camera calibration and image analyses were carried out in a post-processing phase using an in-house finite element-based DIC code (see [168] for further details regarding the DIC software applied in this thesis).

The calibration of the stereovision setup involved recordings of a calibration target with known geometry - in this case a cylinder of diameter 80 mm with a checkerboard pattern printed on the surface as shown in Figure 3.5a. The calibration target was translated and rotated between each recording, and this process was done both prior to and in-between the blast tests to capture any potential permanent movement of the cameras during testing. The calibration target was initially pre-calibrated so that the dimensions, i.e., the diameter, square size and possible deviations, of the cylinder were known with as high accuracy as possible. The location of the corners in the checkerboard pattern was extracted from the images (Figure 3.5b) and the 16 camera parameters including correction of radial and tangential lens distortion were optimized for each of the two cameras. The camera calibration and the 3D-DIC technique have been validated using shock tube experiments and a laser displacement sensor (optoNCDT 2300) with similar experimental setup and sampling rate of data (see **Part III**). The measured mid-point deflection based on the laser and the 3D-DIC were in excellent agreement, and the 3D-DIC technique is therefore considered as well suited to measure the displacements in this study.

Prior to each test, the plates were spray-painted with a speckle pattern. The thin plates were first spray-painted white before a template was used to apply black speckles with appropriate sizes on the white surface (see Figure 3.1c). The image sequences recorded during the blast tests were analysed using a

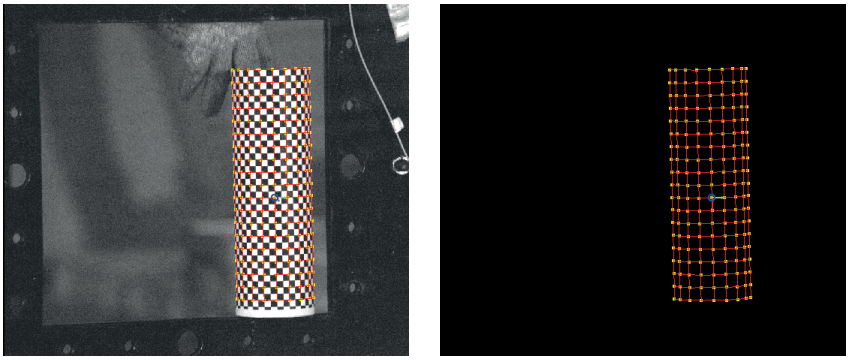

(a) (b)

Figure 3.5: Calibration of the stereovision setup: (a) a recorded image of the calibration target (cylinder) is analysed to find the corners of the checkerboard pattern, and (b) the extracted corner positions in the image (pixels) and in the three-dimensional target coordinate system (mm) is used to calibrate the camera models [168]. Multiple recordings of the calibration target are used to obtain reliable camera models.

finite-element formulation of DIC [168, 169] on a mesh of Q4 elements. Zero-shifting and normalization of the grey values were carried out element-wise in the DIC analyses to handle large background light variations caused by the explosion.

Conversion between pixel locations in the images for the two cameras and the target space were carried out using the camera models presented in [168]. Figure 3.6 illustrates an example of recorded images from test S21 using the two synchronized high-speed cameras with the resulting DIC meshes plotted on top. The corresponding 3D model calculated from the DIC results is also illustrated in the figure.

Some challenges were encountered in the DIC analyses due to reflecting specular highlights, which occurred at various stages during the deformation of the plates. Also flaking of the paint, especially at the centre of the plates, were encountered in some of the tests. These challenges were however easily recognized and the results from the DIC analyses at these locations were disregarded.

3.3 Experimental results

The experimental results are presented in terms of pressure measurements for the calibration tests and both pressure measurements and deformation histories for the steel and aluminium tests.

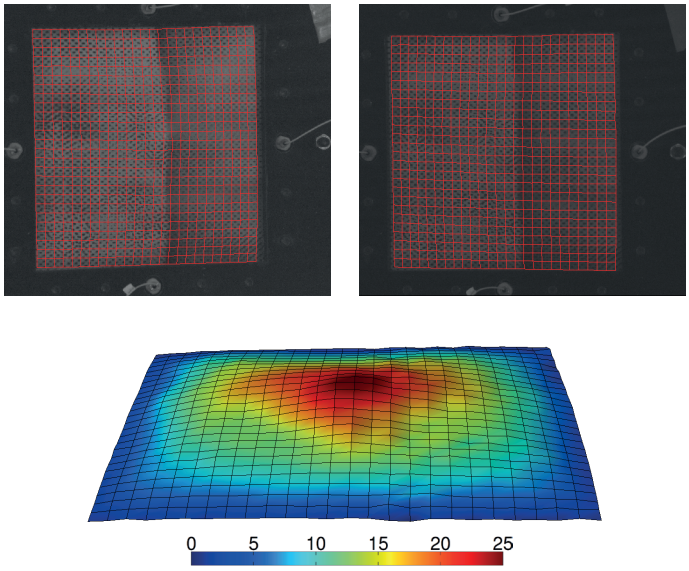

Figure 3.6: Results from 3D-DIC in test S21. The top images show two corresponding images from Camera 1 (top-left) and Camera 2 (top-right). The resulting DIC mesh is plotted on-top of the recorded images. The corresponding 3D model from DIC is presented in the lower image. The colour scale on the 3D-model indicates out-of-plane displacement (in mm).

3.3.1 Pressure measurements

The measured blast properties from all tests against the rigid 15 mm thick steel plate are summarized in Table 3.4, while representative pressure-time histories for each stand-off distance are given in Figure 3.7. The pressure measurements were numbered RXY, where X denotes the subsequent stand-off distance (1, 2 and 3 - see Table 3.1) and Y is the test number. Since it is generally accepted that the structural response is mainly driven by the positive phase of the blast load (see e.g. [40, 41]), this study will merely focus on this phase. The reported blast properties are therefore limited to the time of arrival t_a, peak reflected overpressure $p_{r\alpha}$, positive duration t_{d+} and impulse $i_{r\alpha+}$ for typical pressure curves. These data were taken from the frame and the sensor where the blast wave arrived first. The impulse was found by numerical integration of the pressure-time curve during the positive duration at the respective sensor. Measurements from the centre of the calibration plate (Sensor 1) were also included in Table 3.4 for comparison. It should be noted that the blast parameters were not identical for the three pressure sensors in the frame at the same stand-off distance, but the sensor listed in Table 3.4 gives a good representation of these measurements from each test. All results

were corrected according to the time of detonation using the signal from the break wire.

Table 3.4: Experimental results from pressure measurements. The location of the pressure sensors are given in Figure 3.2.

Test	R [m]	Z [m/kg$^{1/3}$]	Sensor [#]	t_a [ms]	$p_{r\alpha}$ [MPa]	t_{d+} [ms]	$i_{r\alpha+}$ [kPa ms]
R11	0.235	0.69	7	0.12	8.3	0.18	148.6
	0.265	0.77	1	0.10	5.5	0.15	189.8
R12	0.235	0.69	7	0.14	6.9	0.16	148.9
	0.265	0.77	1	0.11	20.4	0.18	303.0
R13	0.235	0.69	6	0.13	7.0	0.15	167.6
	0.265	0.77	1	0.12	10.8	0.17	207.2
R21	0.360	1.05	7	-	3.3	0.22	121.4
	0.390	1.14	1	-	4.8	0.23	168.1
R22	0.360	1.05	5	-	3.6	0.25	123.1
	0.390	1.14	1	-	4.6	0.22	167.7
R23	0.360	1.05	6	0.25	3.4	0.25	128.9
	0.390	1.14	1	0.23	3.9	0.23	151.2
R31	0.485	1.42	6	0.38	1.7	0.39	101.2
	0.515	1.50	1	0.39	1.9	0.51	143.5
R32	0.485	1.42	5	0.40	1.6	0.38	97.0
	0.515	1.50	1	0.39	1.2	0.51	95.6
R33	0.485	1.42	6	0.37	1.5	0.38	101.3
	0.515	1.50	1	0.37	2.0	0.51	144.9

The pressure measurements show that the loading on the rigid calibration plate is in good agreement with the characteristics of an idealized blast wave, i.e., short rise time, exponential pressure decay and a positive phase followed by a negative phase. The variation in arrival time and peak reflected pressure for the blast wave at the respective sensors confirm that the pressure wave is spherical and propagates in a radial manner. This can be observed as the peak reflected pressure is decreasing and the time of arrival is increasing with increasing stand-off distance and oblique angle (Figure 3.7). This behaviour was further confirmed by the difference in arrival time at the respective sensors, which became smaller at larger stand-off distances. It should also be noted that the sensors in the frame (i.e., Sensors 5-7) were located about 30 mm closer to the charge than the sensors in the calibration plate (see Figures 3.1a and 3.2a). These sensors were included for a later comparison with the experiments involving the thin steel and aluminium plates.

For some reason the pressure seemed to arrive simultaneously at Sensors 1 and 8 (see Figure 3.7) independent of stand-off distance. According to theory, it is expected that the blast wave would first arrive at Sensor 1 and then the other sensors depending on their distance and oblique angle from the centre of the explosive charge. The same tendency was observed for the pressure recordings in the frame, where it was noticed that the pressure arrived somewhat earlier at Sensor 6 compared to Sensors 5 and 7. Since Sensor 6 was on the same

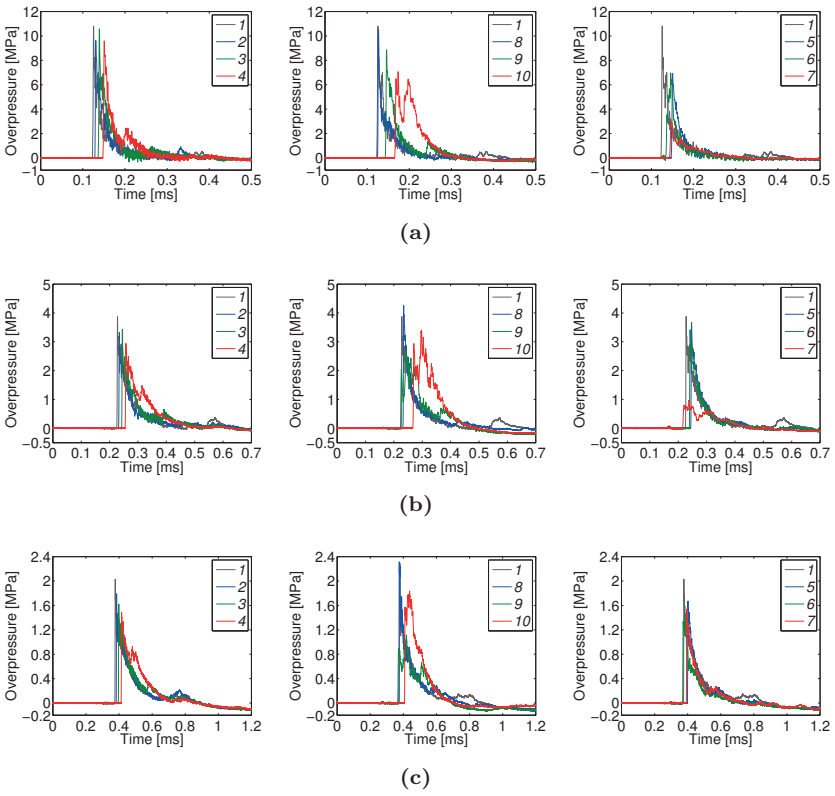

Figure 3.7: Pressure measurements from selected experiments limited to only include the positive phase of the blast load: (a) R13, (b) R23 and (c) R33. The measurements are taken from the pressure sensors located along the vertical (left), diagonal (middle) and frame (right) in the calibration tests (see Figure 3.2).

half of the calibration plate as Sensor 8, these deviations may be explained by an imperfect shape and alignment of the explosive charge. However, since these deviations were relatively small it seems reasonable to assume a spherical shape and centred alignment in the following.

Other deviations worth noticing are the positive impulses from Sensors 4 and 10 which were larger than expected compared to the other sensors. A plausible explanation for these irregular profiles may be a pressure build-up due to geometrical effects at the boundary, as the calibration plate was positioned differently than the clamping frame (Figure 3.1a). This was also confirmed by experimental and numerical investigations by Bonorchis and Nurick [170]. They showed that increased thickness of the clamping frame resulted in a pressure build-up at the plate boundary. However, this did not influence the mid-point deflection in subsequent experiments with deformable plates. It was also noted

abnormal recordings in some sensors, e.g. Sensor 7 in Figure 3.7b and Sensor 9 in Figure 3.7c, in some of the tests. The reason for this is not known.

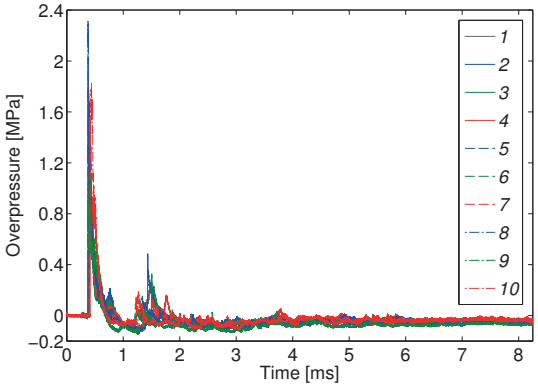

Figure 3.8: Secondary reflections and pressure drift in pressure sensors from test R33.

Figure 3.8 shows that the pressure did not always return to the ambient pressure at the end of the experiments. This indicates that the reference value (or zero level) of the pressure sensors was altered during the experiment, which may be explained by the fact that the Kistler 603B sensors are only designed for temperatures up to 200 °C [158]. It is therefore possible that the zero level changed due to the high temperature from the explosion, which seems reasonable since the drift was larger at the smallest stand-off distances where the temperature exposure was higher. This made it difficult to determine the exact duration of the negative phase. However, by assuming that the drift in pressure appeared after the positive phase, it was possible to determine the duration of the positive phase. This assumption seems reasonable since the fireball from the detonation is lagging behind the pressure wave. Reflection waves from e.g. secondary shocks and ground reflections were also observed in the pressure curves (seen as the peaks between 1 and 2 ms in Figure 3.8), making it even harder to determine the exact duration of the negative phase. Nevertheless, the overall performance of the pressure sensors seemed to be acceptable.

3.3.2 Steel plates

Figure 3.9 shows measured out-of-plane displacement at the centre point versus time for some of the tests based on the DIC analyses, while all experimental results are summarized in Table 3.5. The figure indicates that all plates experienced severe plastic deformation due to the blast load, and that the elastic rebound became smaller as the load-intensity increased. The specimens

at the nearest stand-off distances of 125 mm and 250 mm (S11-S15 and S21-S23) experienced an intuitive response as the test specimen deformed in the same direction as the incident blast wave, before it started to oscillate around its final shape. However, the specimens at the largest stand-off distance of 375 mm (S31-S33) revealed a counter-intuitive behaviour (CIB) as the test specimen experienced reversed snap buckling (RSB) during the elastic rebound, before it started to oscillate around the final configuration in the opposite direction of the incident blast wave. Due to trigger problems and flaking of the paint at the centre part in some specimens, DIC analyses were only possible in 6 out of the 12 experiments conducted (see Table 3.5). Further, the blast pencil recorded that the shock wave reached the cameras after about 9 ms. Beyond this point the correlation of the images has reduced accuracy due to small oscillations of the cameras. Figure 3.9 also shows a non-physical deviation of the displacement curves from the permanent equilibrium configuration in the final part of the experiment. This is due to the slight movement of the mounting frame during the tests.

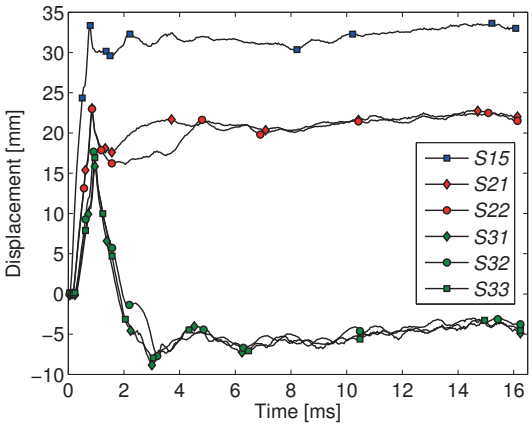

Figure 3.9: Deformation versus time of the centre point for the steel plates based on 3D-DIC.

As already mentioned, Table 3.5 gives characteristic blast parameters for a given pressure sensor and the permanent mid-point deflection from each test. The selected data were taken from the sensor in the clamping frame (see Figure 3.2b) that first recorded reasonable results. Thus, the variation in results observed at each stand-off distance represents both the spread between the sensors and the natural spread in this type of tests. The final mid-point deflection measured with DIC ($d_{\mathrm{z,p1}}$) and the in-situ permanent displacement ($d_{\mathrm{z,p2}}$) of the same point measured using a sliding caliper after the experiment also reveal some differences. The DIC measurements, defined as the average displacement during the elastic rebound phase, are in general slightly larger

than the permanent displacements. One reason for this may be that the plates were not completely at rest when the final picture for the DIC analyses was taken and that the displacement measured by DIC was not corrected for the slight movement of the mounting frame. The contribution from the movement of the mounting frame is indicated in Table 3.5 by including the corrected values in parentheses for $d_{\mathrm{z,p1}}$.

Table 3.5: Experimental results for the steel plates. The permanent mid-point deflections ($d_{\mathrm{z,p1}}$) which are corrected for the slight movement of the mounting frame are given in parentheses.

Test	R [m]	Z [m/kg$^{1/3}$]	Sensor* [#]	$p_{\mathrm{r}\alpha}$ [MPa]	$t_{\mathrm{d}+}$ [ms]	$i_{\mathrm{r}\alpha+}$ [kPa ms]	$t_{\mathrm{d}+}/T_n$ [-]	$d_{\mathrm{z,p1}}$ [mm]	$d_{\mathrm{z,p2}}$ [mm]	DIC [Y/N]
S11	0.125	0.36	11	14.2	0.07	135.7	0.005	-	30.0	N
S12	0.125	0.36	11	14.6	0.07	169.5	0.005	-	29.2	N
S13	0.125	0.36	11	16.2	0.07	156.0	0.005	-	28.8	N
S14	0.125	0.36	11	14.9	0.07	169.8	0.005	-	30.3	N
S15	0.125	0.36	11	11.5	0.07	138.2	0.005	31.7(29.4)	28.0	Y
S21	0.250	0.73	11	7.7	0.17	162.5	0.013	20.7(18.8)	16.5	Y
S22	0.250	0.73	6	6.8	0.14	142.2	0.011	21.0(18.0)	18.3	Y
S23	0.250	0.73	7	7.7	0.14	168.7	0.011	-	18.3	N
S31	0.375	1.09	11	3.5	0.25	139.2	0.019	-6.4(-8.5)	-8.1	Y
S32	0.375	1.09	6	4.9	0.23	154.2	0.017	-6.1(-7.8)	-7.9	Y
S33	0.375	1.09	6	3.3	0.21	136.2	0.016	-6.2(-8.6)	-9.1	Y

*Stand-off distance R refers to the respective plate, and not to the sensor located in the frame.

Pictures of typical steel plates after the tests are shown in Figure 3.10. For the closest stand-off distance (Figure 3.10a), the deformed shape was square pyramidal with plastic hinges around the boundaries and along the diagonals of the plate. Plastic hinges were also observed for the two largest stand-off distances (Figures 3.10b and 3.10c), although not that distinct. In these plates, a local dent at the centre with diameter similar to the spherical charge was observed. Furthermore, there were no visible signs of tearing at the boundaries for the steel plates and these experiments may therefore be classified as failure Mode I [57], i.e., large inelastic deformation. The only visible sign of failure in the test specimens was caused by some minor fragments from the detonator which had perforated the plate at the closest stand-off distance.

Figure 3.11 shows an example of synchronized loading and response histories during an experiment at the intermediate stand-off distance (from test S21). This figure also contains a selection of corresponding DIC images in terms of 3D topography maps, contours of the transverse displacement field and deformation profiles at characteristic times. It is observed from the synchronization of the pressure recordings and the DIC measurements that there was limited fluid-structure interactions (FSI) effects during the positive phase, since the positive duration of the pressure pulse was almost over before the plate started to move. Thus, subsequent motion took place during the negative phase and the

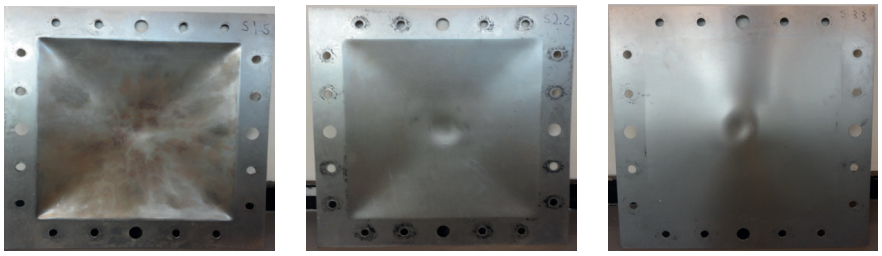

(a) S15 **(b)** S22 **(c)** S33

Figure 3.10: Photographs of deformed shapes for selected steel plates (seen from the explosive charge).

structural response seemed to be driven mainly by the positive impulse from the airblast. The influence of the negative phase on the structural response seemed to be small until maximum deflection, as the shape of the displacement curve was barely altered during this phase. However, abnormal oscillations were observed subsequent to the elastic rebound (see Figure 3.9). The synchronization of pressure and mid-point deflection in Figure 3.11 indicates that this unexpected behaviour may be due to the underpressure during the negative phase, i.e., the elastic rebound was enhanced by the negative phase. From the deformation profiles it is further observed that the maximum displacement had a small offset from the centre of the test specimen. This may stem from the positioning of the charge, which may have had an imperfect alignment relative to the centre of the plate. However, since the structural response seems to be driven by the imparted momentum, this offset may also stem from the boundary conditions or some other geometrical effect.

It was noted that the time of arrival t_a may be determined from the detonation pulse from the EBW detonator or taken from the calibration tests at the same stand-off distance, and the latter approach was used here. The former approach was only used at the closest stand-off distance (S11-S15), as no calibration tests were performed at this configuration. The time of arrival t_a for these tests was determined to be 0.07 ms. It should also be emphasized that the pressure measurements in Table 3.5 must be treated with some caution, since the pressure sensors were located at the clamping frame and not in the centre of the deforming plate. Keep in mind that the pressure may change as the thin plates deform, and this is not captured by these measurements. However, the limited FSI effects shown in Figure 3.11 and the pressure measurements from Section 3.3.1 indicate that the pressure measured at the clamping frame gives a good estimate of the loading on the plates.

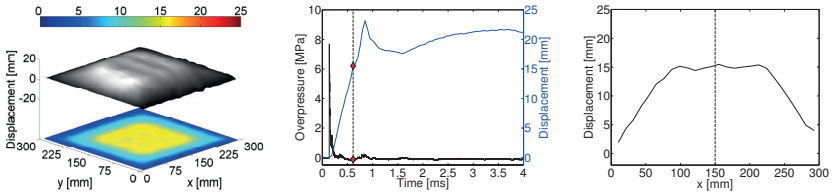

(a) t = 0.612 ms

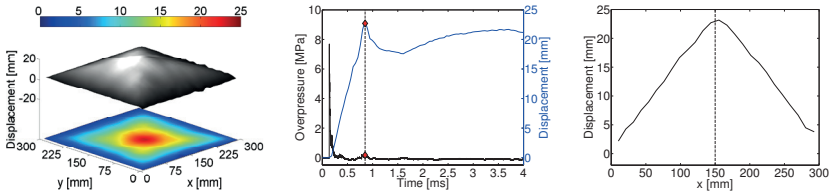

(b) t = 0.850 ms

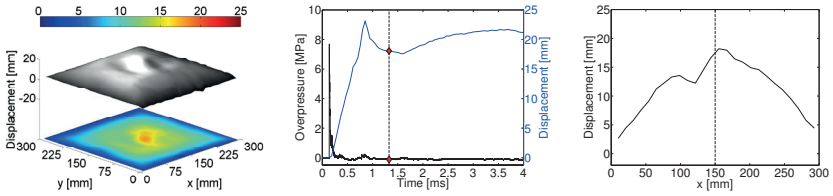

(c) t = 1.326 ms

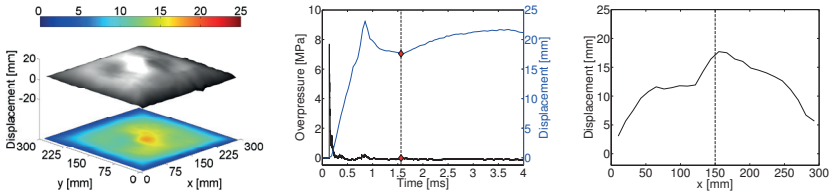

(d) t = 1.565 ms

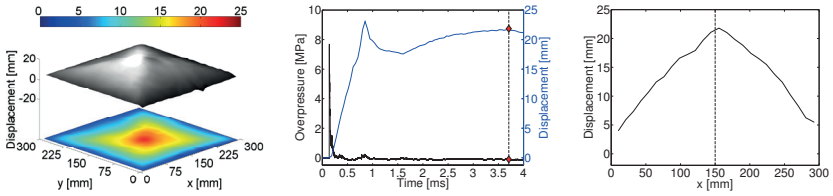

(e) t = 3.707 ms

Figure 3.11: A selection of DIC images from test S21 with 3D topography maps and contours of the transverse displacement (left), its corresponding pressure and centre deformation (middle) and deformation profile at the centre along the x-axis (right). Pressure recordings from Sensor 11 are used in the synchronization. Red diamonds show the corresponding time of recordings.

3.3.3 Aluminium plates

The aluminium plates showed in general a similar dynamic response as the steel specimens, but with some distinct differences. Figure 3.12 shows measured out-of-plane displacement at the centre point versus time for some of the tests based on the DIC analyses, while all results are summarized in Table 3.6. Compared to the steel specimens, it was observed a larger variation in the test results and a wider range in response as the aluminium specimens experienced both larger plastic deformations and failure (see Figure 3.13). It was only possible to perform DIC analyses on 7 out of 9 experiments due to flaking of the paint at the centre part in two of the tests. To reduce the risk of damaging the high-speed cameras it was decided not to use DIC at the closest stand-off distance of 250 mm (A01), as the plate was torn out of the clamping frame due to complete failure at the plate boundary (Figure 3.13a-3.13c). Due to the limited possibility to measure the structural response, it was chosen to only perform one experiment at this stand-off distance. The failure mode observed at the closest stand-off distance (A01) was similar to Mode II as reported by e.g. [55, 58, 59], i.e., tensile tearing at the supports, while the tests at the subsequent stand-off distance of 375 mm (A11-A13) experienced only partial tearing along the boundary (Figure 3.13d). The failure at this stand-off distance was therefore classified as Mode II*, in accordance with [57]. Thus, there was a transition between large inelastic deformations and complete tearing at the plate boundary. The failure was expected to start at the centre of the respective sides and propagate towards the corners with increasing impulse [57, 59]. However, since the pressure sensors were located at these points in the clamping frame (Figure 3.13c), the clamping was locally reduced and failure was first observed at the bolts closest to the centre of the plate boundary (Figure 3.13d). It was also observed a significant inward in-plane deflection at the centre of the plates for these experiments (Figure 3.13c-3.13d). This is sometimes called the "pulling-in" effect [57] and is a result of the plate deformation which continues between the time of first tearing at the boundary (Mode II*) and complete tearing at the corners (Mode II). As shown in Figure 3.13d-3.13f this effect seems to increase with increasing impulse as it was more evident at the closest stand-off distance. Before failure, "pulling-in" was not present and the plate experienced very limited sliding at the supports. As soon as failure occurred, there was a noticeably inward deflection at the centre of the plate. This resulted in some sliding at the supports and some deformation at the bolt holes, which is highlighted for the most evident case in Figure 3.13c. The deformation was most severe at the holes closest to the pressure sensors due to the reduced clamping along the centre lines of the frame. Thus, it is possible that the "pulling-in" effect was enhanced by the reduced clamping at the centre lines of the plate, as experimental evidence (e.g. [59]) has shown a

significant effect of the boundary conditions when predicting tearing.

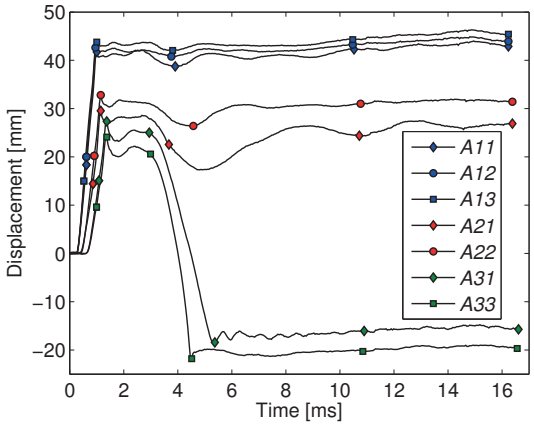

Figure 3.12: Deformation versus time of the centre point for the aluminium plates based on 3D-DIC.

The remaining two stand-off distances of 500 mm and 625 mm (A21-A23 and A31-A33) resulted in large inelastic deformation (Mode I) and RSB, respectively, as shown in Figure 3.13e-3.13f. Synchronized loading and response histories from test A31, i.e., at the largest stand-off distance, can be found in Figure 3.14. In a similar way as for the steel plate in Figure 3.11, this figure contains a selection of DIC images in terms of 3D topography maps, contours of the transverse displacement field and deformation profiles for characteristic times from the same test. Also these results revealed limited FSI effects during the positive phase as the duration of the positive part of the pressure pulse was almost over before the plate started to respond. Besides, the influence of the negative phase on the response up to maximum deformation seemed to be small since the shape of the displacement curve was barely altered during the negative phase. The selected DIC images for this particular test enabled a more detailed investigation of the CIB. Comparing Figure 3.9 and Figure 3.12, it is observed that the CIB in the aluminium plates was somewhat different than in the steel plates, since the RSB did not occur during the elastic rebound. These plates experienced RSB during the oscillations around its new equilibrium position, subsequent to the elastic rebound, and not during the rebound itself. This support previous observations by Symonds and Yu [47], which noted that the RSB phenomenon is extremely sensitive to small changes in the structural and loading properties. The narrow range of structural and loading properties related to this behaviour could be seen from the experiments at the intermediate stand-off distances (A21-A23 in Figure 3.12 and S21-S23 in Figure 3.9). Here abnormal oscillations subsequent to the elastic rebound were observed, indicating that these experiments were close to RSB and that

the transition between intuitive and counter-intuitive behaviour was between the two largest stand-off distances for both materials. Thus, a slight change in the intensity of the loading may result in a severe change in the structural response.

Table 3.6: Experimental results for the aluminium plates. The permanent mid-point deflections ($d_{z,p1}$) which are corrected for the slight movement of the mounting frame are given in parentheses.

Test	R	Z	Sensor*	$p_{r\alpha}$	t_{d+}	$i_{r\alpha+}$	t_{d+}/T_n	$d_{z,p1}$	$d_{z,p2}$	DIC
	[m]	[m/kg$^{1/3}$]	[#]	[MPa]	[ms]	[kPa ms]	[-]	[mm]	[mm]	[Y/N]
A01	0.250	0.73	6	9.8	0.11	185.7	0.008	-	-	N
A11	0.375	1.09	6	3.1	0.22	119.5	0.016	41.2(39.7)	39.1	Y
A12	0.375	1.09	7	3.8	0.18	127.5	0.013	42.2(41.4)	39.5	Y
A13	0.375	1.09	11	4.3	0.23	137.0	0.017	43.4(42.6)	43.3	Y
A21	0.500	1.46	11	1.7	0.40	111.5	0.030	28.3(23.4)	24.5	Y
A22	0.500	1.46	7	1.5	0.35	99.8	0.026	31.6(29.4)	30.8	Y
A23	0.500	1.46	7	1.5	0.36	102.8	0.026	-	25.8	N
A31	0.625	1.82	6	1.0	0.54	82.0	0.040	-17.3(-19.7)	-15.9	Y
A32	0.625	1.82	11	0.9	0.48	83.0	0.036	-	-23.4	N
A33	0.625	1.82	6	0.8	0.54	80.9	0.040	-20.8(-22.9)	-23.7	Y

*Stand-off distance R refers to the respective plate, and not to the sensor located in the frame.

A closer look on Figure 3.12 shows a drop in the displacement curve starting at approximately 3 ms for all experiments with aluminium plates. This drop is more evident at increasing stand-off distances, which makes it reasonable to relate the RSB in tests A31-A33 to the duration of the negative phase. Unfortunately, the drift in the pressure measurements made it difficult to determine the duration of the negative phase and it is challenging to conclude on the effect of the negative phase based on Figure 3.14. The influence of the negative phase on the structural response therefore needs further investigations.

As for the steel plate experiments, the DIC analyses showed that the maximum response was not always appearing at the centre of the plates (see Figure 3.14). However, the offset was small in all tests. This may stem from the positioning of the charge, which may have had a small offset from the centre of the plate. Since the deformation was driven by the impulse from the airblast it is more likely to assume that the boundary conditions, or some other geometrical effect, had a greater influence than the positioning of the charge on the deformed shape. As the plate was given an initial velocity by the transferred impulse, the deformed shape will be determined by the constraints at the boundary and the material properties.

The permanent deformation profile of the test specimens at the largest stand-off distance revealed a local dent at the centre of the thin plate (see Figure 3.13f), similar to that in the steel plate experiments. A closer examination of Figure 3.14b-3.14c indicates that the local dent developed during the elastic rebound.

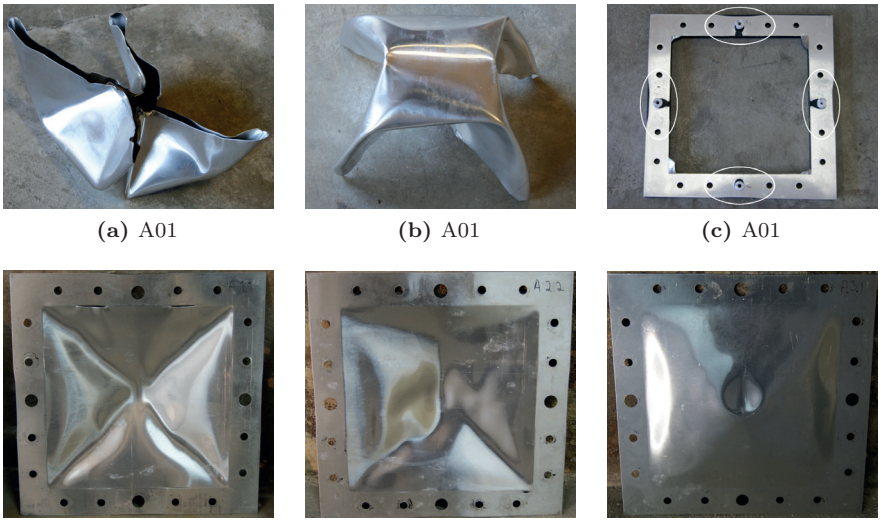

(a) A01 **(b)** A01 **(c)** A01

(d) A11 **(e)** A22 **(f)** A31

Figure 3.13: Photographs of deformed shapes for selected aluminium plates. All pictures are seen from the explosive charge except for (b).

This is also observed for the steel plate in Figure 3.11b-3.11c. Thus, as for the phenomenon of RSB, it was observed that the amount of plastic deformation determines the influence of the elastic rebound on the final shape. That is, large deformations (as in e.g. A11) result in intuitively deformed shape profiles, while smaller deformations reveal local dents at the centre and RSB (as in e.g. A31).

Since no calibration tests were performed at the largest stand-off distance (see Table 3.4), the arrival time t_a for tests A31-A33 was determined using the detonation pulse from the detonator. The shock wave produced by the EBW used to detonate the charge of C-4 was seen on the pressure measurements as an initial peak, and this was used as the best available estimate for the time of detonation. By using this approach, the time of arrival for tests A31-A33 was found to be 0.56 ms.

It should also be noted that the duration of the positive phase was taken from the pressure sensors located on the clamping frame, and that this duration was found to be slightly less compared to the recordings on the calibration plate (Figure 3.7 and Table 3.4). Depending on the stand-off distance, the time of arrival is somewhat different at the calibration plate and the clamping frame. It was also observed that the end time of the positive phase ($t = t_a + t_{d+}$) was approximately the same at both locations. This implies that the pressure recordings in the clamping frame could be used as an estimate of the end-time

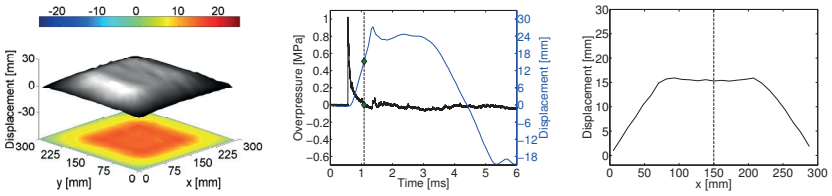

(a) t = 1.087 ms

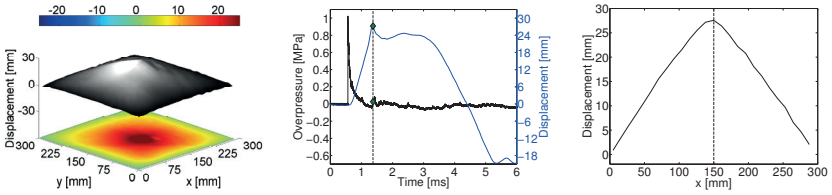

(b) t = 1.372 ms

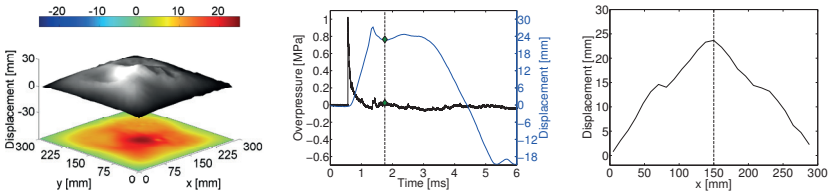

(c) t = 1.753 ms

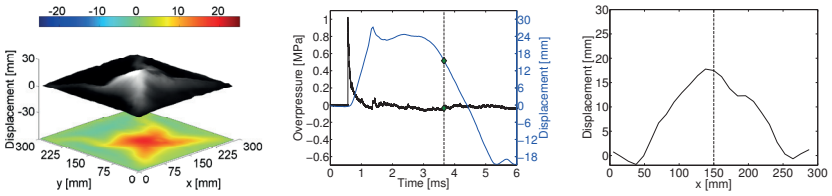

(d) t = 3.658 ms

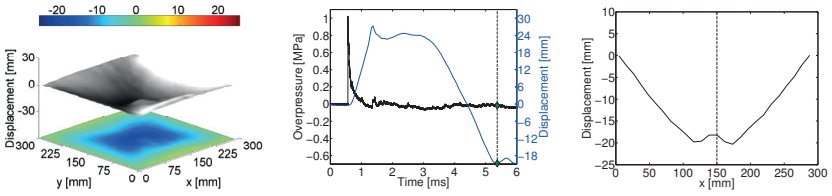

(e) t = 5.372 ms

Figure 3.14: A selection of DIC images from test A31 with 3D topography maps and contours of the transverse displacement (left), its corresponding pressure and centre deformation (middle) and deformation profile at the centre along the x-axis (right). Pressure recordings from Sensor 6 are used in the synchronization. Green diamonds show the corresponding time of recordings.

of the positive phase in the experiments. Despite this minor disagreement in pressure recordings, the loading was still defined as impulsive and the pressure measurements in the clamping frame were assumed reasonable to evaluate potential FSI effects. In a similar way as for the steel plates, the pressure measurements in Table 3.6 should be treated with some caution since the pressure may change as the plate deforms.

3.4 Concluding remarks

The influence of stand-off distance on the dynamic response of thin steel and aluminium plates subjected to airblast loading has been investigated experimentally. The loading was generated by detonating spherical charges of C-4 at various stand-off distances relative to the centre point of the plates, while the structural response was measured using two high-speed cameras in a stereovision setup combined with 3D-DIC analyses. The observations covered the entire range of structural response from complete ductile failure at the supports to CIB in terms of RSB at larger stand-off distances.

The overall trends in the experimental results were increased mid-point displacement of the plates and increased impulse as the intensity of the blast loading increased. This is shown in Figure 3.15 where the measured mid-point deflection-thickness ratio and scaled impulse as a function of scaled distance are plotted for all tests. Both the mid-point deflection and the impulse seem to have a rather linear decrease with increasing stand-off distance. However, the impulse at the closest stand-off distance differs somewhat from this linear trend. This is probably due to reduced accuracy of the pressure sensors due to high temperatures, which is supported by the observation in Figure 3.10a where it is evident that the plate is slightly burned by the fireball at the closest stand-off distance. It is also noted that the plates experiencing RSB deviate from the linear trend in Figure 3.15a.

The increased mid-point displacement with increasing impulse is intuitive as long as the final deflection is in the same direction as the external load. This behaviour is also in accordance with the theory of impulsively loaded plates as discussed by Jones [61]. First, a phase with plastic hinges that starts at the boundary corners of the plate and propagate along the diagonals toward the centre is observed (see Figure 3.11a and Figure 3.14a). Then, when the plastic hinges meet in the centre of the plate (see Figure 3.11b and Figure 3.14b), a final phase develops with oscillations around a permanent deformed shape. However, the response at the largest stand-off distance for both materials was counter-intuitive as the plates experience RSB and the final deflection was in the opposite direction of the incident blast wave.

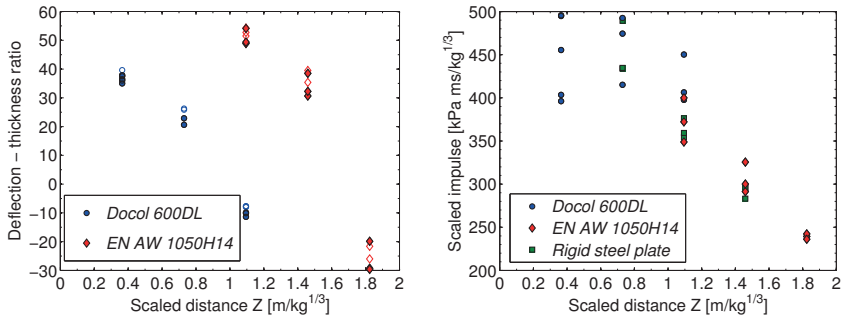

Figure 3.15: Measured mid-point deflection-thickness ratio $d_{z,p}/t$ (a) and scaled impulse $i_{r\alpha}/W^{1/3}$from a representative sensor in the frame (b) versus scaled distance $Z = R/W^{1/3}$. In (a) the open symbols are from the 3D-DIC measurements, while the closed symbols are from the manual measurements using a slide caliper.

The RSB attracted special attention as it occurred both during and subsequent to the elastic rebound. The RSB observed in Figure 3.9 during the elastic rebound is also observed in previous studies [45,46,54]. However, to the author's best knowledge there are no previous experimental studies on metallic plates observing RSB during the free vibrations around its new equilibrium position after the elastic rebound as shown in Figure 3.12. Based on the tests carried out, it is challenging to give an explanation of the observed phenomenon and also on how the negative phase will influence the observed response. The influence of the negative phase needs further investigations to determine the loading properties where this may dominate the response. This will be investigated in a subsequent numerical study in Chapter 5. It is also interesting to note that the response of the steel and aluminium plates at the same stand-off distance of 375 mm (S31-S33 in Figure 3.9 and A11-A13 in Figure 3.12) results in a completely different final deformed shape, as the steel plates experience RSB whereas the permanent displacement of the aluminium plates is in the intuitive direction.

These experiments also illustrate the possibilities of using finite element-based 3D-DIC for a thorough examination of the displacement field of blast-loaded structures. A comparison of the final mid-point deflections measured with DIC ($d_{z,p1}$) and the corresponding permanent displacement ($d_{z,p2}$) measured manually after the experiment indicated that there were some deviations in the two measurements. This was mainly due to the slight movement of the mounting frame during the tests and the DIC measurements were in very good agreement when corrected for this movement (see Tables 3.5 and 3.6). It is therefore assumed that the DIC measurements are more accurate than the

manually measured permanent displacement with the sliding caliper. The permanent displacement ($d_{\mathrm{z,p2}}$) was included to indicate the accuracy in the DIC measurements and to give experimental results when difficulties were observed with DIC. Thus, considering the potential sources of error in the manual measurements, DIC measurements should be used when available. The DIC technique also enabled a synchronization of the loading and response histories during the entire experiment, which provided new and accurate results under such extreme loading conditions.

4

Material modelling

Before performing the numerical study on the blast-loaded plates presented in Chapter 3, it is necessary to ensure that the computational model is able to predict the material behaviour in these types of loading environments. The observations in Chapter 3 showed that the dynamic response of the plates may become significantly different under varying blast intensity and structural properties. The dynamic response may therefore be highly dependent upon a proper treatment of the material modelling. This chapter presents the computational framework, constitutive equations and the implementation of an elastic-thermoviscoplastic material model in the explicit non-linear finite element code EUROPLEXUS.

4.1 Introduction

Blast events often involve large strains, elevated strain rates, temperature softening and ductile failure. A widely used design tool for this type of problems is the non-linear finite element (FE) method. In the FE method, the formulation and numerical solution of non-linear problems in continuum mechanics rely on the weak form of the momentum balance equation (also known as the principal of virtual power [171]). The integral form of the principal of virtual power is well suited for direct application to the FE method, and by spatial discretization the solution is integrated in time. In the particular case of blast events, it is often used an explicit time integration scheme based on the central difference method. Iterations for FE analyses involving non-linear material behaviour can in general be divided into two levels, hereby denoted the global and local level. The global level involves the explicit establishment of global equilibrium between internal stresses and external loads, while the local level updates the corresponding stress state in each FE integration point (for a given strain increment) in terms of the governing constitutive equations. Constitutive equations (also known as material models) are mathematical descriptions of the material behaviour which gives the stress as a function of the deformation history of the body [171]. This implies that the local

integration of the constitutive equations controls the accuracy and stability of the global equilibrium, and that the overall solution in the FE model may be considerably influenced by the accuracy, robustness and effectiveness of the integration algorithm.

A commonly used scheme for the local stress integration is the predictor-corrector method (often called return mapping). The basis for this return mapping is two successive steps, i.e., the predictor step and the corrector step. The predictor step is used to estimate a trial stress state, while the corrector step applies a flow rule by using a return mapping scheme to ensure the consistency condition. That is, ensuring that the stress state is on the yield surface. This thesis uses the explicit cutting plane method proposed by Ortiz and Simo [172]. During this approach an elastic predictor uses the total strain increment to obtain a trial stress state. Then, if the elastic trial stress is outside the plastic domain, the predicted stresses are corrected to return to the updated yield surface by iterations of the plastic corrector. The basis for the cutting plane method is to utilize the known stress state at the last converged time increment to determine the normal to the yield surface.

This work considers a well-known constitutive relation proposed by Johnson and Cook [173] where von Mises plasticity and associated flow are used to update the stresses. A model including elastic-thermoviscoplasticity and ductile failure is implemented as a new material called *VPJC* in EUROPLEXUS (EPX) [130]. The implementation uses a fully vectorized version of the forward Euler integration algorithm. Ductile failure is included in the model through the Cockcroft-Latham criterion [174] which is uncoupled from the constitutive equations. Large deformations are accounted for by using a hypoelastic-thermoviscoplastic formulation of the constitutive equations and a corotational formulation in EPX. This implies that the constitutive equations are defined in a local coordinate system in which the basis system rotates with the material. The subroutine interface uses the Cauchy stress components and all stress and strain quantities are defined in terms of the rate of deformation tensor. The model is applicable for one- (1D), two- (2D) and three-dimensional (3D) stress analyses (i.e., for bar, shell, solid, axisymmetric and plane strain elements). The model is also coupled with the element deletion options available in EPX by introducing a state variable controlling the element erosion. That is, as the failure variable reaches its critical value $D_C = 1.0$ the element is removed. Finally, material parameters are identified and the performance of the model is evaluated based on the tension tests in Section 3.2.2. A complete description of the formulation and implementation of the model is given in [175], while most of the theory presented herein is based on Hopperstad and Børvik [176].

4.2 Computational framework

There are in general two categories within the theory of plasticity, i.e., the mathematical theories and the physical theories [177]. Mathematical theories are purely phenomenological and aim to represent experimental observations through mathematical relations. Most of the common material models today are phenomenological. Physical theories try to describe the underlying mechanisms and quantify the plastic deformation at a microscopical level. A well-known and acknowledged physical theory is the crystal plasticity theory [176]. This section considers the phenomenological-based formulation of the constitutive equations for the computational model used in this thesis.

To account for finite strains and finite rotations, EPX defines all variables in a local coordinate system $\hat{\mathbf{e}}_i$ in which the basis system rotates with the material [130]. This is illustrated in Figure 4.1 where the base vectors of an integration point are expressed as

$$\hat{\mathbf{e}}_i = \boldsymbol{R} \cdot \mathbf{e}_i \tag{4.1}$$

where $\boldsymbol{R}$ is the rotation tensor representing the rigid body motion in the polar decomposition $\boldsymbol{F} = \boldsymbol{R} \cdot \boldsymbol{U}$ while $\boldsymbol{U}$ is the symmetric right stretch tensor. The corotated Cauchy stress $\hat{\boldsymbol{\sigma}}$ and rate-of-deformation tensor $\hat{\boldsymbol{D}}$ then read

$$\hat{\boldsymbol{\sigma}} = \boldsymbol{R}^T \cdot \boldsymbol{\sigma} \cdot \boldsymbol{R} \tag{4.2a}$$

$$\hat{\boldsymbol{D}} = \boldsymbol{R}^T \cdot \boldsymbol{D} \cdot \boldsymbol{R} \tag{4.2b}$$

Assuming negligible elastic strains compared to the plastic strains, an hypoelastic formulation is adopted through an additive decomposition of the rate of deformation tensor [171]

$$\hat{\boldsymbol{D}} = \hat{\boldsymbol{D}}^e + \hat{\boldsymbol{D}}^p \tag{4.3}$$

where $\hat{\boldsymbol{D}}^e$ and $\hat{\boldsymbol{D}}^p$ are the elastic and plastic part, respectively. The rate-of-deformation tensor $\hat{\boldsymbol{D}}$ is also called velocity strain and is a rate measure of the deformation and stretching of the elements.

The starting point for hypoelastic models is the formulation of the constitutive equations in terms of objective stress rates [178]. A generalized form of Hooke's law on rate form is therefore introduced, i.e.,

$$\dot{\hat{\boldsymbol{\sigma}}} = \hat{\boldsymbol{C}} : \hat{\boldsymbol{D}}^e = \lambda_{\mathrm{el}} \left(\mathrm{tr} \hat{\boldsymbol{D}}^{\mathrm{e}} \right) \mathbf{I} + 2\mu_{\mathrm{el}} \hat{\boldsymbol{D}}^e \tag{4.4}$$

where $\dot{\hat{\boldsymbol{\sigma}}}$ is the time derivative of the corotated Cauchy stress tensor and $\hat{\boldsymbol{C}}$ is

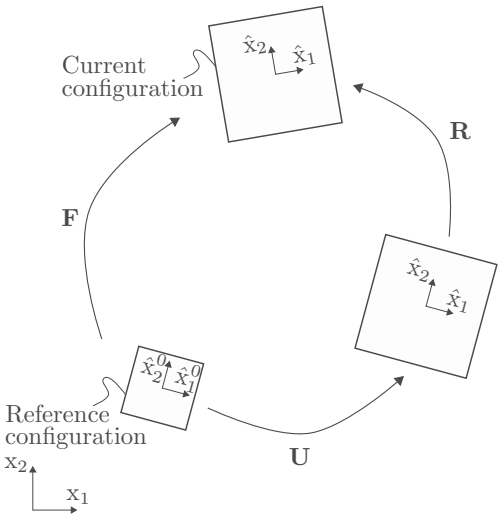

Figure 4.1: Polar decomposition of a typical homogeneous deformation. The Cartesion coordinate system with coordinate axes (x_1, x_2) refers to the global reference frame $\mathbf{e}_i$, while ($\hat{x}_1$, $\hat{x}_2$) represents the local (or corotated) coordinate system $\hat{\mathbf{e}}_i$.

the fourth order elasticity tensor given by

$$\hat{\boldsymbol{C}} = \lambda_{\mathrm{el}} \boldsymbol{I} \otimes \boldsymbol{I} + 2\mu_{\mathrm{el}} \boldsymbol{I} \tag{4.5}$$

and $\boldsymbol{I}$ is the second order identity tensor, while λ_{el} and μ_{el} are the Lamè constants given as

$$\lambda_{\mathrm{el}} = \frac{\nu E}{(1+\nu)(1-2\nu)} \qquad \text{and} \qquad \mu_{\mathrm{el}} = \frac{E}{2(1+\nu)} \tag{4.6}$$

The elasticity tensor $\hat{\boldsymbol{C}}$ is assumed to be constant, E is the Young's modulus and ν the Poisson's ratio. The objective (or frame-invariant) stress rate $\hat{\boldsymbol{\sigma}}^{\nabla}$ typically reads

$$\hat{\boldsymbol{\sigma}}^{\nabla} = \dot{\hat{\boldsymbol{\sigma}}} - \boldsymbol{A} \cdot \hat{\boldsymbol{\sigma}} + \hat{\boldsymbol{\sigma}} \cdot \boldsymbol{A} \tag{4.7}$$

where $\boldsymbol{A}$ is an appropriate angular velocity tensor. Combining Eqs. (4.4) and (4.7) the rate of the corotated Cauchy stress is obtained as

$$\dot{\hat{\boldsymbol{\sigma}}} = \boldsymbol{A} \cdot \hat{\boldsymbol{\sigma}} - \hat{\boldsymbol{\sigma}} \cdot \boldsymbol{A} + \lambda_{\mathrm{el}} \left(\mathrm{tr} \hat{\boldsymbol{D}}^{\mathrm{e}} \right) \boldsymbol{I} + 2\mu_{\mathrm{el}} \hat{\boldsymbol{D}}^{e} \tag{4.8}$$

The choice of an appropriate angular velocity tensor $\boldsymbol{A}$ is typically done by the respective FE codes, where EPX uses the Jaumann rate of the Cauchy stress

$\hat{\boldsymbol{\sigma}}^{\nabla J}$ [130] given as

$$\hat{\boldsymbol{\sigma}}^{\nabla J} = \dot{\hat{\boldsymbol{\sigma}}} - \boldsymbol{W}\cdot\hat{\boldsymbol{\sigma}} + \hat{\boldsymbol{\sigma}}\cdot\boldsymbol{W}, \qquad \boldsymbol{A} = \boldsymbol{W} = \frac{1}{2}\left(\boldsymbol{L} - \boldsymbol{L}^T\right) \tag{4.9}$$

where $\boldsymbol{W}$ is the spin tensor indicating the rate of rotation of an element and $\boldsymbol{L} = \boldsymbol{D} + \boldsymbol{W}$ is the velocity gradient (see e.g. [171] for more details). It is worth noting that when using polar decomposition $\boldsymbol{F} = \boldsymbol{R}\cdot\boldsymbol{U}$ the spin tensor $\boldsymbol{W}$ can be expressed as [179]

$$\boldsymbol{W} = \dot{\boldsymbol{R}}\cdot\boldsymbol{R}^T + \boldsymbol{R}\cdot\frac{1}{2}\left(\dot{\boldsymbol{U}}\cdot\boldsymbol{U}^{-1} - \boldsymbol{U}^{-1}\cdot\dot{\boldsymbol{U}}\right)\cdot\boldsymbol{R}^T \tag{4.10}$$

where it is used that $\dot{\boldsymbol{F}} = \boldsymbol{L}\cdot\boldsymbol{F}$. Thus, for pure rigid motion ($\dot{\boldsymbol{U}} = 0$) the spin tensor $\boldsymbol{W}$ reads

$$\boldsymbol{W} = \dot{\boldsymbol{R}}\cdot\boldsymbol{R}^T \tag{4.11}$$

Using the Jaumann rate in Eq. (4.4), the corotational elastic rate-of-deformation tensor is given as

$$\hat{\boldsymbol{D}}^e = \frac{1+\nu}{E}\hat{\boldsymbol{\sigma}}^{\nabla J} - \frac{\nu}{E}\mathrm{tr}\left(\hat{\boldsymbol{\sigma}}^{\nabla \mathrm{J}}\right)\boldsymbol{I} \tag{4.12}$$

The static yield function is defined as

$$f(\hat{\boldsymbol{\sigma}}, p, T) = \sigma_{eq}\left(\hat{\boldsymbol{\sigma}}\right) - \sigma_y\left(p, T\right) \tag{4.13}$$

where σ_{eq} is the equivalent stress, σ_y is the flow stress, p is the equivalent plastic strain and T is the absolute temperature.

Assuming the plastic flow to be associative, the corotational plastic rate-of-deformation may be written as

$$\hat{\boldsymbol{D}}^p = \dot{\lambda}\frac{\partial f}{\partial \hat{\boldsymbol{\sigma}}} \tag{4.14}$$

where $\dot{\lambda} \geq 0$ is a scalar denoted the plastic multiplier. The plastic multiplier is zero in the elastic domain and positive in the plastic domain. An important remark to the assumption of associated flow is that the shape of the yield surface also determines the direction of the plastic flow, as well as the stress state at which yielding initiates.

The plastic deformation process is governed by the important physical restriction that

$$\mathfrak{D}_p = \hat{\boldsymbol{\sigma}} \colon \hat{\boldsymbol{D}}^p \geq 0 \tag{4.15}$$

where $\mathfrak{D}_p$ expresses the plastic dissipation per unit volume, which is assumed to be dissipated as heat. Eq. (4.15) ensures that work has to be done to the body all the time for the deformation to continue.

The equivalent plastic strain rate $\dot{p}$ is defined to be energy conjugate to σ_{eq}, i.e.,

$$\hat{\boldsymbol{\sigma}} : \hat{\boldsymbol{D}}^p = \sigma_{eq}\dot{p} \tag{4.16}$$

This implies that, under the assumption that σ_{eq} is a positive homogeneous function of order one and using Euler's theorem for such functions (see [176]), $\dot{p}$ equals the plastic multiplier

$$\dot{p} = \dot{\lambda} \tag{4.17}$$

Finally, Eq. (4.17) can be integrated to find the equivalent plastic strain p

$$p = \int_0^t \dot{p}\mathrm{dt} = \int_0^{\mathrm{t}} \dot{\lambda}\mathrm{dt} \tag{4.18}$$

4.3 Constitutive equations

Based on the materials tests in Section 3.2.2 it was assumed that the materials used herein can be considered as isotropic. These experiments also supported the assumption of small elastic strains compared to the plastic strains. The material response is therefore modelled with isotropic hardening and the plastic flow is independent of direction (isotropic) and volume preserving (isochoric). Thermodynamic coupling is not included, however, the temperature evolution is assumed to be adiabatic. Ductile failure is considered by using a simple one-parameter failure criterion which is based on plastic work per unit volume. The implementation of the failure criterion follows an uncoupled approach where the yield criterion, plastic flow and strain hardening are unaffected by the damage evolution.

4.3.1 The von Mises yield criterion

Geometrically, the yield criterion in Eq. (4.13) defines a surface in stress space given by the components of the stress tensor $\hat{\boldsymbol{\sigma}}$ (i.e., the vector space in Figure 4.2). The elastic domain is given by the stress space inside this yield surface $f < 0$, while the plastic domain is the surface itself $f = 0$ (see Figure 4.3).

Assuming isotropic behaviour and no kinematic hardening, the von Mises (or J_2) flow theory for pressure insensitive materials is adopted. From Figure 4.3 it can be shown that the von Mises yield surface is a circular cylinder of radius $\mathbf{R}_v = \sqrt{\frac{2}{3}}\sigma_y$. The stress state on the yield surface could then be represented in the principal stress space as the vector $\mathbf{r} = [\sigma_1 \quad \sigma_2 \quad \sigma_3]$, which has to satisfy the following equation [179]

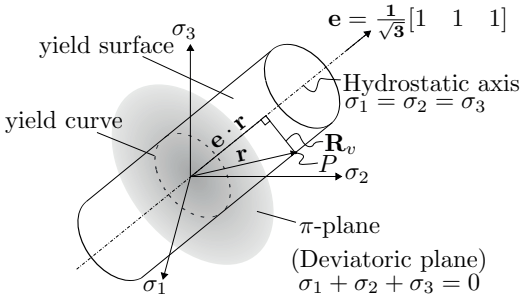

Figure 4.2: Illustration of the von Mises yield criterion in the principal stress space.

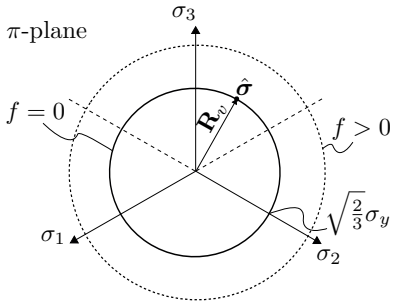

Figure 4.3: The von Mises yield criterion in the deviatoric plane (π-plane).

$$\mathbf{r} \cdot \mathbf{r} - (\mathbf{e} \cdot \mathbf{r})\,(\mathbf{e} \cdot \mathbf{r}) = \mathbf{R}_v^2 \tag{4.19}$$

Splitting the stress into deviatoric and hydrostatic parts

$$\hat{\boldsymbol{\sigma}}^{'} = \hat{\boldsymbol{\sigma}} - \sigma_H \mathbf{I} \tag{4.20a}$$

$$\sigma_H = \frac{1}{3}\mathrm{tr}(\hat{\boldsymbol{\sigma}}) = \frac{1}{3}\left(\sigma_1 + \sigma_2 + \sigma_3\right) \tag{4.20b}$$

where $\hat{\boldsymbol{\sigma}}^{'}$ is the deviatoric stress and σ_H is the hydrostatic stress, the radius of the yield surface $\boldsymbol{R}_v$ could be expressed as

$$\begin{aligned} \boldsymbol{R}_v^2 &= \hat{\boldsymbol{\sigma}} : \hat{\boldsymbol{\sigma}} - \left(\frac{1}{\sqrt{3}}\mathrm{tr}(\hat{\boldsymbol{\sigma}})\right)^2 = (\sigma_{ij}^{'} + \sigma_H \delta_{ij})(\sigma_{ij}^{'} + \sigma_H \delta_{ij}) - 3\sigma_H^2 \\ &= \sigma_{ij}^{'}\sigma_{ij}^{'} = \hat{\boldsymbol{\sigma}}^{'} : \hat{\boldsymbol{\sigma}}^{'} = \frac{2}{3}\sigma_y^2 \end{aligned} \tag{4.21}$$

Eq. (4.21) implies that isotropic (or hydrostatic) stress states do not result in yielding. Thus, the von Mises yield criterion is purely deviatoric and additional hydrostatic stress only translates the stress state along the hydrostatic axis in

Figure 4.2. The result in Eq. (4.21) could then be presented in terms of the yield function f from Eq. (4.13), i.e.,

$$\begin{aligned} f(\hat{\boldsymbol{\sigma}}, p, T) &= \sigma_{eq}(\hat{\boldsymbol{\sigma}}) - \sigma_y(p, T) \\ &= \sqrt{\frac{3}{2}\hat{\boldsymbol{\sigma}}' : \hat{\boldsymbol{\sigma}}'} - \sigma_y(p, T) = \sqrt{3J_2} - \sigma_y(p, T) \end{aligned} \tag{4.22}$$

where the von Mises equivalent stress σ_{eq}, in terms of the stress components, reads

$$\sigma_{eq} = \sqrt{\begin{array}{l} \hat{\sigma}_{11}^2 + \hat{\sigma}_{22}^2 + \hat{\sigma}_{33}^2 - \hat{\sigma}_{11}\hat{\sigma}_{22} - \hat{\sigma}_{22}\hat{\sigma}_{33} - \hat{\sigma}_{33}\hat{\sigma}_{11} \\ + 3(\hat{\sigma}_{12}^2 + \hat{\sigma}_{23}^2 + \hat{\sigma}_{31}^2) \end{array}} \tag{4.23}$$

and the associated flow rule in Eq. (4.14) is then given as

$$\hat{\boldsymbol{D}}^p = \dot{\lambda}\frac{\partial f}{\partial \hat{\boldsymbol{\sigma}}} = \dot{\lambda}\frac{3}{2}\frac{\hat{\boldsymbol{\sigma}}'}{\sigma_{eq}} \tag{4.24}$$

Finally, the rate of the equivalent plastic strain $\dot{p}$, in the particular case of associated flow and von Mises isotropic behaviour, is given as

$$\dot{p} = \sqrt{\frac{2}{3}\hat{\boldsymbol{D}}^p : \hat{\boldsymbol{D}}^p} \tag{4.25}$$

4.3.2 The modified Johnson-Cook constitutive model

As discussed earlier, blast-loaded structures may experience large strains, elevated strain rates and temperature softening in the material. A widely used material model allowing for these effects is the constitutive relation proposed by Johnson and Cook [173], which is empirical and dates back to 1983. This constitutive relation has a multiplicative formulation and is given by

$$\sigma_y = (A + Bp^n)\,(1 + c\ln(\dot{p}^*))\,(1 - T^{*m}) \tag{4.26}$$

where A, B, c, n and m are material constants determined from material tests, and

$$\dot{p}^* = \frac{\dot{p}}{\dot{p}_0} \qquad \text{and} \qquad T^* = \frac{T - T_r}{T_m - T_r} \tag{4.27}$$

represent the dimensionless strain rate $\dot{p}^*$ and the non-dimensional homologous temperature T^*, respectively. The parameter $\dot{p}_0$ is a user-defined reference strain rate, while T_r and T_m are defined as the room and melting temperature, respectively. The first term in Eq. (4.26) represents the strain hardening, the second term describes the strain rate hardening, and the last term represents the temperature softening behaviour. The second and third terms shift the

hardening curve up or down, depending on the strain rate and the temperature conditions. It is observed from Eq. (4.26) that the flow stress σ_y increases with increasing plastic strain rate (which is a necessary characteristic in viscoplasticity), while it decreases with increasing temperature. Thus, an increase in the plastic strain rate expands the yield surface whereas an increase in temperature contracts the yield surface.

To avoid non-physical softening effects when $\dot{p}^* < 1$, the strain-rate-sensitivity term in the Johnson-Cook model can be adjusted [180]. This leads to a modified version of the constitutive model given as [181]

$$\sigma_y = (A + Bp^n)\,(1 + \dot{p}^*)^c\,(1 - T^{*m}) \tag{4.28}$$

This is illustrated by a comparison of Eqs. (4.26) and (4.28) in Figure 4.4, where the ordinate axis refers to the normalized stress $\sigma_y / [(A + Bp^n)]$ at ambient temperature. Note that, since the formulations in Eqs. (4.26) and (4.28) are slightly different, the calibration of the viscoplastic material parameter c may be slightly different in the two versions of the Johnson-Cook model.

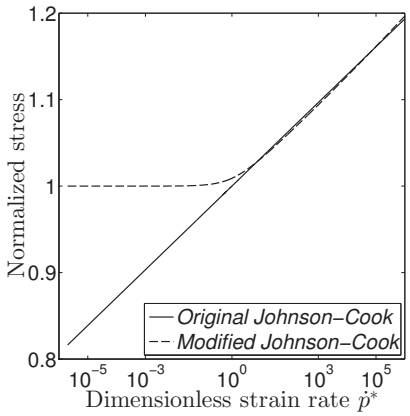

Figure 4.4: Original versus modified Johnson-Cook model when $c_{JC} = 0.014$, $c_{MJC} = 0.013$, and $\dot{p}_0 = 5 \times 10^{-4}$.

The first term of the Johnson-Cook model increases indefinitely with increasing strain and could lead to numerical instabilities when $n < 1$ due to the initial value of p, i.e., p equals zero before any plasticity occurs. This results in an infinite value of the hardening modulus $H_R = Bnp^{n-1}$ during the return mapping in the plastic corrector step. Defining the initial plastic strain as an infinitely small value would avoid this problem. However, it is desirable to formulate the material model as general as possible. Therefore, the first term of Eq. (4.28) is replaced by another hardening rule than that proposed by Johnson and Cook. Replacing the first term of Eq. (4.28) with a two terms

saturation type of hardening rule proposed by Voce [182], the flow stress could be expressed as

$$\begin{aligned}\sigma_y &= (A + R(p))\,(1+\dot{p}^*)^c\,(1-T^{*m}) \\ &= (A + \sum_{k=1}^{2} Q_k[1-\exp(-C_k p)])\,(1+\dot{p}^*)^c\,(1-T^{*m})\end{aligned} \tag{4.29}$$

where the constant A is the initial yield strength of the material, $R(p)$ is introduced as the isotropic hardening variable, and Q_k and C_k $(k = 1, 2)$ define the strain hardening. As before, the rate sensitivity is governed by the constant c while m defines the thermal softening behaviour. The hardening modulus H_R is found from the rate of change in $R(p)$ given as

$$\dot{R} = \frac{dR}{dt} = \frac{dR}{dp}\frac{dp}{dt} = H_R\frac{dp}{dt}\,, \qquad H_R = \frac{dR}{dp} = \sum_{k=1}^{2} Q_k C_k e^{(-C_k p)} \tag{4.30}$$

It is seen from Eq. (4.30) that no numerical instabilities are expected for the hardening modulus H_R when the plastic strain equals zero and that the hardening tends to zero at increasing strain.

Evaluating yielding in the viscoplastic domain and combining Eqs. (4.22) and (4.29), the strain-rate sensitivity of the material is controlled by

$$\dot{p} = \dot{\lambda} = \begin{cases} 0 & , \quad f \le 0 \\ \dot{p}_0\left[\left(\frac{\sigma_{eq}(\hat{\boldsymbol{\sigma}})}{\sigma_y(p,T)}\right)^{\frac{1}{c}} - 1\right], & f > 0 \end{cases} \tag{4.31}$$

Thus, in the viscoplastic domain $(f > 0)$ the equivalent stress is found from Eq. (4.31) as

$$\begin{aligned}\sigma_{eq}(\hat{\boldsymbol{\sigma}}) &= \sigma_y(p,T)\,(1+\dot{p}^*)^c \\ &= (A + \sum_{k=1}^{2} Q_k[1-\exp(-C_k p)])\,(1+\dot{p}^*)^c\,(1-T^{*m})\end{aligned} \tag{4.32}$$

and the dynamic yield function f_d reads

$$f_d(\hat{\boldsymbol{\sigma}}, p, \dot{p}, T) = \sigma_{eq}(\hat{\boldsymbol{\sigma}}) - \sigma_y(p,T)\,(1+\dot{p}^*)^c \tag{4.33}$$

4.3.3 Adiabatic thermal softening

Assuming that the plastic work is dissipated as heat implies that large plastic deformation results in an increase in temperature. The result of this increase

in temperature is a decrease in flow stress. This is already introduced in the last term of Eq. (4.29), which accounts for the thermal softening of the flow stress at elevated temperatures. However, the evolution of the temperature remains to be established. Since the plastic response of the material is of a very short time duration in blast events, the temperature evolution is modeled by assuming adiabatic conditions. This implies that there is no heat transfer into or out of the system during the plastic straining. Using the thermal energy balance per unit volume given by [176]

$$\mathfrak{D}_p = \chi \hat{\boldsymbol{\sigma}} : \mathbf{D}^p = \chi \sigma_{eq} \dot{p} = \rho c_p \dot{T} \tag{4.34}$$

where ρ is the material density, c_p is the specific heat capacity of the solid material and χ is the Taylor-Quinney coefficient. The temperature increase due to adiabatic heating can be computed as

$$\dot{T} = \frac{\mathfrak{D}_p}{\rho c_p} = \frac{\chi \sigma_{eq} \dot{p}}{\rho c_p} \tag{4.35}$$

From Eq. (4.34) it is seen that the Taylor-Quinney coefficient χ represents the fraction of the plastic power that is converted into heat. The remaining fraction $1 - \chi$ is assumed to be stored in the material due to structural rearrangements (e.g. elastic "fields" around dislocations). Typical values used in simulations are $\chi = 0$ for isothermal conditions and $\chi = 0.9$ for adiabatic conditions. However, a conservative choice would be $\chi = 1.0$ in adiabatic conditions which ensures maximum thermal softening. In reality the χ-value will not be constant, however, advanced experimental techniques are necessary to determine the evolution of this parameter. Moreover, one should always keep in mind that while strain hardening (i.e., work hardening due to generation and movements of dislocations) increases the strength locally in the material and distributes the plasticity, softening results in localization of plasticity.

4.3.4 Ductile failure

A material model is not complete without some form of material degradation or failure. The degradation or failure in a material is usually given in terms of a damage parameter and failure occurs through damage evolution. Ductile fracture arises from the nucleation, growth and coalescence of microscopic voids that initiate at inclusions and second phase particles. The voids around particles grow when the material is subjected to plastic straining and hydrostatic tension, and fracture occurs when the growing voids reach a critical size, relative to their spacing, resulting in a local plastic instability between the voids [183]. This work considers only ductile failure which is defined as the first sign of fracture, i.e., the coalescence of voids. This means that the fracture criterion is

uncoupled from the constitutive equations, and is therefore denoted a failure criterion in the following.

Cockcroft and Latham [174] suggested a simple failure criterion which is based on "plastic work" per unit volume. They reasoned that the failure criterion needed to be based on some combination of stress and strain, and that damage accumulates during plastic straining. To account for hydrostatic tension they based the criterion on the magnitude of the major principal stress σ_1, i.e.,

$$D = \frac{W}{W_c} = \frac{1}{W_c} \int_0^p \langle \sigma_1 \rangle \, dp \tag{4.36}$$

where W_c is the failure parameter which can be found by integrating the major principal stress in a uniaxial tension test during the entire equivalent plastic strain path until the plastic strain at failure p_f. The Macaulay brackets imply that $\langle a \rangle = \frac{1}{2}(a + |a|)$ for any real number a and that only positive values of the major principal stress σ_1 contribute to the damage evolution. Material failure emerges when the damage parameter D in Eq. (4.36) reaches unity. This failure criterion is attractive in structural design, since only one damage parameter obtained from a single uniaxial tension test is required for calibration. Moreover, experimental studies by Langdon et al. [184] on blast-loaded steel and aluminium plates indicated that the failure of ductile plates could be related to the specific energy giving tensile failure, and that failure under such conditions could be predicted from simple quasi-static tension tests.

Previous studies in terminal ballistics [185–187] have proven the robustness of the Cockcroft-Latham (CL) criterion. The dependence of both deviatoric and hydrostatic stress states were discussed by Holmen et al. [162, 188], where it was shown that damage will not evolve for sufficiently low values of stress triaxiality. This is seen by using an alternative expression for the major principal stress [188], i.e.,

$$\sigma_1 = \sigma_H + \frac{3 + \mu_\sigma}{3\sqrt{3 + \mu_\sigma^2}} \sigma_{eq} = \left(\sigma^* + \frac{3 + \mu_\sigma}{3\sqrt{3 + \mu_\sigma^2}} \right) \sigma_{eq} \tag{4.37}$$

where the stress triaxiality σ^* and the Lode parameter μ_σ are defined by

$$\sigma^* = \frac{\sigma_H}{\sigma_{eq}} \,, \quad \mu_\sigma = \frac{2\sigma_2 - \sigma_1 - \sigma_3}{\sigma_3 - \sigma_1} \tag{4.38}$$

Remember that $\sigma_1 \geq \sigma_2 \geq \sigma_3$ are the ordered principal stresses. Eq. (4.36) can then be expressed as

$$D = \frac{1}{W_c} \int_0^p \left\langle \sigma^* + \frac{3 + \mu_\sigma}{3\sqrt{3 + \mu_\sigma^2}} \right\rangle \sigma_{eq} dp \tag{4.39}$$

Thus, damage is driven by plastic dissipation and amplified by a factor depending on the stress state through the parameters σ^* and μ_σ. Since material failure occurs when $D = 1.0$ and $p = p_f$, Eq. (4.39) can be written as

$$1 = \frac{1}{W_c} \int_0^{p_f} \left\langle \sigma^* + \frac{3 + \mu_\sigma}{3\sqrt{3 + \mu_\sigma^2}} \right\rangle \sigma_{eq} dp \tag{4.40}$$

Assuming that the stress triaxiality σ^* and Lode parameter μ_σ remain constant throughout the entire loading history (i.e., proportional loading conditions) and using the Voce hardening rule from Eq. (4.29) to express the equivalent stress σ_{eq} through the yield condition in Eq. (4.22), Eq. (4.40) now reads

$$\sigma^* = \frac{W_c}{A p_f + \sum_{k=1}^{2} (Q_k p_f + \frac{Q_k}{C_k} [\exp(-C_k p_f) - 1])} - \frac{3 + \mu_\sigma}{3\sqrt{3 + \mu_\sigma^2}} \tag{4.41}$$

The influence of stress triaxiality σ^* and Lode parameter μ_σ on the plastic failure strain p_f can then be illustrated as shown in Figure 4.5, where the material parameters from Holmen et al. [162] are used to generate the respective curves. Various loading scenarios are now represented by different combinations of the stress triaxiality and the Lode parameter. Some typical examples are $(\mu_\sigma, \sigma^*) = (+1, 1/3)$ which implies uniaxial tension $(\sigma_1 \geq \sigma_2 = \sigma_3)$, $(\mu_\sigma, \sigma^*) = (0, 0)$ corresponding to pure shear $(2\sigma_2 = \sigma_1 + \sigma_3)$ and $(\mu_\sigma, \sigma^*) = (-1, -1/3)$ representing uniaxial compression $(\sigma_1 = \sigma_2 \geq \sigma_3)$.

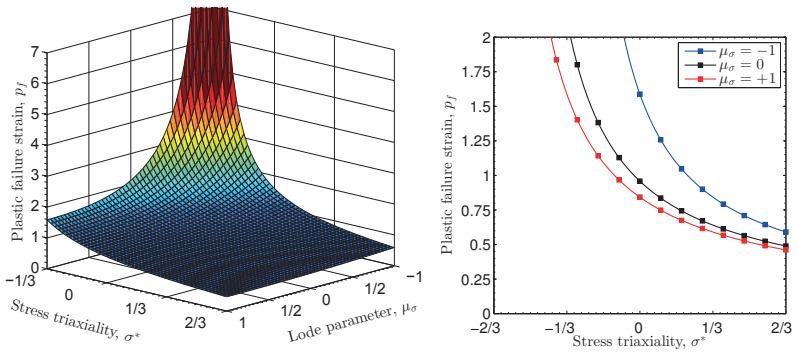

(a) Failure surface **(b)** Selected Lode parameters

Figure 4.5: Representation of the plastic failure strain p_f in the (μ_σ, σ^*) space when using the Cockcroft-Latham failure criterion and assuming proportional loading conditions. Note that the material parameters used in Eq. (4.41) are taken from [162].

From Eq. (4.36) it is observed that, to make the material model as general as possible, it is preferable to compute the principal stresses directly in the subroutine. This is done by following the procedure proposed by [179] which uses the principal deviatoric stresses $\sigma_i^{'}$ to find the principal stresses σ_i. The

principal deviatoric stresses are determined from the eigenvalue problem for the deviatoric stress $\hat{\boldsymbol{\sigma}}^{'}$ in Eq. (4.20a), i.e.,

$$\det(\hat{\sigma}^{'}\mathbf{I} - \hat{\boldsymbol{\sigma}}^{'}) = 0 \tag{4.42}$$

where $\det(\,\cdot\,)$ is the determinant of the matrix argument $(\,\cdot\,)$. The result of this operation is a cubic equation called the characteristic equation, given as

$$(\hat{\sigma}^{'})^3 - I_1^{'}(\hat{\sigma}^{'})^2 - J_2\hat{\sigma}^{'} - J_3 = 0 \tag{4.43}$$

where the principal invariants of the stress deviator are given respectively as

$$\begin{aligned} &I_1^{'} = \mathrm{tr}(\hat{\boldsymbol{\sigma}}^{'}) = \hat{\sigma_{ii}}^{'} = 0, \quad J_2 = -I_2^{'} = \frac{1}{2}\mathrm{tr}(\hat{\boldsymbol{\sigma}}^{'2}) = \frac{1}{2}\hat{\sigma}_{ij}^{'}\hat{\sigma}_{ij}^{'}, \\ &J_3 = I_3^{'} = \det(\hat{\boldsymbol{\sigma}}^{'}) \end{aligned} \tag{4.44}$$

and the J-symbols for the principal invariants are introduced since these are commonly used in the literature for metal plasticity. The general solution is then given as [179]

$$\begin{aligned} &\sigma_1^{'} = 2\sqrt{\frac{J_2}{3}}\cos\frac{\theta}{3}, \quad \sigma_2^{'} = 2\sqrt{\frac{J_2}{3}}\cos\left(\frac{\theta}{3} - \frac{2\pi}{3}\right) \leq \sigma_1^{'}, \\ &\sigma_3^{'} = 2\sqrt{\frac{J_2}{3}}\cos\left(\frac{\theta}{3} + \frac{2\pi}{3}\right) \leq \sigma_2^{'} \end{aligned} \tag{4.45}$$

where the angle θ is defined as

$$\cos\theta = \frac{J_3}{2\sqrt{J_2^3/27}}, \quad 0 \leq \theta \leq \pi \tag{4.46}$$

and the Lode angle is recognized as $\theta_L = \theta/3$. Finally, the principal stresses σ_i of the stress tensor $\hat{\boldsymbol{\sigma}}$ are determined by

$$\sigma_i = \sigma_i^{'} + \sigma_H = \sigma_i^{'} + \frac{1}{3}\mathrm{tr}(\hat{\boldsymbol{\sigma}}) \tag{4.47}$$

where the major principal stress σ_1 is used in the CL criterion in Eq. (4.36).

4.4 Numerical return mapping

Wilkins [189] was one of the first to introduce a return mapping algorithm, and a variety of schemes have been proposed following this work (see e.g. [172,178,190–192]). In general, it is possible to categorize the stress integration methods in two different approaches, i.e., the forward Euler method and the backward Euler method. The choice of method is illustrated in Figure 4.6

and is mainly based on the assumption of the direction of the plastic flow $\boldsymbol{n} = \partial f_d / \partial \hat{\boldsymbol{\sigma}}$. The forward Euler method uses the known stress state at the previous or trial configuration to determine the plastic flow direction $\boldsymbol{n}$ [172] (see Figure 4.6a). This assumption is therefore only valid for very small time steps, and is therefore suitable for the explicit time integration FE method. Since the direction is known, there is only one unknown during the return mapping procedure and that is the plastic multiplier $\dot{\lambda}$. The backward Euler method evaluates the normal $\boldsymbol{n}$ to the yield surface at the current unknown stress state [191] (see Figure 4.6b), which gives good accuracy even for larger time steps making it appropriate for both the explicit and implicit time integration FE methods. However, the variation of the normal to the yield surface must be taken into consideration during the return mapping procedure resulting in a more complex integration due to possible second order derivatives of the yield function. Previous studies by De Borst and Feenstra [193] have shown that the choice of return mapping algorithm is more important for orthotropic yield criteria (e.g. the Hill criterion) than for the isotropic von Mises plasticity theory used in this thesis. The accuracy of the forward and backward Euler method is therefore assumed to be similar in explicit time integration when using von Mises plasticity. Since all variables are defined in a corotational framework in EXP, the notation of the corotated variables is simplified in the following by omitting the circumflex $\hat{}$ (e.g. the corotated Cauchy stress $\hat{\boldsymbol{\sigma}}$ is denoted as $\boldsymbol{\sigma}$).

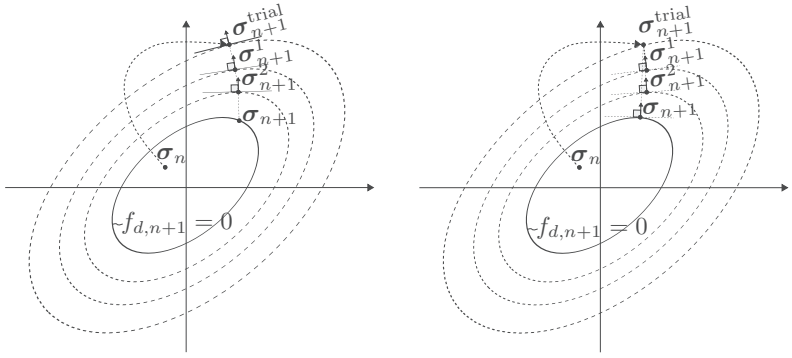

Figure 4.6: Illustration of the elastic predictor-viscoplastic corrector return map algorithms for the von Mises yield criterion and associated plasticity. Starting from an elastic stress state at the last converged increment t_n before arriving at the new converged increment t_{n+1}: (a) explicit stress update (cutting plane method) using the forward Euler method and (b) fully implicit stress update (closest point projection method) using the backward Euler method.

During both approaches an elastic predictor uses the total strain increment

and the hypoelastic relation to obtain a trial stress state. Then, if the elastic trial stress is outside the plastic domain, the elastically predicted stresses are corrected to fit a suitably updated yield surface by iterations of the plastic corrector. Thus, the integration algorithms are typically formulated as an elastic predictor-viscoplastic corrector stress update using a return mapping scheme. The solution is strain controlled in the sense that the total (corotational) strain increment

$$\Delta\boldsymbol{\varepsilon}_{n+1} = \int_{t_n}^{t_{n+1}} \boldsymbol{D}dt = \boldsymbol{D}_{n+1}\Delta t_{n+1} \tag{4.48}$$

within the time interval $\Delta t_{n+1} = t_{n+1} - t_n$ is known from the global equilibrium and used to update the stresses and internal variables at step $n+1$. Then, as in a rate-independent case, it makes sense to first compute an elastic trial state by assuming that the material behaviour is purely elastic within the interval. If the trial state is within the elastic domain ($f_d(\boldsymbol{\sigma}) \leq 0$), no viscoplastic flow takes place within the considered time step and the trial state is the actual state at the end of the step. Otherwise, the evolution of stresses and internal variables is computed by means of a suitable return mapping method. It should be emphasized that the consistency condition ($f(\boldsymbol{\sigma}) = 0$) no longer holds in the viscoplastic case, since the updated stress state at t_{n+1} generally lies outside the static yield surface ($f(\boldsymbol{\sigma}) > 0$). However, the terminology viscoplastic return mapping is justified in the present case since the updated stresses are obtained by returning (or moving) the trial stress towards the dynamic yield surface. Hence, the application of the procedure is similar to that in the rate-independent case, and Eq. (4.4) reads

$$\Delta\boldsymbol{\sigma} = \mathbf{C} : (\Delta\boldsymbol{\varepsilon} - \Delta\boldsymbol{\varepsilon}^p) = \Delta\boldsymbol{\sigma}^e + \Delta\boldsymbol{\sigma}^p \tag{4.49}$$

where the stress update at time t_{n+1} is expressed as

$$\begin{aligned} \boldsymbol{\sigma}_{n+1} &= \boldsymbol{\sigma}_n + \Delta\boldsymbol{\sigma}_{n+1} \\ &= \boldsymbol{\sigma}_n + \mathbf{C} : \Delta\boldsymbol{\varepsilon}_{n+1} - \Delta\lambda_{n+1}\mathbf{C} : \mathbf{n}_{n+1} = \boldsymbol{\sigma}_{n+1}^{\text{trial}} - \Delta\boldsymbol{\sigma}^p \end{aligned} \tag{4.50}$$

in which the viscoplastic corrector $\Delta\boldsymbol{\sigma}^p$ returns the stress to the yield surface.

All internal variables and functions in Eqs. (4.4), (4.22), (4.24), (4.30), (4.31), (4.33), (4.35) and (4.36) are therefore adopted to the return mapping scheme for integration, and replaced with the corresponding incremental values within and at the end of the considered interval Δt_{n+1}. The incremental form of the system of differential equations then reads

$$\boldsymbol{\varepsilon}_{n+1} = \boldsymbol{\varepsilon}_n + \Delta\boldsymbol{\varepsilon}_{n+1}$$

$$\boldsymbol{\varepsilon}_{n+1}^p = \boldsymbol{\varepsilon}_n^p + \Delta\boldsymbol{\varepsilon}_{n+1}^p = \boldsymbol{\varepsilon}_n^p + \Delta\lambda_{n+1}\mathbf{n}_{n+1} = \boldsymbol{\varepsilon}_n^p + \frac{3}{2}\Delta\lambda_{n+1}\frac{\boldsymbol{\sigma}'_{n+1}}{\sigma_{eq,n+1}}$$

$$
\begin{aligned}
\lambda_{n+1} &= \lambda_n + \Delta\lambda_{n+1} = \lambda_n + \dot{p}_0 \Delta t_{n+1} \left[\left(\frac{\sigma_{eq,n+1}}{\sigma_{y,n+1}} \right)^{\frac{1}{c}} - 1 \right] \\
\boldsymbol{\sigma}_{n+1} &= \boldsymbol{\sigma}_n + \Delta\boldsymbol{\sigma}_{n+1} \\
&= \boldsymbol{\sigma}_n + \mathbf{C} : (\Delta\boldsymbol{\varepsilon}_{n+1} - \Delta\boldsymbol{\varepsilon}^p_{n+1}) = \boldsymbol{\sigma}^{\text{trial}}_{n+1} - \Delta\lambda_{n+1} \mathbf{C} : \mathbf{n}_{n+1} \\
R_{n+1} &= R_n + \Delta R_{n+1} = R_n + \Delta\lambda_{n+1} H_{R,n+1} \\
&= R_n + \Delta\lambda_{n+1} \sum_{k=1}^{2} Q_k C_k \exp(-C_k \lambda_{n+1}) \\
\sigma_{y,n+1} &= A + R_{n+1} \\
T_{n+1} &= T_n + \Delta T_{n+1} = T_n + \frac{\chi \sigma_{eq,n+1} \Delta\lambda_{n+1}}{\rho c_p} \\
D_{n+1} &= D_n + \Delta D_{n+1} = D_n + \langle \sigma_{1,n+1} \rangle \, \Delta\lambda_{n+1} \\
f_{d,n+1} &= \sigma_{eq,n+1} - \sigma_{y,n+1} \left(1 + \frac{\Delta\lambda_{n+1}}{\dot{p}_0 \Delta t_{n+1}} \right)^c \left(1 - \left[\frac{T_{n+1} - T_{\text{r}}}{T_{\text{m}} - T_{\text{r}}} \right]^m \right)
\end{aligned}
\tag{4.51}
$$

where $\Delta\lambda_{n+1}$ is the incremental plastic multiplier at time t_{n+1}.

The set of non-linear algebraic equations in Eq. (4.51) are solved by updating the normal to the yield surface gradient $\mathbf{n}_{n+1}$ iteratively, where the viscoplastic corrector is applied from the elastic predictor $\boldsymbol{\sigma}^{\text{trial}}_{n+1}$ throughout the iteration until $f_{d,n+1} = 0$. This thesis is limited to the cutting plane method originally proposed by Ortiz and Simo [172]. The basis for this return mapping is an explicit elastic predictor-plastic corrector stress update using a forward Euler scheme. The objective of the numerical integration is to use the known stress state at the previous or trial configuration n to determine the new converged stress state at step $n + 1$ (see Figure 4.6a).

Using the normal $\boldsymbol{n}^i_{n+1}$ at the previous stress state (see Figure 4.6a) and assuming weak coupling of the temperature, i.e., using T_n instead of T_{n+1}, there is only one unknown variable during the return mapping procedure. That is the incremental plastic multiplier $\Delta\lambda^{i+1}_{n+1}$ and the set of equations in Eq. (4.51) reduces to a single equation which can be solved by a linear Taylor-expansion around $f_{d,n+1}(\boldsymbol{\sigma}, \boldsymbol{X}) = f_{d,n+1}(\boldsymbol{\sigma}, \sigma_y, \upsilon_p(\dot{p}), \Gamma_p(T_n))$, i.e.,

$$
f^{i+1}_{d,n+1} = f^i_{d,n+1} + \left. \frac{\partial f_d}{\partial \boldsymbol{\sigma}} \right|^i_{n+1} \Delta\boldsymbol{\sigma}_{n+1} + \left. \frac{\partial f_d}{\partial \boldsymbol{X}} \right|^i_{n+1} \Delta\boldsymbol{X}_{n+1} \tag{4.52}
$$

which may be written in terms of the internal variables $\boldsymbol{X}$ as

$$
f^{i+1}_{d,n+1} = f^i_{d,n+1} + \frac{\partial f_d}{\partial \boldsymbol{\sigma}_{n+1}} \delta\boldsymbol{\sigma}_{n+1} + \frac{\partial f_d}{\partial \sigma_{y,n+1}} \delta\sigma_{y,n+1} + \frac{\partial f_d}{\partial \upsilon_{p,n+1}} \delta\upsilon_{p,n+1} = 0 \tag{4.53}
$$

where the flow stress $\sigma_{y,n+1}$ and the following expressions are chosen as the internal variables $\boldsymbol{X}$ in the Taylor-expansion

$$\upsilon_p(\Delta\lambda_{n+1}) = \left(1 + \frac{\Delta\lambda_{n+1}}{\dot{p}_0 \Delta t_{n+1}}\right)^c, \qquad \Gamma_p(T_n) = \left(1 - \left[\frac{T_n - T_\mathrm{r}}{T_\mathrm{m} - T_\mathrm{r}}\right]^m\right) \tag{4.54}$$

Introducing the partial derivatives of the internal variables in Eq. (4.53) this now reads

$$\begin{aligned} f_{d,n+1}^{i+1} = f_{d,n+1}^{i} &- \frac{\partial f_d}{\partial \boldsymbol{\sigma}_{n+1}} \boldsymbol{C} \frac{\partial f_d}{\partial \boldsymbol{\sigma}_{n+1}} \delta\lambda_{n+1}^{i+1} - \upsilon_{p,n+1}\Gamma_{p,n} H_{R,n+1} \delta\lambda_{n+1}^{i+1} \\ &- \sigma_{y,n+1}\Gamma_{p,n} \frac{\partial \upsilon_{p,n+1}}{\partial \dot{\lambda}_{n+1}} \delta\dot{\lambda}_{n+1}^{i+1} = 0 \end{aligned} \tag{4.55}$$

Moreover, using $\dot{p} = \dot{\lambda} = \frac{\Delta\lambda}{\Delta t}$ the internal variable controlling the viscoplasticity $\upsilon_p(\dot{p})$ may be expressed as $\upsilon_p(\Delta\lambda)$ and Eq. (4.55) may be written as

$$\begin{aligned} f_{d,n+1}^{i+1} = f_{d,n+1}^{i} &- \frac{\partial f_d}{\partial \boldsymbol{\sigma}_{n+1}} \boldsymbol{C} \frac{\partial f_d}{\partial \boldsymbol{\sigma}_{n+1}} \delta\lambda_{n+1}^{i+1} - \upsilon_{p,n+1}\Gamma_{p,n} H_{R,n+1} \delta\lambda_{n+1}^{i+1} \\ &- \sigma_{y,n+1}\Gamma_{p,n} \frac{\partial \upsilon_{p,n+1}}{\partial \Delta\lambda_{n+1}} \delta\lambda_{n+1}^{i+1} = 0 \end{aligned} \tag{4.56}$$

Finally, the incremental change $\delta\lambda$ in the incremental plastic multiplier $\Delta\lambda$ is expressed as

$$\delta\lambda_{n+1}^{i+1} = \frac{f_{d,n+1}^{i}}{\frac{\partial f_d}{\partial \boldsymbol{\sigma}_{n+1}} \boldsymbol{C} \frac{\partial f_d}{\partial \boldsymbol{\sigma}_{n+1}} + \upsilon_{p,n+1}\Gamma_{p,n} H_{R,n+1} + \sigma_{y,n+1}\Gamma_{p,n} \frac{\partial \upsilon_{p,n+1}}{\partial \Delta\lambda_{n+1}}} \tag{4.57}$$

where

$$\frac{\partial \upsilon_p(\Delta\lambda_{n+1})}{\partial \Delta\lambda} = \frac{c}{\dot{p}_0 \Delta t_{n+1}} \left(1 + \frac{\Delta\lambda_{n+1}}{\dot{p}_0 \Delta t_{n+1}}\right)^{c-1} \tag{4.58}$$

$$H_{R,n+1} = \frac{dR_{n+1}}{dp_{n+1}} = \sum_{k=1}^{2} Q_k C_k \exp(-C_k \lambda_{n+1}) \tag{4.59}$$

$$\begin{aligned} \frac{\partial f_d}{\partial \boldsymbol{\sigma}} \boldsymbol{C} \frac{\partial f_d}{\partial \boldsymbol{\sigma}} &= \frac{\partial f_d}{\partial \sigma_{ij}} C_{ijkl} \frac{\partial f_d}{\partial \sigma_{kl}} \\ &= C_{1111} \left[\left(\frac{\partial f_d}{\partial \sigma_{11}}\right)^2 + \left(\frac{\partial f_d}{\partial \sigma_{22}}\right)^2 + \left(\frac{\partial f_d}{\partial \sigma_{33}}\right)^2 \right] \\ &+ 2C_{1122} \left[\frac{\partial f_d}{\partial \sigma_{11}} \frac{\partial f_d}{\partial \sigma_{22}} + \frac{\partial f_d}{\partial \sigma_{22}} \frac{\partial f_d}{\partial \sigma_{33}} + \frac{\partial f_d}{\partial \sigma_{33}} \frac{\partial f_d}{\partial \sigma_{11}} \right] \\ &+ 4C_{1212} \left[\left(\frac{\partial f_d}{\partial \sigma_{12}}\right)^2 + \left(\frac{\partial f_d}{\partial \sigma_{23}}\right)^2 + \left(\frac{\partial f_d}{\partial \sigma_{31}}\right)^2 \right] \end{aligned} \tag{4.60}$$

It is referred to Aune et al. [175] for a more detailed presentation of the linear

Taylor-expansion. It is also emphasized that since the time increment Δt_{n+1} is often very small during explicit time integration, the change in temperature ΔT_{n+1} is assumed to have a negligible effect on the update of the state variables. Therefore, the temperature is assumed to have an insignificant evolution during the time increment Δt_{n+1}, and a low coupling approach for the temperature is applied. This implies that T_n is used in the return mapping to update the stress and internal variables at time t_{n+1}. Then, the resulting state variables at t_{n+1} are used to calculate and update T_{n+1}. This assumption simplifies the calculations leading to Eq. (4.57) without any significant loss of accuracy in the model. This is also the case for the normal to the yield surface $\boldsymbol{n}_{n+1} = \partial f_d / \partial \boldsymbol{\sigma}_{n+1}$ where the use of the previous normal $\boldsymbol{n}^i_{n+1}$ instead of $\boldsymbol{n}^{i+1}_{n+1}$ violates the associated flow rule in Eqs. (4.24) and (4.51) since a unique normal for the given strain increment $\Delta \varepsilon_{n+1}$ must be found at each stress state. Thus, the deformation does not follow the minimum plastic work path when the cutting plane method is used (see Figure 4.6a). However, when the time increment Δt_{n+1} is very small this is assumed to have negligible effect on the stress state.

The numerical scheme within the time increment Δt_{n+1} may then be summarized as follows:

1. Set the initial values of the internal variables to the converged values of the previous step at t_n, check if the integration point under evaluation has already failed and calculate the speed of sound.

2. Compute the elasticity tensor.
   That is, *IF* a 3D stress state is used *THEN* use Eqs. (4.5) and (4.6)

$$\mathbf{C} = \lambda_{el} \mathbf{I} \otimes \mathbf{I} + 2\mu_{el} \mathbf{I} = \begin{bmatrix} C_{1111} & C_{1122} & C_{1122} & 0 & 0 & 0 \\ C_{1122} & C_{1111} & C_{1122} & 0 & 0 & 0 \\ C_{1122} & C_{1122} & C_{1111} & 0 & 0 & 0 \\ 0 & 0 & 0 & C_{1212} & 0 & 0 \\ 0 & 0 & 0 & 0 & C_{1212} & 0 \\ 0 & 0 & 0 & 0 & 0 & C_{1212} \end{bmatrix}$$

$$C_{1111} = \frac{(1-\nu)E}{(1+\nu)(1-2\nu)}, \quad C_{1122} = \frac{\nu C_{1111}}{1-\nu}, \quad C_{1212} = \frac{1}{2}\frac{E}{1+\nu}$$

   ELSEIF a 2D stress state is used

$$\boldsymbol{C} = \begin{bmatrix} C_{1111} & C_{1122} & 0 \\ C_{1122} & C_{1111} & 0 \\ 0 & 0 & C_{1212} \end{bmatrix}$$

$$C_{1111} = \frac{E}{1-\nu^2},\ C_{1122} = \nu C_{1111},\ C_{1212} = \frac{1}{2}\frac{E}{1+\nu}$$

ELSE a 1D stress state is used

$$\boldsymbol{C} = \begin{bmatrix} C_{1111} & 0 & 0 \\ 0 & 0 & 0 \\ 0 & 0 & 0 \end{bmatrix},\ C_{1111} = E$$

Note that there are used symmetric strain tensors.

3. Use the total stain increment $\Delta\boldsymbol{\varepsilon}_{n+1}$ from the global equilibrium to compute the elastic predictor

$$\boldsymbol{\sigma}_{n+1}^{\text{trial}} = \boldsymbol{\sigma}_n + \mathbf{C} : \Delta\boldsymbol{\varepsilon}_{n+1}$$

4. Compute the von Mises equivalent stress in terms of the elastic trial stress and Eq. (4.23)

$$\sigma_{eq,n+1}^{\text{trial}} = \sqrt{\frac{3}{2}\boldsymbol{\sigma}_{n+1}^{'\text{trial}} : \boldsymbol{\sigma}_{n+1}^{'\text{trial}}}$$

5. Check if temperature softening is included in the material input (i.e., $m \neq 0$).

6. Set the incremental plastic multiplier $\Delta\lambda_{n+1}$ equal to zero.

7. Check for plastic admissibility. That is, *IF* $f(\boldsymbol{\sigma}_{n+1}^{\text{trial}}) > 0$ *THEN* apply return mapping by using the cutting plane algorithm to find the incremental change $\delta\lambda_{n+1}$ in the incremental plastic multiplier $\Delta\lambda_{n+1}$. Note that superscript i denotes the local iteration counter.

   (i) Compute the normal $\mathbf{n}_{n+1}$ to the yield surface based on the initial (i.e., trial) or previous stress configuration.

$$\mathbf{n}_{n+1} = \frac{3}{2}\frac{\boldsymbol{\sigma}_{n+1}^{'}}{\sigma_{eq}}$$

   (ii) Compute the hardening modulus $H_{R,n+1}$ according to Eq. (4.30)

$$H_{R,n+1}^{i} = Q_1 C_1 \exp(-C_1 p_{n+1}^{i}) + Q_2 C_2 \exp(-C_2 p_{n+1}^{i})$$

(iii) Compute the denominator in Eq. (4.57) using Eqs. (4.58), (4.59), (4.60) and (4.54)

$$(\bullet) = \frac{\partial f_d}{\partial \boldsymbol{\sigma}^i_{n+1}} \boldsymbol{C} \frac{\partial f_d}{\partial \boldsymbol{\sigma}^i_{n+1}} + \upsilon^i_{p,n+1} \Gamma_{p,n} H^i_{R,n+1} + \sigma^i_{y,n+1} \Gamma_{p,n} \frac{\partial \upsilon^i_{p,n+1}}{\partial \Delta\lambda^i_{n+1}}$$

(iv) Compute the incremental change in the plastic multiplier $\delta\lambda^{i+1}_{n+1}$ in Eq. (4.57) and update the variable $\Delta\lambda^{i+1}_{n+1}$

$$\begin{aligned} \delta\lambda^{i+1}_{n+1} &= \frac{f^i_{n+1}}{(\bullet)} \\ \Delta\lambda^{i+1}_{n+1} &= \Delta\lambda^i_{n+1} + \delta\lambda^{i+1}_{n+1} \end{aligned}$$

(v) Update internal variables dependent on $\Delta\lambda^{i+1}_{n+1}$

$$\begin{aligned} p^{i+1}_{n+1} &= p^i_{n+1} + \delta\lambda^{i+1}_{n+1} \\ R^{i+1}_{n+1} &= R_n + H^i_{R,n+1} \Delta\lambda^{i+1}_{n+1} \\ \sigma^{i+1}_{y,n+1} &= A + H^{i+1}_{R,n+1} \Delta\lambda^{i+1}_{n+1} \end{aligned}$$

(vi) Update stress components using the generalized Hooke's law according to Eq. (4.50)

$$\boldsymbol{\sigma}^{i+1}_{n+1} = \boldsymbol{\sigma}^{\text{trial}}_{n+1} - \Delta\lambda^{i+1}_{n+1} \mathbf{C} : \mathbf{n}^{i+1}_{n+1}$$

Note that the material routine uses a fully vectorized representation of the stress and strain tensors, i.e.,

$$\begin{aligned} \boldsymbol{\sigma} &= [\sigma_{11}, \sigma_{22}, \sigma_{33}, \sigma_{12}, \sigma_{23}, \sigma_{31}]^T \\ \boldsymbol{\varepsilon} &= [\varepsilon_{11}, \varepsilon_{22}, \varepsilon_{33}, \gamma_{12}, \gamma_{23}, \gamma_{31}]^T = [\varepsilon_{11}, \varepsilon_{22}, \varepsilon_{33}, 2\varepsilon_{12}, 2\varepsilon_{23}, 2\varepsilon_{31}]^T \end{aligned}$$

Moreover, the application of objective stress rates (i.e., the Jaumann rate in EPX) to update the stress tensor $\boldsymbol{\sigma}$ in plane stress states allows for the possibility that the normal stress σ_{33} will not be zero (outside the material routine). The material subroutine should therefore initialize the normal stress σ_{33} to zero ($\sigma_{33} = 0$).

(vii) Compute the updated von Mises equivalent stress using Eq. (4.23)

$$\sigma^{i+1}_{eq,n+1} = \sqrt{\frac{3}{2} \boldsymbol{\sigma}'^{,i+1}_{n+1} : \boldsymbol{\sigma}'^{,i+1}_{n+1}}$$

(viii) Update the yield function in Eq. (4.51) according to the new stress state computed in (vi) and (vii)

$$f_{d,n+1}^{i+1} = \sigma_{eq,n+1}^{i+1} - \sigma_{y,n+1}^{i+1} \left(1 + \frac{\Delta\lambda_{n+1}^{i+1}}{\dot{p}_0 \Delta t_{n+1}}\right)^c \left(1 - \left[\frac{T_n - T_\mathrm{r}}{T_\mathrm{m} - T_\mathrm{r}}\right]^m\right)$$

(viiii) Check for convergence, i.e., *IF*

$$\left|\frac{f_d(\Delta\lambda_{n+1}^{i+1})}{\sigma_{y,n+1} \upsilon_p \Gamma_p}\right| < \mathrm{TOL}$$

THEN continue to 8.
ELSE $i = i + 1$ and *GO TO* (i)

8. Update the temperature according to the low coupling approach using Eq. (4.35)

$$T_{n+1} = T_n + \frac{\chi \sigma_{eq,n+1} \Delta\lambda_{n+1}}{\rho c_p}$$

and check for melting of the material. That is, *IF* $T \geq T_\mathrm{m}$ *THEN* the material point stiffness is deleted.

9. Compute the hydrostatic and deviatoric stress, respectively, according to Eq. (4.20)

$$\sigma_{H,n+1} = \frac{1}{3}\mathrm{tr}(\boldsymbol{\sigma}_{n+1})$$
$$\boldsymbol{\sigma}'_{n+1} = \boldsymbol{\sigma}_{n+1} - \sigma_{H,n+1}\mathbf{I}$$

10. Compute the principal stresses $\sigma_{i,n+1}$ based on the principal deviatoric stresses $\sigma'_{i,n+1}$ as shown in Eqs. (4.45) and (4.47)

$$\sigma'_{1,n+1} = 2\sqrt{\frac{J_{2,n+1}}{3}} \cos\frac{\theta}{3}$$
$$\sigma'_{2,n+1} = 2\sqrt{\frac{J_{2,n+1}}{3}} \cos\left(\frac{\theta}{3} - \frac{2\pi}{3}\right) \leq \sigma'_{1,n+1}$$
$$\sigma'_{3,n+1} = 2\sqrt{\frac{J_{2,n+1}}{3}} \cos\left(\frac{\theta}{3} + \frac{2\pi}{3}\right) \leq \sigma'_{2,n+1}$$

where

$$\cos\theta = \frac{J_{3,n+1}}{2\sqrt{J_{2,n+1}^3/27}}, \quad 0 \leq \theta \leq \pi$$

$$\sigma_{i,n+1} = \sigma_{i,n+1}^{'} + \sigma_{H,n+1} = \sigma_{i,n+1}^{'} + \frac{1}{3}\mathrm{tr}(\boldsymbol{\sigma}_{n+1})$$

11. The damage parameter D_{n+1} is computed by using Eq. (4.36). That is, integrating the major principal stress during the entire equivalent plastic strain path

$$W_{n+1} = W_n + \max(\sigma_{1,n+1}, 0)\Delta\lambda_{n+1}$$
$$D_{n+1} = \frac{W_{n+1}}{W_c}$$

12. Update the state variables to be returned to EPX and check for element erosion. That is, *IF* $D_{n+1} > 1.0$ *THEN* the material point stiffness is deleted.

13. *IF* a 2D stress state is used *THEN* the (actual) total strain $\varepsilon_{33,n+1}$ and incremental strain $\Delta\varepsilon_{33,n+1}$ through the thickness are updated and returned to EPX

$$\Delta\varepsilon_{33,n+1} = \frac{1-2\nu}{E}(\Delta\sigma_{11,n+1} + \Delta\sigma_{22,n+1}) - (\Delta\varepsilon_{11,n+1} + \Delta\varepsilon_{22,n+1})$$
$$\varepsilon_{33,n+1} = \varepsilon_{33,n} + \Delta\varepsilon_{33,n+1}$$

EPX performs this procedure for each integration point in the FE assembly. The stresses are updated in the material interface using a fully vectorized version of the forward Euler integration algorithm and a two-state architecture where the initial values at t_n are stored in the old arrays and the new values at t_{n+1} must be updated and stored in the new arrays returned to the global FE analysis. The *VPJC* material routine is valid for 1D, 2D and 3D stress states, i.e., for bar, shell, solid, axisymmetric, plane strain and plane stress elements. The stresses for 3D elements are stored similar to that of symmetric tensors as $\boldsymbol{\sigma} = [\sigma_{11}, \sigma_{22}, \sigma_{33}, \sigma_{12}, \sigma_{23}, \sigma_{31}]^T$, and plane stress, axisymmetric and plane strain elements are stored as $\boldsymbol{\sigma} = [\sigma_{11}, \sigma_{22}, \sigma_{33}, \sigma_{12}]^T$. The deformation gradient and strains are stored similarly to the stresses, however, one should be aware of that the shear strain is stored as engineering shear strains, e.g. $\gamma_{12} = 2\varepsilon_{12}$. The material model was found to be applicable for a wide range of elements in EPX through an extensive single element verification performed in Aune et al. [175] and Casadei et al. [194]. The performance of the model was verified in uniaxial tension and simple shear and the *VPJC* model was

found to respond well to all the relevant test cases in terms of rate-independent, viscoplastic and thermoviscoplastic behaviour. The dependence of the stress triaxiality on the failure strain was also shown by including ductile failure in the single element verification.

One final remark regarding the cutting plane method is that in the particular case of viscoplasticity the plastic strain rate will change during the local iterations in the forward Euler method. This is seen from Eqs. (4.54) and (4.58) where the plastic strain rate will increase during the iterative return mapping (due to an increase in plastic strain). This implies that the return to the dynamic yield surface ($f_d = 0$) occurs at strain rates that are too low. However, the plastic strain rate at the converge increment Δt_{n+1} should be the same as in the backward Euler method.

4.5 Material parameter identification

The material model requires the user to specify 9 material parameters and 7 physical constants. This work is limited to the identification of A, $Q_{i=1,2}$ and $C_{i=1,2}$ for the aluminium material, while the remaining parameters and physical constants were taken from the literature [162, 167, 195]. Remember that the material data and parameters provided for the steel material in [162] also apply in this thesis (see Section 3.2.2). The parameters A, $Q_{i=1,2}$ and $C_{i=1,2}$ were obtained by inverse modelling using a finite element (FE) model of the material tests presented in Section 3.2.2. It was decided to perform the inverse modelling using the optimization package LS-OPT. This provides a simulation environment where the objective is to minimize the mean-squared-error between the experiment and simulation for a user-defined curve. LS-OPT reads input and result files from the FE software and optimizes the parameters of a constitutive relation through sequential analyses on the same FE model by varying the input parameters. It was considered convenient to establish the FE model in LS-DYNA [196] due to its tailored interface with LS-OPT and the fact that a similar material model exists in LS-DYNA (*MAT_107). The target curve was chosen as the force-displacement curve from a typical tensile test in the rolling (0°) direction, and the FE model consisted of Belytschko-Tsay shell elements with an initial element size in the gauge area equal to the thickness of the specimens in an attempt to capture the local necking. Material constants for both materials are listed in Table 4.1, while physical constants taken from Holmen et al. [162, 195] are provided in Table 4.2. The strain-rate sensitivity constant c for the 1050A-H14 aluminium alloy was taken from [167].

However, since the optimization simulations were carried out using a different FE software it was considered necessary to verify that the material parameters

Table 4.1: Material parameters for the modified Johnson-Cook constitutive relation.

Material	A [MPa]	Q_1 [MPa]	C_1 [-]	Q_2 [MPa]	C_2 [-]	c [-]	m [-]	$\dot{p}_0$ [s^{-1}]	W_c [MPa]
Docol 600DL [162]	370.0	236.4	39.3	408.1	4.5	0.001	1.0	5×10^{-4}	473.0
1050A-H14	80.0	49.3	1457.1	5.2	121.5	0.014	1.0	5×10^{-4}	65.0

Table 4.2: Physical constants for the materials taken from the literature.

Material	E [GPa]	ν [-]	ρ [kg/m^3]	c_p [J/kgK]	χ [-]	T_r [K]	T_m [K]
Docol 600DL [162]	210.0	0.33	7850	452	0.9	293	1800
1050A-H14 [195]	80.0	0.30	2700	910	0.9	293	893

were applicable also in EPX. This also served as a validation of the implementation of the *VPJC* material model. The uniaxial tension tests presented in Section 3.2.2 were therefore modelled in EPX by the same shell elements to be used in the airblast simulations, and by prescribing the same elongation history as in the material tests. The prescribed velocity was ramped up over the first 0.5 % - 1.0 % of the total computational time using a smooth transition curve. It was used exactly the same mesh as in LS-DYNA, resulting in a spatial discretization of 3116 4-node quadrilaterals. The elements were 4-node quadrilaterals (called *Q4GS*) with 6 dofs per node and 20 Gauss integration points (5 through the thickness). Mass-scaling by a factor 10^9 and 10^8 was used to speed up the computational time for the steel and aluminium specimens, respectively. Larger scaling factors resulted in non-physical inertia effects during the necking and a non-negligible kinetic energy in the simulations.

Comparisons between FE analyses and tensile tests are shown in Figure 4.7. Since necking occurred at very small strains for the aluminium alloy, results from the numerical simulations were compared to the experimental data in terms of nominal stress-strain curves. The trend was that the numerical models were able to describe the overall response for both materials, and that the material parameters in Table 4.1 were valid also in EPX. Since necking occurred already at strains of approximately 0.7 % in the aluminium tests, it was necessary to include the strain-rate sensitivity term in Eq. (4.32) to capture the post-necking behaviour (see Figure 4.7b). After the initiation of necking, the strain rate increased by an order of magnitude and delayed the evolution of the neck by increasing the load-carrying capacity of the material. This was also observed in the experiments since barely any diffuse necking occurred before localized necking and failure, which may be explained by the high rate sensitivity in these types of alloys (see e.g. [164–167]).

The CL parameter W_c in Eq. (4.36) was determined based on the numerical simulations by inspecting the element exposed to the largest plastic work. This

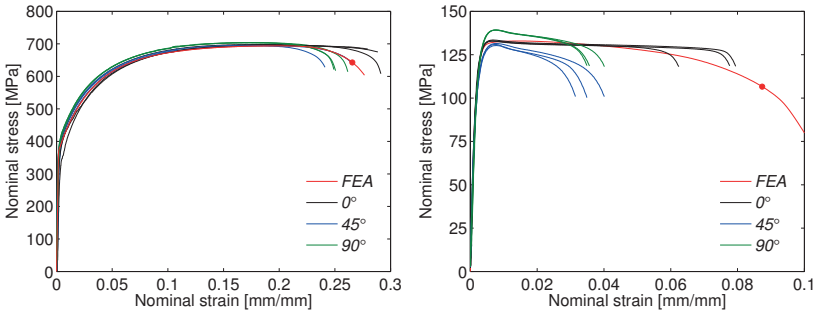

Figure 4.7: Nominal stress-strain curves from uniaxial tensile tests along three different loading directions for (a) the Docol 600 DL steel and (b) the aluminium alloy 1050A-H14. Numerical results from EPX (FEA) with material data from Table 4.1 and Table 4.2 are included for comparison. The red dots denote the point of failure in the calculation of W_c.

element is always located inside the neck, since localization is the first sign of material failure. The accuracy of W_c is therefore highly dependent on a proper representation of the localized necking. That is, when necking localizes in the tension test, damage will evolve rapidly in the critical element. The parameter, as obtained in this work, is therefore mesh dependent because the mesh size influences the representation of the localized necking. Only the tension tests in the rolling direction of the plate were used in the calibration, although the failure strain for the aluminium alloy was somewhat lower in the 45° and 90° directions (see Figure 4.7b). This also implies a spread in W_c between each material direction, which (at least to some extent) may affect the numerical results. However, modelling of anisotropic failure was beyond the scope of this thesis. The points used to extract W_c from the numerical results are indicated by red dots in Figure 4.7 and the values are given in Table 4.1. Figure 4.7 shows that the numerical simulation of the steel captured the localized necking very well, while the simulation of the aluminium did not manage to predict localized necking at the same strain as in the material test. The W_c parameter for the aluminium alloy was therefore determined at the value of the major principal strain where failure occurred in the test.

4.6 Concluding remarks

A material model was implemented and called *VPJC* in EPX. This is an elastic-thermoviscoplastic model which is formulated in a corotational framework allowing for finite strains and finite rotations. Ductile failure is also included by using an energy-based criterion which is uncoupled from the constitutive

equations. The *VPJC* material model is applicable for a wide range of elements and coupled with the element deletion options available in EPX.

The respective material parameters were identified for the materials considered in **Part II** of this thesis and the *VPJC* model was used in the numerical simulations of the tension tests in Section 3.2.2. It was found that the numerical results were in good agreement with the experimental data, indicating that the *VPJC* model is properly implemented in EPX and can be used in the simulations of the blast-loaded plates in Chapter 5.

5

Numerical simulations

The experimental observations of the counter-intuitive behaviour (CIB) and reversed snap buckling (RSB) at relatively small scaled distances in Chapter 3 attracted special attention as it occurred both during and after the elastic rebound. However, since it was challenging to conclude on the effects producing this abnormal response based on the experimental data, the influence of the negative phase and the elastic effects on the dynamic response is investigated numerically in this chapter. The numerical work presented in this chapter is also presented in the third paper published in International Journal of Impact Engineering [197].

5.1 Introduction

The experimental study presented in Chapter 3 investigated the effect of stand-off distance on the dynamic response of thin aluminium and steel plates subjected to airblast loading. The tests covered the entire range of structural response from complete tearing at the supports to a more CIB where the final configuration of the plate was in the opposite direction of the incident blast wave due to RSB. RSB attracted special attention as it occurred at relatively small scaled distances and both during and after the elastic rebound. However, since it was challenging to conclude on the governing parameters for this abnormal response based on the experimental data in Chapter 3, the influence of the negative phase and the elastic effects on the dynamic response is investigated numerically in the present chapter. The numerical simulations are performed by the FE code EUROPLEXUS (EPX) [130] using a Lagrangian formulation. Pressure-time histories are prescribed to the plates based on the mass and position of the charge. This is often called an uncoupled approach and makes the inherent assumption that the blast properties are unaltered by the structural motion and the surroundings [69]. The uncoupled approach is usually the preferred procedure in blast-resistant design [16], due to the increased complexity and computational costs when using fully coupled fluid-structure interaction simulations.

A well-established reference for the properties of the positive phase from airblast experiments is the work by Kingery and Bulmash [4]. The most commonly used negative phase parameters seem to be those given in the traditional diagrams in [16]. However, there still seems to be some uncertainty regarding the representation and treatment of the negative phase of the pressure-time history. As already mentioned in Section 1.2.1, the literature contains three basic representations of the pressure-time history when modelling this phase, i.e., a bilinear approximation, an extended Friedlander equation based on the waveform of the positive phase and a cubic representation. Rigby et al. [30] reviewed these methods and found that bilinear and cubic approximations resulted in the best agreement with experimental data. Before simulating all the 0.8-mm-thick plates in Table 3.1 it was therefore decided to perform a parametric study on the effect of bilinear and cubic representations on the dynamic response. Based on the findings in this parametric study it is carried out numerical simulations of the blast-loaded plates. The numerical model is first validated against the experimental data in Chapter 3, before performing a numerical study to determine the governing parameters for the observed RSB. Special focus is placed on the influence of elastic effects and negative phase on the structural response. The capabilities of the Cockcroft-Latham (CL) failure criterion and element erosion in predicting the crack patterns observed in the experiments are also evaluated. Due to trigger problems and flaking of the paint at the centre part of the plate in some of the tests, 3D-DIC analyses were only possible in 13 out of the 21 experiments conducted. The displacement histories reported in this section are therefore limited to the tests where 3D-DIC analyses were possible. However, the tests showed good repeatability and the reported results are considered to be a good representation of the experimental observations. All deformation profiles presented herein were corrected for the slight movement of the mounting frame during the tests.

5.2 Numerical simulations

This section describes the numerical model, representation of the airblast loading and the numerical simulations of the blast-loaded plates.

5.2.1 Numerical model

All numerical simulations were performed in the FE software EPX [130], an explicit FE code jointly developed by the French Commissariat à l' énergie atomique et aux énergies alternatives (CEA DMT Saclay, France) and the Joint Research Centre (EC-JRC Ispra, Italy). The main application domain of the code is numerical simulations of fast transient phenomena such as explosions and impacts in complex three-dimensional fluid-structure systems.

Figure 5.1 illustrates the assembly of the numerical model, where the symmetry of the problem was utilized to model only one quarter of the experimental setup using symmetric boundary conditions. A mesh sensitivity study showed that an element size of 10 mm was adequate to predict the global deformation observed in the experiments. However, the plate was modelled using a Lagrangian discretization with an element size of approximately 2.5 mm (Figure 5.1b) and 4-node Reissner-Mindlin shells (*Q4GS*) with 6 dofs per node and 20 Gauss integration points (5 through the thickness). The fine mesh size was chosen in an attempt to predict the tearing along the boundary observed in some of the tests using element erosion without too much loss of mass. Moreover, the material behaviour of the plates was governed by the *VPJC* model with material and physical constants from Table 4.1 and Table 4.2. Element erosion was initiated when all integration points in the element reached the critical value of the damage parameter in Eq. (4.36). The bolts and clamping frames were represented by 8-node brick elements (*CUB8*) with 8 Gauss points and the *VPJC* model with a high elastic limit to ensure elastic behaviour using the physical constants for steel in Table 4.2.

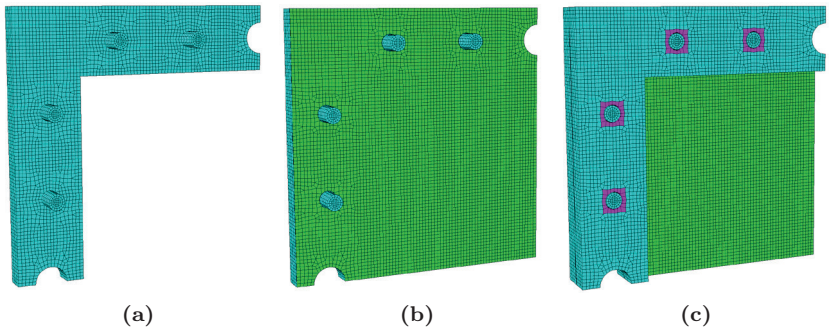

Figure 5.1: Numerical model showing (a) steel mounting frame and bolts as one component (in cyan), (b) plate specimen is added (in green) and (c) complete assembly including the clamping frame (also in cyan) and contact area between bolt heads and clamping frame (in magenta) used to model the effect of the pre-tensioning of the bolts.

The bolted connections used in the experiments were designed with internal (female) threads in the steel mounting frame and external (male) threads on the bolts without using a traditional nut. This made it convenient to model the steel mounting frame and the bolts as one component (Figure 5.1a). Each bolt was pre-stressed to an initial torque (M_t = 200 Nm) in the tests (see Section 3.2.1), resulting in a clamping pressure between the frames and the plate. In the model, this was accounted for by applying an external pressure at the contact area between the bolt head and the clamping frame (see Figure 5.1c) while the bolts were modelled as stress-free. The contact pressure was

determined using the approach suggested in Ref. [157] where the pre-tensioning force $F_p = M_t/k\phi$ in each bolt was found from the applied torque M_t, bolt diameter ϕ, thread geometry and friction in the thread engagements and under the bolt heads. The thread geometry and friction were accounted for by the coefficient k, which is the main uncertainty in this approach. The recommended value for k is usually 0.18. However, according to Ref. [157] it may vary between 0.10 and 0.23. The elements at the surface of the clamping frame and within the diameter of the bolt heads were defined as the contact area A_c, which was determined to be 175 mm^2. Dividing the pre-tensioning force F_p in each bolt by this contact area resulted in a recommended contact pressure of 527 MPa between the bolt head and the clamping frame. Still, there is a large spread between the minimum and maximum values of 410 MPa ($k = 0.23$) and 948 MPa ($k = 0.10$), respectively. This motivated a numerical study on the influence of the contact pressure on the response of the plate, which showed that the recommended value of 527 MPa gave the best agreement with the experimental observations. A contact pressure of 527 MPa was therefore used in this study. Contact between the plate, bolts and frames was modelled using a node-to-surface contact algorithm (*GLIS*) using slave nodes and master surfaces where contact was enforced by Lagrangian multipliers when a slave node penetrated a master surface. The plate was modelled as the slave and the static friction coefficient between the plate and clamping frames was set to 0.15, while the dynamic friction coefficient was taken equal to 0.10.

5.2.2 Airblast loading

The positive phase of the blast load was described using the empirical parameters by Kingery and Bulmash (KB) (see Figure 2.17a) and the pressure-time history was represented by the modified Friedlander equation in Eq. (2.1). In this approach, the charge mass and stand-off distance are used as input to find the corresponding KB parameters (t_a, $t_\mathrm{d+}$, $p_\mathrm{so,max}$, $p_\mathrm{r,max}$ and $i_\mathrm{r+}$). Then, the Friedlander equation provides the pressure-time history on each element of the plate depending on the stand-off distance R and angle of incidence α relative to the charge (see Figure 5.2).

The reflected overpressure $p_{\mathrm{r}\alpha}$ varies as a function of α between the head-on reflected overpressure $p_\mathrm{r,max}$ ($\alpha = 0$) and the incident (side-on) overpressure $p_\mathrm{so,max}$ ($\alpha = 90$). This was accounted for by determining the reflected pressure coefficient $C_{\mathrm{r}\alpha} = p_{\mathrm{r}\alpha}/p_\mathrm{so,max}$ and oblique impulse $i_{\mathrm{r}\alpha+}$ using the data points provided in Refs. [16, 150]. Intermediate values of the peak incident pressure $p_\mathrm{so,max}$ were found using linear interpolation between adjacent data points. The decay parameter b in Eq. (2.1) was determined using the governing parameters (i.e., $p_{\mathrm{r}\alpha}$, $i_{\mathrm{r}\alpha+}$, t_a, $t_\mathrm{d+}$) integrated over the positive phase duration $t_\mathrm{d+}$ in Eq. (2.3). This non-linear equation was solved iteratively to determine the

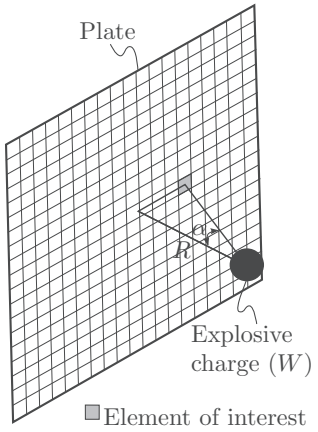

Figure 5.2: Illustration of the computation of the applied pressure-time history at each element on the plate depending on the stand-off distance and angle of incidence relative to the charge.

value of the decay parameter b which produces the impulse $i_{r\alpha+}$. Figure 5.3 shows the positive phase parameters (solid lines) as a function of scaled distance Z, while Figure 2.7 presents the relevant curves used to find the $C_{r\alpha}$ as a function of α. Note that the parameters in terms of impulse and duration in Figure 5.3 are scaled using Hopkinson-Cranz scaling [14].

The negative phase was modelled using either a bilinear or a cubic representation based on the recommendations in [16] and [27–29], respectively. This was motivated by previous findings in Refs. [22, 31, 54], suggesting that the structural response of flexible structures depends on the timing and magnitude of the peak negative pressure relative to the dynamic response. Following the recommendations in [16] and using a bilinear approximation of the negative phase, the pressure-time history for a given stand-off distance and charge mass can be given by the piecewise expression in Eq. (5.1), i.e.,

$$p(t) = \begin{cases} p_1 & t < t_a \\ p_1 + p_{r\alpha}\left(1 - \dfrac{t - t_a}{t_{d+}}\right)\exp\left(\dfrac{-b(t - t_a)}{t_{d+}}\right) & t_a < t < t_1 \\ p_1 - p_{r,\min}\left(\dfrac{t - (t_a + t_{d+})}{0.25 t_{d,lin-}}\right) & t_1 < t < t_2 \\ p_1 - p_{r,\min}\left(1 - \dfrac{t - (t_a + t_{d+} + 0.25 t_{d,lin-})}{0.75 t_{d,lin-}}\right) & t_2 < t < t_3 \\ p_1 & t > t_3 \end{cases} \quad (5.1)$$

where $t_1 = t_a + t_{d+}$, $t_2 = t_a + t_{d+} + 0.25 t_{d,lin-}$ and $t_3 = t_a + t_{d+} + t_{d,lin-}$

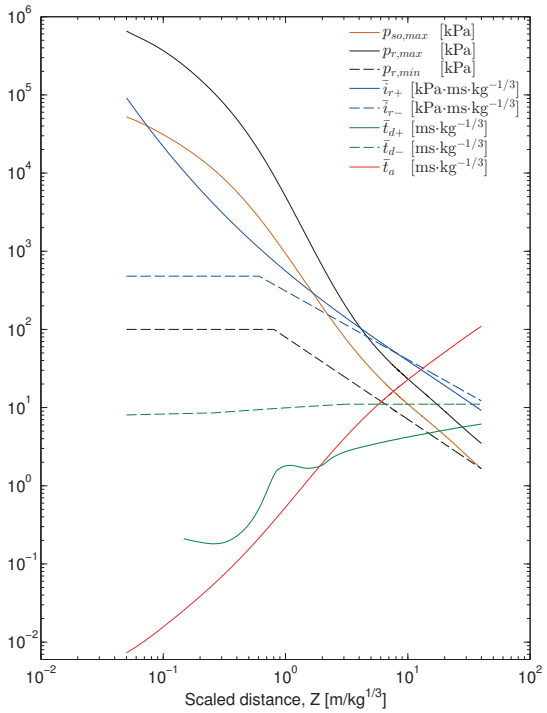

Figure 5.3: Positive and negative phase parameters of the reflected blast wave from a spherical charge of TNT detonated in free air. The positive phase parameters in [4, 16] are plotted with solid lines, while the negative phase parameters are shown with dashed lines.

are introduced to simplify the notation. It is noticed that the rise time to the peak negative pressure $p_{\mathrm{r,min}}$ equals 1/4 of the negative phase duration $t_{\mathrm{d,lin-}}$. Similarly, using the cubic representation of the negative phase suggested in [27–29], the pressure-time history may be represented by the piecewise function in Eq. (5.2), i.e.,

$$p(t) = \begin{cases} p_1 & t < t_{\mathrm{a}} \\ p_1 + p_{\mathrm{r}\alpha}\left(1 - \dfrac{t - t_{\mathrm{a}}}{t_{\mathrm{d+}}}\right)\exp\left(\dfrac{-b(t - t_{\mathrm{a}})}{t_{\mathrm{d+}}}\right) & t_{\mathrm{a}} < t < t_1 \\ p_1 - p_{\mathrm{r,min}}\left(\dfrac{27}{4}\dfrac{t - (t_{\mathrm{a}} + t_{\mathrm{d+}})}{t_{\mathrm{d,cub-}}}\right)\left(1 - \dfrac{t - (t_{\mathrm{a}} + t_{\mathrm{d+}})}{t_{\mathrm{d,cub-}}}\right)^2 & t_1 < t < t_4 \\ p_1 & t > t_4 \end{cases} \tag{5.2}$$

where $t_4 = t_{\mathrm{a}} + t_{\mathrm{d+}} + t_{\mathrm{d,cub-}}$. For a cubic representation it can be shown that the rise time to the peak negative pressure $p_{\mathrm{r,min}}$ equals 1/3 of the negative phase duration $t_{\mathrm{d,cub-}}$. Both approximations of the negative phase are illustrated in Figure 5.4.

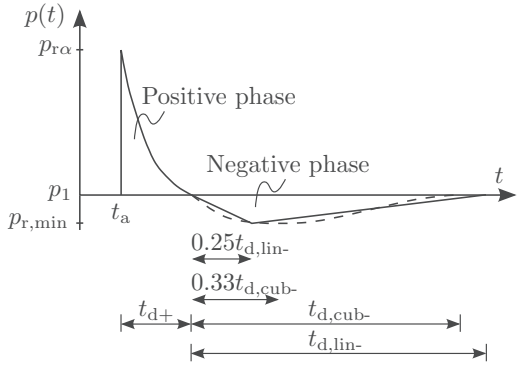

Figure 5.4: Pressure-time history with either bilinear (solid line) or cubic (dashed line) representation of the negative phase.

The negative phase parameters were taken from Ref. [16] which is in good agreement with the analytical work reported by Granström [27]. Thus, the peak negative pressure $p_{\mathrm{r,min}}$ and the impulse $i_{\mathrm{r}-}$ were calculated using empirical expressions based on curve fitting to the diagrams presented for a spherical charge in [16], i.e.,

$$p_{\mathrm{r,min}} = \begin{cases} 100 & Z < 0.803 \\ 79.433 \cdot \mathrm{Z}^{-1.05} & Z \geq 0.803 \end{cases} \quad [\mathrm{kPa}] \tag{5.3}$$

$$i_{\mathrm{r}-} = \begin{cases} 480 \cdot W^{1/3} & Z < 0.608 \\ 10^{-0.87731 \cdot \log(Z)+2.49145} \cdot W^{1/3} & Z \geq 0.608 \end{cases} \quad [\mathrm{kPa\ ms}] \tag{5.4}$$

$$t_{\mathrm{d}-} = \begin{cases} (0.694 \cdot \log(Z) + 8.963) \cdot W^{1/3} & Z < 0.255 \\ (2.305 \cdot \log(Z) + 9.918) \cdot W^{1/3} & 0.255 \leq Z \leq 3.116 \\ 11.056 \cdot W^{1/3} & Z > 3.116 \end{cases} \quad [\mathrm{ms}] \tag{5.5}$$

The negative phase parameters are shown as dashed lines in Figure 5.3, where the expression for the negative phase duration $t_{\mathrm{d}-}$ in Eq. (5.5) is included for completeness. The duration of the bilinear and cubic representations was found by integration of the pressure during the negative phase in Eqs. (5.1) and (5.2) so that the impulse $i_{\mathrm{r}-}$ from Eq. (5.4) is conserved, i.e.,

$$t_{\mathrm{d,lin}-} = 2\frac{i_{\mathrm{r}-}}{p_{\mathrm{r,min}}} \tag{5.6a}$$

$$t_{\mathrm{d,cub}-} = \frac{16}{9}\frac{i_{\mathrm{r}-}}{p_{\mathrm{r,min}}} \tag{5.6b}$$

These equations were implemented in EPX as the *AIRB* directive where the user can choose the preferred negative phase representation. Note that the effect of the angle of incidence during the negative phase was assumed similar

to that during the positive phase. That is, the negative impulse i_{r-} in Eq. (5.4) was corrected for the angle of incidence using the scaling factor $i_{r\alpha+}/i_{r+}$ found from the correction of the positive impulse. Previous studies by Rigby et al. [30] have shown that the angle of incidence has negligible effects on the negative pressure, and it was therefore considered sufficient to use the parameter given in Eq. (5.3) also at oblique angles of incidence.

Finally, a validation of the positive phase predicted by the AIRB directive was performed. This was carried out by comparing experimental measurements with numerical predictions at the sensors located in the clamping frame (see Figure 3.1). The validation was limited to the positive phase only, due to difficulties related to the measurements of the negative phase in Chapter 3. The results are summarized in Table 5.1, while typical pressure-time histories from experiments are compared to numerical results in Figure 5.5. It should be noted that the experimental tests are only denoted by their material and stand-off distance (i.e., S1, S2, S3, A0, A1, A2 and A3) in the following. Moreover, the experimental data were low-pass filtered with a cut-off frequency of 0.05 times the sampling rate (10 MHz). Figure 5.5 shows good agreement between experimental and numerical results, and Table 5.1 shows that the peak reflected overpressure $p_{r\alpha}$ and the positive impulse $i_{r\alpha+}$ are in reasonable correspondence with the experimental values. However, the predicted positive duration t_{d+} from the AIRB directive was found to be significantly longer than that reported in the experiments. This is due to a rather long tail of the pressure history where the corresponding magnitudes were negligible (see Figure 5.5).

Table 5.1: Comparison of experimental and numerical results.

Test	Z^*	Experimental results				Numerical results				
		$p_{r\alpha}$	t_{d+}	$i_{r\alpha+}$	$d_{z,max}$	$p_{r\alpha}$	t_{d+}	$i_{r\alpha+}$	$d_{z,max}$	$i_{r\alpha-}$
	[m/kg$^{1/3}$]	[MPa]	[ms]	[kPa ms]	[mm]	[MPa]	[ms]	[kPa ms]	[mm]	[kPa ms]
S1	0.36	11.5-16.2	0.07	135.7-169.8	33.4	9.5	0.17	161.3	32.0	73.1
S2	0.73	6.8-7.7	0.14-0.17	142.2-168.7	22.3-22.6	6.2	0.54	186.2	23.2	97.9
S3	1.09	3.3-4.9	0.21-0.25	136.2-154.2	15.3-17.2	2.9	0.62	142.6	17.1	84.3
A0	0.73	9.8	0.11	185.7	N/A	6.2	0.54	186.2	N/A	97.9
A1	1.09	3.1-4.3	0.18-0.23	119.5-137.0	41.9-44.4	2.9	0.62	142.6	42.7	84.3
A2	1.46	1.5-1.7	0.35-0.40	99.8-111.5	29.5-32.7	1.4	0.57	109.3	31.0	71.1
A3	1.82	0.8-1.0	0.48-0.54	80.9-83.0	23.8-27.2	0.7	0.60	83.1	23.8	60.1

*Scaled distance Z refers to the respective plate, and not to the sensor located in the frame.

Thus, the pressure-time histories were in close agreement with the pressure levels contributing to the structural response. This is also confirmed by the

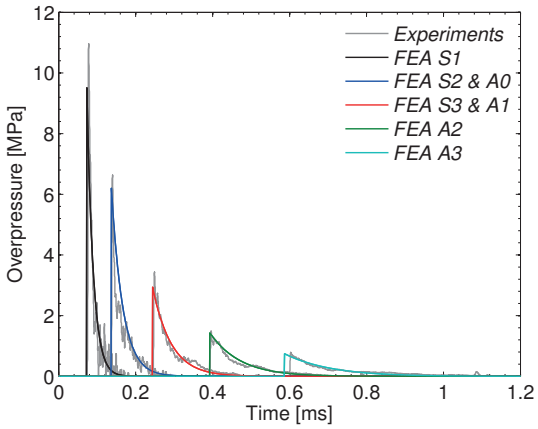

Figure 5.5: Comparison between experimental and numerical pressure recordings during the positive phase. The numerical results are taken from the clamping frame for comparison with the experimental data from Chapter 3.

good agreement between experiments and numerical results in terms of peak reflected pressures and impulses. It is also emphasized that when considering only the positive phase of the blast loading these experiments were in the impulsive loading domain due to the short duration compared to the natural period of vibration of the plates (see Tables 3.5 and 3.6). The response to such short pulses is essentially independent of the pulse shape and the magnitude of the impulse is the parameter governing the structural response. Hence, the AIRB directive was found to be able to predict the positive phase of the blast loading.

5.2.3 Parametric study

Before simulating all the experiments for the 0.8-mm-thick plates in Table 3.1, it was decided to perform a parametric study on the negative phase representation since the recommendations in the literature are somewhat contradictory. The study was performed on plates experiencing CIB due to RSB (i.e., tests S3 and A3). The timing of the peak negative pressure was studied using both bilinear and cubic negative phase representations, because they used the same magnitude of impulse and peak negative pressure (Figure 5.4). The influence of the boundary conditions was also studied since some sliding at the supports occurred in the experiments due to the reduced clamping at the pressure sensors. The model presented in Section 5.2.1 (hereafter denoted the "contact model") was therefore compared to a simplified model (called the "fixed model") where all nodes located between the mounting and clamping frames were fully fixed against translation in all directions. Figure 5.6 summarizes the results in terms

of mid-point deflection versus time, while deformation profiles at maximum and minimum deflection are presented in Figure 5.7. Solid and dashed lines are related to the representation of the negative phase. That is, solid lines are the mid-point deflection when the negative phase was represented as bilinear, while dashed lines are from simulations with a cubic representation of the negative phase. Cyan and blue lines represent the simulations considering only the positive phase of the loading for the contact and fixed model, respectively.

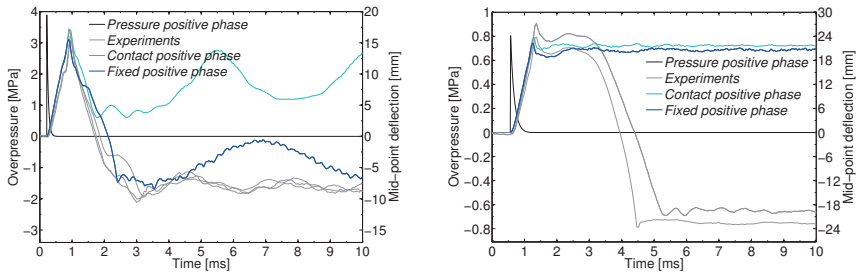

(a) S3 **(b)** A3

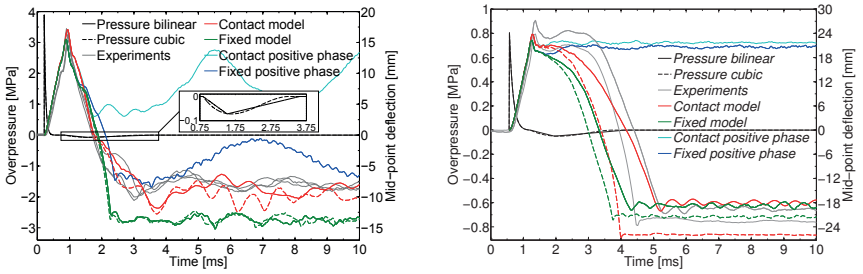

(c) S3 **(d)** A3

Figure 5.6: Results from parametric studies on tests S3 and A3: (a) and (b) represent positive phase loading only, while (c) and (d) also include the negative phase. Both pressure and deflection were taken from the centre of the plates. Solid lines correspond to a bilinear representation of the negative phase, while dashed lines indicate a cubic representation. Cyan and blue lines represent only positive phase loading for the contact and fixed model, respectively.

In general, the parametric study showed that CIB was dependent on the timing and magnitude of the peak negative pressure relative to the dynamic response of the plates. In most of the cases, CIB was not predicted without including the negative phase of the blast loading (Figure 5.6a-b). Moreover, as in the experiments, two distinctive types of CIB were identified (Figure 5.6c-d). It is therefore necessary to extend the Type III category in Section 1.2.2 and Figure 1.3 to also include the RSB occurring during the oscillations after the elastic rebound (Figure 5.6d). This is therefore denoted Type III* in the following. CIB of Type III was driven by elastic effects during the rebound after peak

deflection in the intuitive direction (i.e., the positive direction in Figure 5.6c). This type of CIB occurred in the S3 tests and was dependent on the axial restraint at the boundary where the elastic rebound was enhanced by the negative phase which occurred during the rebound itself. However, CIB was also observed in the simulation with only positive phase loading and fixed boundary conditions. This resulted in rather large oscillations around the final equilibrium configuration (blue line in Figures 5.6a and 5.6c). In general, the contact model including the negative phase of the loading resulted in the best agreement with the experimental observations. It was also evident that for CIB of Type III observed in the S3 tests, the effect of including the negative phase was more significant than the chosen representation (bilinear versus cubic in Figure 5.6c).

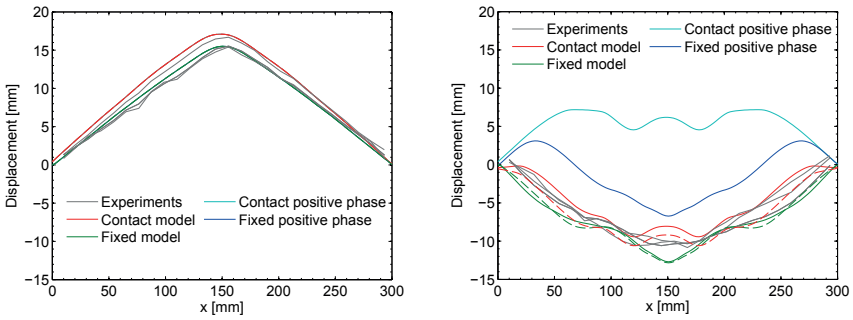

(a) Maximum deformation S3 **(b)** Minimum deformation S3

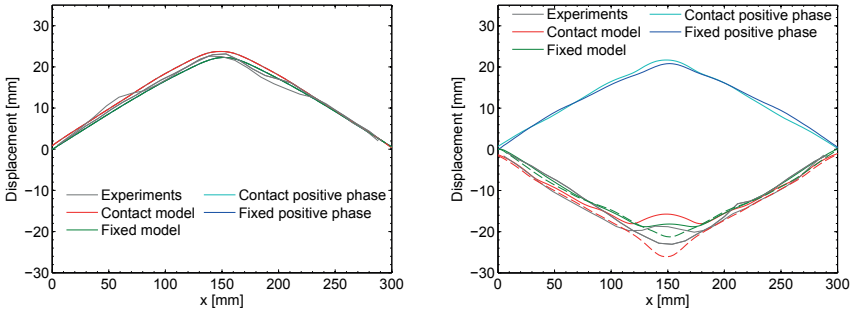

(c) Maximum deformation A3 **(d)** Minimum deflection A3

Figure 5.7: Comparison of deformation profiles at maximum and minimum mid-point deflection when varying the negative phase representation and boundary conditions. Solid lines correspond to a bilinear representation of the negative phase, while dashed lines indicate a cubic representation. Cyan and blue lines represent only positive phase loading for the contact and fixed model, respectively.

The A3 tests experienced another type of CIB which is referred to as Type III*. This type of CIB also occurred due to the negative phase, but during

the oscillations following the elastic rebound (Figure 5.6d). CIB of Type III* was highly dependent on the timing of the peak negative pressure relative to the oscillations around the permanent equilibrium state of the plate. Since this is an unstable configuration, sensitive to small changes in loading and structural conditions, the timing of the negative phase may result in significant enhancement of the elastic oscillations subsequent to the elastic rebound. It was also observed that the cubic representation of the negative phase resulted in somewhat earlier RSB compared to the bilinear representation. This makes it reasonable to assume that the initial pressure gradient of the negative phase is important in determining the timing of RSB, since the initial pressure gradient was significantly steeper in the cubic representation (see Figures 5.4 and 5.6).

With one exception, the general trend was that RSB is not predicted without including the negative phase of the blast loading. By investigating the deformation profiles at maximum and minimum permanent deflection in Figure 5.7, it was observed that the local dent occurring at the centre of the plates in the experiments was only captured in the numerical simulations with the contact model. It should be emphasized that this dent made the comparison of the mid-point deflections in Figure 5.6 somewhat misleading since the dent was not captured when using the fixed model (Figures 5.7b and 5.7d). Thus, modelling the contact boundary conditions and including the negative phase resulted in the best agreement with the experimental data. As expected, the deformation profiles at maximum deflection in Figure 5.7a and Figure 5.7c were only dependent on the boundary conditions because the maximum deformation occurred before the negative phase. Thus, the deformation profiles of the bilinear and cubic representation of the negative phase coincided since the deformation was unaltered by the negative pressure at this point in time.

5.2.4 Simulations of blast-loaded plates

Based on the parametric study it was decided to use the assembly presented in Figure 5.1 and to follow the recommendations in Ref. [16] with a bilinear representation of the negative phase when simulating all the tests on blast-loaded plates in Table 3.1. The numerical results are summarized and compared to the experimental data in terms of mid-point deflection versus time in Figure 5.8, while the maximum mid-point deflection $d_{\mathrm{z,max}}$ is compared to the experimental data in Table 5.1. A comparison of the experimental and numerical test configurations experiencing failure is presented in Figure 5.9. The total positive and negative impulses transmitted to the blast-loaded plates and the corresponding maximum deflection-thickness ratios obtained from the numerical simulations are reported in Table 5.2. This may be valuable information when discussing these experiments and findings in view of similar impulsively loaded plates reported in the literature (see e.g. [61, 104]).

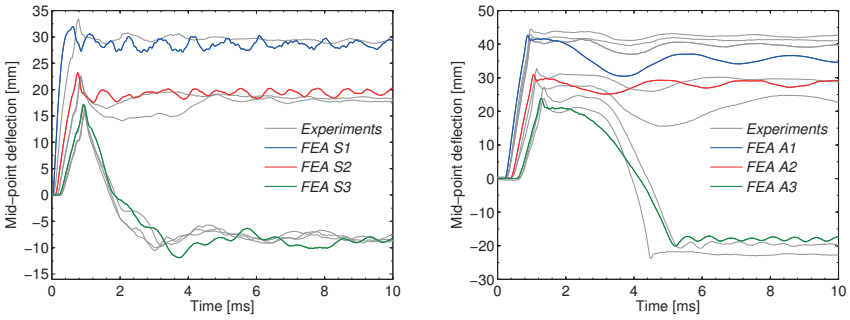

(a) Steel plates **(b)** Aluminium plates

Figure 5.8: Comparison of numerical (FEA) and experimental results in terms of mid-point deflection histories.

It is observed that the numerical simulations were in good agreement with the experimental observations, and the numerical model was able to predict the entire range of structural response from RSB at the largest stand-off distances (Figure 5.8) to tearing along the boundary (Figure 5.9). However, the oscillations subsequent to the elastic rebound were somewhat overestimated in the numerical simulations of the A1 tests compared with the experiments. This was probably due to a slightly overestimated width of the crack, resulting in reduced stiffness during the negative loading phase. Failure cannot occur in less than one element size when using element erosion and a better prediction of the crack propagation would require a refined mesh.

It is emphasized that W_c is mesh size dependent when determined from inverse modelling and the same element size should be used in both simulation and calibration. Larger elements may diffuse the failure process and suppress the crack propagation [198]. A mesh size of 0.8 mm was necessary to capture the localized necking in the material tests (see Section 4.5), but this mesh size was not feasible in the evaluation of the blast-loaded plates. The computational costs would be very high with such a fine mesh. However, a separate analysis of the A1 configuration with the 0.8 mm mesh size was performed to evaluate the influence of mesh size on the crack propagation. This resulted in complete tearing along the boundary, while the global response until failure remained the same. The W_c parameter in Table 4.1 should therefore be treated with some caution. Still, the numerical simulations using an element size of 2.5 mm captured the failure observed in the experiments well using a rather simple material model. This also indicated that the modelling of reduced clamping in the vicinity of the pressure sensors is an important aspect in predicting the failure observed in the experiments (Figure 3.1 and Figure 5.1). Due to the reduced clamping, failure was first observed at the bolts closest to the centre

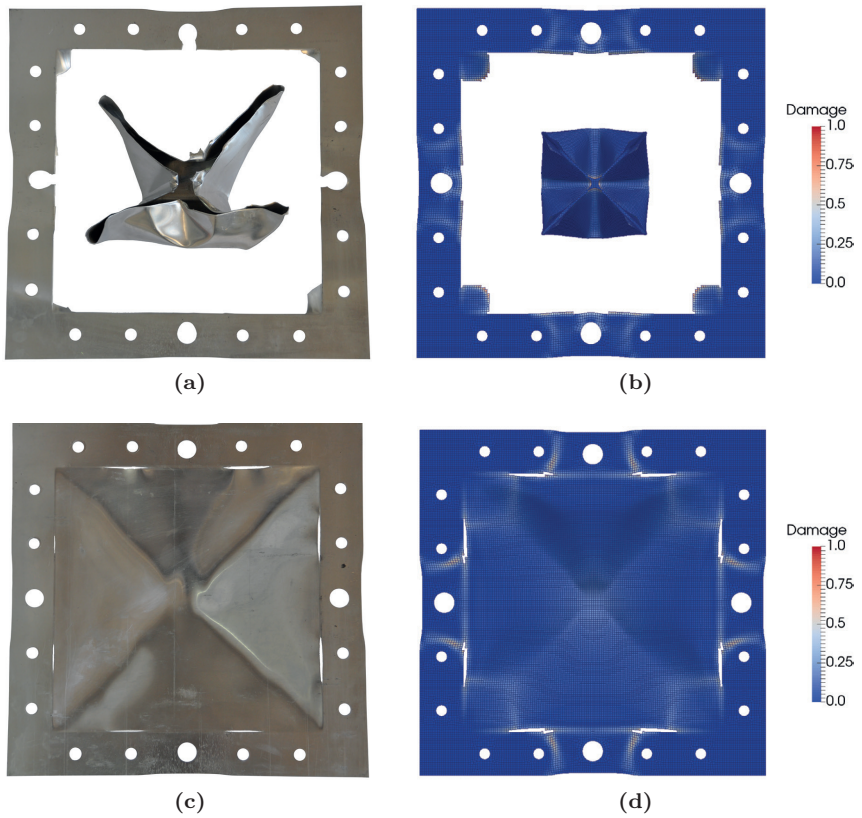

Figure 5.9: Comparison of experimental (left) and numerical (right) observations on test configurations that experienced failure. (a) and (b) contains the A0 configuration experiencing complete tearing at the supports, while (c) and (d) represents the partial tearing observed in the A1 tests. Fringe colours represent the contour map of the damage parameter in Eq. (4.36).

of the plate boundary (Figure 5.9c-5.9d). The distinct inward deflection of the plates at the boundary was also captured in the numerical simulations experiencing failure. This is the so-called pulling-in effect [59] and is a result of the plate deformation which continues between the time of first tearing at the boundary (Figure 5.9c - 5.9d) and complete tearing at the corners (Figure 5.9a-5.9b). A more detailed investigation of the failure process is beyond the scope of this thesis.

Since the numerical model was able to predict the experimental response with good accuracy, a numerical investigation was performed on which combinations of stand-off distance R and plate thickness t resulted in CIB due to RSB. All stand-off distances within the domain $R \in [0.525, 1.000]$ m and $R \in$

$[0.275, 0.775]$ m for the aluminium and steel plates, respectively, were simulated in combination with thicknesses in the range $t \in [0.2, 3.6]$ mm and $t \in [0.2, 2.2]$ mm. The results are shown in terms of response spectra of the permanent mid-point deflection in Figure 5.10, while mid-point deflection versus time for some typical thicknesses and stand-off distances are shown in Figure 5.11. The grey markers in Figure 5.10 illustrate the combination of stand-off distance and plate thickness used in the numerical simulations to generate the response spectra. Keep in mind that the discussion in the following is limited to these particular domains. Also recall that CIB is characterized by a permanent deflection in the opposite direction to the incident blast wave. This implies a negative permanent mid-point deflection which is indicated by a blue colour in Figures 5.10 and 5.11. Similarly, a red colour indicates a permanent deflection in the same direction as the incoming blast wave, while a green colour indicates a final configuration with negligible mid-point deflection.

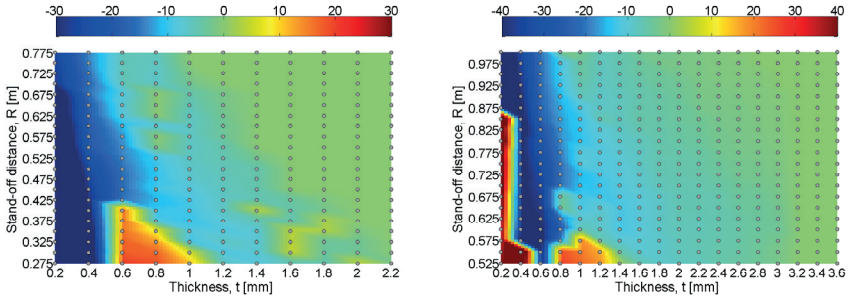

(a) Steel plates **(b)** Aluminium plates

Figure 5.10: Blast-structure response spectrum in terms of permanent mid-point deflection. The grey markers illustrate the combinations of stand-off distances and thicknesses used in the numerical simulations to generate the response spectra. The colour scaling indicates the permanent mid-point (out-of-plane) deflection: a red colour indicates a permanent deflection in the same direction as the incoming blast wave, a green colour represents zero permanent mid-point deflection and a blue colour represents CIB.

The numerical investigation observed both types of CIB (either Type III during or Type III* subsequent to the elastic rebound) within a narrow range of stand-off distances and plate thicknesses for both materials. Thus, the study confirms that CIB is a response which occurs within a limited range of loading and structural conditions, and that this behaviour is related to thin flexible structures. In particular, the results indicated that CIB Type III is related to the starting time of the negative phase $t_{\mathrm{d}+}$ relative to the elastic rebound after maximum deflection, while CIB Type III* may occur at small thicknesses when the ratio between the positive and negative impulses approaches the same

order of magnitude. The simulations also provide some other interesting results, such as failure at the centre of the plate and complete tearing at the boundary during RSB for the smallest thicknesses (see Figure 5.11). In the simulations experiencing failure, the mid-point deflection at the point of complete failure was used in the response spectra. This indicates that although the ultimate deflection is most often used as a design criterion since this is related to the maximum stress state, damage accumulates during RSB and thin plates may fail during reversed motion. The different types of CIB were characterized by a transition zone where the turning point seemed to be at a thickness $t = 0.6$ mm for the steel plates (Figure 5.10a) and $t = 1.0$ mm for the aluminium plates (Figure 5.10b). That is, Type III* CIB occurred in the dark blue area at thicknesses smaller than 0.6 mm for the steel plates, and in the dark blue area at thicknesses smaller than 1.0 mm for the aluminium plates. CIB of Type III and III* are indicated by solid and dashed blue lines, respectively, in Figure 5.11b-d. As expected, increased stand-off distance and plate thickness resulted in oscillations approaching the initial configuration of zero mid-point deflection (a green colour in Figure 5.10 and Figure 5.11).

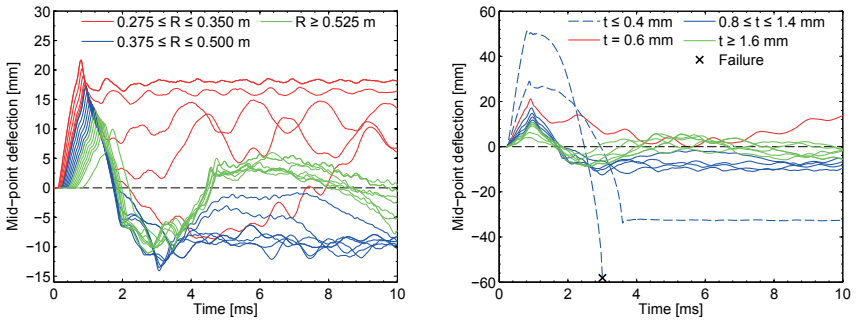

(a) Steel plates (t = 0.8 mm)

(b) Steel plates (R = 0.375 m)

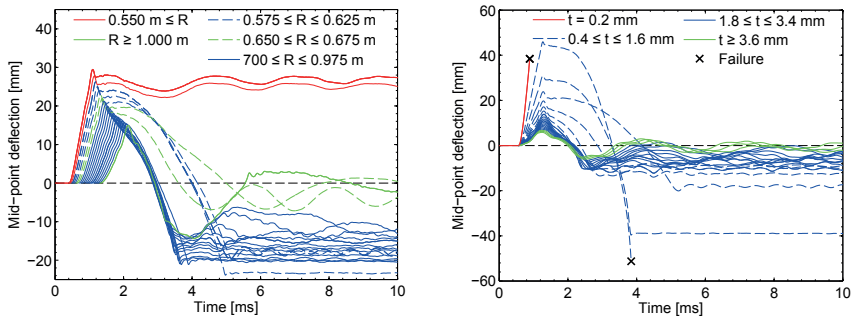

(c) Aluminium plates (t = 0.8 mm)

(d) Aluminium plates (R = 0.625 m)

Figure 5.11: Typical mid-point deflection histories for the aluminium and steel plates when varying the stand-off distance and plate thickness.

The findings in this study therefore broaden the range of loading properties resulting in RSB, because previous studies (see e.g. [45–47]) mainly consider projectile impacts or positive pulses as the loading. In such environments there is no negative phase loading and the CIB is driven by the ratio between the bending and membrane energy (i.e., the maximum deflection and the corresponding rotation in the plastic hinges at which reverse motion starts). This is further argued by the fact that the response is membrane dominated due to the large deflection-thickness ratios observed in these experiments (see Table 5.2). Jones [61] showed that the bending contributions are negligible compared to the membrane forces for plated structures experiencing a deflection-thickness ratio larger than one.

Table 5.2: Summary of the numerical results in terms of the maximum deflection-thickness ratios ($d_{z,max}/t$) and total impulses (I_{r+} and I_{r-}) transmitted to the plate from the blast loading. The negative deflection-thickness ratio is given in parentheses for the configurations experiencing CIB.

Test	$d_{z,max}/t$ [-]	I_{r+} [Ns]	I_{r-} [Ns]	CIB [Y/N]
S1	40.0	32.1	12.2	N
S2	29.0	21.0	10.7	N
S3	21.4 (-14.9)	14.0	8.0	Y (Type III)
A0	N/A	21.0	10.7	N
A1	53.4	14.4	8.0	N
A2	38.8	10.5	6.5	N
A3	29.8 (-25.1)	7.9	6.0	Y (Type III*)

*Note that this table reports the total impulses transmitted to the plates, while Table 5.1 contains the specific impulse recorded by the pressure sensors.

5.3 Concluding remarks

A numerical model in EPX has been validated against experimental data in predicting the inelastic response of thin aluminium and steel plates exposed to blast loading. The numerical results were generally in good agreement with the experimental data and covered the entire range of inelastic response. This included partial and complete tearing along the boundaries at the closest stand-off distances and a counter-intuitive behaviour (CIB) where the permanent deflection of the plate was in the opposite direction to the incoming blast wave due to reversed snap buckling (RSB). The influence of elastic effects and negative phase on RSB was studied numerically, and two types of CIB were identified within a narrow range of loading and structural conditions. Both types of CIB were found to depend on the timing and magnitude of the peak negative pressure relative to the dynamic response of the structure. In particular, CIB of Type III was driven by elastic effects enhanced by the

negative phase during the elastic rebound, while Type III* occurred during the subsequent oscillations after the elastic rebound and was related to the timing of the peak negative pressure and the ratio between positive and negative impulses. The plate thickness and material were found to be the governing structural properties, where plate thicknesses less than about 1.6 mm and 3.2 mm may result in CIB for the steel and aluminium material, respectively. The influence of the material was evident by comparing steel and aluminium plates at the same stand-off distance ($R = 0.375$ m), which resulted in a completely different structural response since the steel plates experienced RSB whereas the permanent displacement of the aluminium plates was in the intuitive direction.

It is also emphasized that the characteristic loading domain is often determined based on the duration of the positive phase relative to the natural period of the structure (see e.g. [32]). The loading domain will then determine the computational method to be used in the blast-resistant design. Following this classification, the experiments presented herein fall into the impulsive loading domain where the blast load has vanished before the structure undergoes any significant deformation. Consequently, the response is assumed to depend only on the magnitude of the positive impulse and not on the evolution of the pressure-time history. This study shows that the blast-loaded plates experienced severe blast-structure interaction effects during the negative phase. Thus, the loading domain of thin flexible plates should not be determined solely based on the positive phase of the blast load. In particular, if the timing of the negative phase is such that it will enhance elastic oscillations during (CIB Type III) or subsequent (CIB Type III*) to the elastic rebound, thin plates cannot be categorized into the impulsive loading domain since the negative phase may dominate the response. Finally, previous studies have suggested that the negative phase can be ignored at scaled distances with relatively small magnitudes in peak negative pressure $p_{\mathrm{r,min}}$ compared to the peak reflected overpressure $p_{\mathrm{r}\alpha}$ (e.g. [22]). However, the observations in this study extend the range of applications where the negative phase should be considered, because CIB was observed at relatively large peak reflected overpressures. This implies that the relative pressure magnitudes are not the only important parameter of the loading, but also the ratio between the specific positive and negative impulses could be used as an indication for CIB. In particular, it is found that RSB (i.e., CIB Type III*) may dominate the response of thin aluminium and steel plates when the positive and negative impulses are of the same order of magnitude.

Part III

Shock Tube Loading

6

Shock tube

The shock tube technique is chosen as an alternative to explosive detonations when generating blast loading in **Part III** of this thesis. This enable studies on the dynamic response of flexible plates and fluid-structure interaction (FSI) effects in blast environments without the need to consider the inherent complexity in close-in and near-field detonations. Before moving into shock tube design, experiments and numerical simulations, it is necessary to understand the initiation and propagation of shock waves in a shock tube. This chapter therefore starts with a brief review of some basic concepts in the fields of thermodynamics and shock physics, before the shock tube operation with respect to blast loading is presented. Finally, the Riemann problem is introduced as a solution technique and used to obtain a basic understanding of the influence of FSI when the blast wave interacts with a moving surface.

6.1 Introduction

As discussed in Section 1.2.4, an alternative to explosive detonations when generating blast loading is the shock tube technique (see Refs. [113–121]). This is a well-known experimental technique within the field of gas dynamics using well-defined and easily controllable initial conditions providing good repeatability of each test. The properties of a shock wave acting on a structure may be studied by placing a structure inside or at the end of the tube. Using a movable or deformable structure, the pressure is altered by the structural response and this setup is well-suited to study the influence of fluid-structure interaction (FSI) effects on blast-loaded structures. Such a setup therefore allows for the evaluation of FSI in controlled laboratory environments without the need to consider the inherent complexity in close-in and near-field detonations. A more detailed discussion on the shock tube problem is presented later in this chapter and also found in the literature (see e.g. [87, 123–125]).

The use of shock tubes is not new and one of the first shock tube facilities was established in 1899 by the French scientist Paul Vieille [199] to study

the deflagration of explosive charges. The shock tube technique comes in different types and has a wide variety of applications. This has attracted the interest from many engineering disciplines, e.g. chemical kinetics, aerodynamics (supersonic aircraft flight and shuttle atmospheric entry), thermodynamics and blast-structure interactions. In some cases, high explosives are used to generate the shock wave and these are often denoted explosive-driven shock tubes (see e.g. [118]). However, the most common application is the so-called pressure-driven shock tubes where compressed gas is used as the energy source to generate the shock wave (see e.g. [119–121]). This is also the type of shock tube to be considered in this thesis.

For most practical applications involving shock physics (e.g. blast events or bursting pressure vessels) there are no closed form analytical solutions of the governing equations due to the multi-dimensional space, complex boundaries and non-linearity in the problem. Numerical methods are therefore frequently used to solve these types of problems involving wave propagation and FSI. Neglecting heat transfer in or out of the system and viscous effects in the flow, the governing equations may be reduced to the Euler equations. In the particular case of the Euler equations the so-called Riemann problem is often sought for the solution to the shock tube problem [88]. Using hyperbolic conservation equations for mass, momentum and energy with an additional equation of state (EOS), the Riemann problem provides the basic understanding of shock wave propagation in any kind of matter, be it gaseous, liquid or solid. The relatively simple and analytical solvable case of a one-dimensional (1D) system of waves in an infinitely long tube gives an intuitive understanding of the governing physics and phenomena in the shock tube. This analytical solution to the Riemann problem is also a valuable reference solution when evaluating the performance of computational fluid dynamics (CFD) codes in describing shock waves and their corresponding discontinuities. As will be showed later in Chapter 9, the solution of the Riemann problem (analytical or approximate) can also be used to solve the local flux between neighboring computational cells in numerical methods (see e.g. [88, 200]). Thus, an understanding of the shock tube problem is also beneficial when evaluating and developing approximate Riemann solvers. Before presenting the Riemann solution, basic principles, operation and distinctive features of a shock tube with application to blast loading, a brief review of some basic concepts within thermodynamics and shock physics will be given. Although the fundamental aspects of these topics are well established in the literature, such a presentation is necessary for the understanding and discussion of the results later in this thesis. It is also emphasized that the thermodynamics and shock physics presented herein are written from a structural engineering point of view and limited to the relations necessary to understand shock wave propagation and FSI in the idealized gas theory. Compressible fluid flow is an active field of research and detailed studies

of the physics within this topic are beyond the scope of this thesis.

6.2 Review of thermodynamics

The kinetic energy per unit mass is given as $v^2/2$ for a 1D flow [201, 202], where v is introduced as the notation for the velocity. This implies that high-speed flow is synonymous to high-energy flow. In most cases high-speed flow is also equivalent to compressible flow and the corresponding energy changes are significant enough to interact with other properties of the flow. Energy concepts therefore play an important role in obtaining an understanding of compressible flow. The theory of energy (and entropy) is commonly known as thermodynamics and is an essential ingredient in the study of compressible flow. This section therefore briefly reviews some of the thermodynamic state variables and relations necessary to understand the physics involved in the solution of the shock tube problem. Please note that this section is based mainly on the presentation given in Refs. [201, 202].

6.2.1 Equation of state

An equation of state (EOS) is a constitutive equation relating state variables which describe the state of matter under a given set of physical conditions. It is a mathematical relationship between several state variables associated with the matter, such as its temperature, pressure, volume, density, or internal energy. An EOS is useful in describing the properties of gas, liquids or solids, and is frequently used to relate densities of gases and liquids to temperatures and pressures. It can therefore be thought of as a constitutive relation for materials at high pressures.

A gas is a collection of particles (e.g. molecules, atoms, ions and electrons) that are in more or less random motion. Due to the electronic structure of these particles, a force field is introduced in the space around them. The force field around one particle interacts with neighboring particles, and vice versa. These fields are therefore often called intermolecular forces. The intermolecular forces varies with the distance between the particles. For most atoms and molecules it takes the form of a weak attractive force at large distance, changing quickly to a strong repelling force at close distance. In general, these intermolecular forces influence the motion of the particles and, consequently, also influence the thermodynamic properties of the gas which can be considered as the macroscopic framework of the particle motion.

At temperatures and pressures characteristic of many compressible flow applications, the gas particles are widely spread. The average distance between particles is usually in the range of 10 molecular diameters, which corresponds

to a weak attractive force. As a result, for a large number of engineering applications, the effect of intermolecular forces on the gas properties is negligible. By definition, an ideal (or perfect) gas is one in which intermolecular forces are neglected. Neglecting intermolecular forces, the EOS for a perfect gas can be derived from statistical mechanics or kinetic theory. However, historically it was found from experimental observations resulting in the following empirical equation known as the ideal gas law

$$pV = MRT \tag{6.1}$$

where p, V and T are the pressure, volume and temperature of the system, M is the mass of the system, and R is the specific gas constant which is unique for each gas. The EOS in Eq. (6.1) is found in many forms and variations in the literature. However, all these representations are basically the same where this thesis will use the particular forms given by

$$p = \rho RT \tag{6.2a}$$

$$p = \rho(\gamma - 1)e \tag{6.2b}$$

where ρ is the density, e is the specific internal energy per unit mass, γ is the ratio of specific heats given by the specific heat at constant pressure c_p and the specific heat at constant volume c_v.

In the vast majority of gas dynamic applications, Eqs. (6.2a) and (6.2b) can be applied with confidence. However, at very cold temperatures and high pressures, the molecules of the gas are more closely packed together, and intermolecular forces become more important. Under these conditions, the gas is defined as a real gas. In such cases, it may be necessary to replace the perfect gas EOS with more elaborate relations.

6.2.2 Internal energy and entalphy

Returning to the microscopic view of gas as a collection of particles in random motion, the individual kinetic energy of each particle contributes to the overall energy of the gas. The energy of a particle consists of several different forms of motion (e.g. translational, rotational, vibrational and electronic motions). These energies, summed over all the particles of the gas, constitute the internal energy per unit mass (or specific internal energy) e of the gas.

From an engineering point of view, equilibrium is considered in a macroscopic perspective where the gas is viewed as a continuum (or control volume) of a large number of molecules. Equilibrium is then characterized by no gradients in velocity, pressure, temperature, and chemical concentrations throughout the system. That is, the system has uniform properties. For a system of real gases,

and also for a chemically reacting mixture of perfect gases, the internal energy e is a function of both temperature and volume. A related quantity is the specific enthalpy h defined as

$$h = e + p\varrho = e + \frac{p}{\rho} \tag{6.3}$$

where $\varrho = 1/\rho$ is the specific volume, and

$$e = e(T, \varrho) \tag{6.4a}$$
$$h = h(T, p) \tag{6.4b}$$

for both a real gas and a chemically reacting mixture of perfect gases. The enthalpy is therefore a measure of the energy in a thermodynamic system and includes both the internal energy and the amount of energy necessary to produce a change in the volume of the system.

If the gas is not chemically reacting and the intermolecular forces are neglected, the resulting system is a thermally perfect gas. Then, the internal energy, enthalpy and the specific heats (c_v and c_p) are all functions of the temperature only. Furthermore, if the specific heats are assumed constant, the system is defined as a calorically perfect gas where

$$e = c_v T \tag{6.5a}$$
$$h = c_p T \tag{6.5b}$$

and it is also assumed that $h = e = 0$ at $T = 0$.

In many compressible flow applications, the pressure and temperatures are moderate enough such that the gas can be considered as calorically perfect. Real gas effects and chemically reacting mixtures of perfect gases are considered beyond the scope of this thesis. As discussed in Section 6.2.1, such effects can be of importance at high magnitudes of pressure (e.g. as the blast event becomes increasingly near-field). The interested reader is referred to the literature (see e.g. [124, 125, 202]) for a more detailed presentation of these effects.

Assuming the EOS of a calorically perfect gas given in Eq. (6.2), the constants of specific heats are related through the following relation

$$c_p - c_v = R \tag{6.6}$$

where the specific heats at constant pressure and volume are defined, respectively, as

$$c_p = \left(\frac{\partial h}{\partial T}\right)_p \quad \text{and} \quad c_v = \left(\frac{\partial e}{\partial T}\right)_\varrho \tag{6.7}$$

where the subscripts p and ϱ denote that the partial derivatives are taken at constant pressure and volume, respectively. Moreover, two useful terms of Eq. (6.6) can be obtained by first dividing it by c_p

$$1 - \frac{c_v}{c_p} = \frac{R}{c_p} \tag{6.8}$$

and introducing the ratio of specific heats as $\gamma = c_p/c_v$. Eq. (6.8) then reads

$$1 - \frac{1}{\gamma} = \frac{R}{c_p} \tag{6.9}$$

which can be solved for c_p as

$$c_p = \frac{\gamma R}{\gamma - 1} \tag{6.10}$$

and by combining Eqs. (6.5b) and (6.10) the entalphy of a perfect gas reads

$$h = \frac{\gamma}{\gamma - 1} RT \tag{6.11}$$

Similarly, by dividing Eq. (6.6) by c_v, the specific volume can be expressed as

$$c_v = \frac{R}{\gamma - 1} \tag{6.12}$$

where the internal energy of the perfect gas in Eq. (6.5a) now reads

$$e = \frac{RT}{\gamma - 1} \tag{6.13}$$

These are useful relations when discussing compressible high-speed flow. However, it is emphasized that Eqs. (6.10) and (6.12) only holds for a calorically perfect or a thermally perfect gas. They are not valid for either a chemically reacting or a real gas. Note that for air at atmospheric conditions $\gamma = 1.4$.

6.2.3 First law of thermodynamics

Consider the system in Figure 6.1, which is a fixed mass of gas separated from the surroundings by a flexible boundary. The system is assumed to be stationary, i.e., it has no directed kinetic energy. Let Δq be an incremental amount of heat added to the system across the boundary. Examples of sources for Δq are radiation from the surroundings that is absorbed by the mass in the system and thermal conduction due to temperature gradients across the boundary. Also, let Δw denote the work on the system by the surroundings

(e.g. deformation of the boundary reducing the volume of the system). As discussed earlier, due to the molecular motion of the gas, the system has a specific internal energy e (which can be considered as the internal energy by assuming a unit mass). The heat added and work done on the system cause a change in energy, and since the system is stationary, this change in energy reads

$$de = \Delta q + \Delta w \tag{6.14}$$

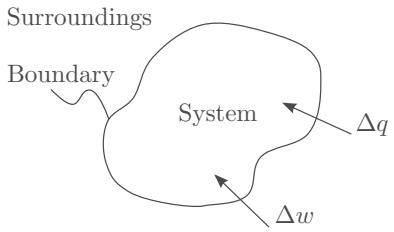

Figure 6.1: Thermodynamic system.

This is the first law of thermodynamics, which is an empirical result confirmed by experiments and practical experience [201, 202]. Thus, the first law of thermodynamics is the conservation of energy and requires that the sum of mechanical and thermal energy is constant in a closed system. Any change in the specific internal energy must be balanced by the power of forces from the surroundings and the rate of heat flux through the boundary. In Eq. (6.14), e is a state variable and de is differentiable where its value depends only on the initial and final states of the system. In contrast, Δq and Δw depend on the process in going from the initial to the final states.

For a given de, there are in general an infinite number of different processes by which heat can be added and work done on the system. However, the literature often operates with three types of processes [201, 202], i.e.,

- An adiabatic process where no heat is added to or taken away from the system.
- A reversible process where no dissipative phenomena occur, i.e., where the effects of viscosity, thermal conductivity, and mass diffusion are absent.
- An isentropic process which is both adiabatic and reversible.

For a reversible process, the work on the system from the surroundings can be expressed as $\Delta w = -pd\varrho$ where $d\varrho$ is an incremental change in specific volume

ϱ due to a displacement of the boundary of the system. Thus, Eq. (6.14) now reads

$$de = \Delta q - p d\varrho \tag{6.15}$$

If, in addition, the process is adiabatic (i.e., isentropic) $\Delta q = 0$ and Eq. (6.15) leads to some useful thermodynamic relations which will be presented in the following.

6.2.4 Entropy and the second law of thermodynamics

The first law of thermodynamics provides limited information regarding the evolution of heat and mechanical work, other that the energy must be conserved during the process. The observation that heat always flows from regions of higher to regions of lower temperature and that the amount of thermal energy needed to provide mechanical work is always larger than the gained external work lead to the formulation of the second law of thermodynamics. To ensure the validity of the first law, a new state variable s has to be defined

$$ds = \frac{\Delta q_{\text{rev}}}{T} \tag{6.16}$$

which is called the entropy of the system, Δq_{rev} is an incremental amount of heat added reversibly to the system and T is as before the temperature. It is emphasized that the entropy s is a state variable, and it can be used in combination with any type of process (reversible or irreversible). The quantity Δq_{rev} is just an artifice. An effective value of Δq_{rev} can always be assigned to relate the initial and final points of an irreversible process, where the actual amount of added heat is Δq. Thus, an alternative and probably more intuitive relation is

$$ds = \frac{\Delta q}{T} + ds_{\text{irrev}} \tag{6.17}$$

This is a general statement and may be interpreted such that the change in entropy during any incremental process is equal to the actual heat Δq added divided by the temperature T plus a contribution ds_{irrev} from the irreversible dissipative phenomena of viscosity, thermal conductivity, and mass diffusion occurring within the system. These dissipative phenomena always increase the entropy, i.e.,

$$ds_{\text{irrev}} \geq 0 \tag{6.18}$$

The equal sign denotes a reversible process, where, by definition, the dissipative phenomena are absent. Hence, entropy can be thought of as a measure of

the molecular disorder within a macroscopic system (i.e., a measure of a system's thermal energy per unit temperature that is unavailable for doing useful work).

A combination of Eqs. (6.17) and (6.18) reads

$$ds \geq \frac{\Delta q}{T} \tag{6.19}$$

Moreover, if the process is adiabatic $\Delta q = 0$ Eq. (6.19) becomes

$$ds \geq 0 \tag{6.20}$$

Eqs. (6.19) and (6.20) are therefore typical representations of the second law of thermodynamics. The concept of entropy in combination with the second law enables prediction of the direction in which a process will take place. A process will proceed in a direction such that the entropy of the system and the surroundings always increases or stays the same. That is, thermodynamic processes are basically changes in state variables initiated through exchange of the system with its environment. The process itself can be described as a path in the space of state variables. Any natural process starting from a condition of thermodynamic equilibrium follows subsequent conditions of non-equilibrium until a new equilibrium condition is reached [201, 202].

The starting point of the calculation of the entropy is the first law of thermodynamics in Eq. (6.15). Assuming that the heat is reversible and using the definition of entropy in Eq. (6.16) (i.e., $\Delta q_{\text{rev}} = Tds$), then Eq. (6.15) reads

$$Tds = de + pd\varrho \tag{6.21}$$

An alternative form can be obtained in terms of enthalpy. Differentiation of Eq. (6.3) gives

$$dh = de + pd\varrho + \varrho dp \tag{6.22}$$

Then, combining Eqs. (6.21) and (6.22) reads

$$Tds = dh - \varrho dp \tag{6.23}$$

For a thermally perfect gas, $dh = c_p dT$ may be substituted into Eq. (6.23), i.e.,

$$ds = c_p \frac{dT}{T} - \frac{\varrho dp}{T} \tag{6.24}$$

Substituting the perfect gas EOS (i.e., $p\varrho = RT$) from Eq. (6.2a) into Eq. (6.24)

gives

$$ds = c_p \frac{dT}{T} - R\frac{dp}{p} \tag{6.25}$$

Integrating Eq. (6.25) between states 1 and 2 now reads

$$s_2 - s_1 = \int_{T_1}^{T_2} c_p \frac{dT}{T} - R\ln\left(\frac{p_2}{p_1}\right) \tag{6.26}$$

The result in Eq. (6.26) holds for a thermally perfect gas. It can be evaluated if c_p is known as a function of T. If one further assumes a calorically perfect gas, where c_p is constant, Eq. (6.26) gives

$$s_2 - s_1 = c_p\ln\left(\frac{T_2}{T_1}\right) - R\ln\left(\frac{p_2}{p_1}\right) \tag{6.27}$$

Similarly, starting with Eq. (6.21) and $de = c_v dT$, the change in entropy may also be expressed as

$$s_2 - s_1 = c_v\ln\left(\frac{T_2}{T_1}\right) + R\ln\left(\frac{\varrho_2}{\varrho_1}\right) \tag{6.28}$$

Eqs. (6.27) and (6.28) enable the calculation of the change in entropy between two states of a calorically perfect gas in terms of either the pressure and temperature, or the volume and temperature. Note that the entropy is a function of both p and T, or ϱ and T, even for the simplest case of a calorically perfect gas.

6.2.5 Isentropic relations

An isentropic process is already defined in Section 6.2.3 as both adiabatic and reversible (i.e., $\Delta q = 0$ and $ds_{\text{irrev}} = 0$). The system has no heat exchange, no viscosity and no external sources of energy. Eq. (6.17) then gives an isentropic process as one in which $ds = 0$, i.e., the entropy is constant.

Useful relations for an isentropic process can then be obtained directly from Eqs. (6.27) and (6.28) by setting $s_2 = s_1$. Thus, Eq. (6.27) may be written as

$$\frac{p_2}{p_1} = \left(\frac{T_2}{T_1}\right)^{c_p/R} \tag{6.29}$$

Combining Eqs. (6.10) and (6.29) results in the following relation

$$\frac{p_2}{p_1} = \left(\frac{T_2}{T_1}\right)^{\gamma/(\gamma-1)} \tag{6.30}$$

Similarly, from Eq. (6.28)

$$\frac{\varrho_2}{\varrho_1} = \left(\frac{T_2}{T_1}\right)^{-c_v/R} \tag{6.31}$$

Using the result in Eq. (6.12) in Eq. (6.31) gives

$$\frac{\varrho_2}{\varrho_1} = \left(\frac{T_2}{T_1}\right)^{-1/(\gamma-1)} \tag{6.32}$$

Recall that $\rho_2/\rho_1 = \varrho_1/\varrho_2$. Hence, from Eq. (6.32) it follows that

$$\frac{\rho_2}{\rho_1} = \left(\frac{T_2}{T_1}\right)^{1/(\gamma-1)} \tag{6.33}$$

Finally, by using Eqs. (6.30) and (6.33) the isentropic relations read

$$\frac{p_2}{p_1} = \left(\frac{\rho_2}{\rho_1}\right)^{\gamma} = \left(\frac{T_2}{T_1}\right)^{\gamma/(\gamma-1)} \tag{6.34}$$

This is an important result since it relates pressure, density and temperature for an isentropic process, and it is frequently used in the analysis of compressible flow. Also note that Eq. (6.34) originates from the first law of thermodynamics and the definition of entropy. Therefore, Eq. (6.34) is basically an energy relation for an isentropic process. This is a valuable observation and it is also seen from Eq. (6.34) that $p/\rho^{\gamma} = \text{constant}$.

6.3 Shock physics

Information about loads applied to a system is propagated through the medium by waves at the local speed of sound. If the induced waves take the shape and amplitude of so-called shock waves, then the waves move faster than the local speed of sound and their propagation through the system needs to be resolved in time and space [203].

The shock waves considered in this chapter are strong compression waves caused by the sudden release of the high pressure in a shock tube. However, it should be noted that most of this theory is general and may be used in a large variety of applications involving other shock loading environments (e.g. high-speed impact events). Shock physics, which is a combination of fluid- and thermodynamics, allows for quantitative evaluations of shock waves. The topic is too broad to be fully covered in this thesis, and it is referred to the many papers and textbooks on the subject for a more detailed representation (see e.g. [122, 141, 201–205]).

6.3.1 Compressible flow

This section is mainly based on the presentation of compressible flow given in Refs. [201, 202]. Compressible flow is commonly defined as variable density flow. This is in contrast to incompressible flow, where the density is assumed to be constant. The definition of compressible flow can be studied by considering a small element of gas (or fluid) of specific volume ϱ (see Figure 6.2a). The pressure exerted on the sides of the element by the neighboring gas is p. Now, assume that the pressure is increased by an infinitesimal quantity dp. The volume of the element will be correspondingly compressed by the amount $d\varrho$ (illustrated in Figure 6.2b). The change in volume $d\varrho$ is a negative quantity since the volume is reduced, and the portion of which a gas (or fluid) can be compressed is given by its compressibility β defined as [201]

$$\beta_s = -\frac{1}{\varrho}\left(\frac{\partial \varrho}{\partial p}\right)_s \tag{6.35}$$

where the subscript s denotes that the partial derivative is taken at constant entropy (i.e., assuming an isentropic process).

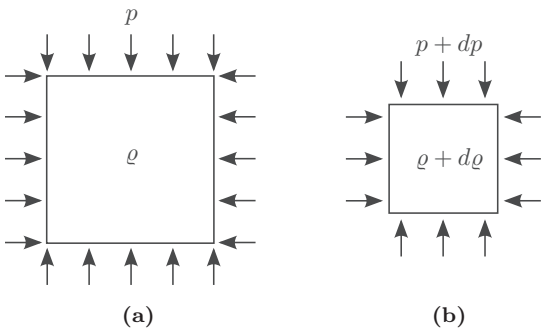

Figure 6.2: Definition of compressibility [202]: (a) initial volume and (b) compressed volume.

Hence, the physically interpretation of compressibility is the relative change in volume of a gas (or fluid) as a response to a pressure change. As a rule of thumb, gas velocities less than about 0.3 of the speed of sound are associated with relative low pressure changes and low-speed flow. These type of flows are often considered as incompressible, despite the relatively high value of β since dp is considered small enough to neglect the corresponding $d\varrho$. However, flow velocities higher than 0.3 of the speed of sound are associated with relatively high pressure changes, accompanied by correspondingly large changes in density and the flow should therefore be considered as compressible.

6.3.2 Shock waves

A shock wave is characterized by a distinct wave front, traveling through a medium at supersonic speed compared to the undisturbed media. Shock waves in air are very thin transition layers of rapid changes of physical quantities such as pressure, density and temperature. The thickness of a strong shock wave is of the same order of magnitude as the mean-free path[i] of the molecules, i.e., about 10^{-7} m (0.1 μm) [88]. In the idealized case, the compressed gas reaches its equilibrium values of pressure, density and pressure in this distance.

The structure of the shock front and the processes through which the gas must pass to obtain its new equilibrium will depend upon the strength of the shock and the properties of the gas. Equilibrium in the state variables (T, p, ρ and v) is established within the timescale of nanoseconds (10^{-9} seconds). It will be shown in the following that an idealized shock wave forms as a result of the steepening of the compressive part of a finite, continuous disturbance and that through the action of the pressure and inertia forces this gradient ultimately becomes nearly infinite. In a real gas this steepening is resisted by the diffusive effects of viscosity and heat conduction and the final form of the shock transition must involve a balance between these two events. It follows that in any real gas a shock wave will have a finite thickness and a definite structure. Viscous effects are important within the shock front since these effects cause the shock in the first place. The flow across a shock wave is considered adiabatic (i.e., no external heating) and the total enthalpy is constant across the wave. However, outside this layer, viscous effects are small on scales larger than the mean free path [201, 204]. Thus, for most practical engineering purposes the shock thickness may be ignored, but in certain types of flow, at low gas densities for example, the shock structure becomes important. The details of the shock structure are beyond the scope of this thesis and the shock waves will in the following be considered as mathematical discontinuities. Thus, shock waves are considered as extremely thin regions and involve discontinuities which has to be carefully considered when solving the governing equations.

Shock waves are often classified based on the supersonic speed which is the rate of propagation of an object that exceeds the speed of sound (Mach 1). In fluid dynamics, the Mach number M is a dimensionless quantity representing the ratio of the speed of an object moving through a fluid (gas or liquid) and the local speed of sound, given as

$$M = \frac{v}{c} \tag{6.36}$$

[i] In physics, the mean free path is the average distance traveled by a moving particle (such as an atom, a molecule, a photon) between successive impacts (collisions), which modify its direction or energy or other particle properties.

where v is the velocity of the object relative to the medium and c is the speed of sound in the medium. Thus, any speed lower than the speed of sound in a sound-propagating medium is called subsonic ($M < 1$), while any speed higher than the speed of sound in the medium is denoted supersonic ($M > 1$). Speeds greater than five times the speed of sound ($M > 5$) are often referred to as hypersonic. For objects traveling in dry air at a temperature of 20° at sea level, $M = 1$ corresponds to a wave velocity of $v = 343.1$ m/s.

In general, the principles are equally applicable for all types of matter (i.e., solids, liquids or gases) and it is important to distinguish between elastic and plastic waves. A starting point for understanding shock phenomena may therefore be obtained by considering the compression characteristics of most solid materials. From 1D elastic stress-wave theory (see e.g. [203]), the longitudinal wave speed (or the speed of sound) c_L in a solid is given as

$$c_L = \sqrt{\frac{E}{\rho}} \tag{6.37}$$

where E is the elastic modulus (or elastic stiffness) and ρ is (as before) the density of the medium. In the more general 3D case, the speed of sound in a solid becomes

$$c_S = \sqrt{\frac{K + 3/4G}{\rho}} \tag{6.38}$$

where K and G are the bulk and shear modulus, respectively. Introducing the possibility of non-linear material behaviour for the longitudinal wave speed in Eq. (6.37) may be carried out by replacing the elastic modulus E with the tangent stiffness $\partial\sigma/\partial\varepsilon$ of the material at a specific loading state (σ, ε). The 1D longitudinal waves speed then reads

$$c_L = \sqrt{\frac{1}{\rho}\frac{\partial\sigma}{\partial\varepsilon}} \tag{6.39}$$

Similarly, in a perfect fluid or gas (3D medium with $G = 0$) the bulk speed of sound becomes

$$c_B = \sqrt{\frac{K}{\rho}} \tag{6.40}$$

for hydrostatic pressure waves. Here, K is the bulk modulus that measures the substance's resistance to uniform deformation under isentropic conditions (i.e., reversible and adiabatic conditions so that the entropy remains constant). It is defined as the derivative of pressure p with respect to density (or volume),

i.e.,

$$K = \rho \frac{\partial p}{\partial \rho} \tag{6.41}$$

The speed of sound may then be obtained by inserting Eq. (6.41) into Eq. (6.40) and reads

$$c^2 = c_B^2 = \left(\frac{\partial p}{\partial \rho} \right)_s \tag{6.42}$$

which can be considered as a simple EOS that provides a mathematical relationship between the change in pressure and density. Again, the subscript s denotes that the partial derivative is taken at constant entropy and it is seen that the speed of sound in the gas is related to the isentropic compressibility in Eq. (6.35).

Following Eqs. (6.37)-(6.42) it is observed that shock waves differ strongly from linear elastic waves regarding their expansion and propagation. High pressure magnitudes introduce the material to the non-linear and plastic region of the pressure-density relation. This is illustrated in Figure 6.3a where the gradient is the square of the speed of sound as given by Eq. (6.42). The speed of sound in the material is constant in the elastic region, which implies that the pressure and density are linearly related. Beyond the elastic region, the wave velocity increases with the pressure and density and the pressure-density relation becomes non-linear. That is, beyond the elastic region, the speed of sound increases with increasing pressure.

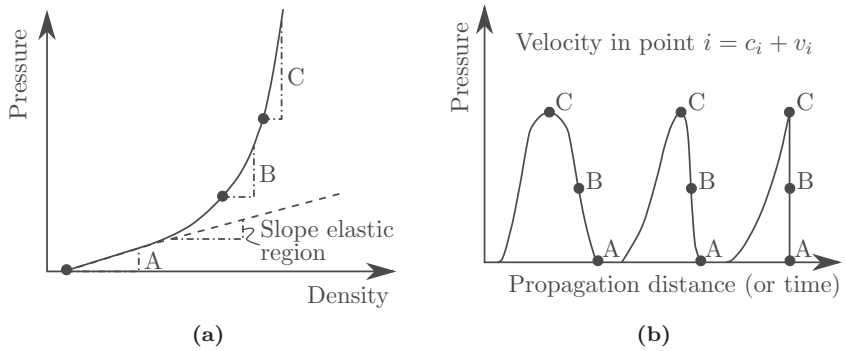

Figure 6.3: Typical relation between pressure and density, and formation (shocking-up) of a shock wave [141]: (a) pressure versus density and (b) the steepening of the shock wave.

This is described by Cooper [141] and may be illustrated by studying the pressure front of the shock in Figure 6.3b. At point A the pressure is low and,

consequently, the speed of sound c_A is low (see corresponding point in Figure 6.3a). Also the particle velocity v_A, i.e., the speed to which the material locally has been accelerated, is relatively low. Thus, the velocity of the pressure wave $c_A + v_A$ is quite low. At point B there is an increase in pressure compared to point A which implies that the speed of sound c_B increases (since we are evaluating a strong shock beyond the elastic limit). The particle velocity v_B is also higher, resulting in a pressure wave at point B travelling faster than at point A ($c_B + v_B > c_A + v_A$). Moreover, the same argument holds for point C that has a faster wave velocity than point B. Thus, since the propagation velocity of the wave depends on the gradient of the pressure-density relation, the peak pressure (C in Figure 6.3b) of the shock wave propagates faster than its leading and trailing edges (A and B in Figure 6.3b), resulting in the formation of a steep shock front (right pressure profile in Figure 6.3b) characterized by a virtually discontinuity in pressure and density. Thus, the initially smooth pressure front disturbance has been "shocked-up" because the wave speed increases with increasing pressure.

When the pressure wave takes on this vertical front, it is, as pointed out earlier, called a shock wave. Thus, from a mathematical point of view, there is no smooth transition from the medium in front of the wave to the medium behind the wave. The material "jumps" from the non-shocked to the shocked state. It is important to keep track of the different velocities, i.e., the sound, particle and pressure wave, and to remember that the pressure wave velocity is the sum of the sound and particle velocity. It may be challenging to visualize how the pressure wave velocity can be faster than the particle velocity since the particles are also moving. However, one should be aware that the shock wave is caused by a sudden and violent disturbance of the material (e.g. a sudden release of high pressure or an explosive detonation). The shock wave then propagates through the undisturbed material, by accelerating, compressing and heating the material, inducing a mass motion with the particle velocity behind the shock wave. This will be shown mathematically using the method of characteristics in Section 6.4.2 (see Eq. (6.61) and Figure 6.8).

The pressure-density relation in Figure 6.3a is commonly found in the literature in terms of the pressure-specific volume relation (see Figure 6.4). This is called the Hugoniot curve and represents the locus of all the possible equilibrium states in which a particular material can exist [141]. It must be emphasized that this is not an EOS or a path along which shock waves arise. It should also be noted that the isentropic curve, i.e., $p\varrho^{\gamma} = \text{constant}$ and the path function that describes a continuity and not a jump, is different from the Hugoniot curve. A rarefaction wave is an example of a continuous process and its path would be along the unloading isentrope. Remember that the rarefaction wave brings the pressure back down to the ambient pressure. Since the Hugoniot curve

represents the locus of all possible states (p_2, ϱ_2) behind the shock front reached from an initial state (p_1, ϱ_1) in front of the shock, the line joining the initial and final states on the Hugoniot curve represents the jump condition [141]. This line is called the Rayleigh line and is shown in Figure 6.4. That is, the shock is assumed to be acheived along a non-equilibrium path, assumed to be a straight line in the $p - \varrho$ space. Above the value p_2 in Figure 6.4, strong shocks will occur.

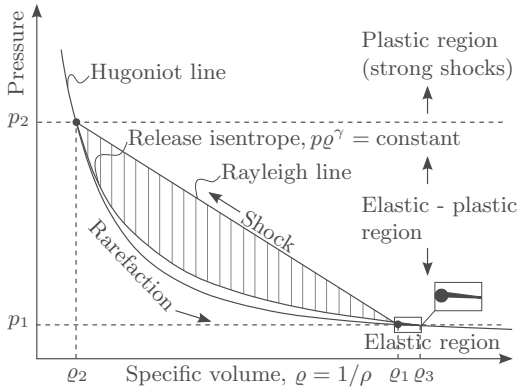

Figure 6.4: A typical representation of the pressure-specific volume (Hugoniot curve) [141]. Shock compression along Rayleigh line followed by an isentropic release resulting in dissipated energy. Shock waves produced at magnitudes beyond p_2.

Figure 6.4 illustrates a shock compression from an ambient state (p_1, ϱ_1) to a Hugoniot pressure p_2 followed by a subsequent isentropic release to the initial pressure p_1 at the end volume ϱ_3. Whereas the loading path to the Hugoniot state is described by the Rayleigh line, i.e., a straight line of non-equilibrium states, the isentropic release follows a curved line in the $p - \varrho$ plane. Thus, the portion of dissipated energy in the irreversible process of a shock transition is the difference between the energy stored during the shock loading, i.e., the triangular area under the Rayleigh line, and the recovered energy during the isentropic release [203]. The dissipated energy is represented by the shaded area in Figure 6.4. It is emphasized that the shaded area is highly exaggerated. Moreover, the final state ϱ_3 is larger than the initial volume ϱ_1 and the released energy equals the difference between the two shaded areas indicated with vertical lines and in black, respectively. The irreversible thermodynamic process of an almost instantaneous jump from initial conditions at ambient or other equilibrium conditions to a Hugoniot state therefore enhances the entropy of the compressed gas. The released energy is dissipated as heat and results in a heating of the gas. The portion of dissipated energy can be calculated from the thermodynamics involved in the process [141].

6.3.3 Rankine-Hugoniot relations

Shock waves occurring in an ideal gas have neither viscosity nor thermal conductivity and are assumed to follow the EOS in Eq. (6.2). To quantify the changes of the state variables after the passage of a shock wave, it is convenient to evaluate the behaviour ahead and behind the shock front. For simplicity, the problem is treated as a 1D stationary phenomenon as illustrated in Figure 6.5. Since the structure of the shock is not of interest, the shock front is represented as a moving discontinuity. The shock front now produces entropy in a well-defined system.

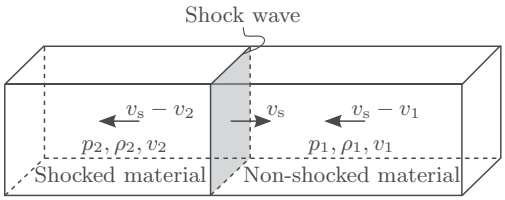

Figure 6.5: A non-shocked material moving through a stationary shock wave, where the state variables are defining the conditions ahead and behind a shock wave.

The relationship between the physical properties in the two states on both sides of the shock wave is given by the Rankine-Hugoniot relations (also known as the jump conditions). These equations were developed in their original form independently by Rankine [146, 147] and Hugoniot [148, 149] at the end of the 19th century, and express the conservation of mass, momentum and energy of a supersonic gas passing through a stationary shock wave into a subsonic state. Considering Figure 6.5 and assuming an ideal gas, the state in the shocked material is given by the hydrostatic pressure p_2, density ρ_2 and particle velocity v_2, where v_2 is supersonic ($M_2 = v_2/c_2 > 1$). In the non-shocked material, the corresponding properties are p_1, ρ_1 and v_1, where v_1 is subsonic ($M_1 = v_1/c_1 < 1$). The equations representing the conservation of mass, momentum and energy across the discontinuity is then expressed, respectively, as

$$\rho_2 v_2 = \rho_1 v_1 \tag{6.43a}$$

$$p_2 + \rho_2 v_2^2 = p_1 + \rho_1 v_1^2 \tag{6.43b}$$

$$\frac{p_2}{\rho_2} + e_2 + \frac{1}{2} v_2^2 = \frac{p_1}{\rho_1} + e_1 + \frac{1}{2} v_1^2 \tag{6.43c}$$

where it should be noted that the cross-sectional area of any tube geometry is the same on either side of the normal shock wave due its negligible thickness.

Now, using Eqs. (6.11), (6.13) and (6.43), the following jump relations can be

derived

$$\frac{p_2}{p_1} = \frac{1 - \dfrac{\rho_1}{\rho_2}\left(\dfrac{\gamma-1}{\gamma+1}\right)}{\dfrac{\rho_1}{\rho_2} - \dfrac{\gamma-1}{\gamma+1}} \tag{6.44a}$$

$$\frac{\rho_2}{\rho_1} = \frac{\dfrac{\gamma-1}{\gamma+1} + \dfrac{p_2}{p_1}}{\dfrac{\gamma-1}{\gamma+1}\dfrac{p_2}{p_1} + 1} = \frac{v_1}{v_2} \tag{6.44b}$$

These relations are often expressed in terms of the Mach number $M_\mathrm{s} = v_\mathrm{s}/c_1$ of the shock wave (see e.g. [202]), i.e.,

$$\frac{p_2}{p_1} = \frac{2\gamma M_\mathrm{s}^2 - (\gamma-1)}{\gamma+1} \tag{6.45a}$$

$$\frac{\rho_2}{\rho_1} = \frac{(\gamma+1)M_\mathrm{s}^2}{2 + (\gamma-1)M_\mathrm{s}^2} \tag{6.45b}$$

where c_1 is the speed of sound in the non-shocked material given by

$$c_1 = \sqrt{\gamma\frac{p_1}{\rho_1}} = \sqrt{\gamma R_1 T_1} \tag{6.46}$$

6.4 General shock tube theory

This section briefly reviews the operation and the distinctive features of a shock tube in blast applications. The propagation of a shock wave and the corresponding change in shape during its way through the tube and how this influences the respective state variables will also be presented.

6.4.1 Shock tube principle and operation for blast applications

A brief presentation of the basic principles, operation and distinctive features of an idealized shock tube with application to blast loading will be given in the following. This is assumed to be important for the understanding and discussion of the results later in this thesis.

The scope is limited to a compressed-gas driven shock tube with a closed-end configuration and constant tube cross-section. It consists of a high-pressure chamber (called driver section) which is separated from a low-pressure chamber (denoted driven section) by a diaphragm. A sudden opening of the diaphragm

generates a shock wave and rarefaction (or expansion) waves with corresponding discontinuities. Figure 6.6 illustrates the events occurring in such an idealized shock tube for blast applications with a right-running shock wave and left-running rarefaction waves (i.e., $p_4 > p_1$). It is emphasized that the subindices of the pressures and velocities in the following refer to the respective regions in Figure 6.6.

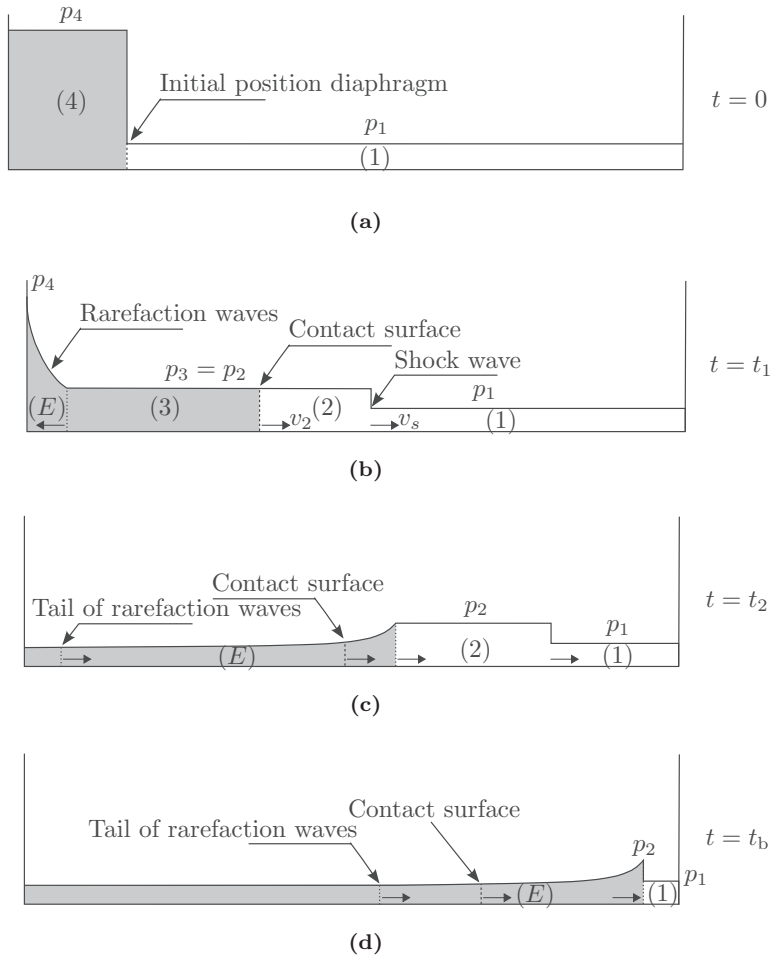

Figure 6.6: Schematic representation of the events occurring in a shock tube for blast applications and the corresponding pressure distributions along the longitudinal axis of the tube at characteristic times: (a) initial configuration, (b) wave pattern immediately after bursting diaphragm, (c) reflected rarefaction waves catch up with contact surface and (d) reflected rarefaction waves catch up with shock wave.

At time $t = 0$ the diaphragm is ruptured (Figure 6.6a), generating a shock

wave moving into the gas at low pressure p_1 and rarefaction waves that expand into the gas at higher pressure p_4 (Figure 6.6b). The high pressure gas acts as a piston expanding into the low pressure chamber and generates a shock wave moving at a velocity v_s larger than the sonic velocity c_1 of the undisturbed driven gas. The shock wave induces a mass (or particle) motion with velocity v_2 and pressure p_2 immediately behind the shock wave by compressing, heating and accelerating the driven gas in region 1. This near instantaneous acceleration of the driven gas is accompanied by a jump in pressure, temperature and density over the shock front. As discussed in Section 6.3.2, the shock wave has a thickness in the order of nanometers and (in the ideal case) the compressed gas reaches its equilibrium values of pressure, density and temperature in this distance (i.e., within the time scale of nanoseconds). From a mathematical point of view, assuming 1D gas flow with the EOS for an ideal gas, this can be represented as an instantaneous rise in pressure, temperature and density by using the Rankine-Hugoniot jump relations from Eq. (6.45) to relate the two states on both sides of the shock wave. The corresponding overpressure reads [125]

$$p_{\mathrm{so,max}} = p_2 - p_1 = p_1 \left(\frac{2\gamma(M_s^2 - 1)}{\gamma + 1} \right) \tag{6.47}$$

where we recall that the notation $p_{\mathrm{so,max}}$ is used for the peak incident (side-on) overpressure. This representation of the shock strength is convenient since the shock velocity v_s is easily measured in the experiments. In fact, the accuracy of Eq. (6.47) is so high that this approach is often used to calibrate electronic gauges and pressure sensors (see Ref. [206]). Using two time-of-arrival indicators (e.g. pressure sensors with a known distance between their respective locations), the shock velocity v_s is readily obtained. The corresponding Mach number M_s can then be inserted into Eq. (6.47) and used to determine the rise in pressure across the shock.

The initial interface between the high pressure and low pressure chambers (Figure 6.6a) moves from the diaphragm at a velocity v_2, and is called the contact surface (Figure 6.6b). At the same time as the shock wave propagates downstream the diaphragm, a system of rarefaction waves develops in the expanding high pressure gas. This series of rarefaction waves are denoted E in Figure 6.6b, and will reflect from the rear end of the driver section and then travel to the right and in the same direction as the shock wave (Figure 6.6c). If the driver section is short enough, these reflected rarefaction waves catch up with the contact surface and shock wave before reaching the test object (Figure 6.6d). The shock then decays in strength, increases in duration and decreases in velocity as it propagates towards the test specimen as a blast wave. The decreasing velocity is due to the rarefaction waves which reduce the driving pressure and hence the shock wave velocity. This is a result of the

non-linear relation between pressure, density and wave velocities in Eq. (6.42) which is illustrated in Figure 6.3. The reflected rarefaction waves are moving into the shocked air (at higher pressure and density) in regions 2 and 3, and will therefore have a higher velocity than the shock wave. Thus, the head of the reflected rarefaction waves will eventually catch up with the shock wave. On the contrary, the tail of the rarefaction waves is relieved back to ambient conditions (Figure 6.6c) and will therefore gradually lag further behind and stretch out region E. The experimental setup shown in Figure 6.6 differs from traditional shock tubes by using a relatively small ratio between the lengths of the two pressure chambers, such that the reflected rarefaction waves catch up with the shock wave resulting in pressure profiles similar to that from an explosive detonation. As the complexity of the system increases, numerical methods should be used to solve these types of interaction phenomena and wave patterns. These interactions are frequently expressed in the distance-time space where, in the absence of dissipative phenomena, the respective waves appear as linear curves and the respective slope of these curves represent the velocity of each wave (see Figure 6.7).

6.4.2 Properties of the one-dimensional Euler equations

Before introducing the Riemann solution to the shock tube problem it is necessary to discuss some properties of the governing equations. Since the shock tube is basically a 1D problem that involves compressible flow where heat transfer and viscosity effects are neglected, the governing equations are reduced to the Euler equations. The Euler equations can be expressed using vector form [88] as

$$\frac{\partial}{\partial t}\mathbf{U} + \frac{\partial}{\partial x}\mathbf{F}(\mathbf{U}) = \mathbf{0} \tag{6.48}$$

where $\mathbf{U}$ and $\mathbf{F}(\mathbf{U})$ are the vectors of conserved variables and fluxes, given respectively as

$$\mathbf{U} = \begin{bmatrix} U_1 \\ U_2 \\ U_3 \end{bmatrix} = \begin{bmatrix} \rho \\ \rho v \\ E \end{bmatrix} \quad , \quad \mathbf{F} = \begin{bmatrix} f_1 \\ f_2 \\ f_3 \end{bmatrix} = \begin{bmatrix} \rho v \\ \rho v^2 + p \\ v(E+p) \end{bmatrix} \tag{6.49}$$

where v is the first component of the velocity vector $\mathbf{v}$ and $E = \rho(e + \frac{1}{2}v^2)$ is the corresponding total energy per unit volume. Comparing Eqs. (6.43a) to (6.43c) and Eq. (6.49) it is observed that the flux vector $\mathbf{F}$ contains the same fluxes as the Rankine-Hugoniot relations. Thus, Rankine and Hugoniot solved the Euler equations in 1D for an inviscid calorically perfect gas in terms of the jump conditions.

Applying the chain rule to the second term in Eq. (6.48) reads

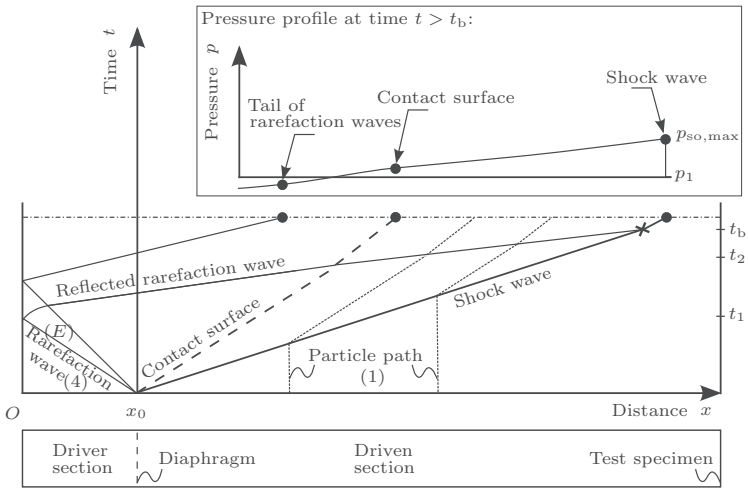

Figure 6.7: Lagrange (distance - time) diagram illustrating the formation of a blast wave in a shock tube. The black x denotes the point in time t_b for the formation of the blast wave. The characteristic times correspond to the schematic representation in Figure 6.6.

$$\frac{\partial}{\partial \mathbf{x}}\mathbf{F}(\mathbf{U}) = \frac{\partial \mathbf{F}}{\partial \mathbf{U}}\frac{\partial \mathbf{U}}{\partial x} \tag{6.50}$$

and the non-linear system of equations in Eq. (6.48) may be conveniently expressed on the form

$$\frac{\partial}{\partial t}\mathbf{U} + \mathbf{A}(\mathbf{U})\frac{\partial}{\partial x}\mathbf{U} = \mathbf{0}\,, \quad \mathbf{A}(\mathbf{U}) = \frac{\partial \mathbf{F}}{\partial \mathbf{U}} \tag{6.51}$$

resulting in a linear system of equations with variable coefficients which are denoted quasi-linear since the coefficient matrix $\mathbf{A}$ is a function of $\mathbf{U}$ [88]. That is, the non-linearity of Eq. (6.51) is present in the dependence of $\mathbf{A}$ on the unknown vector $\mathbf{U}$. This is usually the basis for the mathematical analysis of the Euler system of partial differential equations (PDEs), where the coefficient matrix $\mathbf{A}(\mathbf{U})$ is the Jacobian matrix containing the partial derivatives of the components f_i of the vector $\mathbf{F}$ with respect to the components U_i of the vector of conserved variables $\mathbf{U}$, i.e.,

$$\mathbf{A}(\mathbf{U}) = \frac{\partial \mathbf{F}}{\partial \mathbf{U}} = \begin{bmatrix} \dfrac{\partial f_1}{\partial U_1} & \dfrac{\partial f_1}{\partial U_2} & \dfrac{\partial f_1}{\partial U_3} \\ \dfrac{\partial f_2}{\partial U_1} & \dfrac{\partial f_2}{\partial U_2} & \dfrac{\partial f_2}{\partial U_3} \\ \dfrac{\partial f_3}{\partial U_1} & \dfrac{\partial f_3}{\partial U_2} & \dfrac{\partial f_3}{\partial U_3} \end{bmatrix} \tag{6.52}$$

Before establishing the Jacobian matrix $\mathbf{A}(\mathbf{U})$, it is necessary to express the components f_i in terms of the conserved components U_i. It is readily seen from Eq. (6.49) that $f_1 = U_2 = \rho v$. The remaining components f_2 and f_3 are found by expressing the pressure p in terms of the conserved variables U_i. Combining the expression for the total energy per unit volume ($E = \rho e + \frac{1}{2}\rho v^2$) and Eq. (6.2b) gives the following expression for the pressure

$$p = (\gamma - 1)(E - \frac{1}{2}\rho u^2) = (\gamma - 1)(U_3 - \frac{1}{2}\frac{U_2^2}{U_1}) \tag{6.53}$$

Introducing this result in Eq. (6.49) the flux vector is expressed in terms of the conserved variables U_i as

$$\mathbf{F} = \begin{bmatrix} f_1 \\ f_2 \\ f_3 \end{bmatrix} = \begin{bmatrix} U_2 \\ \frac{U_2^2}{U_1} + (\gamma - 1)(U_3 - \frac{1}{2}\frac{U_2^2}{U_1}) \\ \frac{U_2}{U_1}(U_3 + (\gamma - 1)(U_3 - \frac{1}{2}\frac{U_2^2}{U_1})) \end{bmatrix} = \begin{bmatrix} U_2 \\ \frac{1}{2}(3-\gamma)\frac{U_2^2}{U_1} + (\gamma - 1)U_3 \\ \gamma\frac{U_2}{U_1}U_3 - \frac{1}{2}(\gamma - 1)\frac{U_2^3}{U_1^2}) \end{bmatrix} \tag{6.54}$$

and direct evaluation of all partial derivatives in Eq. (6.52) gives the corresponding Jacobian matrix, i.e.,

$$\mathbf{A}(\mathbf{U}) = \begin{bmatrix} 0 & 1 & 0 \\ \frac{1}{2}(\gamma - 3)\left(\frac{U_2}{U_1}\right)^2 & (3-\gamma)\frac{U_2}{U_1} & (\gamma - 1) \\ -\gamma\frac{U_2}{U_1^2}U_3 + (\gamma - 1)\left(\frac{U_2}{U_1}\right)^3 & \gamma\frac{U_3}{U_1} - \frac{3}{2}(\gamma - 1)\left(\frac{U_2}{U_1}\right)^2 & \gamma\frac{U_2}{U_1} \end{bmatrix} \tag{6.55}$$

Inserting the conserved variables from Eq. (6.49) and using the total energy per unit volume ($E = \rho e + \frac{1}{2}\rho v^2$) and the EOS in Eq. (6.2), the Jacobian matrix can be written in terms of the speed of sound $c = \sqrt{\gamma RT} = \sqrt{\gamma\frac{p}{\rho}}$ and the particle velocity v. That is [88],

$$\mathbf{A}(\mathbf{U}) = \begin{bmatrix} 0 & 1 & 0 \\ \frac{1}{2}(\gamma - 3)v^2 & (3-\gamma)v & (\gamma - 1) \\ \frac{1}{2}(\gamma - 2)v^3 - \frac{c^2 v}{\gamma - 1} & \frac{3-2\gamma}{2}v^2 + \frac{c^2}{\gamma - 1} & \gamma v \end{bmatrix} \tag{6.56}$$

Using the definition of the specific enthalpy h in Eq. (6.3) and the EOS in Eq. (6.2) gives the total enthalpy as

$$H = \frac{E + p}{\rho} = \frac{1}{2}v^2 + \frac{c^2}{\gamma - 1} \tag{6.57}$$

and the Jacobian matrix in Eq. (6.56) can be expressed in terms of the total specific enthalpy H as

$$\mathbf{A}(\mathbf{U}) = \begin{bmatrix} 0 & 1 & 0 \\ \frac{1}{2}(\gamma-3)v^2 & (3-\gamma)v & (\gamma-1) \\ \frac{1}{2}(\gamma-1)v^3 - vH & H-(\gamma-1)v^2 & \gamma v \end{bmatrix} \tag{6.58}$$

It is interesting to note that the Jacobian matrix $\mathbf{A}(\mathbf{U})$, with the ideal gas EOS in Eq. (6.2), satisfies the following property

$$\mathbf{F}(\mathbf{U}) = \mathbf{A}(\mathbf{U})\mathbf{U} \tag{6.59}$$

This is observed by multiplying the Jacobian matrix $\mathbf{A}(\mathbf{U})$ in Eq. (6.58) by the vector of conserved variables $\mathbf{U}$ in Eq. (6.49), which reproduce the vector of fluxes $\mathbf{F}(\mathbf{U})$ in Eq. (6.49). This property of the Euler equations forms the basis for several numerical schemes involving approximate Riemann solvers. The reader is referred to the literature for more information regarding these numerical methods (see e.g. [88, 200, 207]).

The eigenvalues of the Jacobian matrix is now found from the characteristic polynomial

$$|\mathbf{A} - \lambda\mathbf{I}| = 0 \tag{6.60}$$

as

$$\lambda^0 = v \ , \quad \lambda^+ = v + c \ , \quad \lambda^- = v - c \tag{6.61}$$

representing linear curves with associated propagation velocities, known as characteristics C^i, in the $x-t$ plane. The superscripts $+$ and $-$ indicate the direction of propagation of the respective curves. A physical interpretation of the right- and left-running characteristics with corresponding velocities λ^+ and λ^- for the hyperbolic equations in Eq. (6.51) are shown in Figure 6.8.

Originating from an initial point $(x = x_0, t = t_0)$ in a 1D formulation, two waves run into positive and negative x-direction, respectively. In a 3D representation of the wave amplitude $\mathbf{U}(x,t)$ over the propagation direction x and t, the characteristics are lines connecting propagating wave points of constant amplitude [203]. The result in Eq. (6.61) therefore illustrates the important concept that the (pressure) wave speed is equal to the sum of the particle velocity v and the speed of sound c.

The corresponding right eigenvectors $\mathbf{k}^i$ are determined from

$$\mathbf{A}\mathbf{k} = \lambda\mathbf{k} \tag{6.62}$$

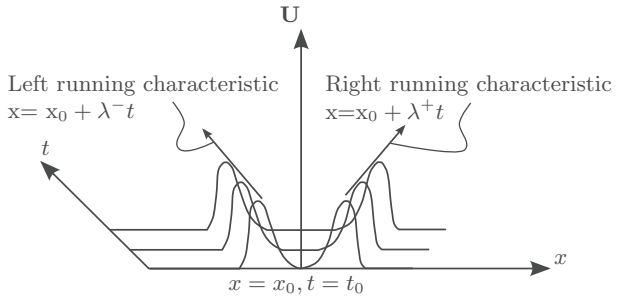

Figure 6.8: Physical interpretation of the real characteristics of hyberbolic equations as connecting lines between points of constant amplitude of propagating waves (inspired by [203]).

by substituting $\lambda = \lambda^i$ in turn and solving for each component i of the vector $\mathbf{k}$. Selecting appropriate values for the scaling factors, the eigenvectors read [88]

$$\mathbf{k}^0 = \begin{bmatrix} 1 \\ v \\ \frac{1}{2}v^2 \end{bmatrix} \quad , \quad \mathbf{k}^+ = \begin{bmatrix} 1 \\ v+c \\ H+cv \end{bmatrix} \quad , \quad \mathbf{k}^- = \begin{bmatrix} 1 \\ v-c \\ H-cv \end{bmatrix} \tag{6.63}$$

It is observed from Eqs. (6.61) and (6.63) that the eigenvalues are real and that the eigenvectors form a set of linearly independent eigenvectors. This shows that the Jacobian matrix $\mathbf{A}(\mathbf{U})$ is diagonalizable, i.e.,

$$\mathbf{A} = \mathbf{K}\mathbf{\Lambda}\mathbf{K}^{-1}, \qquad \mathbf{\Lambda} = diag\{\lambda^i\} \tag{6.64}$$

where the columns of the matrix $\mathbf{K} = [\mathbf{k}^0\ \mathbf{k}^+\ \mathbf{k}^-]$ are formed by the right eigenvectors $\mathbf{k}^i$. This proves that the time-dependent 1D Euler equations for ideal gases are hyperbolic (see e.g. [88, 200, 207]). The hyperbolic character of the system of equations in Eq. (6.51) contains important information on the propagation of waves in the flow field. Certain quantities, called Riemann invariants, are constant and transported along the characteristics C^i in the $x-t$ plane. The fluid properties are continuous along these characteristics. However, the derivatives of the fluid properties can be discontinuous [88]. The characteristic curves may therefore be considered as signals which transmit information (with associated propagation velocities) about infinitesimal flow disturbances in the $x-t$ plane. These signals contain important information on the propagation of waves in the flow field. From a numerical point of view, this suggests a convenient approach to calculate the solution in any point $P^*(x,t)$ by using the information transported through the characteristics starting from point P^* and going back to regions where the solution is already known (e.g. the initial condition). This approach is illustrated in Figure 6.9.

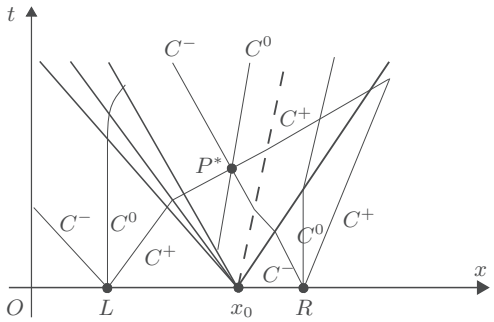

Figure 6.9: Characteristics used to calculate the Riemann solution (inspired by [208]).

Introducing the left eigenvector $\mathbf{a}^i$ of $\mathbf{A}$ corresponding to the respective eigenvalue λ^i (i.e., ${\mathbf{a}^i}^T\mathbf{A} = \lambda^i {\mathbf{a}^i}^T$) and multiplying Eq. (6.51) by ${\mathbf{a}^i}^T$ gives

$$ {\mathbf{a}^i}^T \left[\frac{\partial}{\partial t}\mathbf{U} + \lambda^i(\mathbf{U}) \frac{\partial}{\partial x}\mathbf{U} \right] = \mathbf{0} \tag{6.65} $$

This reduces each of these equations to an ordinary differential equation along the characteristic curve C^i whose slope in the $x-t$ plane are $dx/dt = \lambda^i$. Thus,

$$ {\mathbf{a}^i}^T \left[\frac{\partial}{\partial t}\mathbf{U} + \lambda^i(\mathbf{U}) \frac{\partial}{\partial x}\mathbf{U} \right] = {\mathbf{a}^i}^T \frac{d}{dt}\mathbf{U} = \mathbf{0} \quad \text{along} \quad C^i : \frac{dx}{dt} = \lambda^i \tag{6.66} $$

where the substantial (or material) derivative $d\mathbf{U}/dt$ is introduced. That is, the change of variation in time of the conserved variables $d\mathbf{U}/dt$ along the respective characteristic C^i, equals the variation of the conserved variables at a location fixed in space $\partial\mathbf{U}/\partial t$ plus the space variation of the conserved variables $\partial\mathbf{U}/\partial x$ multiplied by the velocity of the characteristic $\lambda^i = dx/dt$. The representation of the wave system in the $x-t$ plane is therefore also sometimes called a Lagrange diagram in the literature. That is, each individual variation in time of $\mathbf{U}$ follows the associated characteristic line in the $x-t$ plane.

The representation in Eq. (6.66) is known as the characteristic equations since the invariant r^i is constant (i.e., $d\mathbf{U}/dt = \mathbf{0}$) along the respective characteristic C^i, i.e.,

$$ \frac{dr^i}{dt} = \frac{\partial r^i}{\partial t} + \frac{\partial r^i}{\partial x}\frac{dx}{dt} = 0 \ , \quad \text{or} \quad \frac{\partial r^i}{\partial t} + \lambda^i \frac{\partial r^i}{\partial x} = 0 \tag{6.67} $$

The invariants can be generally expressed as differential relations (i.e., $\mathbf{a}^i d\mathbf{U}$),

given as [88]

$$dr^0 = dp - c^2\, d\rho = 0 \;\;,\quad dr^+ = dp + \rho c\, dv = 0 \;\;,\quad dr^- = dp - \rho c\, dv = 0 \tag{6.68}$$

where each of these relations have to be integrated along the corresponding characteristic curve C^i. In the particular case of an isentropic flow using the EOS in Eq. (6.2) the invariants of the 1D Euler equations read [88]

$$r^0 = \frac{p}{\rho^\gamma} \;\;,\quad r^+ = v + \frac{2c}{\gamma - 1} \;\;,\quad r^- = v - \frac{2c}{\gamma - 1} \tag{6.69}$$

These relations will be used in the following to derive the Riemann solution of the shock tube problem. It should also be noted that the characteristics may be formulated and solved using other variables than the conserved variables $\mathbf{U}$. Another possibility is to choose a vector $\mathbf{W} = [\rho\ v\ p]^T$ of primitive (or physical) variables, where p is as before given by the EOS. The quasi-linear form of Eq. (6.48) is then given as [88]

$$\frac{\partial}{\partial t}\mathbf{W} + \mathbf{A}(\mathbf{W})\frac{\partial}{\partial x}\mathbf{W} = \mathbf{0}\;,\;\; \mathbf{A}(\mathbf{W}) = \frac{\partial \mathbf{F}}{\partial \mathbf{W}} \tag{6.70}$$

where

$$\mathbf{W} = \begin{bmatrix} \rho \\ v \\ p \end{bmatrix} \;\;,\;\; \mathbf{A}(\mathbf{W}) = \begin{bmatrix} v & \rho & 0 \\ 0 & v & 1/\rho \\ 0 & \rho c^2 & v \end{bmatrix} \tag{6.71}$$

6.4.3 The Riemann solution to the shock tube problem

The objective of this section is to find the Riemann solution of the shock tube problem introduced in Section 6.4.1. The non-linear hyperbolic system of PDEs in Eq. (6.51) with the piecewise constant initial condition

$$\mathbf{U}(x,0) = \begin{cases} \mathbf{U_L}(\rho_4, \rho_4 v_4, E_4) & \text{if } x \le x_0 \\ \mathbf{U_R}(\rho_1, \rho_1 v_1, E_1) & \text{if } x > x_0 \end{cases} \tag{6.72}$$

define the Riemann problem for the shock tube [87, 88]. Thus, the Riemann solution gives the resulting wave pattern for a flow field with discontinuous initial data. The Riemann solution of the shock tube problem therefore follows the mathematical description given in Section 6.4.2, and provides a basic understanding of the governing equations in Eq. (6.51) because all properties (such as shock and rarefaction waves) appear as characteristics in the solution.

In the following, the mathematical description of the shock tube problem is simplified by considering an infinitely long tube (see Figure 6.10), neglecting viscous effects in the flow. Hence, the following only considers the incident

shock and expansion (i.e., rarefaction) waves and is not valid when reflections occur at the tube ends or at obstacles inside the tube. Even though this is an idealized case, it provides an understanding of the governing physics and phenomena in the shock tube. To study reflected wave patterns and pressures due to closed ends, it is often necessary with numerical simulations.

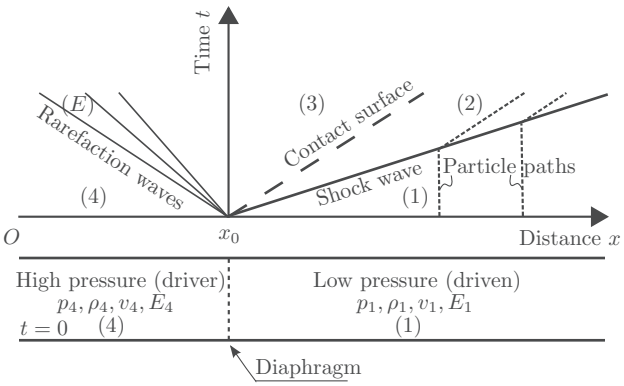

Figure 6.10: Simplified shock tube problem considering an infinitely long tube.

The diaphragm is positioned at x_0 and completely removed at $t = 0$. Under the assumption of no dissipative phenomena, the compressible flow in the shock tube is described by the 1D Euler equations in Section 6.4.2. The solution involves discontinuities, such as the shock wave and contact discontinuity, and smooth transition waves such as the rarefaction waves. This makes it convenient to separated the tube into four uniform regions with constant parameters (see Figure 6.10). The respective regions are separated by the waves centered and originating at the initial position of the diaphragm ($t = 0$, $x = x_0$). Regions 1 and 4 are given by the initial conditions in Eq. (6.72) and the two intermediate regions, occurring after the removal of the diaphragm, are denoted 2 and 3. An important part of the solution is to identify these regions in the $x - t$ plane. Since the shock and the contact discontinuity propagate in uniform zones (i.e., assuming no dissipative phenomena), the slope of these curves represent the (constant) velocity of each wave acting as lines in the $x - t$ plane. The expansion wave extends through the new zone E, denoted the expansion fan, in which the flow parameters vary continuously since the gas is rarefied when passing through E from 3 to 4. Remember that the shock wave and the contact discontinuity propagate to the right, while the expansion wave moves to the left (i.e., $\rho_4, \rho_4 v_4, E_4 > \rho_1, \rho_1 v_1, E_1$). As before, the subindices of the conserved variables refers to the respective regions (e.g. v_4 refers to the velocity in region 4).

The jump relations over the shock wave discontinuity in terms of the Mach

number $M_s(= v_s/c_1)$ are already introduced in Eq. (6.45) and Section 6.3.3. A similar expression may also be found for the particle velocity v_2 [125], i.e.,

$$\frac{v_2}{c_1} = \frac{2}{\gamma+1}\left(M_s - \frac{1}{M_s}\right) \tag{6.73}$$

where v_2 and v_s are constant (see Figure 6.10). These jump relations and the information propagated along the characteristics can then be used to find the Riemann solution.

First, recall from the previous section (Section 6.4.2) that the Riemann invariants make it possible to associate the parameters in regions 3 and 4 by considering a point P^* inside region 3 and going back along the characteristics to regions where the solution is already known (i.e., the initial condition). Figure 6.11a illustrates the characteristics passing through P^*, where it is noticed that C^0 and C^+ are the only characteristics intersecting the expansion fan to search for information in region 4.

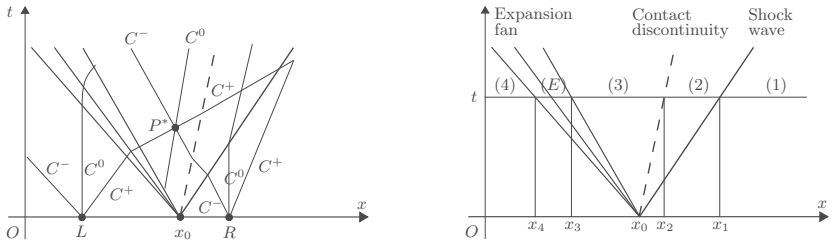

Figure 6.11: Illustration of the Riemann solution to the shock tube problem: (a) characteristics C^i and (b) $x-t$ diagram.

The relation between these regions are therefore given by the corresponding invariants r^0 and r^+ in Eq. (6.69) as

$$\frac{\rho_3}{\rho_4} = \left(\frac{p_3}{p_4}\right)^{1/\gamma} \quad \text{and} \quad v_3 = \frac{2}{\gamma-1}(c_4 - c_3) \tag{6.74}$$

where $v_4 = 0$ from the initial conditions and the solution is obtained by following the characteristics back to the curve on which initial data are prescribed to determine r^0 and r^+ in Eq. (6.69). It is also noticed that the first invariant r^0 is related to the isentropic relation presented in Section 6.2.5 and Eq. (6.34).

Moreover, recall that the contact surface is a jump in the density (see Section 6.4.1), while the pressure and velocity remain constant and continuous across

this discontinuity. Thus,

$$v_3 = v_2 \quad , \quad p_3 = p_2 \tag{6.75}$$

The solution in regions 2 and 3 are then found by combining Eqs. (6.73), (6.74) and (6.75), i.e.,

$$M_s - \frac{1}{M_s} = \frac{\gamma+1}{2}\frac{v_2}{c_1} = \frac{\gamma+1}{2}\frac{v_3}{c_1} = \frac{c_4}{c_1}\frac{\gamma+1}{\gamma-1}\left(1 - \frac{c_3}{c_4}\right) \tag{6.76}$$

Using that $c = \sqrt{\gamma p/\rho}$ and once again Eqs. (6.74)-(6.75), the ratio c_3/c_4 reads

$$\begin{aligned} \frac{c_3}{c_4} &= \left(\frac{p_3}{p_4}\frac{\rho_4}{\rho_3}\right)^{\frac{1}{2}} = \left(\frac{p_3}{p_4}\right)^{\frac{\gamma-1}{2\gamma}} \\ &= \left(\frac{p_2}{p_4}\right)^{\frac{\gamma-1}{2\gamma}} = \left(\frac{p_2}{p_1}\frac{p_1}{p_4}\right)^{\frac{\gamma-1}{2\gamma}} \end{aligned} \tag{6.77}$$

and replacing p_2/p_1 according to Eq. (6.45a), the solution to the shock tube problem in Eq. (6.76) may be expressed as the following implicit equation

$$M_s - \frac{1}{M_s} = \frac{c_4}{c_1}\frac{\gamma+1}{\gamma-1}\left[1 - \left(\frac{p_1}{p_4}\frac{2\gamma M_s^2 - (\gamma-1)}{\gamma+1}\right)^{\frac{\gamma-1}{2\gamma}}\right] \tag{6.78}$$

with the only unknown M_s. This non-linear equation can be solved by an iterative method (e.g. Newton-Raphson), and the value of M_s is then used in Eqs. (6.45), (6.73), (6.74) and (6.75) to determine all the parameters of the uniform regions 2 and 3. The result in Eq. (6.78) is also commonly expressed in the literature as [125]

$$\frac{p_4}{p_1} = \frac{2\gamma M_s^2 - (\gamma-1)}{\gamma+1}\left[1 - \frac{\gamma-1}{\gamma+1}\frac{c_1}{c_4}\left(M_s - \frac{1}{M_s}\right)\right]^{-\frac{2\gamma}{\gamma-1}} \tag{6.79}$$

which, by using the jump relation in Eq. (6.45a), may be expressed in terms of the shock strength as [202]

$$\frac{p_4}{p_1} = \frac{p_2}{p_1}\left[1 - \frac{(\gamma-1)\dfrac{c_1}{c_4}\left(\dfrac{p_2}{p_1} - 1\right)}{\sqrt{2\gamma\left(2\gamma + (\gamma+1)\left(\dfrac{p_2}{p_1} - 1\right)\right)}}\right]^{-\frac{2\gamma}{\gamma-1}} \tag{6.80}$$

Figure 6.12 shows the respective solutions in Eqs. (6.79) and (6.80) for the resulting Mach number M_s (Figure 6.12a) and shock strength p_2/p_1 (Figure 6.12b) at given initial conditions of p_4 and p_1.

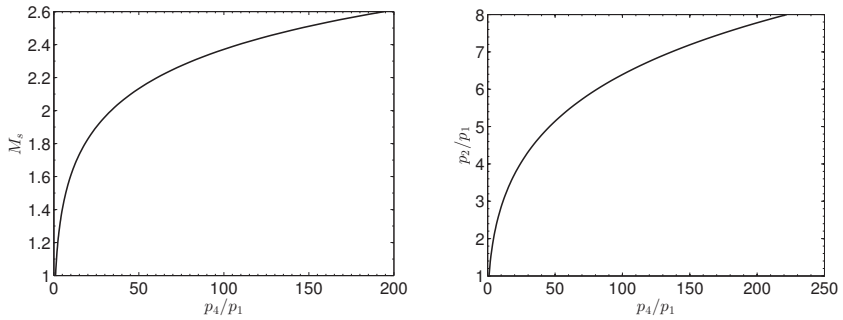

Figure 6.12: Riemann solution to the shock tube problem as a function of the initial conditions p_4/p_1: (a) Mach number M_s in Eq. (6.79) and (b) the shock strength p_2/p_1 in Eq. (6.80). Note that these solutions are only valid for $t < t_\mathrm{b}$ in Figures 6.6 and 6.7.

It is emphasized that the solutions in Eqs. (6.79) and (6.80) are only valid until the formation of the blast wave in Figures 6.6 and 6.7 (i.e., for $t < t_\mathrm{b}$).

To complete the solution, it is necessary to determine the range of each region, i.e., to calculate the values of the abscissas x_1, x_2, x_3 and x_4 in Figure 6.11b for a given time t. Starting with the expansion fan E (see Figure 6.11a), it is observed that this is left-bounded by the C^- characteristic starting from the point x_0 and considered to belong to region 4 (i.e., the line of slope $dx/dt = v_4 - c_4 = -c_4$). The right bound of the expansion fan is the C^- characteristic starting from the same point x_0, however, now considered to belong to region 3 (i.e., the line of slope $dx/dt = v_3 - c_3$). Thus, according to Eq. (6.61), the values of x_4 and x_3 are given as

$$x_4 = x_0 - c_4 t \quad , \quad x_3 = x_0 + (v_3 - c_3)t \tag{6.81}$$

Note that if $v_3 > c_3$, i.e., v_3 is supersonic, the tail of the rarefaction wave propagates to the right although the front of the wave is left-running.

Now, considering a point (x, t) inside the region E ($x_4 \leq x \leq x_3$), the properties of the expansion fan can be established. Since this point belongs to the C^- characteristic starting from x_0, Eq. (6.61) states that

$$\frac{dx}{dt} = \frac{x - x_0}{t} = v - c \tag{6.82}$$

Using the C^+ characteristic from point L and the corresponding invariant r^+

(i.e., $v_4 + 2c_4/(\gamma-1) = v + 2c/(\gamma-1)$), it further observed that

$$c_4 = c + \frac{\gamma-1}{2}v \tag{6.83}$$

Combining the last two equations and remembering the relations from Eq. (6.74) and Eq. (6.77), the solution inside the expansion fan is given by

$$\begin{gathered} v = \frac{2}{\gamma+1}\left(c_4 + \frac{x-x_0}{t}\right)\ ,\ c = c_4 - (\gamma-1)\frac{v}{2}\ , \\ p = p_4\left(\frac{c}{c_4}\right)^{\frac{2\gamma}{\gamma-1}}\ ,\ \rho = \rho_4\left(\frac{p}{p_4}\right)^{\frac{1}{\gamma}} \end{gathered} \tag{6.84}$$

Since the contact discontinuity is transported at constant velocity $v_3 = v_2$, its location is given by

$$x_2 = x_0 + v_2 t = x_0 + v_3 t \tag{6.85}$$

where v_2 is found from Eq. (6.73) since M_s is known from Eq. (6.78). Finally, the shock wave propagating at constant velocity v_s is located at

$$x_1 = x_0 + v_s t \tag{6.86}$$

From this it is shown that the solution $\mathbf{U}(x,t)$ of the shock tube problem is only dependent on the ratio x/t, and is therefore commonly expressed in the $x-t$ plane in the literature.

6.4.4 Reflected shock waves from a rigid wall

Upon reaching a closed end of the tube, the incoming shock wave reflects and travels back toward the left (Figure 6.13a). The gas particles behind the reflected wave have zero velocity, resulting in a build-up of pressure p_5 immediately behind the reflected wave which is significantly greater than that of the incoming wave. The reflected shock wave can therefore be interpreted as an extending column which advances from the right end of the tube containing a static gas at high pressure, density and temperature. The speed of the reflected shock v_r is reduced on its way through the subsequent flow behind the incident shock wave. This is due to resistance from the induced flow behind the shock wave, i.e., flow in region E in Figure 6.13a. The flow in region E gives up its kinetic energy on passing through the front v_r and into the region of the reflected shock (i.e., region 5 in Figure 6.13a where $v_5 = 0$). The result is a further compression and heating of the gas in region 5.

The reflected pressure can be expressed in terms of the shock strength of the

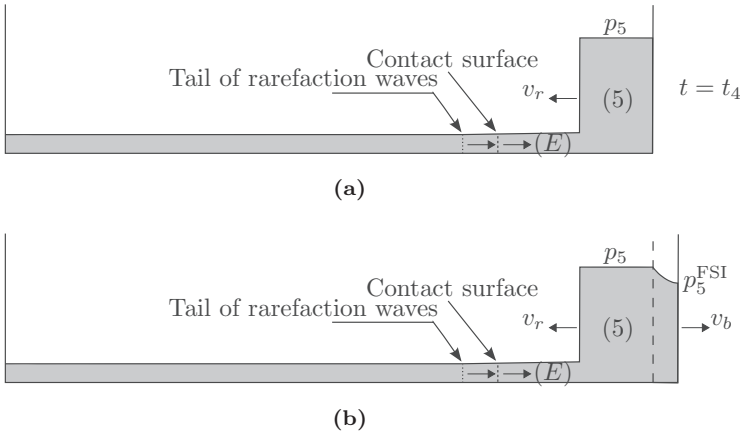

Figure 6.13: Schematic representation of the reflected pressure and the corresponding distributions along the longitudinal axis of the tube: (a) reflection of incoming shock wave from rigid boundary and (b) reflection of incoming shock wave at moving boundary.

incoming shock wave [125], i.e.,

$$p_5 = p_2 \left(\frac{\dfrac{\gamma+1}{\gamma-1} + 2 - \dfrac{p_1}{p_2}}{1 + \dfrac{\gamma+1}{\gamma-1} \cdot \dfrac{p_1}{p_2}} \right) \tag{6.87}$$

and the corresponding overpressure reads

$$p_{\mathrm{r,max}} = p_5 - p_1 = p_{\mathrm{so,max}} \left(\frac{\left(2 \cdot \dfrac{(\gamma-1)}{\gamma+1} + 1 \right) + \dfrac{p_1}{p_2}}{\dfrac{\gamma-1}{\gamma+1} + \dfrac{p_1}{p_2}} \right) \tag{6.88}$$

where we recall that the notation $p_{\mathrm{r,max}}$ is used for the peak reflected (head-on) overpressure. The shape of the reflected pressure-time history depends on the shape of the incoming wave and the relative strength between the left-running reflected shock wave and the remaining right-running flow behind the incoming shock wave (i.e., region E in Figure 6.13).

The jump in temperature may be found by using the speed of sound and expressing ρ_5/ρ_2 in terms of the jump conditions similar to that in Eq. (6.44b), i.e.,

$$\frac{\rho_5}{\rho_2} = \frac{\dfrac{\gamma-1}{\gamma+1} + \dfrac{p_5}{p_2}}{\dfrac{\gamma-1}{\gamma+1}\dfrac{p_5}{p_2} + 1} \tag{6.89}$$

From the ideal gas law $c = \sqrt{\gamma \frac{p}{\rho}} = \sqrt{\gamma RT}$ and the temperature ratio T_5/T_2 may be expressed as

$$\frac{T_5}{T_2} = \frac{c_5^2}{c_2^2} = \frac{\gamma p_5}{\rho_5}\frac{\rho_2}{\gamma p_2} = \frac{p_5}{p_2}\frac{\rho_2}{\rho_5} = \frac{p_5}{p_2}\frac{\dfrac{\gamma-1}{\gamma+1}\dfrac{p_5}{p_2} + 1}{\dfrac{\gamma-1}{\gamma+1} + \dfrac{p_5}{p_2}} \tag{6.90}$$

These last three equations enable the state of the gas behind the reflected shock to be determined from the pressure ratio p_2/p_1 across the incident shock, which may be obtained through Eq. (6.45) and the Mach number M_s. The relations of the pressure, density and temperature behind the reflected shock in terms of the incident Mach number, are then given respectively as [125]

$$\frac{p_5}{p_1} = \left[\frac{2\gamma M_s^2 - (\gamma-1)}{\gamma+1}\right]\left[\frac{(3\gamma-1)M_s^2 - 2(\gamma-1)}{(\gamma-1)M_s^2+2}\right] \tag{6.91}$$

$$\frac{\rho_5}{\rho_1} = \frac{\left[(\gamma+1)M_s^2\right]\left[2\gamma M_s^2 - (\gamma-1)\right]}{\left[2(\gamma-1)M_s^2 - (\gamma-3)\right]\left[(\gamma-1)M_s^2+2\right]} \tag{6.92}$$

$$\frac{T_5}{T_1} = \frac{\left[2(\gamma-1)M_s^2 + (3-\gamma)\right]\left[(3\gamma-1)M_s^2 - 2(\gamma-1)\right]}{(\gamma+1)^2 M_s^2} \tag{6.93}$$

It is interesting to note that all the parameters behind the reflected shock are limited to finite values. In the particular case of weak shocks, i.e., $p_2/p_1 \approx 1$, Eq. (6.88) gives $p_{\mathrm{r,max}}/p_{\mathrm{so,max}} = 2$. This represents the lower limit of the reflected overpressure, and is the same result as the reflected pressure in elastic waves. However, as discussed in Section 6.3.2, the elastic wave theory is not valid for strong shocks. Eq. (6.88) shows that the reflected overpressure to incident overpressure ratio increases steadily with shock strength tending asymptotically to the value $2 + (\gamma+1)/(\gamma-1)$ for very strong shocks. This upper limit is 8 for air ($\gamma = 1.4$), whereas for monatomic gases such as helium ($\gamma = 5/3$) the upper limit is 6. The results for strong shocks therefore illustrate the different behaviour of shock waves compared to that of elastic waves.

It should be emphasized that the relations in Eqs. (6.91) to (6.93) are only

valid for the state immediately behind the reflected wave. This state will persist until the left-running front v_r meets the remaining right-running flow in region E (Figure 6.13a). Then, the interaction of these waves are depending on their relative strength. The wave fronts and interaction of waves will continue back and forth in the tube until a static overpressure p_{static} is reached when the gas comes to rest. The relevant timescale of the experiments depends on the application and therefore limits the time-window of interest. The static overpressure p_{static} may be found by considering the energy balance before and after the experiment [15], i.e.,

$$E_4 + E_1 = E_{\text{static}} \ , \quad E = \frac{pV}{\gamma - 1} \tag{6.94}$$

where E is the total energy in the volume V.

6.4.5 Reflected shock waves from a moving wall

Introducing a moving wall as the blind flange of the tube (see Figure 6.13b) enables studies of the interaction between the reflected shock wave and the dynamic response of the boundary. Such a moving wall could be visualized as a free-standing plate. A basic understanding of the FSI effects when the shock wave interacts with a movable surface is given in the works of Courant and Friedrichs [87], Toro [88] and Subramaniam et al. [72]. The solution depends on the ratio of the velocity of the moving wall v_b and the velocity behind the reflected wave v_5 [88]. This is illustrated in Figure 6.14, where $v_5 < v_b$ results in two rarefaction waves (Figure 6.14a) and $v_5 > v_b$ implies two shock waves (Figure 6.14b). The scope of this chapter is limited to the case resulting in two rarefaction waves, since $v_5 = 0$ in the experimental setups considered.

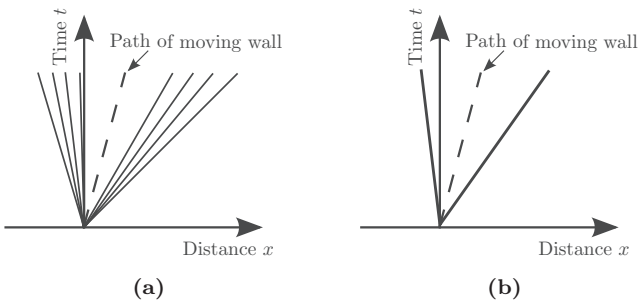

Figure 6.14: Riemann solution to a shock tube with a moving wall. Contact interface coincides with the moving wall: (a) solution consists of two rarefactions ($v_5 < v_b$) and (b) the solution consists of two shock waves ($v_5 > v_b$). This figure was inspired by [88].

The velocity of the contact interface (or path of the moving wall) in Figure 6.14a coincides with the velocity of the moving wall v_b. Remember that rarefaction waves are related to the C^- characteristic and corresponding invariant r^- in Eq. (6.69). The two rarefaction waves are therefore related through

$$v_b - \frac{2c_b}{\gamma - 1} = v_5 - \frac{2c_5}{\gamma - 1} \tag{6.95}$$

where it is assumed that $\gamma_5 = \gamma_b = \gamma$. After some mathematical operations Eq. (6.95) can be written as

$$\frac{\gamma - 1}{\gamma + 1} \frac{(v_b - v_5)}{c_5} = \frac{2}{\gamma + 1} \left(\frac{c_b}{c_5} - 1 \right) \tag{6.96}$$

Using $c = \sqrt{\gamma \frac{p}{\rho}}$ and the isentropic relation in Eq. (6.34) give

$$\frac{c_b}{c_5} = \left(\frac{\rho_b}{\rho_5} \right)^{\frac{\gamma - 1}{2}} \tag{6.97}$$

Now, inserting the result in Eq. (6.97) into Eq. (6.96), and using Eq. (6.34), this reads

$$\begin{aligned} \frac{\gamma - 1}{\gamma + 1} \frac{(v_b - v_5)}{c_5} &= \frac{2}{\gamma + 1} \left[\left(\frac{\rho_b}{\rho_5} \right)^{\frac{\gamma - 1}{2}} - 1 \right] = \\ &= \frac{2}{\gamma + 1} \left[\left(\frac{p_b}{p_5} \right)^{\frac{1}{\gamma} \frac{\gamma - 1}{2}} - 1 \right] \end{aligned} \tag{6.98}$$

Finally, solving Eq. (6.98) for the pressure p_5 at the surface of the boundary, it is observed that the velocity v_b and pressure p_b at the moving wall are related through the following relation

$$p_b = p_5 \left(1 + \frac{\gamma - 1}{2} \cdot \frac{v_b}{c_5} \right)^{\frac{2\gamma}{\gamma - 1}} \tag{6.99}$$

where we recall that $v_5 = 0$. Thus, if the structure starts to move, the motion alters the pressure at its surface. In particular, when the motion of the boundary is in the opposite direction to the reflected shock front in Figure 6.13b, there will be a decrease in pressure and a mitigation of the shock wave due to FSI effects (i.e., $p_b < p_5$). Eq. (6.99) therefore gives a basic understanding of the underlying physics of FSI in a shock tube when a moving or deformable object is used as a blind flange. It is emphasized that, as the complexity of the system increases, numerical methods should be used to solve these types of interaction phenomena and wave patterns.

6.4.6 Real shock tube behaviour and performance

The results in this chapter are derived from ideal gas conditions (i.e., particle interactions do not play a significant role), assuming an instantaneous diaphragm rupture and no dissipative phenomena (e.g. viscocity and heat). In the absence of dissipative phenomena, chemical reactions and particle interactions, the shock wave preserves a constant velocity. However, the existence of these phenomena will change the equilibrium in the thermodynamic relations presented herein.

As already pointed out earlier, real gas effects and chemically reacting mixtures of perfect gases are considered as beyond the scope of this thesis. Such effects can be of importance in blast events and close-in detonations, and the reader is referred to the literature (see e.g. [124, 125, 202]) for a more detailed presentation of these effects. However, as a rule of thumb one may state that shock temperatures larger than 1000 K and pressures stronger than 1 MPa introduces additional degrees of freedom in the air molecules (i.e., air ionizes and dissociates), and the ratio of specific heats is no longer constant and must be modified to allow for these effects. Typically, experiments have shown that for shocks with velocities larger than about 3.5 of the speed of sound (i.e., hydrostatic pressures of about 1.4 MPa), the assumption of a calorically perfect gas leads to an error of more than 1 %. For shocks with velocities greater than about 5.5 of the speed of sound (i.e., hydrostatic pressures of approximately 3.5 MPa), the error is more than 5 % [145].

The state of a shocked gas in a shock tube is therefore not completely described by the idealized theory presented herein. Moreover, even if the real gas properties are known, other phenomena such as diaphragm rupture and boundary (or friction) effects cause deviations from the idealized theory and must be considered when evaluating the shock tube experiments and performance. Experiments show that failure of the diaphragm often initiates at the centre and propagates to the edges during tearing and folding of the petals [123]. The gas flow therefore starts as a jet and increases in diameter as the diaphragm opens until the cross-section of the tube is completely filled. The shock wave is formed due to the coalesce and overtaking of compression waves during this opening process. The imperfect burst of a shock tube diaphragm results in multi-dimensional disturbances that can significantly modify the flow field predicted by the idealized 1D theory and a complete opening is seldom observed in experiments. Despite this disturbance in the flow field, experimental work shows that most of the disturbances related to the diaphragm opening process vanish in the distant flow field (i.e., at distances larger than $10 \times$ diameter) [123]. Due to the higher temperature and flow velocity in the compressed gas, post-shock waves move faster than the leading shock and eventually coalesce into

the single shock front in Figure 6.6b (see also Figure 6.3).

Therefore, the assumption of an instantaneous diaphragm burst in analytical and numerical studies does not introduce any relevant error in the prediction of a normal shock wave in the distant flow field. However, the distant flow field is characterized by the occurrence of a normal shock front of constant strength whose intensity is lower than that expected from the 1D theory (i.e., a complete and instantaneous opening of the diaphragm). Thus, when considering shock tube performance at distances larger than 10 $\times$ diameter downstream the diaphragm, the effect of diaphragm opening may be limited to the reduced strength of the leading shock compared to the expected strength from the 1D theory. Recent numerical and experimental work [119] on shock tube performance using steel diaphragms suggests that the deviation from the idealized theory in terms of loss in intensity of the reflected pressure could be in the range of 50-60 %.

Even though the diaphragm dynamics play a negligible role in the distant flow field, experimental evidence often reveals a shock attenuation (i.e., decreasing velocities) at distances larger than 10 $\times$ diameter downstream the diaphragm. Experiments indicate that the shock does not travel at constant velocity in the distant flow field but tends to decelerate. At the same time the contact discontinuity may be accelerated. These effects are due to dissipative phenomena introduced by viscous forces resulting from the relative motion between the gas and the interior walls of the tube. A boundary layer is formed with a thickness which varies from zero at the shock front to a maximum at the contact discontinuity. In well-designed shock tubes with limited friction at the side walls, the effects of viscous attenuation is small [124]. The most severe contribution to shock attenuation is usually due to the reflected rarefaction waves catching up with the shock wave due to small driver to driven length ratios (illustrated in Figure 6.6d).

A further description of these real effects are beyond the scope of this thesis. However, it should be noted that even though the relations in this chapter are derived for ideal gas conditions, the theory and principles presented herein give a fundamental understanding of the underlying physics of the shock tube problem. Moreover, the shock attenuation observed in experiments are most evident when predicting the shock parameters based on the initial conditions using Eqs. (6.79) and (6.80). The shock attenuation effects are not that important when measuring the velocity in the vicinity of the plate, and it is possible to calculate the shock parameters with high accuracy by using the Mach number M_s and Eqs. (6.45), (6.73) and Eqs. (6.91) to (6.93). This is useful since this velocity can easily be measured in the experiment.

7

The SIMLab Shock Tube Facility

Chapter 6 introduced the shock tube as an alternative to explosive detonations when studying the dynamic response of flexible structures and fluid-structure interaction effects in blast environments. Shock tubes produce shock waves under controlled laboratory conditions, where the shock strength is determined by the initial conditions. It was therefore decided to establish such a test facility at SIMLab, NTNU. This chapter presents the premises and design of the SIMLab Shock Tube Facility (SSTF). The shock tube presented herein is developed for blast applications where the properties of a planar shock wave acting on a structure may be studied by placing a test object inside or at the end of the tube. Finally, two different camera models to be used in the 3D-DIC analyses are evaluated to ensure an accurate calibration of the mathematical relation between the target and image coordinates. The shock tube design presented in this chapter is also presented in the second paper published in International Journal of Protective Structures [209].

7.1 Introduction

Shock tube designs are typically specialized according to the application, and the literature reveals a rather widespread use of the shock tube as a research tool (see e.g. [123]). Tube length and internal cross-section shape and area are therefore determined by the particular application and, of course, the funds available. The test time, driving method and temporal distribution of the pressure are dependent on the driver and driven section lengths (see Section 6.4.1). Choice of tube internal cross-section geometry is typically influenced by the desired flow conditions, dimensions of the test specimens, and the type of instrumentation to be used for flow measurement.

Use of optical techniques (such as high-speed cameras and schlieren photography) is simplified with rectangular or square tube cross-sections which can

accommodate plane parallel windows. However, rectangular and square cross-sections are inferior to the circular cross-section when considering structural strength and general ease of construction and sealing [123]. The circular cross-section is preferable from a structural viewpoint, particularly for the driver section of the tube. This may be combined with a square driven section using a transition from a circular to a square shape at or downstream the diaphragm(s). For high-pressure applications, the structural limitations of the square cross-section may then be overcome by encasing it in a pipe with a practically incompressible material.

The European [210] or ASME standards for Unfired Pressure Vessels and traditional design methods for material strength ensure sufficient static strength of the tube sections. However, the most severe stress conditions arise from transient loadings during the operation of the tube. High-pressure loading of the low-pressure section(s) typically results from reflection of the incident shock wave (see Sections 6.4.1 and 6.4.4). Eq. (6.88) shows that the (initial) reflected overpressure to incident overpressure ratio increases steadily with shock strength tending asymptotically to the value $2 + (\gamma + 1)/(\gamma - 1)$ for very strong shocks. For air ($\gamma = 1.4$) the upper limit is 8, whereas for monatomic gases such as helium ($\gamma = 5/3$) the upper limit is 6. However, depending on the properties of the remaining right-running flow (illustrated in Figure 6.13a) additional compression and heating of the reflected shock wave may result in a further pressure increase of the order of 20 (see e.g. [123–125]). The transient stressing of the material usually reduces to an estimation of what is considered an adequate safety factor over the expected maximum static loadings. The influence of the recoil induced in the gas during diaphragm burst and momentum changes in the gas (when the gas comes to rest during reflections at the closed ends) depend on the tube diameter. Impulsive loads in the tube and supports which restrain axial movement may be neglected for small diameters, while limited recoil and axial movement may be desirable to avoid excessively transient stressing for larger diameters and high driver pressures. More detailed information on shock tube design may be found in Ref. [123].

Based on the general design and construction aspects discussed hitherto, the following premises were established for the SIMLab Shock Tube Facility (SSTF):

- The overall design was limited by the dimensions of the location where the shock tube was installed. The height, width and length of the room are 3.0 m, 4.0 m and 23.5 m, respectively.
- The shock tube diameter depends on the dimension of the test specimens. The design should enable mounting of test specimens either inside or at the end of the tube. A literature review [44, 65, 103, 113, 114, 116, 117, 211, 212]

indicated that the dimensions of blast-loaded plates are typically in the range of 0.1 to 0.6 m. Moreover, internal reflections may interfere with the flow field around test specimens located inside the tube. A rule of thumb for minimizing this effect is that the area of test specimens located inside the tube should be less than approximately 10 % of the cross-sectional area (see e.g. [213]). It was therefore decided to use a constant cross-section area throughout the tube and a square geometry of 0.3 m $\times$ 0.3 m downstream the diaphragm.

- Since the shock tube was installed at the University campus it was decided to used compressed air rather than high-explosives to generate the shock wave. Experimentation with high-explosives involves legal restrictions which often make such experiments less available for research and educational purposes.
- An important part of the design is the possibility to rearrange the facility without to much machinery. Each part of the modular design must be movable, i.e., both with respect to weight and location.
- The design should facilitate several driver lengths and a wide range of firing pressures such that the temporal pressure distribution may be varied. This implies both uniform and exponential decaying pressure profiles.
- Pressure magnitudes should be sufficient to damage a wide range of plated structures of different materials (e.g. glass, concrete and metals).
- A certain number of ports and threaded holes must be provided along the tube to monitor the filling of the driver, venting of the driver and measurement of the pressure throughout the driven section during testing. Windows should be installed for optical measurements.
- The design should be performed according to the requirements in the European standard EN 13445 [210]. Tolerances on the tube geometry and alignment follow the requirements in ISO 2768-1 [214].

7.2 Shock tube design

The SSTF consists of several parts joined together using bolted connections of 24 M24 socket-head screws at the end flanges of each part (see Figures 7.1 and 7.2). Rubber O-rings are recessed into the flange surfaces to ensure sealing at the joints. Each part is equipped with steel wheels and is carried by a two-rail support of L-shaped angle brackets for convenient assembly and disassembly of the tube. This provides flexibility in varying the length of the driven section. If necessary, it is also possible to fully restrain the tube from axial movement

by clamping the rear end of the driver section to the floor. The overall length of the tube is 18.355 m and it is made from stainless steel of grade P355NH which is intended for pressure purposes according to the European standard EN 13445 [210].

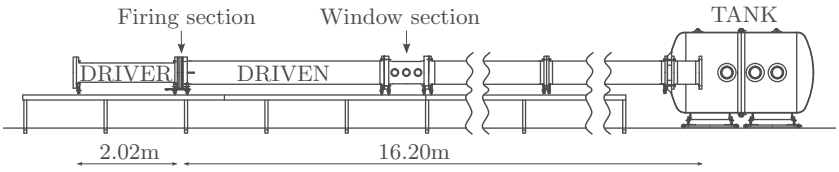

Figure 7.1: Sketch of the SIMLab Shock Tube Facility (seen from the side).

The driver section (Figure 7.1 and 7.2a) is manufactured with a total length of 2.02 m and has an inner diameter of 0.331 m where the internal wall is dull polished to obtain a smooth surface. Aluminium inserts may be used to vary the length of the driver section in 0.25 m increments. The driver is followed by a 0.14-m-long firing section which consists of several intermediate pressure chambers separated by diaphragms (Figure 7.2b). This enables the total pressure difference between the driver and driven sections to be achieved stepwise. Several ports have been machined on the driver flange and circumference of the firing section to provide connections to pressure sensors, venting, and evacuation lines. The experiment starts by filling the driver and firing sections with compressed air, where the pressures in the intermediate chambers are operated below the diaphragm rupture strength such that the desired pressure p_4 is obtained in the driver. A LabVIEW program has been developed and solenoid valves (ASCO Series 223) are installed on the gas-filling lines to control the filling process, making this operation fully automated based on signals given by the pressure sensors (BAUMER PBMN-24B31) monitoring the driver and intermediate pressure chambers. Rupture of the diaphragms is initiated by controlled and rapid venting of the intermediate pressure closest to the driver section (see Figure 7.3), using two solenoid valves (ASCO Series 223). This ensures a controlled rupture of the diaphragms and reproducible bursting pressures. The bursting pressure may be varied by changing the thickness of the diaphragms. Melinex sheets are used as diaphragms due to its strength and repeatability. It is also possible to use metallic diaphragms if required.

The inner cross-section in the driven section starts with a 0.6-m-long transition region from circular to a square cross-section, where an epoxy material is used to obtain a smooth surface and a square cross-section of 0.3 m $\times$ 0.3 m inside the surrounding tube (Figure 7.2c). The epoxy material works as a practically incompressible material while the surrounding tube ensures the structural strength. The square cross-section downstream the firing section was chosen to

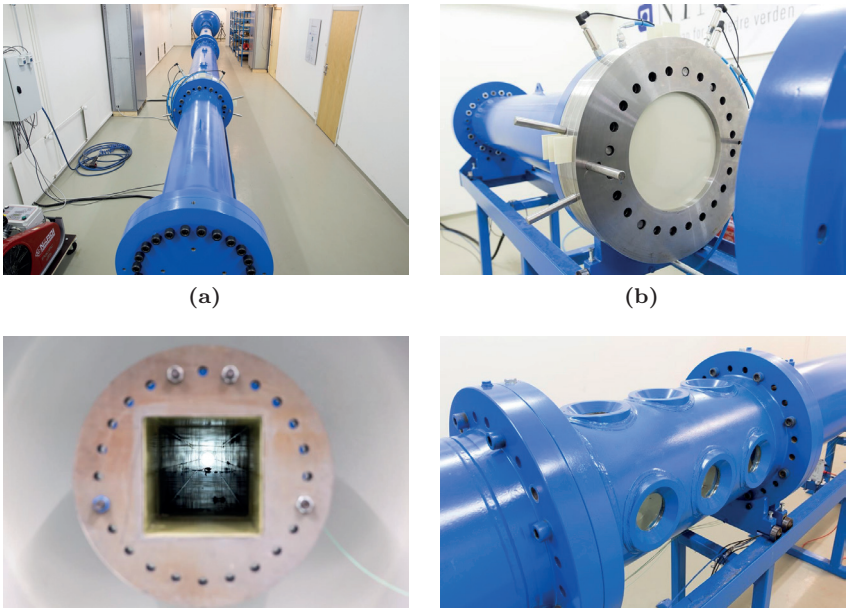

Figure 7.2: Pictures of the SIMLab Shock Tube Facility: (a) overview (seen from the driver), (b) firing section (seen from the driven section), (c) internal cross-section driven section (seen from the tank) and (d) window section.

enable the installation of test objects in threaded holes in the tube floor, and to accommodate plane parallel windows (see window section in Figure 7.2d) which simplifies the use of optical techniques (such as high-speed cameras).

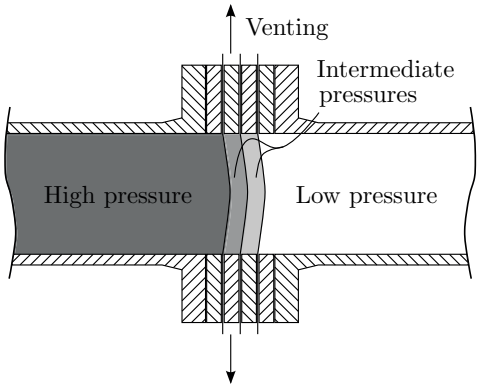

Figure 7.3: Cross-sectional view of the firing section immediately before firing.

The driven section ends in a tank of 5.1 m^3 with an internal diameter of 1.6 m

(see Figures 7.1, 7.2a and 7.4). This enables mounting of larger test specimens (exposed to localized blast loading) at the end of the tube, and an increase in volume and overall decrease in pressure after the experiment in open-end configurations.

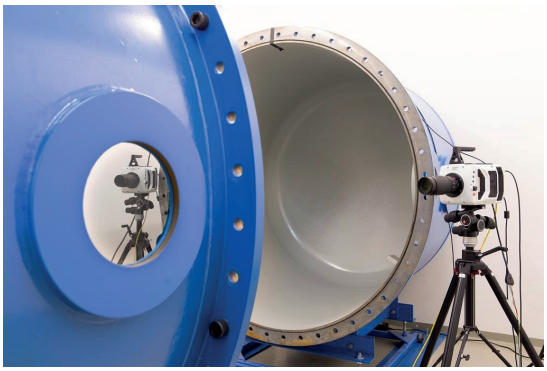

Figure 7.4: Picture of the tank located at the end of the tube. High-speed cameras may be placed next to the tank for optical measurements.

Piezoelectric pressure sensors (Kistler 603B), corresponding charge amplifiers (Kistler 5064) and data acquisition system from National Instruments (NI USB-6356) are used to measure the pressure downstream the firing section. The mounting of pressure sensors are possible at 20 locations along the driven section by using threaded adapters (Kistler 6501) flush mounted with the internal wall of the tube. A thin layer of insulating silicone (Kistler 1051) is used to shield the pressure sensors against heat transfer from the shock wave since the sensors are only designed for temperatures up to 200 °C.

The maximum working pressure of the driver section is limited to 17 MPa while the driven section, window section and tank are limited to 10, 5 and 1.4 MPa, respectively. All respective parts of the SSTF have been tested at a static pressure 45 % higher than the working pressure for a few minutes to ensure sufficient strength for routine use.

The project timeline started with preliminary studies and planning in October 2012, before the work with the detailed design and construction drawings started in January 2013. This was carried out in collaboration with Siving Olav H. Fismen AS. The final design and drawings were approved by Teknologisk Institutt AS in February 2014. Heimdal Industriservice AS and Risør Plast AS carried out the construction between April and September 2014, before the shock tube facility was installed at NTNU in September 2014. The first experiment was performed in October 2014.

7.3 3D-DIC technique

A three-dimensional digital image correlation (3D-DIC) technique may be used to capture displacement and strain fields of flexible test specimens as well as the axial movement of the entire facility during testing. This is the same technique as that used in **Part II** and Section 3.2.3 of this thesis. An important premise for a successful 3D-DIC analysis is an accurate calibration of the camera models, i.e., the mathematical relation between 3D target coordinates and image coordinates. It was therefore performed a more detailed evaluation of the available camera models prior to the shock tube testing of the deformable plates. This was accomplished by positioning two Phantom v1610 high-speed cameras with 100 mm Nikon lenses in the same stereovision setup to be used in the experiments with deformable plates (see Section 8.2.1).

The camera models were calibrated by recording a set of image pairs of calibration targets with known geometries. These images were used to extract a set of corresponding image and target coordinates which served as the input for the camera-model optimization. The calibration targets were located at the end of the tube (Figure 7.5), where two different calibration targets were applied to find the most suitable calibration procedure for this particular setup, i.e., a cylinder with 80-mm diameter and a 10-mm-thick glass plate. 16 image pairs of the glass-plate target and 8 image pairs of the cylinder target were recorded. The calibration targets were translated and rotated between each recording. Checkerboard patterns with squares of 6.527 mm and 4.669 mm were printed on the surface of the cylinder and glass plate, respectively. The corners of the checkerboard pattern were found for each image using a corner detection algorithm [215], and 14 camera model parameters (including radial and decentring distortions) were optimized for each camera following a calibration procedure based on the work by Heikkilä [216]. The optimization procedure incorporates a non-linear least-squares algorithm to minimize the difference between extracted image corner coordinates and the corresponding image coordinates calculated from known 3D target coordinates.

From the 16 glass-plate images, approximately 14,000 calibration points were extracted and used in the least-squares optimization for both cameras. The calibration points covered a volume of approximately 350 mm × 350 mm × 80 mm. The standard deviation of the camera model residuals in the XY-plane was 0.050 pixels (0.025 mm) for Camera 1 and 0.055 pixels (0.03 mm) for Camera 2. To evaluate the stereovision model, i.e., the coupling of the two camera models, a 3D model of the glass plate was calculated for each image pair using the extracted corners and the optimized camera models. The deviations of this 3D model compared to an exact plane were then calculated for each extracted

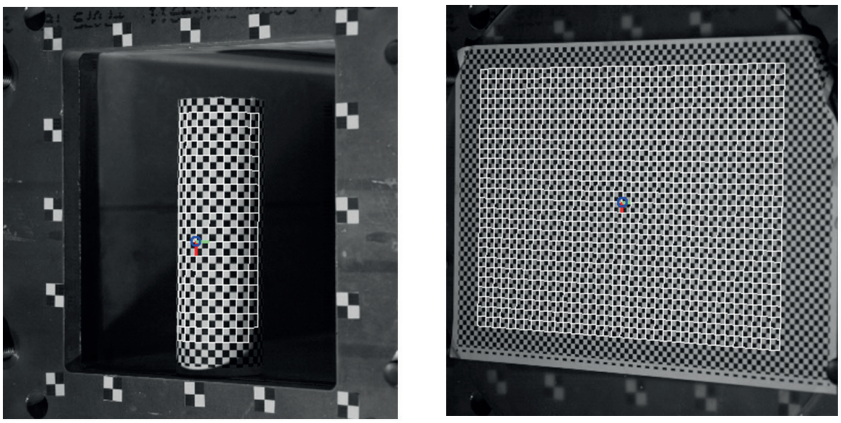

(a) (b)

Figure 7.5: Pictures of the calibration targets. Both images show meshes were the nodes represent extracted corners (with known target coordinates) that are used for camera calibration: (a) cylindrical calibration target and (b) glass-plate calibration target.

corner. For all 16 image pairs, the standard deviation of the calculated errors was less than 0.05 mm. These minor residual errors seem to be a combination of systematic errors and random noise. It is not clear whether the systematic part of these resultant errors arise from inaccuracies in the calibration target or lens distortions. However, for the particular tests considered in this thesis, these levels of errors are regarded as acceptable.

From the 8 cylinder images, approximately 6000 calibration points were extracted for each camera and used for optimization. Here, the covered volume was approximately 250 mm $\times$ 250 mm $\times$ 60 mm. The standard deviation of the camera model residuals in the XY-plane was 0.11 pixels (0.06 mm) for both cameras. Similarly, as for the glass plate, the resulting stereovision model from the cylinder target was checked against an exact plane. The standard deviation of the errors in the calculated 3D model (compared to an exact plane) was found to be 0.07 mm.

This implies that the glass-plate target provided slightly better calibration residuals compared to the cylinder target. This is probably because it is somewhat more challenging to create a cylinder with a checkerboard pattern with the same accuracy as a planar target. Moreover, the checkerboard pattern extraction from a curved surface may not be ideal. However, the cylinder target provides some additional features compared to a plane target. The non-coplanar calibration points from a cylinder allow a full camera model to be optimized from a single image, whereas the coplanar calibration points from

a single glass-plate image causes singularities in the solution that needs special attention [217]. A single-image camera model may still be beneficial from a practical point of view, and serves as a robust starting point for the multiple-image least-square optimization of the camera models. Further, for cylindrical targets, the relation between cylinder diameter and checkerboard square size may be utilized. Assuming that the cylinder diameter is known, the square size of the checkerboard pattern (as well as misalignment) may be optimized from recorded images. This can provide better estimates of the checkerboard square size than those obtained with manual methods. Despite the practical advantages of using a cylinder target, the camera models optimized from the glass-plate target were used in **Part III** of this thesis since these resulted in slightly lower residuals.

7.4 Concluding remarks

The shock tube presented in this chapter is developed for blast applications where the properties of a shock wave acting on a structure may be studied by placing a test object inside or at the end of the tube. An important quality of the test facility is the synchronization of high-speed images and pressure measurements. Post-processing the high-speed images using 3D-DIC enables a thorough investigation of the entire experiment and evaluation of blast-structure interaction without the need to consider the inherent complexity in close-in and near-field detonations.

8

Shock tube experiments

This chapter starts by evaluating the performance of the SIMLab Shock Tube Facility (SSTF) in producing blast loading in controlled laboratory environments. Then, the dynamic response of blast-loaded steel and aluminium plates is studied experimentally. Both massive and flexible plates were mounted at the tube end during testing, where the massive plate tests serve as a basis for comparison with respect to fluid-structure interaction effects. Special focus is placed on the influence of pre-formed holes on the dynamic response and failure characteristics of the flexible plates.

8.1 Introduction

Due to the complexity in both the loading and the resulting response, numerical methods are often required for sufficient insight. Before using such computational methods their performance should be validated in terms of reliability, robustness and effectiveness in predicting both the loading and the response. Experimental validation is ideal since it represents the actual physics of the problem, and controlled small-scale experiments could therefore be used to evaluate current computational methods and improve the understanding of the structural response during blast events. An alternative to explosive detonations is the shock tube technique presented in Chapters 6 and 7. This is a well-known experimental technique within the field of gas dynamics using well-defined and easily controllable initial conditions providing good repeatability of each test. The shock tube presented in Chapter 7 is developed for blast applications where the properties of a planar shock wave acting on a structure may be studied by placing a test object inside or at the end of the tube. This shock tube therefore allows for the evaluation of blast-structure interaction without the need to consider the inherent complexity in close-in and near-field detonations.

The objective of this chapter is to investigate the performance of the SSTF in generating a loading similar to that from actual free-field explosive detonations. The performance of the shock tube in producing blast loading is evaluated with

respect to requirements given in International [100] and European [138, 139] standards. This is carried out by comparing the pressure histories on a massive steel plate to relevant blast load models found in the literature [4, 16]. The dynamic response of flexible plates and corresponding FSI effects are also studied experimentally using synchronized pressure measurements and two high-speed cameras in a stereovision setup, in which the deformation field was found using three-dimensional digital image correlation (3D-DIC). Special focus is placed on the influence of pre-formed holes on the dynamic response and failure characteristics of square plates. The investigated plates have similar geometry as those studied by Rakvåg et al. [65]. However, the SSTF facilitates a blast environment with larger pressure magnitudes compared to that used in [65], resulting in failure of the plates. Material tests were also performed to determine the materials' behaviour at large plastic strains.

8.2 Experimental study

This section starts with a presentation of the experimental setup and programme before presenting the 3D-DIC procedure and the material tests.

8.2.1 Experimental setup and programme

The tests were performed in the SSTF presented in Chapter 7. An illustration of the experimental setups and pictures of the test specimens are shown in Figure 8.1. Aluminium inserts of diameter 0.33 m were used to obtain driver lengths of 0.27 m and 0.77 m, where the latter configuration is illustrated in Figures 8.1a and 8.1b. The driven section was operated with a length of 16.20 m. The loading was varied by changing the initial pressure p_4 in the driver section, while the initial pressure in the driven section was operated at ambient conditions (p_1 and T_1). Table 8.1 gives the complete test matrix, where each test is numbered MX-Y-Z in which M denotes rigid plate (R), aluminium plate (A), steel plate without (D) or with pre-formed (P) holes, X gives the driver length (in cm), Y indicates the firing overpressure (in bars) in the driver and Z is the test number. The massive steel plate was used to obtain a rigid blind flange (Figure 8.1c), while thin flexible plates (both with and without holes) were used to introduce moving boundary conditions (Figures 8.1d and 8.1e). Pressure measurements from the massive plate tests could then be used as a basis to investigate potential FSI effects in the tests with flexible (aluminium and steel) plates. These measurements also serve as a quantitative measure for evaluation of purely Eulerian numerical simulations in an uncoupled FSI approach (see Chapter 9) and to evaluate the performance of the SSTF. Both the massive steel plate with thickness 0.05 m and the flexible plate specimens with dimensions of 0.625 m $\times$ 0.625 m $\times$ 0.0008 m were clamped to the end

flange of the tube (Figures 8.1c - 8.1e) in an attempt to achieve fixed boundary conditions. As in **Part II** and Section 3.2.1, each of the 12 bolts was tightened using a wrench with a torque M_t of 200 Nm. This is equivalent to a pre-tensioning force F_p of 46.6 kN [157] for the M24 bolts used in the SSTF. The geometry of the flexible plates and clamping are illustrated in Figure 8.2, where the exposed area was 0.3 m × 0.3 m (equal to the internal cross-section of the tube in Figure 7.2c). Two repetitive tests were performed for the steel plates with pre-formed holes to investigate variations in deformation histories and possible failure patterns. It is also worth noting the good repeatability of the bursting characteristics of the diaphragms by comparing the firing pressure p_4 between tests with the same initial conditions in Table 8.1.

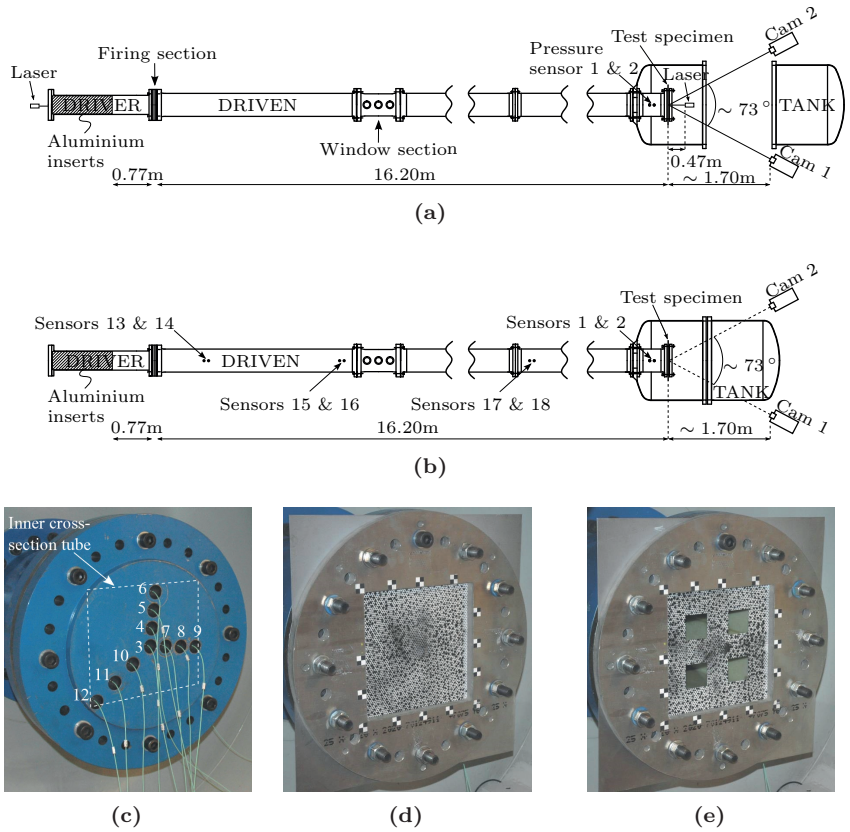

Figure 8.1: Experimental setup: sketches of the setup for (a) evaluation of the 3D-DIC technique (seen from above), (b) flexible blast-loaded plates (seen from above), pictures of (c) massive steel plate, (d) clamping and DIC speckle pattern for the flexible plates, and (e) clamping and plate with pre-formed holes. Both the massive steel plate in (c) and the flexible plates in (d) and (e) are seen from the cameras.

Table 8.1: Experimental programme.

Test	Initial conditions		
	Pressure driver (p_4) [kPa]	Pressure driven (p_1) [kPa]	Ambient temperature ($T = T_1 = T_4$) [°C]
R27-05-01	661.8	100.3	20.5
R27-7.5-01	866.4	99.8	22.6
R27-10-01	1200.8	100.3	20.8
R27-15-01	1608.5	100.3	20.9
R27-20-01	2127.0	100.6	21.1
R27-25-01	2458.8	100.3	21.4
R27-35-01	3330.0	100.5	21.6
R27-40-01	3990.1	100.5	21.8
R27-60-01	6024.7	99.8	22.8
R27-75-01	7104.8	99.9	22.9
R77-05-01	618.5	99.7	22.0
R77-10-01	1099.1	99.6	21.5
R77-15-01	1594.0	99.8	24.0
R77-20-01	2074.3	99.8	23.8
R77-25-01	2821.6	99.7	23.9
R77-35-01	3811.8	99.8	23.6
R77-60-01	6073.2	99.8	23.9
R77-75-01	7765.5	99.6	23.2
A27-05-01	660.9	100.9	22.3
A27-7.5-01	882.2	100.9	22.3
A27-10-01	1190.7	100.9	22.1
D77-05-01	616.9	100.5	21.9
D77-15-01	1683.8	100.8	22.4
D77-25-01	2715.9	100.8	22.5
D77-35-01	3793.1	100.7	22.2
P77-05-01	622.7	100.5	22.1
P77-05-02	618.4	100.5	22.4
P77-15-01	1638.8	100.4	21.4
P77-15-02	1660.0	100.8	21.9
P77-25-01	2738.1	100.7	22.0
P77-25-02	2697.5	100.7	23.1
P77-35-01	3801.0	100.3	22.0
P77-35-02	3778.8	100.7	23.5

A closed-end configuration of the SSTF is favorable to avoid leakage of pressure in the circumferential direction of the test specimens at the blast-structure interface and will therefore maintain a uniform and plane shock wave also around the perimeter of the tube. Placing the test specimen even the smallest distance from the end of the tube would lead to a non-uniform spatial and temporal distribution around the periphery of the tube, due to partial venting of the gas into the expanding tank volume (see [118, 120]). Moreover, such a venting results in rarefaction waves travelling back upstream the tube causing increased complexity of the subsequent wave patterns.

Piezoelectric pressure sensors (Kistler 603B), corresponding charge amplifiers (Kistler 5064) and data acquisition system from National Instruments (NI USB-6356) were used to measure the pressure during the tests. In all tests, two sensors flush mounted in the tube wall measured the pressure behind the incident and reflected shock wave 24.5 cm (Sensor 2) and 34.5 cm (Sensor 1)

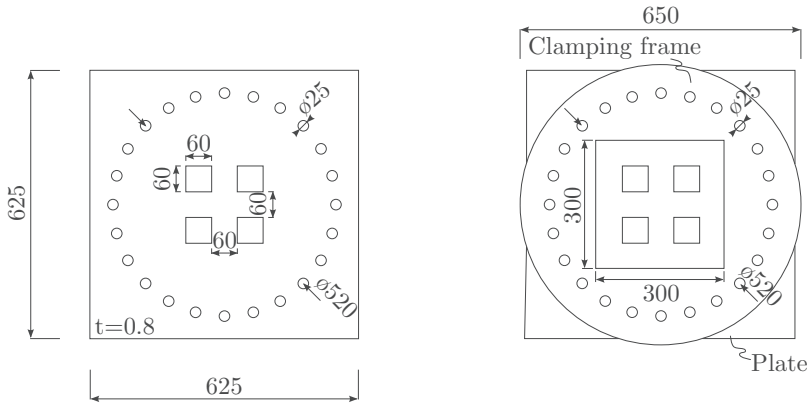

Figure 8.2: Geometry of the flexible plates: (a) plate with pre-formed holes and (b) clamping assembly. All measurements are in mm.

upstream the test specimens (see Figures 8.1a and 8.1b). The delay in arrival time at the pressure sensors was used to determine the shock velocity v_s and the corresponding Mach number M_s. This is valuable information in validating the pressure measurements during the experiments against the idealized shock tube theory in Section 6.4. The number of sensors was limited by the available channels in the data acquisition system, which was 12 at the time of these tests. In the particular case of the massive plate tests, the remaining 10 channels were used to measure the pressure distribution on a rigid boundary in sensors positioned along the horizontal, vertical and diagonal and numbered Sensors 3-12 (Figure 8.1c). In the flexible plate tests, 4 of the channels were needed for synchronization of pressure measurements and high-speed images while the remaining 6 channels were used for sensors positioned downstream the firing section. Sensors 3-8 were therefore renamed Sensors 13-18 to avoid confusions with previous numbering of pressure sensors and located 0.97, 1.07, 3.70, 3.80, 10.51 and 10.61 m downstream the firing section (see Figure 8.1b). The pressure sensors were automatically triggered when the shock wave arrived at the first sensor downstream the firing section and operated with a sampling frequency of 500 kHz. A thin layer of insulating silicone (Kistler 1051) was used to shield the pressure sensors against heat transfer from the shock wave during the tests.

Due to large momentum changes induced in the gas during firing, considerable forces exist along the axis of the tube during the tests. This axial recoil was accounted for by allowing the entire facility to move as a rigid body along the two-rail support. This movement was used to evaluate the accuracy of the 3D-DIC technique by comparing it to the laser measurements at the rear end

of the driver section (see Figures 8.1a and 8.3).

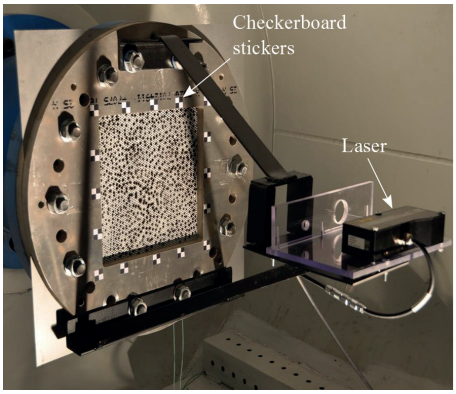

Figure 8.3: Picture of clamping, DIC speckle pattern and positioning of a laser for evaluation of the 3D-DIC technique (seen from the cameras).

8.2.2 3D-DIC measurements

The 3D-DIC technique presented in **Part II** and Section 3.2.3 was used to capture the displacement fields of the flexible plates in the shock tube experiments. The same technique was also used to measure the axial movement of the entire facility during testing. Two Phantom v1610 high-speed cameras were located approximately 1.70 m from the plates in a symmetric stereovision setup, and the angle between the optical axes of the cameras was approximately 73° (Figures 8.1a and 8.1b). The recording rate was chosen to 24 kHz in all tests with an exposure time of 30 μs and an image size of 768 $\times$ 800 pixels at 12-bit grey level digitization. These high-speed images were synchronized with the pressure measurements which enabled a thorough investigation of each test. To avoid damaging the high-speed cameras and loss of calibration in the stereovision setup, the tank was closed during the tests where failure was expected (see Figure 8.1b). Failure was not expected in the experiments of the thin steel plates without holes and the tank was therefore kept open during these experiments (see Figure 8.1a).

Prior to each test, the flexible plates were spray-painted white before a template was used to apply a black speckle pattern with a size distribution in the range of 2-4 mm equivalent to 3.4-6.7 pixels (Figures 8.1d and 8.1e). The choice of speckle size was based on minimizing the effect of aliasing in the DIC [128], and the pixel-to-millimetre ratio is estimated to be approximately 1.7 in the XY-plane for both cameras. This resulted in an effective sensor size of 21.5 mm $\times$ 22.4 mm since the cameras operate with a pixel size of 28 μm $\times$ 28 μm (and image size of 768 $\times$ 800 pixels). Image sequences from the two cameras

were then post-processed using an in-house 3D-DIC code (eCorr) [168] based on the finite element (FE) formulation of DIC presented by Besnard et al. [129]. Element-wise grey value normalization was applied in the DIC analyses to account for highlights observed on the surface of the test specimens [128]. These highlights were mainly caused by direct reflections of the halogen studio lights that were used during the tests. In cases where large jumps in displacements between two subsequent images were observed, a coarse-search multi-scale approach [218] was applied prior to the FE-DIC optimization of the particular image.

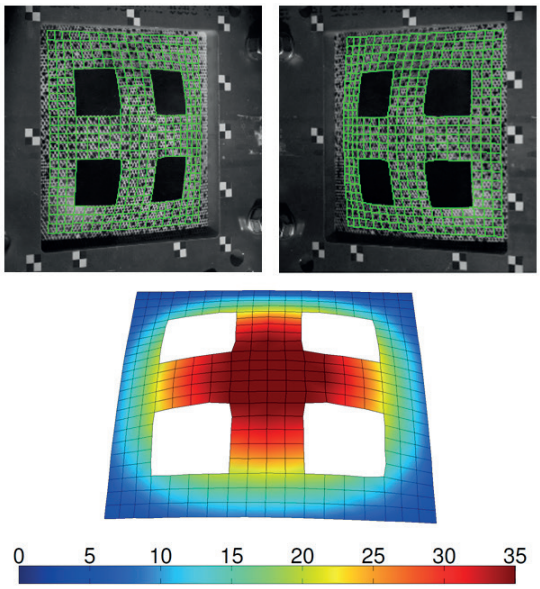

Figure 8.4: Results from 3D-DIC in test P77-25-02. The resulting DIC mesh is plotted on top of the recorded images from Camera 1 (top left) and Camera 2 (top right), while the corresponding 3D model is presented in the lower image. The colour scaling on the 3D model indicates out-of-plane displacement (in mm).

The axial movement of the entire facility was measured using a set of 2 × 2 checkerboard stickers glued to the clamping frame at the end flange (see Figures 8.1d, 8.1e and 8.3). These checkerboard stickers were observed by the two cameras during the test. The centre corner of the checkerboard patterns were tracked using the corner finder algorithm [215] and subsequently coupled with the camera models discussed in Section 7.3 to provide the movement in 3D space. All deformation profiles presented herein were corrected for this slight movement. Figure 8.4 illustrates a set of recorded images in test P77-25-02 from the two synchronized high-speed cameras with the resulting DIC meshes plotted on top. The corresponding 3D model calculated from the DIC results is also illustrated in the figure.

8.2.3 Materials

As in **Part II**, the 0.8-mm-thick plates were manufactured from the low-strength aluminium alloy EN AW 1050A-H14 and the medium-strength steel Docol 600 DL. However, these plates were from different batches than those presented in **Part II** and Section 3.2.2. The aluminium plates were mainly included to study the influence of FSI effects at smaller magnitudes of pressure, while the steel plates were used to study FSI effects at larger magnitudes of pressure and the influence of pre-formed holes on the dynamic response. The steel plates were produced by Swedish Steel Ltd. (SSAB), while the aluminium plates were manufactured by Hindalco Industries Ltd. Tables 8.2 and 8.3 provide the nominal chemical composition of the materials, while the nominal yield stress and ultimate tensile strengths were given, respectively, by the manufacturers to be 299 MPa and 677 MPa for the steel sheets and 110 MPa and 116 MPa for the aluminium sheets.

Table 8.2: Chemical composition of shock-tube batch of Docol 600DL (in wt.%).

C	Si	Mn	P	S	Al
0.10	0.40	1.50	0.010	0.002	0.040

Table 8.3: Chemical composition of shock-tube batch of EN AW 1050A-H14 (in wt.%).

Si	Fe	Cu	Mn	Mg	Zn	Ti	Cr	Al
0.100	0.280	0.003	0.010	0.002	0.002	0.009	0.002	Rest

Uniaxial tensile tests were carried out on dog-bone specimens cut from the sheets using the same geometry as in Figure 3.3 and tested according to the procedure described in Section 3.2.2. Thus, the tests were performed in a Zwick/Roell Z030 testing machine at a constant deformation rate of 2.1 mm/min. This corresponds to an initial strain rate of $\dot{\varepsilon} = 5 \times 10^{-4}$ s^{-1} for a gauge length of 70 mm. Three parallel tests were performed in three different directions (0°, 45° and 90°) with respect to the rolling direction of the plate. Two-dimensional digital image correlation (2D-DIC) [168, 169] was used to measure the displacement field and synchronized with the force F measured by the hydraulic test machine at a sampling rate of 4 Hz for all tests. A virtual extensometer of 50 mm initial gauge length L_0 was used to obtain the elongation history $u(t)$ from the 2D-DIC. In an attempt to validate the DIC measurements, the first test in each direction was instrumented with an extensometer to measure the elongation over the same initial gauge length (50 mm). The DIC measurements and the extensometer showed excellent agreement, and only the DIC recordings are therefore used in the following.

Force-elongation curves from the tensile tests are shown in Figures 8.5a and 8.5c.

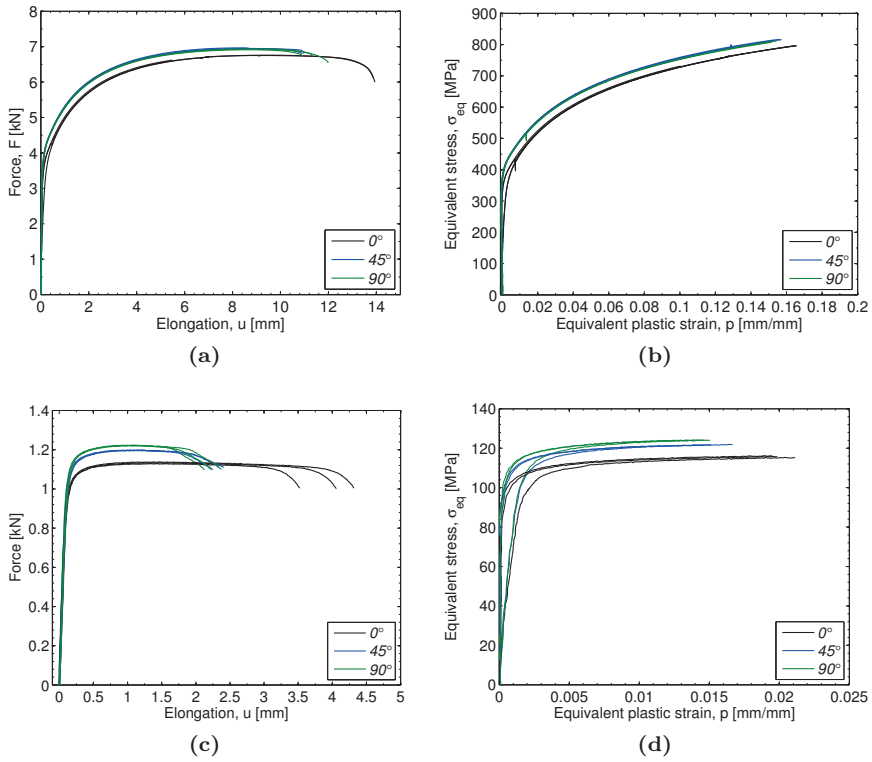

Figure 8.5: Experimental data from uniaxial tensile tests at three different loading directions: (a) force-elongation curves and (b) equivalent stress-plastic strain curves until necking for the steel material, and (c) force-elongation curves and (d) equivalent stress-plastic strain curves until necking for the aluminium material.

As in Section 3.2.2, it is observed that both materials are slightly anisotropic both in flow stress and in elongation to failure. This is most evident in the 45° and 90° directions and particularly for the aluminium material. Gruben et al. [219] showed that the plastic anisotropy is negligible for this type of steel material. This was also confirmed by a review of previous quasi-static and dynamic material tests in Section 3.2.2, which showed that the steel material can be considered as isotropic with a small variation in failure strain while both materials are moderately strain-rate sensitive [164–166, 219]. Figures 8.5b and 8.5d show the equivalent stress-plastic strain curves until necking. The true stress σ, true strain ε and true plastic strain ε^p before necking is found using the relations

$$\sigma = \sigma_{\mathrm{e}}(1+\varepsilon_{\mathrm{e}}) \ , \quad \varepsilon = \ln(1+\varepsilon_{\mathrm{e}}) \ , \quad \varepsilon^p = \varepsilon - \frac{\sigma}{E} \tag{8.1}$$

where σ equals the equivalent stress σ_{eq} before necking, ε^p corresponds to the equivalent plastic strain p in a uniaxial tension test, E is the Young's modulus, and the nominal stress σ_{e} and strain ε_{e} are given by

$$\sigma_{\mathrm{e}} = \frac{F}{A_0}\,, \quad \varepsilon_{\mathrm{e}} = \frac{u}{L_0} \tag{8.2}$$

in which A_0 is the initial cross-sectional area in the gauge region.

8.3 Experimental results

Successful operation of the shock tube requires information about the bursting pressures and characteristics of the diaphragms. Therefore, this section starts by presenting an experimental investigation of the bursting properties of the Melinex diaphragms used in this thesis. Then, the performance of the SSTF with respect to blast loading and the accuracy of the 3D-DIC technique in predicting the dynamic response are evaluated. Finally, the influence of FSI effects on the loading and dynamic response of flexible plates are studied before briefly discussing the shock wave propagation in the flexible plate tests.

8.3.1 Membrane capacity

The shock strength may be varied by changing the thickness of the diaphragms. Melinex sheets are used as diaphragms due to its strength and reproducing bursting pressures. Melinex comes in various thicknesses and several adjacent thicknesses may be used to increase the bursting pressure of the diaphragms. Such multilayer sheets then acts as a single diaphragm holding the total pressure difference between each intermediate chamber in the firing section. Since there is relatively limited information on the bursting characteristics of Melinex diaphragms in the literature, it was necessary with an experimental investigation of the bursting properties at selected thicknesses. Single- and double-layered diaphragms were tested by increasing the pressure in the driver until rupture. A summary of the bursting pressures for the available thicknesses are given in the Table 8.4 and Figure 8.6. The bursting pressure for the respective thicknesses of the single-layered diaphragms are plotted as filled markers, while double-layered combinations are plotted as empty markers in Figure 8.6.

In general, the test campaign on these diaphragms showed that the Melinex sheets have good bursting characteristics by folding and petalling, allowing for relatively large bursting areas through which the driver gas can propagate into the driven section. Table 8.4 and the error bars in Figure 8.6 also indicate that each combination of diaphragms produced consistent bursting pressures,

Table 8.4: Experimental results from testing of Melinex capacities.

Thickness	Bursting overpressure [kPa]					Combination	Recommended overpressure
[mm]	1	2	3	4	5		[kPa]
0.125	156.2	158.3	160.5	158.7	160.5	Singel	150
0.190	213.6	210.0	209.4	207.2	207.8	Singel	200
0.250	301.0	293.6	296.9	290.5	292.1	Singel	290
0.250	314.3	303.0	315.0	303.7	311.6	0.125+0.125	300
0.315	364.0	363.8	362.3	362.9	364.1	0.125+0.190	360
0.380	411.6	413.2	411.7	411.0	411.7	0.190+0.190	410
0.440	492.0	499.9	504.6	498.4	495.6	0.190+0.250	490
0.500	439.7	431.5	434.3	428.2	434.3	Singel	430
0.500	606.7	589.9	591.4	585.0	593.3	0.250+0.250	590
0.690	648.5	654.6	652.5	638.1	669.6	0.190+0.500	640
0.750	719.3	705.6	720.5	720.8	717.8	0.250+0.500	710
1.000	888.0	865.2	866.7	861.5	863.7	0.500+0.500	860

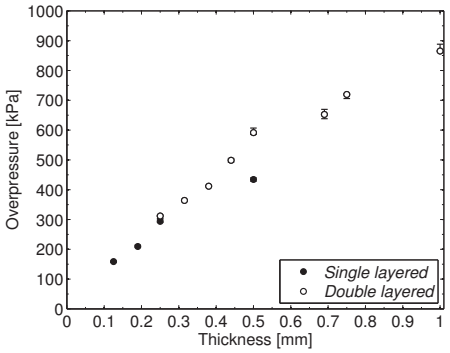

Figure 8.6: Capacity of single- and double-layered Melinex diaphragms.

where the bursting pressure is (more or less) proportional to both its thickness and to the total thickness for double-layered diaphragms. A slight deviation from this trend was observed for the 0.5-mm single-layered diaphragms, which experienced a significant reduction in the bursting pressure compared to the double-layered diaphragms with the same total thickness. This indicates a small change in the bursting properties as the single-layered diaphragms approaches a thickness of 0.5 mm (i.e., less ductile behaviour, probably due to the increased stiffness, and reduced folding and petalling). The observations in Table 8.4 and Figure 8.6 are valuable information to obtain successful operation of the shock tube.

8.3.2 Shock tube performance

The purpose of the SSTF is to produce a loading similar to that from blast events within controlled laboratory environments. Shock tubes are widely used to study structures exposed to blast loading (see e.g. [72,114,116,119]), however, such studies often report the pressure histories without fully addressing the

requirements to blast performance. According to relevant European [138, 139] and International [100] standards, a shock tube used in blast applications should ensure the consistent reproduction of a plane shock wave normal to the surface of the test object. Moreover, the positive phase of the pressure history should be of a form which can be related to that from a spherical unconfined high explosive charge of a known weight of TNT detonating at a known distance from the target. The blast performance may be assessed by using a massive plate equipped with pressure sensors distributed over the cross-sectional area of the tube. This enables an investigation of the planarity of the shock wave, and the pressure histories may be related to approximate free-field airblast conditions resulting in similar blast loads as experiments with spherical and hemispherical explosive detonations found in the literature [4, 16]. This approach was used by Lloyd et al. [115] and Riedel et al. [220] and will also be used in the following to evaluate the blast performance of the SSTF with the closed-end configuration presented in Section 8.2.1.

The spatial and temporal pressure distribution were therefore evaluated by comparing the time of arrival t_a and pressure magnitudes at the sensors along the vertical, horizontal and diagonal of the massive plate (Figure 8.1c). Figure 8.7 contains the results from two representative tests, where Sensor 3 was located at the centre, Sensors 4-6 along the vertical, Sensors 7-9 along the horizontal and Sensors 10-12 along the diagonal. The number of sensors was limited by the available channels in the data acquisition system, and all sensors were flush mounted with the internal surface of the massive plate. Also note that Sensors 6 and 9 were positioned 15 mm from the inner walls, while Sensor 12 was positioned in the very corner of the cross-section (Figure 8.1c). It was found that the SSTF produced a near planar shock wave with a maximum variation of 0.002 ms arrival time. This was similar to the sampling rate (500 kHz) and the shock wave can therefore be considered as planar. The only exception was the measurements from Sensor 12 (see Figure 8.7), which was located in the corner of the cross-section and therefore experienced some minor corner effects. The rise time in Sensor 12 was found to be 5-20 times larger than in the other sensors. This is expected when operating with square cross-sections, because the velocity is approaching zero near the walls due to friction effects. However, it was seen negligible influence of these friction effects in the sensors closest to the walls (Sensors 6 and 9). Based on this, only the pressure measurement at the centre of the plate (i.e., Sensor 3) is used in the following to represent the pressure at the massive plate.

Figure 8.7 also shows that the loading is characterized by the same distinctive features as the positive phase of a blast wave from a high explosive detonation. That is, an almost instantaneous rise from ambient pressure p_1 to a peak reflected (head-on) overpressure $p_{\mathrm{r,max}}$, followed by an exponential decay in

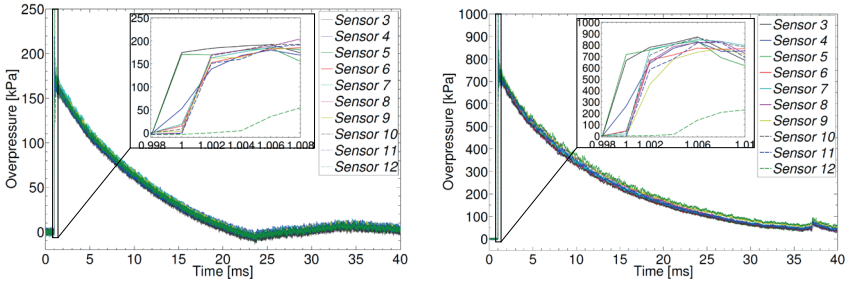

Figure 8.7: Pressure measurements at the centre (Sensor 3), along the vertical (Sensors 4-6), horizontal (Sensors 7-9) and diagonal (Sensors 10-12) of the massive steel plate for two representative tests: (a) R27-05 and (b) R27-40.

pressure back to the ambient pressure during the positive phase duration t_{d+}. It is emphasized that the wave fronts and interaction of waves will continue back and forth in the tube until a static overpressure is reached when the gas comes to rest (see Section 6.4.1). This is observed as multiple peaks (secondary and tertiary reflections) of decreasing magnitude on the pressure measurements, and leads to multiple loading events on the plate such that the final configuration may not be representative for the primary loading event. However, the relevant timescale of the experiments depends on the application and therefore limits the time-window of interest. The time-window of interest in these experiments is limited to the first positive part of the overpressure history. Note that tertiary reflections are the internal reflections within the tube as the reflected wave interacts with the end of the driver section and returns to the massive plate. The timing of these reflections depends on the driver pressure p_4 and the ratio between the lengths of the driver and driven sections. Using a sufficiently long driven section, these reflections occur after the end of the first positive phase.

Figure 8.8 and Table 8.5 present the measured blast properties on the massive plate (reflected overpressure, duration, impulse and Mach number) of the positive phase for all the driver pressures and driver lengths in Table 8.1. Note that the massive plate tests are only denoted by their material (R), driver length and (intended) firing overpressure in the following because the respective tests consisted of only one repetition (see Table 8.1). It is evident that the blast properties are a function of both the driver length and driver pressure, where (as expected) larger driver pressures result in increasing magnitudes of the blast properties. It is also observed that the driver length has a significant influence on the blast properties, where the reflected overpressure $p_{r,max}$ for the largest length (0.77 m) was almost twice that produced from the smallest length (0.27 m) for approximately the same bursting pressures (see Figure 8.8a and Table

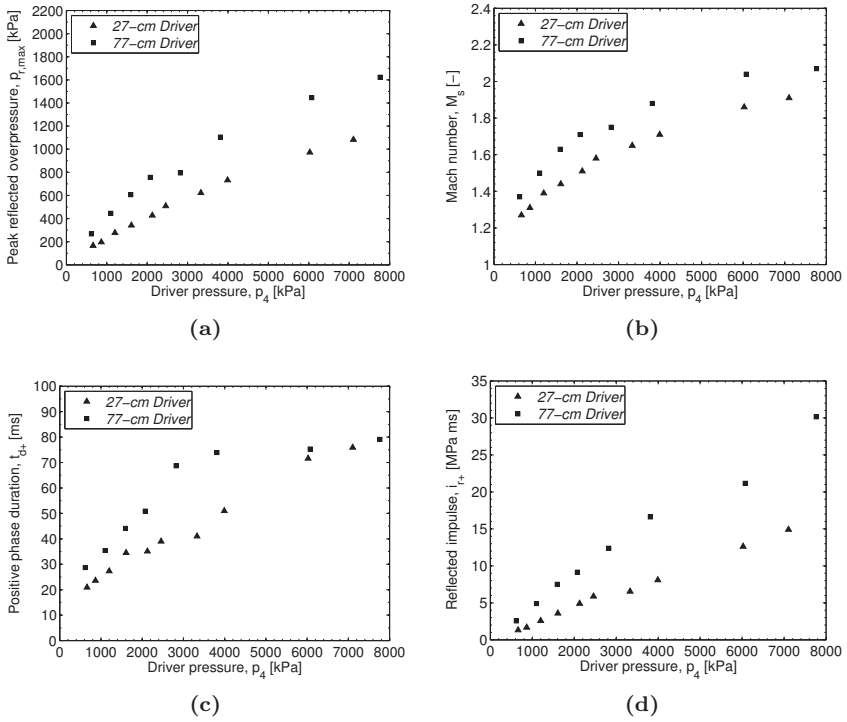

Figure 8.8: Blast parameters measured on the massive plate as a function of driver length and driver pressure (see Table 8.1). The time window of interest is limited to the positive phase measured by Sensor 3: (a) peak reflected overpressure $p_{\mathrm{r,max}}$, (b) Mach number M_s, (c) positive phase duration $t_{\mathrm{d+}}$ and (d) reflected impulse $i_{\mathrm{r+}}$.

8.5). Following the argumentation in Section 6.4.1, this is explained by the fact that larger driver pressures p_4 result in larger Mach numbers M_s (Figure 8.8b) and increasing driver lengths delays the reflected rarefaction waves in catching up with and slowing down the shock wave. The shock wave velocity was determined based on the pressure measurements at Sensors 1 and 2 (Figure 8.1a), and by dividing the distance between their respective locations (0.1 m) by the delay in time of arrival. It should be noted that Sensor 6 (see Figure 8.1c) and Sensor 2 could provide an even better estimate of the shock velocity; however, it was chosen to focus on the performance of Sensors 1 and 2 because these will be used in future investigations involving flexible plates. In general, the shock wave was characterized by supersonic velocities ($M_s > 1$) since the rate of propagation exceeds the speed of sound c_1 in the driven section (Figure 8.8b). Moreover, increasing driver pressures and driver lengths produce blast waves with a longer positive phase duration t_{d+} (Figure 8.8c). A noticeable effect of the driver length on the positive phase duration is observed due to

the increased volume of compressed air released at the respective bursting pressures. The combination of increasing peak reflected overpressures (Figure 8.8a) and positive phase durations (Figure 8.8c) results in an increase in the corresponding impulse i_{r+} (Figure 8.8d), where the impulse i_{r+} was found by numerical integration of the reflected overpressure during the positive phase duration. Note that before determining the properties of the blast loading in Figure 8.8 and Table 8.5, the experimental data were low-pass filtered with a cutoff frequency of 0.15 times the sampling rate (500 kHz). This enabled consistent determination of the blast parameters and reduced the effect of high-frequency oscillations in the pressure measurements without altering the characteristic shape of the curves. Such high-frequency oscillations (see Figure 8.7) are due to the relatively high eigen frequency of the pressure sensors and the high sampling rate used to capture the near instantaneous rise in pressure over the shock front. In general, the effect of the low-pass filtering was a reduction in peak reflected pressure of approximately 2 %.

Table 8.5: Measured blast parameters at Sensors 1-3 and Friedlander parameters curve-fitted to data from Sensor 3.

Test	Parameters (Sensors 1 and 2)		Friedlander parameters (Sensor 3)				Shock tube theory		Deviation experiment versus theory	
	M_s	$p_{so,max}$	$p_{r,max}$	t_{d+}	b	i_{r+}	$p_{so,max}$	$p_{r,max}$	$\Delta p_{so,max}$	$\Delta p_{r,max}$
	[-]	[kPa]	[kPa]	[ms]	[-]	[kPa ms]	[kPa]	[kPa]	[%]	[%]
R27-05	1.27	71.7	166.3	20.9	0.900	1316.8	71.7	183.3	0.0	-10.2
R27-7.5	1.31	82.3	196.3	23.6	1.011	1675.6	83.4	220.1	-1.3	-12.1
R27-10	1.39	111.4	276.7	27.3	1.237	2587.2	109.1	306.1	2.1	-10.6
R27-15	1.44	133.2	341.6	34.5	1.692	3576.8	125.6	365.7	5.7	-7.0
R27-20	1.51	164.3	427.6	35.1	1.390	4906.1	150.2	459.0	8.6	-7.3
R27-25	1.58	189.2	508.7	39.0	1.664	5883.9	175.1	559.9	7.5	-10.1
R27-35	1.65	223.1	622.7	41.0	2.072	6544.3	202.0	674.2	9.5	-8.3
R27-40	1.71	253.9	732.8	51.0	1.847	8081.1	225.6	779.9	11.1	-6.4
R27-60	1.86	326.1	973.1	71.6	2.721	12,608.4	286.4	1072.3	12.2	-10.2
R27-75	1.91	352.6	1083.2	75.9	2.417	14,907.6	308.6	1184.3	12.5	-9.3
R77-05	1.37	108.0	267.5	28.7	1.306	2557.9	102.0	282.0	5.6	-5.4
R77-10	1.50	161.7	446.2	35.4	1.571	4904.5	145.3	440.8	10.2	1.2
R77-15	1.63	219.1	606.6	44.1	2.025	7510.0	192.9	636.3	11.9	-4.9
R77-20	1.71	260.8	756.8	50.9	2.666	9147.0	224.0	774.4	14.1	-2.3
R77-25	1.75	274.7	795.2	68.7	2.044	12,383.3	239.9	848.0	12.7	-6.6
R77-35	1.88	365.9	1105.2	73.9	1.904	16,613.4	295.1	1116.0	19.4	-1.0
R77-60	2.04	429.4	1446.1	75.3	1.768	21,151.7	368.1	1498.4	14.3	-3.6
R77-75	2.07	460.2	1623.2	79.1	1.088	30,149.0	381.7	1573.7	17.1	3.1

Peak incident and reflected overpressures compared to the idealized shock tube theory using Eqs. (6.47) and (6.88).

As already discussed in Section 2.1, the modified Friedlander equation in Eq. (2.1) is typically used to represent the pressure history when the parameters governing the positive phase are known. Moreover, the corresponding positive impulse has an analytical solution given by Eq. (2.3). The blast parameters in Table 8.5 (i.e., $p_{r,max}$, t_{d+} and i_{r+}) were used to iteratively find the exponential decay coefficient b in Eq. (2.3), which enables the corresponding Friedlander curve to be expressed by Eq. (2.1). A selection of representative Friedlander curves is compared to the corresponding experiments in Figure 8.9, while the

Friedlander parameters for all tests are given in Table 8.5.

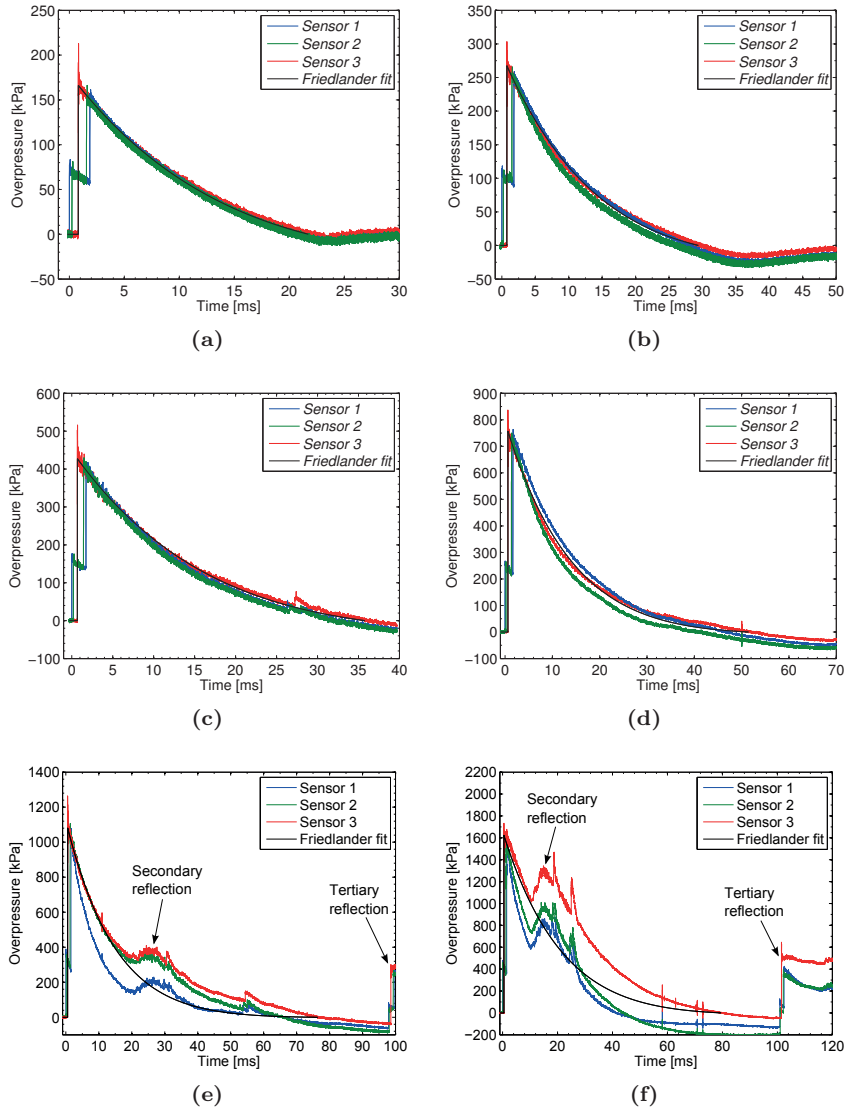

Figure 8.9: Representative pressure histories from experiments (Sensors 1-3). Friedlander curves fitted to Sensor 3 are also included: (a) R27-05, (b) R77-05, (c) R27-20, (d) R77-20, (e) R27-75 and (f) R77-75.

Note that the experimental data from Sensors 1 and 2 are also included in Figure 8.9, and that time zero ($t = 0$) is taken as the arrival of the shock wave at Sensor 1 located upstream the test specimen (Figure 8.1a). Figure 8.9 shows

excellent agreement between the Friedlander curves and experimental data until secondary reflections occur during the positive phase duration (Figure 8.9e-f). These secondary reflections occurred at larger driver pressures and driver lengths, that is, in test R27-60, R27-75, and R77-25 to R77-75. In the particular cases of secondary reflections, the exponential decay parameter b was determined by using the peak reflected overpressure $p_{\mathrm{r,max}}$, positive phase duration $t_{\mathrm{d+}}$ and curve-fitting of Eq. (2.1) to the experimental curves until the secondary reflections occurred. Thus, Eq. (2.3) was not used in the case of secondary reflections.

A well-established reference for the properties of the positive phase from airblast experiments is the research by Kingery and Bulmash [4]. They used spherical and hemispherical charges of TNT detonating at a given stand-off distance R from an infinite reflecting surface and curve-fitted a large set of experimental data to high-order polynomials. These empirical relations are widely used in the literature (see e.g. [16]). The peak reflected overpressure $p_{\mathrm{r,max}}$, corresponding impulse $i_{\mathrm{r+}}$, and the empirical relations by Kingery and Bulmash were therefore used to relate the pressure histories in the shock tube to approximate free-field conditions (i.e., a particular weight W of TNT detonating at a given distance R from the target). The approximate free-field conditions are given in Table 8.6 for selected tests, while Figure 8.10 compares the corresponding pressure histories to tests R27-05 and R27-20. It is observed that the blast waves generated in the SSTF closely resemble that from high explosive far-field detonations (Table 8.6), and that the Friedlander curves from the experiments are in good agreement with the pressure histories from the corresponding free-field conditions. Moreover, a retrospective of events [221] and practical implications of size and weight of explosives that can be transported by personnel and various vehicles [99] shows that the SSTF is capable of generating a loading similar to that of representative free-field detonations at typical stand-off distances used in protective design [100, 101].

Table 8.6: Experimental results on the massive plate and corresponding charges of TNT at given stand-off distances.

Test	Friedlander parameters		Spherical charge			Hemispherical charge		
	$p_{\mathrm{r,max}}$	$i_{\mathrm{r+}}$	W	R	Z	W	R	Z
	[kPa]	[kPa ms]	[kg]	[m]	[m/kg$^{1/3}$]	[kg]	[m]	[m/kg$^{1/3}$]
R27-05	166.3	1316.8	1006.1	33.4	3.34	513.6	31.7	3.96
R27-7.5	196.3	1675.6	1680.6	37.0	3.11	850.5	34.9	3.69
R27-10	276.7	2587.2	3893.2	42.8	2.72	1945.9	40.1	3.21
R27-15	341.6	3576.8	7809.0	49.9	2.51	3886.5	46.6	2.96
R27-20	427.6	4906.1	15,117.4	57.2	2.31	7506.7	53.4	2.73
R27-25	508.7	5883.9	20,943.8	60.0	2.17	10,395.5	56.0	2.57
R77-05	267.5	2557.9	3932.9	43.5	2.76	1967.5	40.8	3.25
R77-10	446.2	4904.5	14,308.1	55.3	2.28	7103.5	51.7	2.69

Scaled distances ($Z = R/W^{1/3}$) are found using Hopkinson-Cranz scaling [14].

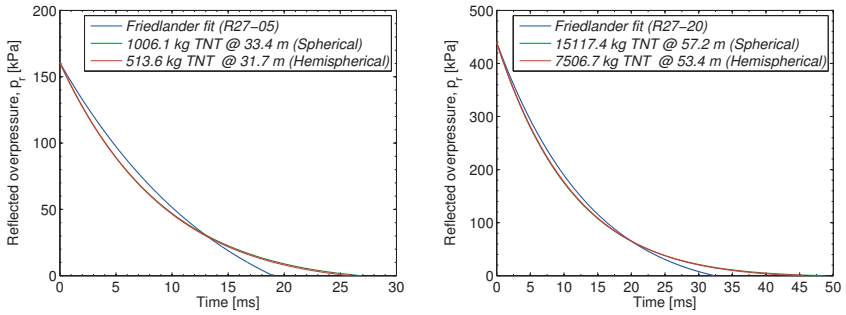

(a) **(b)**

Figure 8.10: Experimental pressure-time histories (Friedlander fit) compared with that from approximate free-field spherical and hemispherical detonations found by using the empirical equations by Kingery and Bulmash [4]: (a) R27-05 and (b) R27-20.

Knowing the shock velocity v_s and Mach number $M_s = v_s/c_1$ from the experiment (see Table 8.5), Eqs. (6.47) and (6.88) from the idealized shock theory (in Section 6.4) may be used to calculate the peak incident (side-on) overpressure $p_{\mathrm{so,max}}$ and the peak reflected (head-on) overpressure $p_{\mathrm{r,max}}$, respectively. This representation of the shock strength is convenient since the shock velocity v_s is easily measured in the experiments. Using the measured shock velocity v_s, the corresponding Mach number M_s, and assuming a constant ratio of specific heats ($\gamma = 1.4$), the rise in pressure across the shock can be determined by Eq. (6.47). The pressures found from this idealized theory is included and compared to the experimental measurements in Table 8.5, where negative values of $\Delta p_{\mathrm{so,max}}$ and $\Delta p_{\mathrm{r,max}}$ implies that the theoretical values are larger than the corresponding experimental measurements. The increasing deviation of the peak incident overpressures $\Delta p_{\mathrm{so,max}}$ at larger pressures may be related to the filtering of high-frequency noise of the pressure measurements, because the experimental values reported in Table 8.5 still contain some noise. Moreover, the peak reflected overpressures $p_{\mathrm{r,max}}$ calculated from the idealized shock theory are conservative since the Mach number M_s is calculated based on the measurements in Sensors 1 and 2 located upstream Sensor 3. The shock velocity will continue to decrease travelling from Sensor 2 to Sensor 3 and the actual Mach number M_s immediately before impact is slightly less than that used to calculate the reflected pressures. Nevertheless, it is observed that the experimental measurements and the idealized theory are in acceptable agreement indicating that the pressure measurements reported herein are reliable. It should also be noted that an alternative approach to validate the pressure measurements against the idealized theory is to produce a temporally uniform pressure pulse as a basis for comparison. However, this is considered beyond the scope of this thesis and suggested as future work.

A final observation regarding the design premises given in Section 7.1 is that, in addition to producing a blast loading in controlled laboratory environments, the SSTF is capable of generating pressure magnitudes sufficient to damage a wide range of plated structures of different materials (e.g. glass [222] and concrete [223, 224]).

8.3.3 Evaluation of the 3D-DIC technique

Even though the evaluation of the 3D-DIC technique in **Part II** and Sections 3.3.2 to 3.3.3 showed encouraging results, it was decided to perform a more thorough evaluation of the 3D-DIC technique before studying the flexible plate tests in Table 8.1. This was to ensure that the generated displacement fields are reliable and could be used to quantify the dynamic response. A single test was therefore carried out with the same experimental setup (Figure 8.1a) and sampling rate of data as in the flexible plate tests. A laser displacement sensor (optoNCDT 2310-50) mounted at the end of the tube was used to measure the mid-point deflection of the flexible plate (relative to the tube) during the experiment (Figure 8.3). This was then used as basis for comparison to ensure that the corresponding displacement predicted by 3D-DIC is reasonable. Since the high-speed cameras were located on the floor and not in contact with the SSTF (Figures 7.4 and 8.1a), it is necessary to correct the 3D-DIC measurements for the rigid body movement of the tube during each experiment. The 3D-DIC technique is therefore evaluated in two steps. First, the rigid body movement of the entire facility is measured by a laser positioned on the floor at the rear end of the driver (Figure 8.1a) and compared to the movement of the opposite end of the tube measured by 3D-DIC using the checkerboard stickers on the clamping frame (Figure 8.3). Then, the mid-point deflection of the plate measured by 3D-DIC was corrected for the rigid body motion of the tube and compared to the corresponding deflection measured by the laser device (Figure 8.3). The plate material was Docol 600DL and the loading conditions were similar to those in test D77-35-01 in Table 8.1. However, note that it was used a different material batch than that presented in Section 8.2.3 due to a limited number of plates.

The results are shown in Figure 8.11, where Figure 8.11a compares the rigid body movement of the entire facility and Figure 8.11b shows the measured mid-point deflection of the plate. Both the rigid body movement and the mid-point deflection measured by the laser and the 3D-DIC were in excellent agreement, and the 3D-DIC technique is therefore considered to provide reliable displacements. Note that the minor deviations in Figure 8.11a are related to the eigen oscillations in the longitudinal axis of the tube interacting with the wave pattern inside the tube, while the high-frequency noise in the laser measurements in Figure 8.11b are due to the eigen oscillations of the laser

mounting frame (Figure 8.3) induced by the recoil when the diaphragms burst. These latter oscillations are not observed in the 3D-DIC measurements since the high-speed cameras were not in contact with the tube.

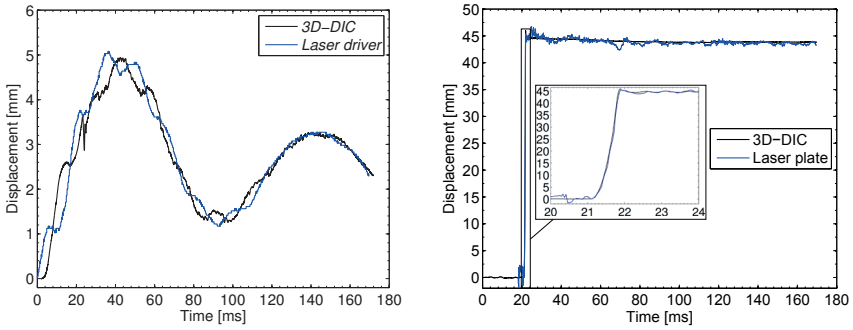

Figure 8.11: Evaluation of the 3D-DIC technique in predicting (a) the rigid body movement and (b) the mid-point deflection.

As in Sections 3.3.2 and 3.3.3, the 3D-DIC measurements are desirable since these enable the determination of 3D surface deformation and strain fields. Figure 8.12 shows selected 3D topography maps, contours of the transverse displacement field and deformation profiles at characteristic times during the test, while displacement, strain and strain rate histories from selected elements in the 3D-DIC analysis are shown in Figure 8.13. Figure 8.12 also contains synchronized loading and response in terms of the pressure measured at Sensor 2 and the mid-point deflection. Remember that Sensor 2 is located upstream the test specimen (Figure 8.1a) since it is challenging to mount pressure sensors in the thin plate without altering its structural characteristics. In an attempt to estimate the actual loading on the plate, the Friedlander equation in Eq. (2.1) was curve-fitted to the measurements at Sensor 2 and extrapolated back to the time of impact. This approach assumes a rigid plate and can be used to discuss FSI effects. The Friedlander fit is plotted as a dashed line in the second column of Figure 8.12.

The deformation is in accordance with the theory presented by Jones [61] where plastic hinges start at the boundary corners (Figure 8.12a) and propagate along the diagonals towards the centre (Figure 8.12b) before they meet in the centre (Figure 8.12c), forming a square pyramidal with plastic hinges at the boundaries and along the diagonals of the plate. Based on these deformation fields, it is possible to obtain deformation histories (Figure 8.13b), strain histories (Figure 8.13c) and an indication of the corresponding strain rate histories (Figure 8.13d) in selected elements during the experiment. The selection of elements is shown in Figure 8.13a. It is observed that the plate experiences a non-uniform

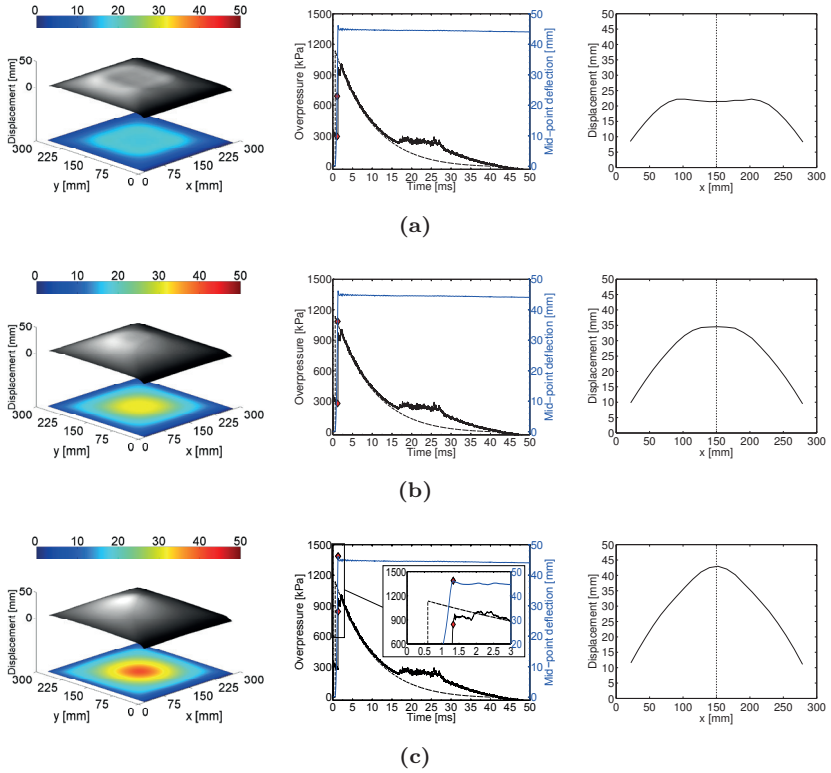

Figure 8.12: 3D topography maps and contours of the transverse displacement field (left), its corresponding pressure and mid-point deflection (middle) and deformation profile at the centre along the x-axis (right): (a) t = 1.084 ms, (b) t = 1.208 ms and (c) t = 1.334 ms. Pressure recordings from Sensor 2 are used in the synchronization. Red diamonds show the corresponding time of recordings.

spatial and temporal strain rate distribution during the response from zero to maximum deformation (Figure 8.13d). This is important information for validation of computational methods in predicting the structural response during blast events.

Note that the noise in the strain at the centre of the plate (Element 1 in Figure 8.13c) is due to the eigen oscillations of the laser mounting frame (Figure 8.3) which caused the laser point to move and altered the greyscale value in this element. Still, this disturbance of the 3D-DIC occurs after the maximum deformation (t = 1.334 ms) and is not expected to affect the strain-rate measurements during the time of interest (Figure 8.13d). This noise would not occur if the laser is removed.

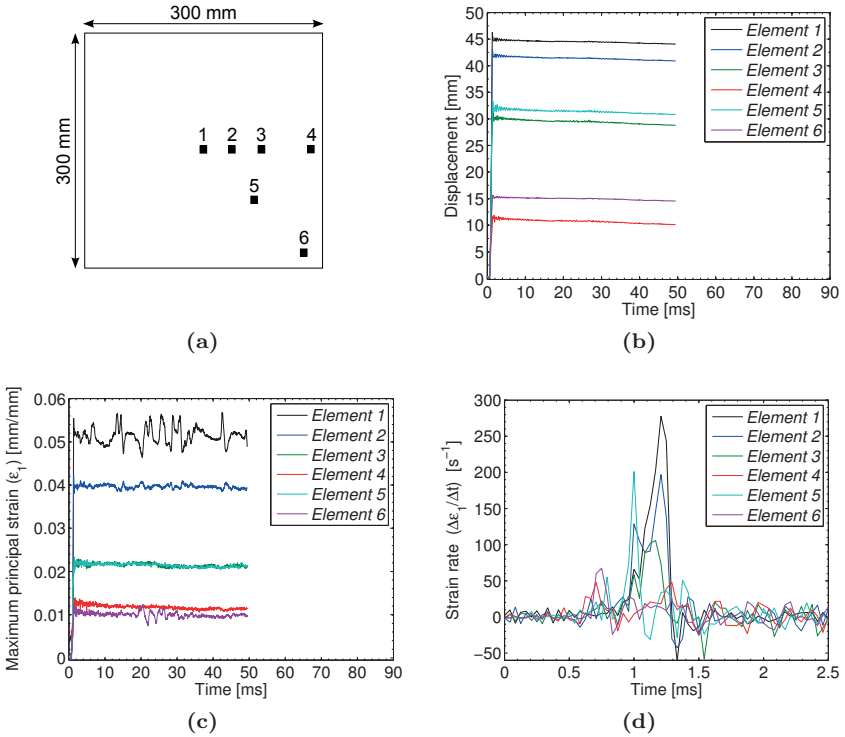

Figure 8.13: Results from selected elements in the 3D-DIC analysis: (a) selected elements, (b) displacement, (c) major principal strain and (d) strain rate.

8.3.4 Flexible plates

A basic understanding of the role of FSI when the shock wave interacts with a moving boundary was given in Section 6.4.5. That is, if the boundary (i.e., the flexible plate) starts to move, the motion alters the pressure at its surface. FSI effects could also be investigated by comparing pressure histories at Sensor 2 in the massive and flexible plate tests with the same driver length and similar firing pressures (e.g. R27-05 and A27-05, and R77-05, D77-05 and P77-05 in Table 8.1). This is presented in Figures 8.14 and 8.15 for the thin aluminium and steel plates, respectively, while the shock velocity v_s, peak incident $p_{\mathrm{so,max}}$ and peak reflected $p_{\mathrm{r,max}}$ overpressures measured at Sensor 2 are reported in Table 8.7. Positive values of $\Delta p_{\mathrm{so,max}}$ and $\Delta p_{\mathrm{r,max}}$ imply a reduced pressure in the flexible plate tests (AX-Y, DX-Y or PX-Y) compared to the corresponding massive plate test (RX-Y). Note that the flexible plate tests are only denoted by their material (A, D or P), driver length (X) and firing overpressure (Y) in the following because the plates with pre-formed holes (PX-Y) showed very

good repeatability and the remaining tests (AX-Y and DX-Y) consisted of only one repetition (see Table 8.1). As before, the data were low-pass filtered with a cutoff frequency of 0.15 times the sampling rate (500 kHz) when determining the blast properties in Table 8.7. Also note that the time of interest is limited to the positive phase of the blast load, and that the curves are shifted in time such that time equal zero when the shock wave arrives at Sensor 1.

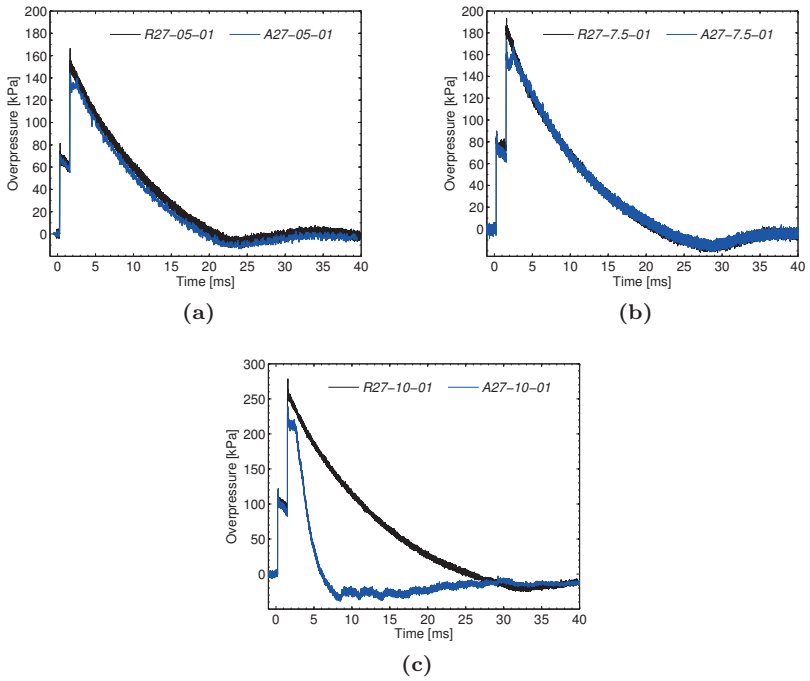

Figure 8.14: Comparison of pressure measurements at Sensor 2 for selected tests with massive steel and flexible aluminium plates subjected to similar blast intensities: (a) R27-05 and A27-05, (b) R27-7.5 and A27-7.5, and (c) R27-10 and A27-10.

Sensor 2 first record the incident overpressure p_{so} right before impact and then the reflected overpressure p_{r} after impact when the blast wave travels back towards the driver (see Figures 8.14 and 8.15). It is observed that the incident (side-on) pressures are in excellent agreement in the tests with similar firing conditions, while there is a reduction in the reflected pressure for the flexible plates (see Table 8.7). The flexible plates without holes (A and D) induce a small reduction in the peak reflected overpressure $p_{\mathrm{r,max}}$, while the subsequent flow seems to be barely altered when allowing for finite deformations of the plate. The only exception seems to be test D77-25 where it is a negligible reduction in the peak reflected pressure (see Table 8.7) and test D77-15 in Figure 8.15b which experience a reduced pressure throughout the positive

Table 8.7: Experimental results from Sensor 2 and 3D-DIC.

Test	Shock velocity	Overpressure (Sensor 2)				Mid-point deflection		
	v_s [m/s]	$p_{so,max}$ [kPa]	$\Delta p_{so,max}$ [%]	$p_{r,max}$ [kPa]	$\Delta p_{r,max}$ [%]	$d_{z,max}$ [mm]	$d_{z,p}$ [mm]	Δd_z [%]
R27-05-01	431.0	71.7	-	155.9	-	N/A	N/A	N/A
A27-05-01	400.0	71.0	1.0	144.2	7.5	24.3	22.7	6.6
R27-7.5-01	446.4	82.3	-	188.7	-	N/A	N/A	N/A
A27-7.5-01	438.6	80.5	2.2	163.6	13.3	27.5	26.1	5.1
R27-10-01	471.7	111.4	-	264.9	-	N/A	N/A	N/A
A27-10-01	467.3	112.3	-0.8	231.2	12.7	N/A*	N/A*	N/A*
R77-05-01	467.3	109.3	-	253.7	-	N/A	N/A	N/A
D77-05-01	463.0	109.2	0.1	242.6	4.4	15.7	11.4	27.4
P77-05-01	467.3	112.8	-3.2	226.8	10.6	18.3	14.4	21.3
P77-05-02	467.3	110.2	-0.8	225.9	11.0	18.3	14.2	22.4
R77-15-01	555.6	221.5	-	599.2	-	N/A	N/A	N/A
D77-15-01	555.6	223.5	-0.9	555.6	7.3	25.0	22.1	11.6
P77-15-01	555.6	221.4	0.0	490.1	18.2	29.2	26.2	10.3
P77-15-02	555.6	220.3	0.5	484.6	19.1	29.5	26.6	9.8
R77-25-01	595.2	279.6	-	796.4	-	N/A	N/A	N/A
D77-25-01	602.4	292.0	-4.4	767.6	3.6	30.8	28.4	7.8
P77-25-01	609.8	303.3	-8.5	706.6	11.3	36.2	33.8	6.6
P77-25-02	609.8	300.1	-7.3	716.8	10.0	37.2	34.9	6.2
R77-35-01	641.0	367.4	-	1112.4	-	N/A	N/A	N/A
D77-35-01	641.0	347.5	5.4	992.7	10.8	36.2	34.6	4.4
P77-35-01	649.4	362.6	1.3	879.6	20.9	N/A*	N/A*	N/A*
P77-35-02	641.0	354.9	3.4	849.9	23.6	N/A*	N/A*	N/A*
R77-60-01	694.4	437.4	-	1487.6	-	N/A	N/A	N/A
D77-60-01	704.2	452.6	-3.5	1312.7	11.8	45.8	44.5	2.8

*Test resulted in complete failure of the plate.

The delay in arrival time at Sensors 1 and 2 was used to determine v_s.

phase. A plausible explanation for the former observation is that the incident pressure is slightly lower in test R77-25 compared to the remaining tests (D and P) at this driver length and firing pressure (see $p_{so,max}$ in Table 8.7), while the reason for the latter observation in test D77-15 is not known. It is important to emphasize that Sensor 2 is located 24.5 cm upstream the test specimen flush mounted with the inner wall (see Figure 8.1b), and that the peak reflected overpressure immediately after reflection is often assumed to be independent of the stiffness of the test object (see e.g. [72]). The influence of the pre-formed holes is a reduction of the pressure upstream the test specimen (Figure 8.15). This decrease in pressure implies that there may be reduced pressure in the vicinity of the holes. However, Figure 8.15 indicates that most of the pressure remains in front of the plate. The noticeable decrease in pressure in tests A27-10 (Figure 8.14c) and P77-35 (Figure 8.15d) is due to complete failure of the plate. As soon as the plate is completely removed from the tube end, the pressure is allowed to enter freely into the expanding volume in the tank. This results in a left-running rarefaction wave and is recorded as a sudden drop in pressure at Sensor 2. The observations of reduced reflected pressures in the flexible plate tests are interesting in view of FSI and blast mitigation.

It is however challenging to further identify which factor is more important for the observed decrease in pressure based on these experimental results. This therefore requires numerical investigations which will be performed in Chapter 9. Also note the good repeatability between tests with the same initial conditions by comparing the shock velocity v_s for corresponding tests in Tables 8.1 and 8.7.

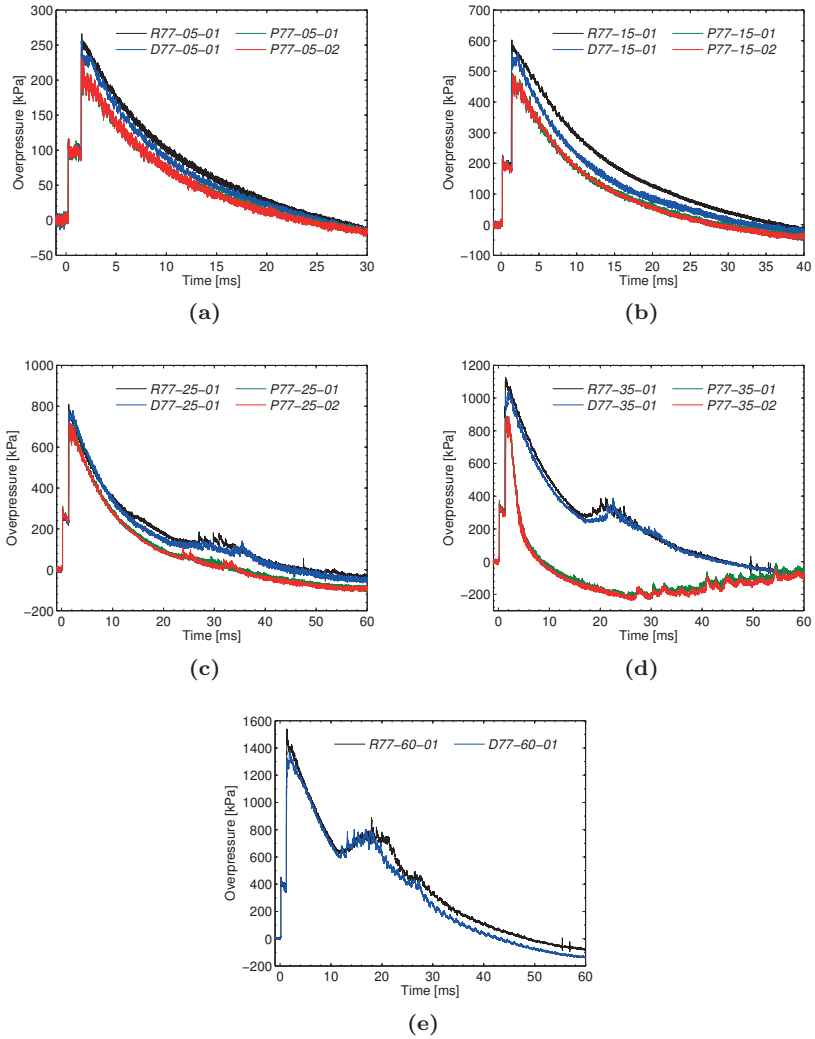

Figure 8.15: Comparison of pressure measurements at Sensor 2 for selected tests with massive steel and flexible steel plates subjected to similar blast intensities: (a) R77-05, D77-05 and P77-05, (b) R77-15, D77-15 and P77-15, (c) R77-25, D77-25 and P77-25, (d) R77-35, D77-35 and P77-35, and (e) R77-60 and D77-60.

Figures 8.16 and 8.17 contain the mid-point deflection histories measured with 3D-DIC for the aluminium (Figure 8.16) and steel plates without (Figure 8.17a) and with (Figure 8.17b) holes. The corresponding maximum $d_{z,max}$ and permanent $d_{z,p}$ mid-point deflections and $\Delta d_z = d_{z,max} - d_{z,p}$ are summarized in Table 8.7. All curves are corrected for the rigid body movement of the facility, and also shifted in time such that time equal zero when the shock wave arrives at Sensor 1. As for the pressure measurements, the repetitive tests for the plates with holes (P) showed excellent agreement also for the deformation histories. Therefore, only one of these tests is reported in the following. No deformation histories were recorded in test A27-10 due to an synchronization error with the high-speed cameras. However, this experiment resulted in complete tearing along the boundary and the images therefore serve as a qualitative basis of comparison (see Figure 8.18).

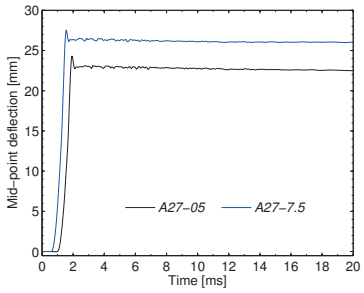

Figure 8.16: Mid-point deflection based on 3D-DIC measurements for the A27-05 and A27-7.5 tests. All curves are corrected for the rigid body movement of the shock tube. Also note that the curves are shifted in time such that time equal zero when the shock wave arrives at Sensor 1.

All tests experienced inelastic deformations with a permanent deflection in the same direction as the incident shock wave, and the elastic rebound Δd_z became smaller as the load-intensity increased (Table 8.7). It was observed an increased mid-point deflection for the perforated plates (Figure 8.17b) when compared to the plates without holes (Figure 8.17a) under similar loading conditions. The perforated plates also involved larger oscillations after the elastic rebound, while the difference Δd_z between the maximum mid-point deflection $d_{z,max}$ and permanent mid-point deflection $d_{z,p}$ was found to be approximately the same for the steel plates (DX-Y and PX-Y) exposed to similar loading conditions (see Table 8.7). There were no visible signs of tearing at the boundaries for the steel plates without holes. However, failure was observed in all tests involving perforated plates, except for tests P77-05. Cracks initiated at the corners of the pre-formed holes and propagated along the diagonals of the plates where the extent of the crack growth was dependent on the intensity of the loading. This is illustrated in Figure 8.19, where high-speed images of representative tests at

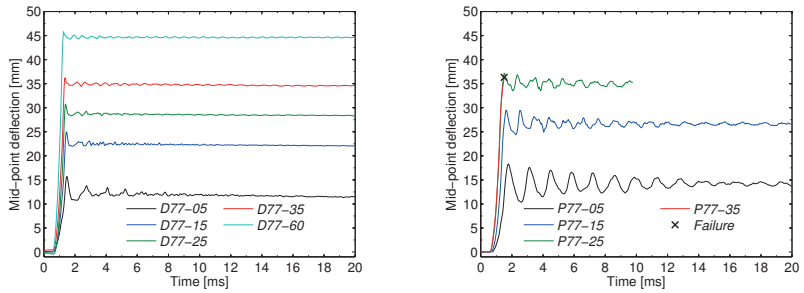

(a) (b)

Figure 8.17: Mid-point deflection based on 3D-DIC measurements in the tests with thin steel plates: (a) without holes and (b) with pre-formed holes. All curves are corrected for the rigid body movement of the shock tube. Also note that the curves are shifted in time such that time equal zero when the shock wave arrives at Sensor 1. The black marker illustrates the point of complete failure in P77-35.

the time of maximum deflection are shown. It is observed that the tests cover the entire range from no visible signs of failure in tests P77-05 (Figure 8.19a), crack initiation in the extremities of the holes in P77-15 (barely seen in Figure 8.19b), to noticeable crack growth along the diagonals of the plates in P77-25 (Figure 8.19c) and, finally, complete tearing along the diagonals in P77-35 (Figure 8.19d). Figure 8.20 shows more details of the failure process in test P77-35, where it is observed that the crack propagation is nearly symmetric (Figure 8.20a-b) until the cracks meet in the centre of the plate (Figure 8.20c-d). After the cracks meet in the centre (Figure 8.20c), they propagate towards the outer corners of the plate boundary resulting in complete failure (Figure 8.20d). A plausible explanation for the crack propagation along the diagonals of the plates may be a reduced pressure in the vicinity of the holes. This will result in a larger pressure at the plate centre and may force the crack to propagate along the diagonals. Since it is challenging to conclude on the influence of the pre-formed holes on the observed crack propagation in the tests with perforated plates, this will be investigated numerically in Chapter 9.

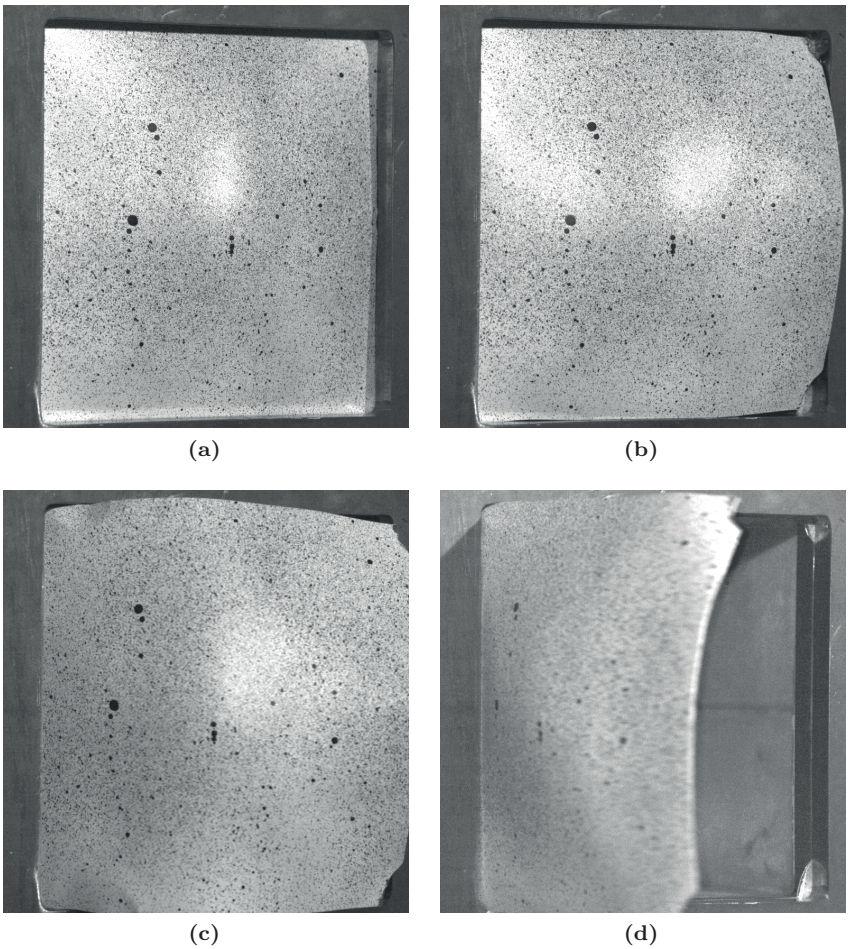

Figure 8.18: High-speed images of the failure process in test A27-10: (a) initiation of tearing along the right vertical ($t = 0.92$ ms), (b) before propagating along the upper and lower horizontals ($t = 1.75$ ms). (c) Eventually the tearing arrive at the left vertical ($t = 3.00$ ms), and (d) the entire plate rotates about the left vertical ($t = 4.46$ ms). Note that time zero is taken as the arrival of the shock wave at Sensor 1.

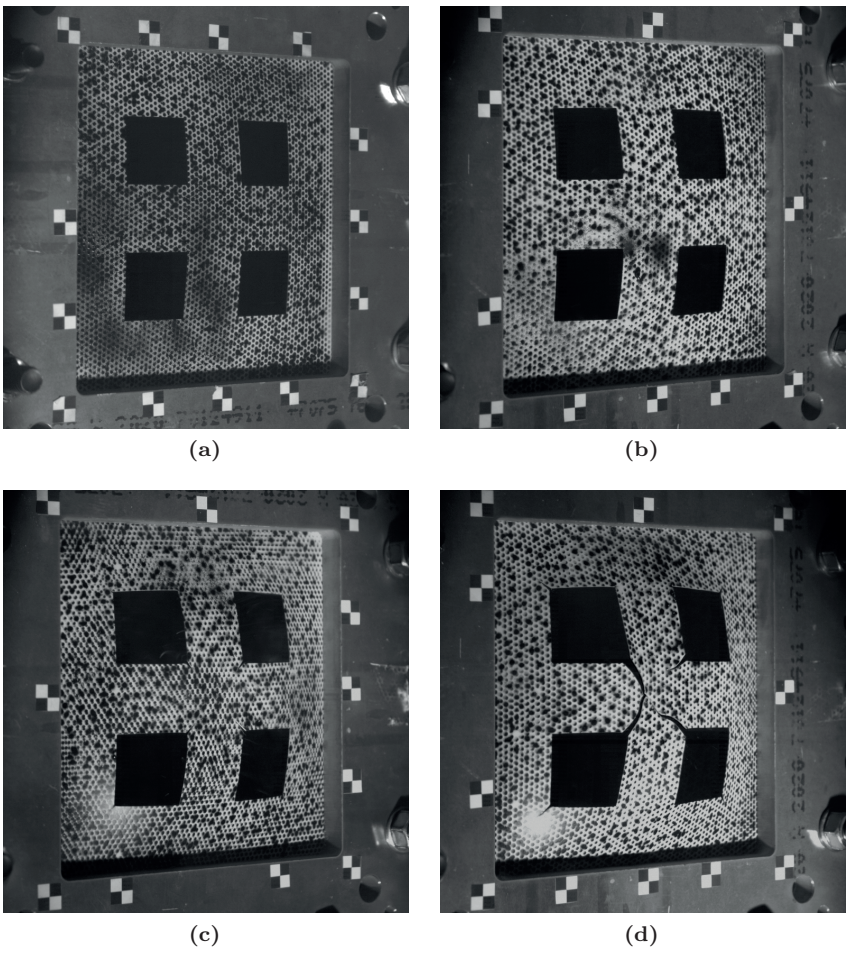

Figure 8.19: High-speed images at maximum mid-point deflection for representative plates with pre-formed holes: (a) P77-05, (b) P77-15, (c) P77-25 and (d) P77-35.

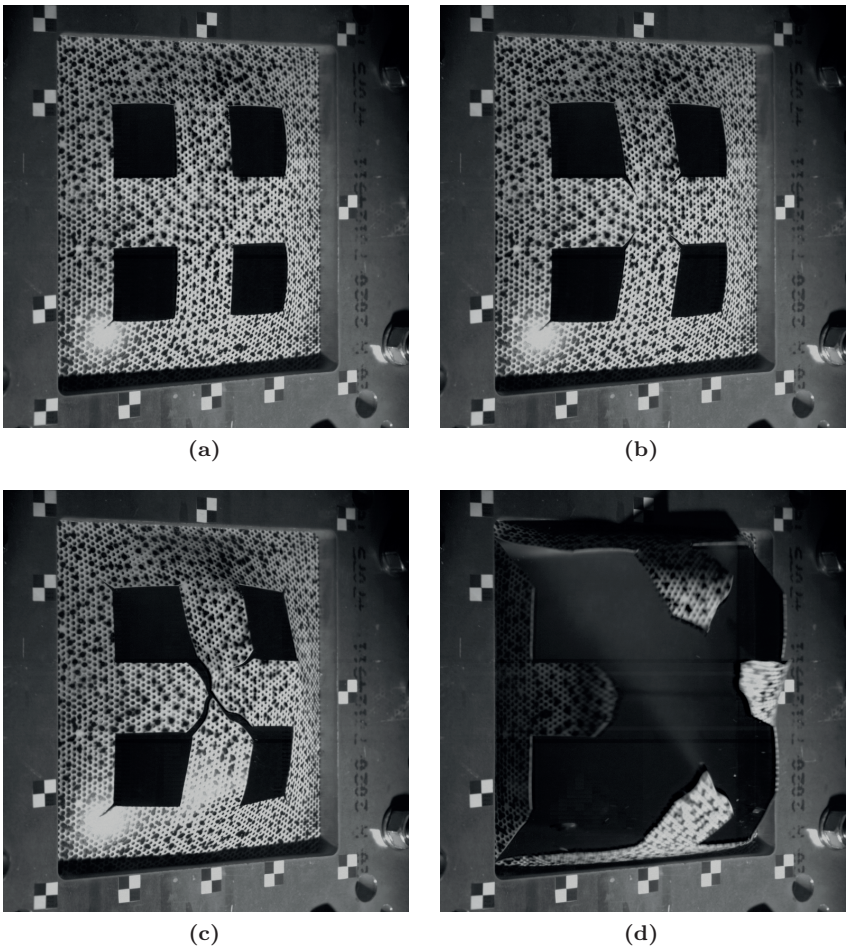

Figure 8.20: High-speed images of the failure process in test P77-35: (a) Crack initiation along the diagonal in the outer corners of the holes ($t = 1.13$ ms), (b) before it propagates towards the centre ($t = 1.42$ ms). (c) Eventually the cracks meet in the centre ($t = 1.75$ ms), and (d) propagates towards the outer corners of the plate resulting in complete failure ($t = 2.63$ ms). Note that the respective times correspond to the shifted time in Figure 8.17b.

8.3.5 Shock wave propagation

This section provides pressure histories downstream the firing section for selected tests. Since the number of sensors were limited by the 12 channels in the data acquisition system, such measurements were not possible in the massive plate tests. However, due to the good repeatability in the firing pressure p_4 between tests under similar initial conditions in Table 8.1, the flexible plate tests are considered to be representative when discussing the shock wave propagation until the time of impact. Tests D77-05, D77-15, D77-25 and D77-35 were therefore chosen for this purpose. These tests will also be used as a basis of comparison for the subsequent Eulerian simulations in Chapter 9.

Figure 8.21 contains the pressure histories at the respective sensors. The sensors were flush mounted with the roof of the internal cross-section and positioned 0.97 (Sensor 13), 1.07 (Sensor 14), 3.70 (Sensor 15), 3.80 (Sensor 16), 10.51 (Sensor 17), 10.61 (Sensor 18), 15.85 (Sensor 1) and 15.95 m (Sensor 2) downstream the firing section (see Figure 8.1b). The pressure sensors were automatically triggered when the shock wave arrived at Sensor 13 and operated with a sampling frequency of 500 kHz. It is clear that increasing bursting pressures result in a significantly less decay in pressure at Sensors 13 and 14, while the characteristic shape of a blast wave is observed at Sensors 15 and 16 in all tests. This may indicate that there are some loss of directional energy due to an initial 3D flow in the vicinity of the firing section during the diaphragm opening process. The diaphragm burst starts by tearing at the centre, followed by diagonal tearing and folding back of the petals formed during the opening process. This results in a high velocity jet and 3D flow of the driver gas originating from the expanding hole. The finite opening time causes the shock wave to travel several tube diameters before the blast wave is fully formed (at Sensors 15 and 16), and this effect is more evident as the diaphragms become thicker. Thus, increased driver pressures involve more diaphragms of larger thickness resulting in a slower diaphragm opening process preventing satisfactory folding back and increased 3D flow during the opening process.

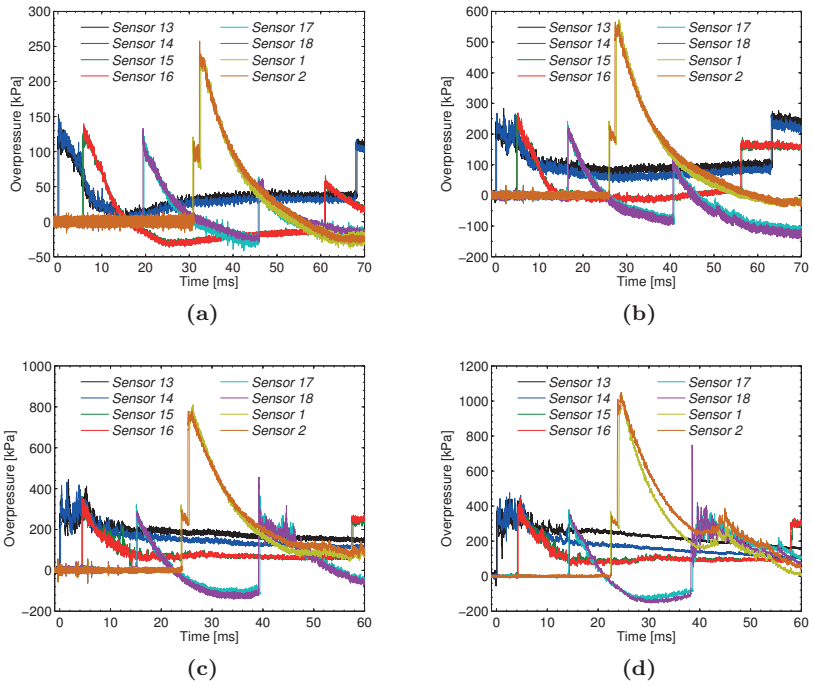

Figure 8.21: Shock wave propagation at increasing driver pressure: (a) D77-05, (b) D77-15, (c) D77-25 and (d) D77-35. The number of sensors were limited by the available channels in the data acquisition system and the respective sensors were positioned 0.97 (Sensor 13), 1.07 (Sensor 14), 3.70 (Sensor 15), 3.80 (Sensor 16), 10.51 (Sensor 17), 10.61 (Sensor 18), 15.85 (Sensor 1) and 15.95 m (Sensor 2) downstream the firing section.

8.4 Concluding remarks

The SIMLab Shock Tube Facililty is found to produce a positive phase loading similar to that of an unconfined far-field airblast, and the recorded incident Mach numbers showed that the pressure measurements are in good agreement with the idealized shock tube theory. Several pressure transducers were positioned upstream and on a massive steel plate located at the tube end to measure the incident and reflected overpressures. The spatial and temporal distribution were found to be planar over the cross-section, and the positive phase of the blast loading was obtained by using a relatively long driven section. Moreover, the blast parameters were found to be a function of driver length and driver pressure.

An in-house three-dimensional digital image correlation (3D-DIC) technique

was evaluated by clamping a thin steel plate at the tube end. The mid-point deflection during the test was measured using both a laser displacement sensor and the 3D-DIC technique. The mid-point deflections were in excellent agreement, and the 3D-DIC technique was considered to provide reliable results. The 3D-DIC technique was therefore used to quantify the dynamic response of thin aluminium and steel plates during shock tube testing. Special focus was placed on the influence of pre-formed holes on the dynamic response of the steel plates. Synchronization of the 3D-DIC and pressure measurements enabled a thorough investigation of the experiments and identification of fluid-structure interaction (FSI) effects. The tests covered a wide range of response from large inelastic deformations to complete failure along the supports in the aluminium plates and along the diagonals of the plates with pre-formed holes. FSI effects were investigated by comparing the loading on massive and flexible plates under similar initial conditions. A trend of reduced reflected pressures was found when introducing pre-formed holes and allowing for large deformations in the plates.

The set of experimental data presented in this chapter will now be used to evaluate numerical models in the FE code EUROPLEXUS in predicting the experimental observations (see Chapter 9). Special focus will be placed on the influence of FSI effects during large deformations and failure of the plates.

9

Numerical simulations

The experimental observations in Chapter 8 of a reduced pressure after impact in the vicinity of the flexible plates were interesting in view of FSI and blast mitigation. This will be further studied numerically in this chapter in an attempt to obtain more insight into the FSI effects during the dynamic response. Special focus will be placed on the capabilities of the numerical simulations in predicting the failure patterns observed in the tests involving plates with pre-formed holes. All of the numerical simulations are performed in the finite element code EUROPLEXUS [130].

9.1 Introduction

As already discussed in Section 1.2.3, the uncoupled approach is often the preferred procedure in today's blast-resistant design. The underlying assumption in this approach is that FSI effects are neglected. The loading is then obtained using either empirical relations based on experimental data (see Chapter 5) or numerical simulations of the blast wave propagation in an Eulerian (fixed) reference frame. It is assumed no deformation of the structure when computing the spatial and temporal pressure distribution at the structural surface. Then the obtained pressure history is imposed on the structure to determine the corresponding dynamic response. The uncoupled approach therefore makes the inherent assumption that the blast properties are unaltered by the structural motion and vice versa. Since the response of blast-loaded plates is highly non-linear (both in geometry and in material behaviour), this may not be an adequate approach for flexible structures and could result in a non-physical response or exaggerated conservative designs. Both the pressure distribution and dynamic response may be significantly influenced due to FSI effects. This was illustrated by Casadei et al. [69] and Børvik et al. [71] by comparing uncoupled and fully coupled FSI simulations for typically industrial applications. Børvik et al. [71] observed considerable variations in the predicted results from uncoupled and coupled methods and emphasized the importance of an accurate quantification of the loading.

Recent advancements in the finite element (FE) code EUROPLEXUS (EPX) [93, 94] enable studies on the FSI effects in blast events involving complex geometries, large deformations, failure and fragmentation. In particular, adaptive mesh refinement (AMR) [95, 98, 225] in both the fluid and structural sub-domains allows for a sufficiently fine mesh size to represent the near instantaneous rise in pressure over the blast wave and to predict structural failure without too much loss of mass when using element erosion. These techniques will be used in the following to investigate the effect of FSI on the dynamic response of the blast-loaded plates presented in Chapter 8, both with and without holes.

This chapter starts with an identification of the material parameters for the tests presented in Section 8.2.3. Then, a review of the recent advancements in the field of FSI and fast transient dynamics is presented. Finally, numerical simulations are performed using available techniques for fluid discretization and FSI in EPX [130]. This enables studies of the wave patterns and FSI during the experiments presented in Chapter 8, where an uncoupled FSI approach is compared to the couple approach in an attempt to investigate potential interaction effects. The numerical results are also compared to experimental data in Chapter 8 in an attempt to evaluate their reliability.

9.2 Material parameter identification

Before moving on to the numerical simulations, it was considered necessary to identify the material parameters for the batches used in the shock tube experiments. The material tests presented in Figure 8.5 deviate slightly with the results from the batches of the same materials used in Section 4.5. It was therefore considered necessary to determine the quasi-static parameters (A, Q_i and C_i) for the material batches used in the shock tube experiments. The calibration was performed using exactly the same procedure as in Section 4.5, where the parameters of the extended Voce hardening rule (A, Q_i and C_i) were obtained by inverse modelling using a FE model of the material tests and the optimization package LS-OPT [196]. Material parameters from LS-OPT are listed in Table 9.1, while physical constants and the remaining material parameters were taken from Table 4.2. Note that the strain-rate sensitivity constant c for the steel material was set equal to 0.01 in Table 9.1 based on the recent findings in Ref. [219]. As before, the initial yield stress A was defined as the stress at 0.2 % plastic strain in the representative tests.

Table 9.1: Material parameters for the shock tube batch.

Material	A [MPa]	Q_1 [MPa]	C_1 [-]	Q_2 [MPa]	C_2 [-]	c [-]	m [-]	$\dot{p}_0$ [s^{-1}]	W_c [MPa]
Docol 600DL	325.7	234.8	56.2	445.7	4.7	0.01	1.0	5×10^{-4}	555.0
1050A-H14	80.0	31.2	1090.0	12.2	20.4	0.014	1.0	5×10^{-4}	60.0

As in Section 4.5, a separate analysis with the same shell elements to be used in the simulations of the flexible plates was performed in EPX to evaluate the material parameters. Figures 9.1a and 9.1b compare the force-elongation curves from the material tests and the simulation in EPX with the optimized material parameters, while Figures 9.1c and 9.1d compare the equivalent stress - plastic strain until necking from the representative tests to the first term of the analytical expression in Eq. (4.32) using the optimized Voce parameters. It is observed that the identified material parameters are able to describe the overall response and material behaviour very well for both materials.

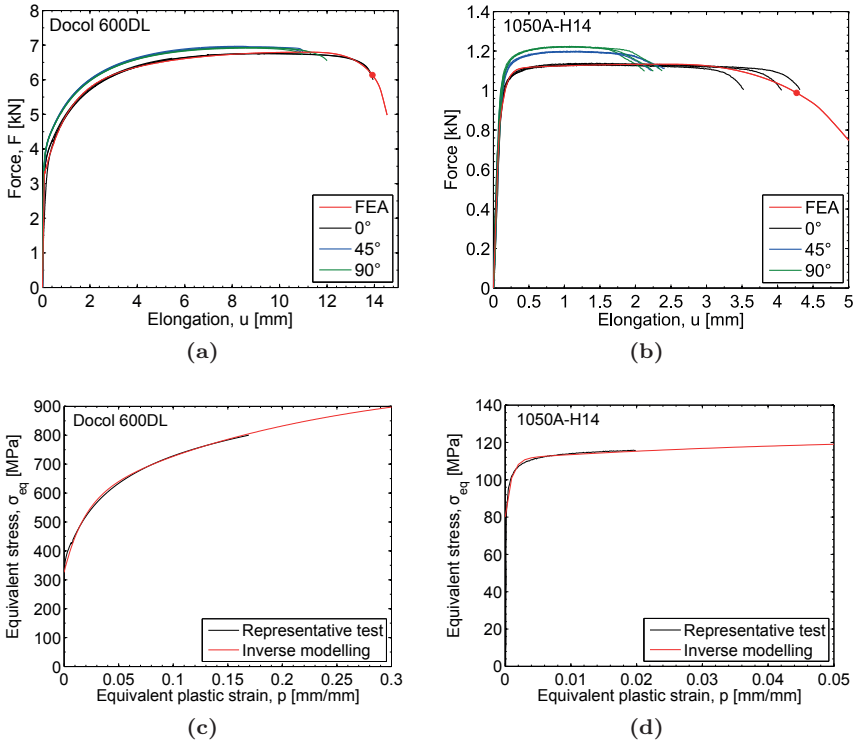

Figure 9.1: Comparison of numerical and experimental results: (a) and (b) give force-elongation curves from uniaxial tensile tests for steel and aluminium, respectively, and the simulation from EPX (FEA) with the material data from Table 4.2 and Table 9.1 are included for comparison. The red dot illustrates the point of failure in the identification of W_c. (c) and (d) show equivalent stress-plastic strain curves until necking for the representative tests in the rolling direction, and extended Voce hardening rule based on the material parameters from the inverse modelling in Table 9.1.

The CL parameter W_c in Eq. (4.36) was determined based on the FE simulation by inspecting the element exposed to the largest plastic work W. It is empha-

sized that the W_c parameter found from this approach is mesh size dependent. This is due to the fact that the element of interest is always located inside the neck and the mesh size will influence the representation of the localized necking. Only the tension tests in the rolling direction of the plate were used in the calibration, although the flow stress and the failure strain were somewhat lower in the 45° and 90° directions (see Figure 8.5). This also implies a spread in W_c between material directions, which (at least to some extent) may affect the numerical results. However, modelling of anisotropy is beyond the scope of this thesis. The points used to extract W_c from the numerical results are indicated by a red dot in Figures 9.1a and 9.1b, and the values are given in Table 9.1. Figure 9.1a shows that the numerical simulation of the steel captured the localized necking very well, while the simulation of the aluminium alloy almost predicted localized necking at the same level as in the representative test (Figure 9.1b). The CL parameter W_c was therefore determined at the same force level as failure occurred in the test.

9.3 Fluid-structure interaction

The FSI algorithms considered herein use the available methods in EPX to couple the fluid and structural sub-domains. While a finite element (FE) discretization is typical for structural applications, the most suitable discretization within computational fluid dynamics is based on finite volume (FV) formulations [88]. FVs are another way of expressing the conservation laws in which the governing equations for the computational cells are formulated and solved in integral form. This method is conservative since the formulation ensures that the flux entering a given volume is identical to that leaving the adjacent volume. Thus, the FV method requires less smoothness of the solution compared to the FE method which is favourable in discontinuous solutions such as shock waves [88, 226]. This thesis is therefore limited to a FE discretization of the structure and FVs in the fluid. It should be noted that EPX also has the possibility of using FEs for the fluid sub-domain (see [130] for more details).

For the FV discretization of the fluid sub-domain, the FSI may be nodally conforming or non-conforming (with one corresponding fluid node for each structural node), or the structure may be embedded in the fluid mesh. Based on the chosen discretization of the FVs (node-centred or cell-centred volumes), there are also two different types of coupling between the fluid and structure (i.e., strong and weak coupling). This section therefore gives a brief presentation of the governing equations and FSI algorithms used in this thesis. The reader is referred to Refs. [93, 94] for further details.

9.3.1 Overview of fully coupled FSI techniques

FSI is an active field of research and there are a wide variety of numerical techniques that have been developed for simulating these types of problems (see e.g. [69, 71, 93, 94, 98, 227–229]). These techniques include Eulerian, Lagrangian, Arbitrary Lagrangian-Eulerian (ALE) and so-called fixed (or embedded) mesh methods. FSI simulations can be challenging for a number of reasons and are therefore often dependent on the application. One of these challenging applications is the simulation of blast-loaded flexible structures undergoing large deformations, possibly up to complete failure and fragmentation, which requires robust and specific FSI algorithms.

Some current efforts in the field of FSI are the advancement from special purpose problems to more general approaches, i.e., approaches that have the potential to turn over from being a challenging research topic to a design tool with actual predictive capabilities that could be used in industrial applications [69, 93, 94, 228, 229]. The earliest research and commercial codes available for simulations of the interaction of flows and structures undergoing large deformations are based on the ALE method (Figure 9.2a). The ALE approach stems from the early works in Refs. [230–235] and allows the analysis to proceed in a framework which is neither Eulerian nor Lagrangian. That is, the ALE formulation tries to utilize the advantages of both formulations by performing the computations on a fluid mesh following the motion of the structure. The mesh may be moved with the material by using the Lagrangian formulation, it may be kept fixed using an Eulerian framework, or the mesh can be moved arbitrarily using mesh rezoning (i.e., repositioning) algorithms to reduce the distortion. The process of mesh generation, i.e., re-meshing where the whole or parts of the fluid sub-domain is spatially re-discretized multiple times during a computation, can be a troublesome and time consuming task and the mapping (i.e., transfer) of solutions from the distorted mesh to the new mesh may introduce artificial diffusion and loss of accuracy. Furthermore, for large translations and rotations of the structure (or non-uniform movements of the mesh points) fluid elements tend to become ill-shaped which also reflects on the accuracy of the solution.

Recent advances have led to more flexible techniques that overcome these difficulties and limitations related to large deformations and ALE (see e.g. [94, 98, 228, 229, 236–243]). These techniques include so-called fixed mesh methods, and is often denoted immersed [236–238], embedded [94, 98, 239–241], fictitious domain [242] or overlapping mesh methods [243]. In contrast to the ALE technique, where the fluid-structure (F-S) interface is accurately captured (see Figure 9.2a), these types of methods do not require any changes of the fluid mesh. This is due to the basically different approach to represent the FSI by discretizing the structural sub-domain S and the fluid sub-domain F in a

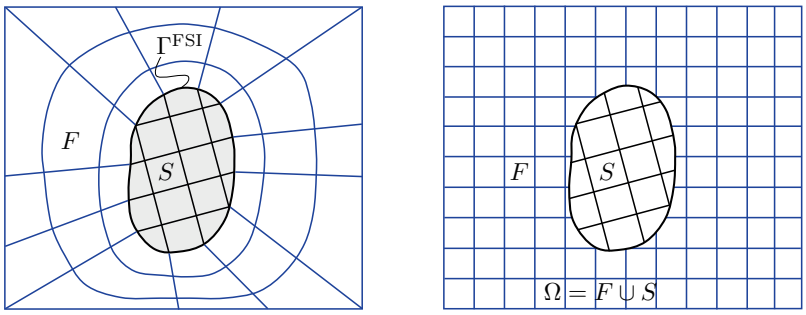

(a) **(b)**

Figure 9.2: Illustration of fully coupled FSI techniques: (a) the structural fitted (conforming) ALE approach where the fluid sub-domain F ends at the structural surface $\Gamma^{FSI} = F \cap S$ and the boundary fluid nodes move with the structure S. The fluid mesh deforms with the structure at the interface Γ^{FSI} and then the mesh deformation is extended into the fluid sub-domain by rezoning algorithms and/or using mesh smoothing. (b) the embedded approach where the structural sub-domain S and the fluid sub-domain F are discretized in a completely independent manner. Thus, the structural mesh is embedded in the fluid mesh, i.e., the two meshes are simply superposed $\Omega = F \cup S$.

completely independent manner (Figure 9.2b). Then, the structural mesh is embedded (or immersed) within the fluid mesh, i.e., the two meshes are simply superposed, allowing the moving and independent Lagrangian structure to slide through the fluid sub-domain [94, 98]. With this technique, it is no longer necessary to use an unstructured (conforming or non-conforming) fluid mesh (Figure 9.2a). The fluid mesh can be structured, and even regular (Figure 9.2b). Furthermore, it is no longer necessary to use an ALE formulation in the fluid sub-domain. This sub-domain can be simplified to a fixed Eulerian background mesh, which completely avoids the problem of mesh distortions. However, as a counterpart, the embedded methods may be somewhat less accurate than the ALE methods for the same mesh size of the fluid [94].

9.3.2 Governing equations

Structures are characterized by definite shapes, which makes a material framework suitable to express their motion since each individual node of the computational mesh follows the associated material particle. The computations in the structural sub-domain are therefore performed using a Lagrangian formulation, where the governing equation is the conservation of momentum also known as

the dynamic equilibrium arising from the principal of virtual power [171]

$$\int_V \delta \mathbf{v}_S^T \rho \frac{\partial \mathbf{v}_S}{\partial t} dV + \int_V \mathrm{tr}((\nabla \delta \mathbf{v}_S)^T \cdot \boldsymbol{\sigma}) dV - \int_V \delta \mathbf{v}_S^T \rho \mathbf{f}_b dV - \int_S \delta \mathbf{v}_S^T \mathbf{t} dS = 0 \quad (9.1)$$

where ρ is the mass density of the current volume V with boundary surface S, $\mathbf{v}_S$ and $\delta \mathbf{v}_S$ are the vectors of velocities and virtual velocities at any point (x, y, z) within V, $\boldsymbol{\sigma}$ is the Cauchy (true) stress, $\nabla \delta \mathbf{v}_S$ is the spatial gradient of the virtual velocity vector, $\mathbf{f}_b$ are the volumetric forces per unit mass and $\mathbf{t}$ are boundary surface tractions. Spatial discretization of the structure (using FEs) in Eq. (9.1) then reads

$$\boldsymbol{M} \boldsymbol{a}_S = \boldsymbol{F}^{\mathrm{ext}} - \boldsymbol{F}^{\mathrm{int}} \quad (9.2)$$

where $\boldsymbol{M}$ is the lumped (diagonal) mass matrix, $\boldsymbol{a}_S$ is the vector of nodal accelerations, $\boldsymbol{F}^{\mathrm{ext}}$ are the external forces and $\boldsymbol{F}^{\mathrm{int}}$ are the internal forces. $\boldsymbol{F}^{\mathrm{ext}}$ and $\boldsymbol{F}^{\mathrm{int}}$ are found by spatial integration over the elements as

$$\boldsymbol{F}^{\mathrm{ext}} = \sum_{n=1}^{N_{\mathrm{els}}} \int_{S_n} \boldsymbol{N}^{\mathrm{T}} \mathbf{t} dS + \sum_{n=1}^{N_{\mathrm{els}}} \int_{V_n} \boldsymbol{N}^{\mathrm{T}} \rho \mathbf{f}_b dV \ , \quad \boldsymbol{F}^{\mathrm{int}} = \sum_{n=1}^{N_{\mathrm{els}}} \int_{V_n} \boldsymbol{B}^{\mathrm{T}} \boldsymbol{\sigma} dV \quad (9.3)$$

where V_n is the volume of element n, $\boldsymbol{N}$ is the matrix of shape functions, $\boldsymbol{B}$ is the matrix of shape functions derivatives, and the summation sign Σ is the assembly operator over all elements from 1 to N_{els}. Eq. (9.2) is solved explicitly using the lumped mass matrix and directly integrated in time using finite differences. The Cauchy stress $\boldsymbol{\sigma}$ is updated in each integration point using the numerical return mapping algorithm in Section 4.4. It is emphasized that the vector of structural velocities $\mathbf{v}_S$ should not be confused with the shock wave velocity v_s.

As already discussed in Chapter 6, shock or blast wave propagation is essentially a problem dealing with inviscid compressible flow (i.e., the density is not constant), where the viscosity is assumed to be zero and the fluid is incapable of developing shear stresses. It is therefore preferable to express the conservation laws in a spatial framework. This is also known as the Eulerian formulation and considers the computational mesh as fixed while the fluid (particles) moves relative to these grid points. Thus, the governing equations for the fluid subdomain express the conservation of mass, momentum and energy, respectively, on conservative form as

$$\begin{aligned} \frac{\partial \rho}{\partial t} + \nabla \cdot (\rho \mathbf{v}_F) &= 0 \\ \frac{\partial \rho \mathbf{v}_F}{\partial t} + \nabla \cdot (\rho \mathbf{v}_F \otimes \mathbf{v}_F) + \nabla p &= 0 \\ \frac{\partial E}{\partial t} + \nabla \cdot (\mathbf{v}_F (E + p)) &= 0 \end{aligned} \tag{9.4}$$

where ρ is the fluid density, $\mathbf{v}_F = v_{F,i}\mathbf{e}_i = [v_{F,1}\ v_{F,2}\ v_{F,3}]^T$ is the fluid (particle) velocity vector with components $v_{F,1}$, $v_{F,2}$ and $v_{F,3}$ along each of the basis vectors in a Cartesian coordinate system $\mathbf{e}_i$, $E = \rho(e + \frac{1}{2}\mathbf{v}_F^T\mathbf{v}_F)$ is the total energy per unit volume, e is the specific internal energy per unit mass (given by an EOS), $\frac{1}{2}\mathbf{v}_F^T\mathbf{v}_F$ is the kinetic energy per unit mass, p is the pressure, ∇ is the spatial gradient, and $\otimes$ gives the tensor product. Eq. (9.4) is known as the Euler equations in differential form. An alternative and rather concise form to represent these equations may be obtained using the vector form already presented in Eq. (6.48), i.e.,

$$\frac{\partial \mathbf{U}}{\partial t} + \nabla \cdot \mathbf{F}(\mathbf{U}) = \mathbf{0} \quad \text{with} \quad \begin{cases} \mathbf{U} = [\ \rho \quad \rho \mathbf{v}_F \quad E\ ]^T \\ \mathbf{F} = [\ \rho \mathbf{v}_F \quad \rho \mathbf{v}_F \mathbf{v}_F + p\mathbf{I} \quad (E+p)\mathbf{v}_F\ ]^T \end{cases} \tag{9.5}$$

where $\mathbf{U}$ is the vector of conserved variables and $\mathbf{F}$ is the associated flux matrix. It is noted that Eq. (9.5) contains five conservation equations, i.e., conservation of mass, conservation of momentum (in the three spatial dimensions) and conservation of energy, with six unknowns. Hence, to find an unique solution of Eq. (9.5) it is necessary to use a suitable EOS to relate the pressure to the conserved variables. This work is limited to the EOS given by the ideal gas law in Eq. (6.2).

Integrating the local conservative form of the Euler Equations in Eq. (9.5) over a control volume fixed in space reads

$$\frac{\partial}{\partial t} \int_{V_f} \mathbf{U} dV + \int_{S_f} \mathbf{F}(\mathbf{U}) \cdot \mathbf{n} dS = 0 \tag{9.6}$$

where $\mathbf{n}$ is the outward unit normal to the boundary surface S_f of the fixed control volume V_f, and the Gauss (divergence) theorem is used to find the flux through the boundary surface of the control volume. The physical interpretation of Eq. (9.6) is that the time variation of $\mathbf{U}$ included in the fixed volume V_f is balanced by the flow of $\mathbf{U}$ through its boundary surface S_f. Using an appropriate discretization in space for the fluid and choosing a suitable discretization of the flux through the boundary surface, the non-linear set of differential equations in Eq. (9.5) may be solved for the discretized unknowns $\mathbf{U}_i$ located at the cell centroid (typically represented by an average value).

However, Eq. (9.6) is no longer valid when the fluid boundary moves to follow the motion of a neighboring and deformable structure. Then, the integration over the control volume is no longer constant in time and its location varies. Thus, the time derivative cannot be moved outside of the volume integral since the time-derivative operator $\partial/\partial t$ corresponds to a fixed position in space, whereas the volume moves in space and deforms. When considering traditional ALE F-S coupling, the fluid mesh has to move and deform to follow the structural motion. Then, Eq. (9.5) is integrated over a moving volume V_m as

$$\int_{V_m} \frac{\partial \mathbf{U}}{\partial t} dV + \int_{S_m} \mathbf{F}(\mathbf{U}) \cdot \mathbf{n} dS = 0 \tag{9.7}$$

where the motion of the moving volume is given by a suitable mesh rezoning (i.e., re-meshing) algorithm. Using the Gauss theorem twice and known relations [244], the first term in Eq. (9.7) may be expressed on a moving volume as

$$\int_{V_m} \frac{\partial \mathbf{U}}{\partial t} dV = \frac{\partial}{\partial t} \int_{V_m} \mathbf{U} dV - \int_{S_m} \mathbf{U}(\mathbf{w}_F \cdot \mathbf{n}) dS \tag{9.8}$$

where $\mathbf{w}_F$ is the velocity of the fluid mesh. This can be interpreted such that the integral over the time variation of $\mathbf{U}$ on a moving volume equals the time variation of the integral over the volume minus the flux of $\mathbf{U}$ across the boundaries due to the edge motion. Combining Eqs. (9.7) and (9.8), the integral on local conservative form over a moving volume reads

$$\frac{\partial}{\partial t} \int_{V_m} \mathbf{U} dV + \int_{S_m} \left[\mathbf{F}(\mathbf{U}) \cdot \mathbf{n} - \mathbf{U}(\mathbf{w}_F \cdot \mathbf{n}) \right] dS = 0 \tag{9.9}$$

where it is observed that the moving mesh introduces an additional flux term corresponding to the flux of $\mathbf{U}$ through the boundary of the volume due to the mesh motion. Since this formulation uses an observation frame which is not fixed in space (Eulerian) nor moves with the material (Lagrangian), but has an arbitrary motion to follow specific boundary condition, this approach is known as the arbitrary Lagrangian-Eulerian (ALE) formulation (also known as the dynamic mesh formulation within the field of fluid mechanics). In the particular case of a FV discretization, the numerical fluxes in Eqs. (9.6) and (9.9) are typically computed using Riemann solvers [88].

9.3.3 FSI algorithms in EUROPLEXUS

Despite the fact that node-centred finite volumes (NCFVs) may be applied for both the strong and weak approach, this thesis focuses only on cell-centred finite volumes (CCFVs) because recent research (see e.g. [94]) considers this as

the most promising formulation (especially if structural failure is of interest). In the particular case of representing the fluid sub-domain with CCFVs, the FV mesh looks similar to a FE mesh. However, all state variables are discretized at the volume centres [130]. From a practical point of view, CCFV discretization is convenient since the same computational grid can be used as in the FE formulation. However, the nodes contain no relevant information other than their Cartesian coordinates used to compute the individual computational volumes since all computations are performed at the centre of each computational cell (thereby the name cell-centred finite volume).

Using the traditional ALE formulation in the fluid sub-domain, the simplest case is obtained by using a nodally conforming mesh. This is illustrated in Figure 9.3a for a shell type of structure S and a fluid F in 2D. Then, each structural node corresponds to a fluid node and the respective nodes are superposed, i.e., having the same coordinates and the nodes may be either merged or distinct. The FSI is then enforced by using the weak approach through a direct application of the fluid pressure forces to the structure without using any constraints. These pressure forces are assembled with other potential external forces $\boldsymbol{F}^{\text{ext}}$ and subsequently used to calculate the dynamic equilibrium in Eq. (9.2). The motion of the ALE nodes at the F-S interface are restricted to follow the motion of the structure and the mesh velocities are governed by the following compatibility condition

$$\mathbf{w}_F = \mathbf{w}_S = \mathbf{v}_S \tag{9.10}$$

ensuring that the structure and fluid meshes move and deform together at the F-S interface (see Figure 9.3a). Thus, the fluid transmits a pressure force to the structure while the interaction only occurs during the motion of the structure, which again is influencing the numerical flux in the fluid at the F-S interface. This is the reason for the name weak coupling.

The weak approach is also applicable in the case of nodally non-conforming F-S meshes [245]. This particular application may be important in practical applications, since a finer fluid mesh is often needed (compared to the structural mesh) to obtain an accurate pressure field. This is often the case when the structure is modeled using shell elements [94]. Figure 9.3b illustrates the so-called hierarchic approach which is considered convenient, since each structural node at the F-S interface corresponds to a fluid node. The opposite is not advisable since the stability step in the fluid elements is usually larger than in the structural elements, and non-matching nodes and a coarser fluid mesh may produce gaps and overlaps at the F-S interface. Eq. (9.10) is still valid for the matching (or conforming) nodes. However, at a non-matching fluid node it is necessary to use the corresponding structural point S^* (see Figure 9.3b) and

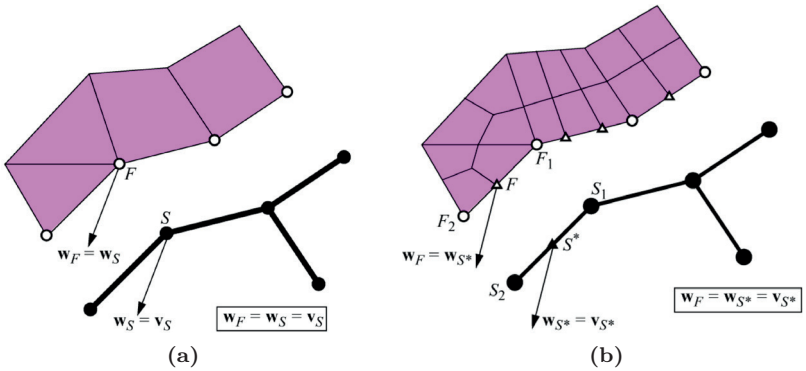

Figure 9.3: Compatibility of fluid and structure mesh velocities: (a) conforming and (b) non-conforming mesh [94]. Note that the fluid (F) and structural (S) nodes are actually superposed, but are shown separately to ease the visualization.

the mesh velocity is given by

$$\mathbf{w}_F = \mathbf{w}_{S^*} = \mathbf{v}_{S^*} = N_1 \mathbf{w}_{S_1} + N_2 \mathbf{w}_{S_2} \tag{9.11}$$

where the velocity $\mathbf{v}_{S^*}$ of the structural point is expressed in terms of nodal structural degrees of freedom (dofs) and suitable shape functions N_i.

The weak approach may also be used in scenarios where structural failure and fragmentation are of interest. Since the velocities are discretized at the volume centres (not at nodes) and represent the average value of the entire volume for CCFVs, the neighboring fluid meshes on either side of the structure can be generated as a continuous mesh (see Figures 9.4b and 9.5a). That is, assuming that fluid nodes are located at the same positions on either side of the structure, these nodes can be merged together independently of whether the fluid mesh are conforming or non-conforming and merged with the structure. Each CCFV then transmits the pressure force to the structure until an element is eroded from from the computation. Then, the fluid flow is allowed to pass freely through the failed structural element.

In the particular case of conforming F-S nodes, the simplest strategy is to merge each structure and fluid node along the boundary (Figure 9.4a). Then, the pressure forces computed in the CCFV act directly upon the structure using the force assembly procedure in Eq. (9.2). The pressure force contribution from the respective CCFV is computed using a pressure $\times$ length (area in 3D) computation (see Figure 9.4a). That is, for each volume with a pressure p the force $\mathbf{f}_p$ is given by

$$\mathbf{f}_p = pL\mathbf{n}_S \tag{9.12}$$

operating along a length L with a unit normal $\mathbf{n}_S$. This force is equally distributed to the structural nodes on L, and is therefore contributing to the motion of the structure.

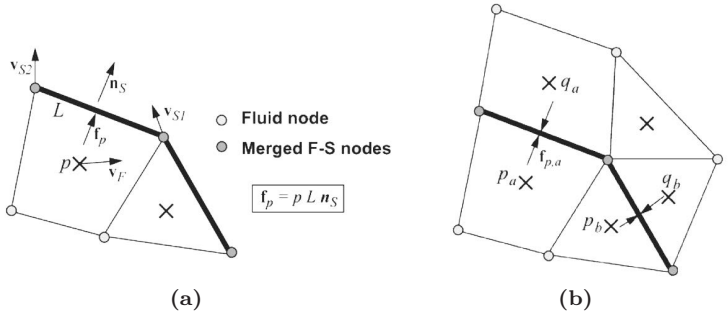

Figure 9.4: Weak approach for a nodally conforming F-S mesh using CCFVs in the fluid sub-domain: (a) fluid sub-domain on one side and (b) fluid sub-domain on both sides [94].

As discussed earlier for the non-conforming case, only some fluid nodes on the F-S interface are matching the structural nodes (Figure 9.5). Since the residual fluid nodes cannot be merged with the structure, the FSI algorithm is then independent of one chooses to merge the matching F-S nodes or not. Figure 9.5a illustrates an example where the matching F-S nodes are kept distinct. Except from this, the only difference from the conforming case is the distribution of fluid pressure forces to the structural nodes. The difference may be explained using Figure 9.5b, where the fluid pressure in the i^{th} CCFV is working over a length L_i (area in 3D) resulting in a pressure force $\mathbf{f}_p$ acting on point C_i (located at the centre of the FV) along the structural element's unit normal $\mathbf{n}_S$, i.e.,

$$\mathbf{f}_{p,i} = p_i L_i \mathbf{n}_S \tag{9.13}$$

where the structural unit normal $\mathbf{n}_S$ coincide with the normal to the fluid face L_i. There is, however, no structural node at point C_i which introduces the need to choose an appropriate method to distribute the pressure to the neighboring structural nodes. This is done by using the fraction of the lengths on each side of C_i, i.e.,

$$\mathbf{f}_{p,Ai} = (L_{Bi}/L_S)\mathbf{f}_{p,i}\ , \qquad \mathbf{f}_{p,Bi} = (L_{Ai}/L_S)\mathbf{f}_{p,i} \tag{9.14}$$

As discussed in Section 9.3.1, the FSI algorithms using an ALE formulation of the fluid sub-domain suffer during large deformations and rotations of the

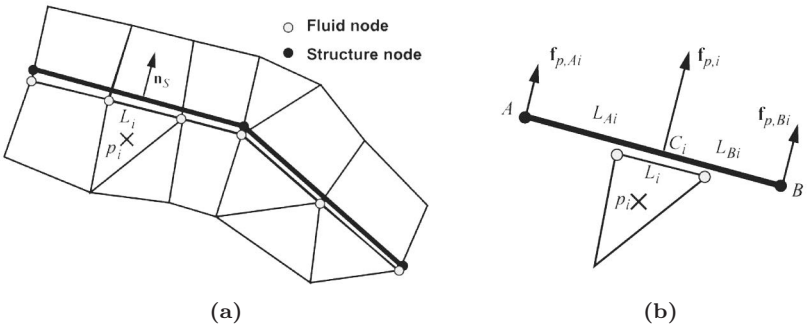

Figure 9.5: Weak approach for a nodally non-conforming F-S mesh using CCFVs in the fluid sub-domain: (a) hierarchic approach with two (continuous) fluid meshes and (b) distribution of pressure forces [94].

structure. The mesh rezoning algorithms are then unable to maintain a regular fluid mesh, resulting in loss of accuracy and the simulation may be aborted. In an attempt to overcome such limitations a somewhat different approach to FSI is introduced, i.e., the embedded mesh method. This method uses a Lagrangian formulation for the structure and an Eulerian formulation of the fluid, where the two sub-domains are discretized independently of each other. The structural mesh is then embedded (or immersed) in a regular Eulerian fluid mesh (see Figure 9.6) and all difficulties related to the mesh rezoning and entangled fluid meshes are therefore avoided since the fluid mesh is fixed. Since the CCFV formulation evaluates the numerical fluxes at the face centres, it is more convenient to search for coupled faces located inside the influence domain (illustrated as small squares in Figures 9.6 and 9.7) rather than searching for coupled fluid nodes. To establish the FSI conditions it is therefore necessary to determine which of the fluid faces that are located at the F-S interface. This is carried out by placing spheres with a given radius (large enough to include the fluid faces at the F-S interface) at each structural node. The spheres are then connected by quadrangles in 2D (or cones, prisms and hexahedra in 3D) creating an area (volume in 3D) around the structure. This is defined as the influence domain and contains the coupled F-S faces (see Figure 9.6a). As the computation proceeds the structure moves and deforms, resulting in the need to continuously updated the faces in the influence domain. Fast search algorithms for the identification of the current F-S faces are therefore essential to keep the computational cost reasonable. It should be noted that too small radius of the spheres allows for spurious flux across the structure, while too large radius link too much of the fluid to the motion of the structure. Thus, the choice of the radius influences the accuracy and CPU cost of the solution.

The basic idea for the weak approach is the same in the embedded method as

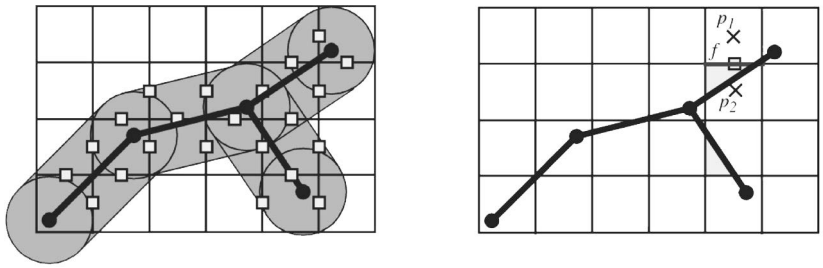

(a) (b)

Figure 9.6: Weak coupling using CCFVs in the embedded FSI approach: (a) faces in the influence domain and (b) calculation of the pressure drop force $\mathbf{f}_{\Delta p}$ [94].

in the traditional ALE methods, i.e., pressure forces in the fluid are computed and then transmitted to the structure rather than imposing certain conditions on the particle velocities. Then, with reference to Figure 9.6b, the coupled face f separates the two volumes V_1 and V_2 with pressures p_1 and p_2, respectively. The pressure drop force $\mathbf{f}_{\Delta p}$ is then evaluated as

$$\mathbf{f}_{\Delta p} = (p_1 - p_2) L \mathbf{n}_f \tag{9.15}$$

where L is the length (area in 3D) of the face and $\mathbf{n}_f$ its unit normal. The force is then distributed from point S^* of the structure closest to the face centre (Figure 9.7a) and to the nodes like in Eq. (9.14), i.e.,

$$\mathbf{f}_{\Delta p,A} = (L_B/L_S)\mathbf{f}_{\Delta p} \,, \qquad \mathbf{f}_{\Delta p,B} = (L_A/L_S)\mathbf{f}_{\Delta p} \tag{9.16}$$

where $L_S = L_A + L_B$. Finally, to avoid spurious leakage of the fluid through the structure, it is necessary to set the numerical fluxes of mass and energy to zero across faces in the influence domain (indicated as a thick shaded line in Figure 9.7b). A classification of the discussed FSI algorithms is presented in Table 9.2.

Table 9.2: A classification of FSI algorithms [130].

FSI algorithm	FSI detection	Basic	Limited structural failure, moderate rotations
		Embedded	Structure can fail, arbitrary rotations
	FSI enforcement	Strong	Constraints on fluid and structure velocities are imposed, e.g. by Lagrange multipliers
		Weak	Pressure forces are transmitted from the fluid (slave) to the structure (master) and structure motion provides weak feedback on the fluid

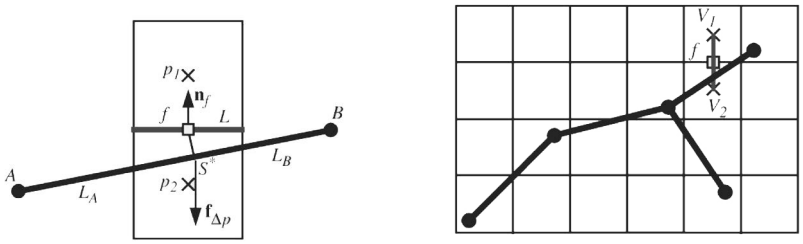

(a) **(b)**

Figure 9.7: Forces and blockages in embedded FSI with weak coupling with CCFV: (a) F-S coupling force and (b) blocking of fluxes [94].

9.4 Uncoupled FSI approach

First, numerical simulations using the uncoupled FSI approach are performed to evaluate the performance of the computational models in each sub-domain and to establish a basis of comparison to the subsequent fully coupled simulations. Purely Eulerian simulations are carried out to evaluate the fluid sub-domain in predicting the pressure histories measured during the massive plate tests in Section 8.3.2. Then, the loading from the massive plate tests in Section 8.3.2 will be used in purely Lagrangian simulations to evaluate the structural sub-domain in predicting the observed dynamic response during the flexible plate tests in Section 8.3.4. Thus, these simulations make the inherent assumption that the pressure is unaltered by the structural motion, and vice versa.

9.4.1 Eulerian simulations

Since the SIMLab Shock Tube Facility (SSTF) was found to produce uniform shock waves over the cross-section in Section 8.3.2, these experiments are basically a 1D problem. The air in the fluid sub-domain was therefore discretized as a 1D model using cell-centred finite volumes ($TUVF$) with a cell size of 10 mm. The diaphragm burst was assumed to be instantaneous and the firing section was not explicitly included in the numerical model. This implied that the initial discontinuity between the driver and driven sections was located at the beginning of the driven section at time $t = 0$. The cell size was determined based on a sensitivity study which showed that this mesh size is sufficient to capture the near instantaneous rise in pressure and distinct peak reflected pressure (see Figure 9.8). Due to the discrete nature (i.e., spatial discretization) of the data sampling in the numerical solution, discontinuities are represented by a finite slope since the pressure values are only defined at the centre of each

computational cell. Variations can therefore not occur in less than one cell size.

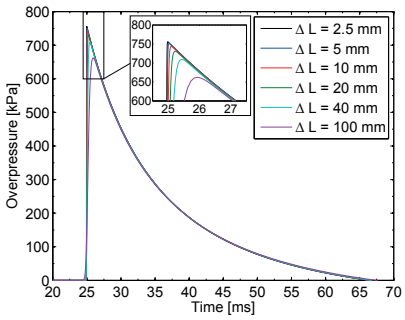

Figure 9.8: Influence of cell size on the near instantaneous rise time and peak reflected pressure in test R27-40.

Stability in the convection phase of the explicit solution in time was ensured by using a Courant-Friedrichs-Lewy (C_{CFL}) coefficient of 0.75. This was to ensure that the exchange of flux only occurred between neighbouring cells, i.e., the fluid material could not be transported through more than one computational cell during one time step $\Delta t < C_{\mathrm{CFL}}\Delta L/c_{\max}$ where ΔL is the length of the cell and $c_{\max}$ is the maximum wave speed at the current time step. The air was modelled using the EOS for the ideal gas material (*GAZP*) in Eq. (6.2), and the initial conditions for each simulation were taken from the massive plate tests in Table 8.1. The solution was obtained by using an Eulerian framework assuming a regular and fixed mesh with rigid boundary conditions at the fluid envelope (i.e., no deformation of the plate) and using the approximate Harten-Lax-van Leer-Contact (HLLC) Riemann solver proposed by Toro [88] to calculate the numerical fluxes. It is noted that *TUVF* in EPX operates with a second order accuracy in time and first order accuracy in space for the HLLC solver [130]. In this approach, the computational domain is basically considered as many neighboring shock tubes to estimate the fastest signal velocity emerging from the initial discontinuity at the interface between adjacent cells. The numerical solution assumed an inviscid flow by using the Euler equations in Eq. (9.5) and will therefore serve as an idealized solution with zero energy loss.

Figure 9.9 compares the blast properties in the experiments and numerical simulations, while Figure 9.10 shows a comparison of the pressure histories for the representative tests discussed earlier in Section 8.3.2. The blast properties from the simulations in Figure 9.9 were extracted and calculated following the same procedure as in the experiments. In most of the cases, there is a good agreement between the numerical and experimental results. However, there seems to be a trend of increasing deviation at peak reflected overpressures $p_{\mathrm{r,max}}$ larger than 800 kPa (i.e., in test R27-60, R27-75, and R77-25 to R77-75).

Figure 9.10 also confirms this trend. That is, the pressure histories are in good agreement in terms of the timing and magnitude of the incident pressures (Figure 9.10a-f), while the peak reflected pressures start to deviate from the numerical simulations at approximately 800 kPa (Figure 9.9a and Figure 9.10d-f). Although the curves are shifted in time such that the time is equal to zero when the shock wave arrives at Sensor 1, the timing of the direct jump from ambient pressure to peak reflected pressure at Sensor 3 and the recordings of the incident and reflected waves at Sensors 1 and 2 corresponds well with the experimental measurements. This indicates that the simplified Eulerian model captures most of the events occurring in the experiments. However, there are also some physical phenomena that may not be predicted by this model. Possible explanations for these deviations may be a minor leakage of pressure in the vicinity of the massive steel plate during the tests, the assumption of an instantaneous release of the high pressures in the simulations, friction against the interior walls of the tube, or a combination of all these events.

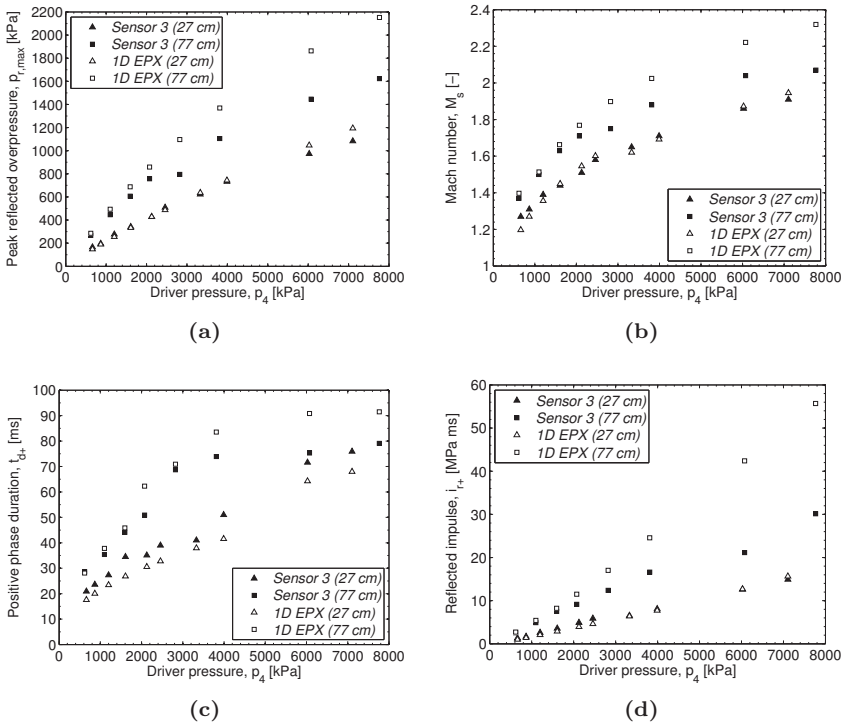

Figure 9.9: Comparison of numerical and experimental results in terms of the blast parameters as a function of driver length and driver pressure. The time window of interest is limited to the positive phase measured by Sensor 3: (a) peak reflected overpressure $p_{\mathrm{r,max}}$, (b) Mach number M_{s}, (c) positive phase duration $t_{\mathrm{d}+}$ and (d) reflected impulse $i_{\mathrm{r}+}$. The position of the pressure sensors is shown in Figure 8.1a-c.

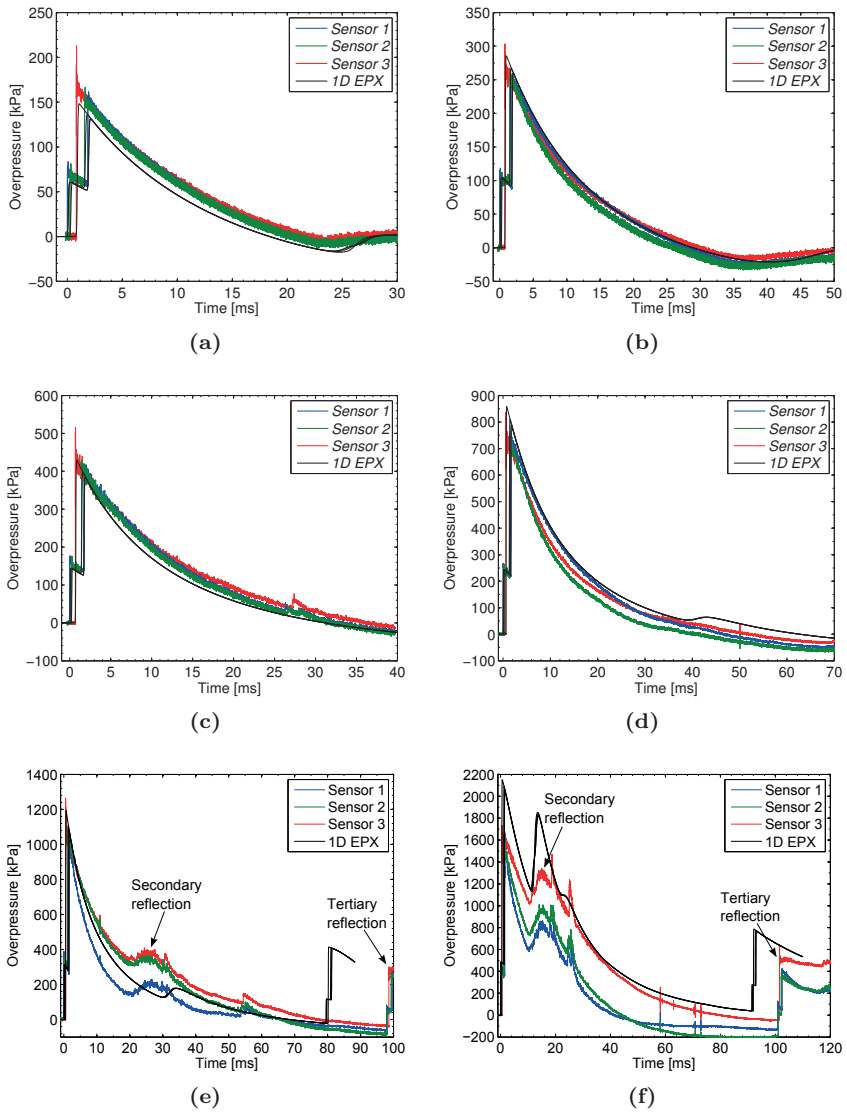

Figure 9.10: Representative pressure histories from experiments (Sensors 1-3) and corresponding numerical simulations in EPX: (a) R27-05, (b) R77-05, (c) R27-20, (d) R77-20, (e) R27-75 and (f) R77-75.

A comparison of experimental and numerical results in terms of the pressure propagation downstream the diaphragm would be useful in an attempt to identify the governing parameter for the observed deviations. Unfortunately, the number of sensors were limited by the available channels in the data acquisition system which at the time of these experiments consisted of 12

channels. The experimental setup was therefore only capable of measuring the pressure in Sensors 1-12 during the massive plate tests (see Figures 8.1a and 8.1c). However, the remaining tests with flexible plates enabled the measurement of the pressure at 8 different locations downstream the tube (see Figure 8.1b). A comparison of the numerical and experimental results at these locations are therefore shown in Figure 9.11 for test D77-05 (Figure 9.11a), D77-15 (Figure 9.11b), D77-25 (Figure 9.11c) and D77-35 (Figure 9.11d). Note that the curves were shifted in time such that the time is equal to zero when the shock wave arrives at Sensor 13.

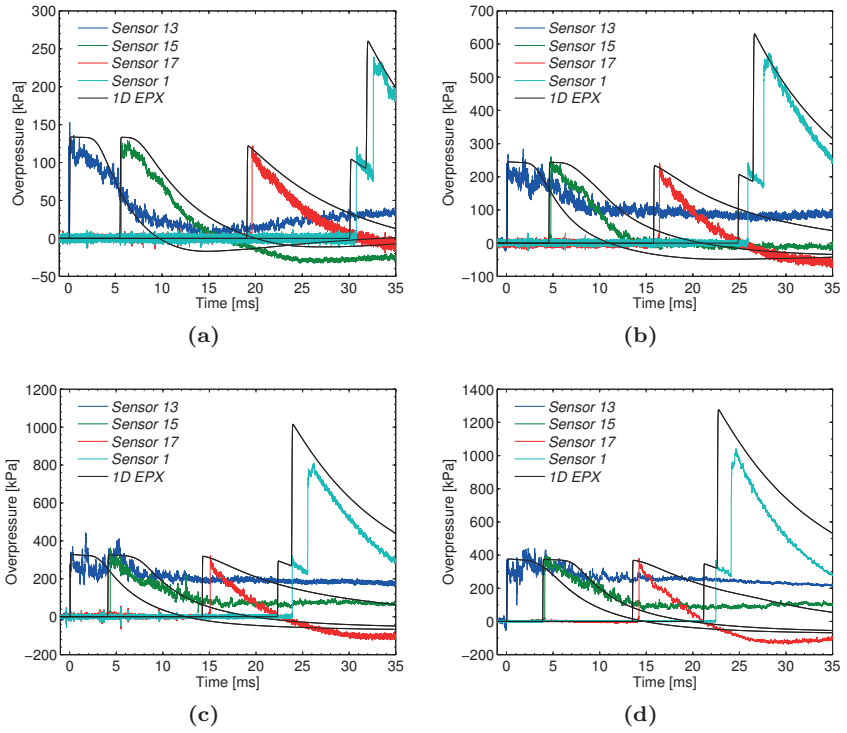

Figure 9.11: Comparison of experimental and numerical results in terms of the recorded overpressure at Sensors 13, 15, 17 and 1: (a) D77-05, (b) D77-15, (c) D77-25 and (d) D77-35. Recall that the respective sensors were positioned 0.97 (Sensor 13), 3.70 (Sensor 15), 10.51 (Sensor 17) and 15.85 m (Sensor 1) downstream the firing section (see Figure 8.1b).

It is evident that the numerical model is unable to predict the experimental measurements closest to the firing section (i.e., Sensor 13). This indicates that some directional energy seems to be lost in the beginning of the tests due to diaphragm opening effects, while the reduced shock velocity point towards friction effects against the interior tube walls. The reduced shock velocity is

observed as a delay in time-of-arrival at the respective sensors compared to the numerical simulations and this trend increases with distance downstream the diaphragms. In reality there are some energy lost due to an initial 3D flow in the vicinity of the firing section during the diaphragm opening process. The diaphragm burst starts by tearing at the centre followed by diagonal tearing and folding back of the petals formed during the opening process. This results in a high-velocity jet and 3D flow of the driver gas originating from the expanding hole. The finite opening time causes the shock wave to travel several tube diameters before the blast wave is fully formed (see Section 6.4.6), and this effect is more evident at increasing firing pressures. Increasing driver pressures involve more diaphragms of larger thicknesses resulting in a slower diaphragm opening process preventing satisfactory folding back and increased obstructed flow during the opening process. This is also indicted in Figure 9.11 where it seems that the blast wave is formed somewhere between Sensors 13 and 15 in the experiments. The issue related to loss of directional energy during 3D flow in the diaphragm opening process can be overcome by using a 3D model including the diaphragm [119], or by reducing the shock strength and delaying the reflected rarefaction wave by increasing the driver length and reducing the firing pressure to obtain the experimental pressure profile in the vicinity of the test specimen [120]. Still, it must be emphasized that increasing the driver length and reducing the firing pressure will alter the physics of the wave pattern upstream the test specimen. A more detailed investigation of the diaphragm opening process and friction against the interior walls are considered beyond the scope of this thesis. Modelling and simulation of the diaphragm opening process would also require a characterization of the Melinex material. The numerical model is therefore considered sufficient for qualitative studies on the influence of FSI effects on the dynamic response of blast-loaded plates.

Finally, it is also observed that the numerical simulations predict the secondary and tertiary reflections observed in the experiments (Figure 9.10e-f). However, the tertiary reflections occur earlier in the simulations. Plausible explanations for this observation may again be friction along the interior walls or that the solenoid valves in the firing section remain open during testing. Both of these explanations allow for loss of directional energy (and velocity) when the waves reflect at the rear end of the driver section. Note that the tertiary reflection in tests R77-60 and R77-75 was observed before the reflected pressure returned to ambient conditions in the simulations (Figure 9.10f). This implies that the corresponding values in Figure 9.9c are somewhat underestimated, since the end of the positive phase duration in these simulations was taken as the point of the tertiary reflection. Figure 9.12 contains pressure and density profiles along the longitudinal axis of the tube at characteristic times for representative tests. R77-20 (Figure 9.12a) follows to a large extent the schematic representation given in Section 6.4.1, while R77-75 (Figure 9.12b) shows that the relative

strength between the left-running reflected shock wave and the remaining right-running flow (contact surface and rarefaction waves illustrated as region E in Figure 6.13a) produces a secondary reflection at the right end of the tube after 35 ms to obtain pressure equilibrium. This is the same secondary reflection as that observed in Figure 9.10f, where it should be noted that the time is corrected for the time of arrival ($t_a \approx 21$ ms) at Sensor 1 in Figure 9.10f. The secondary reflections occur before the reflected shock wave interacts with the end of the driver section (at $x = 0$ in Figure 9.12).

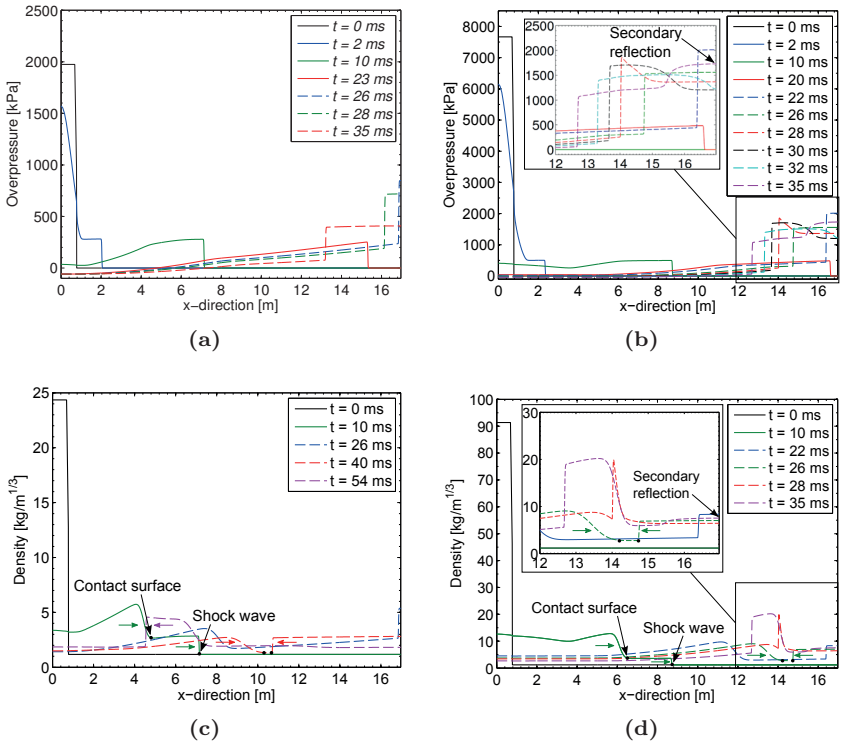

Figure 9.12: Pressure and density distribution along the longitudinal axis of the tube illustrating the wave pattern for representative tests: (a) pressure in R77-20, (b) pressure in R77-75, (c) density in R77-20 and (d) density in R77-75.

This may be explained by studying the density profiles along the tube, because the contact surface represents the mass motion of the gas compressed by the shock wave and therefore also a jump in density. Figures 9.12c-d show that the secondary reflection depends on the momentum and timing of the impact between the contact surface and the reflected shock wave. Although the remaining tail of the right-running wave has smaller magnitudes in pressure compared to the reflected left-running shock front (Figures 9.12a-b), the velocity

of the reflected shock wave is decreasing as it travels through the remaining tail of the right-running wave. Moreover, depending on the relative strength in density at the interface between the right-running contact surface and the left-running reflected shock wave, there may be an increase of density behind the reflected shock wave to restore pressure equilibrium (Figure 9.12d). This is observed as a second peak on the pressure measurements at the massive plate in Figure 9.10e-f during the exponential decay to ambient conditions, and illustrates the importance of choosing a suitable combination of driver length and driver pressure to produce pressure profiles similar to that in idealized blast environments.

9.4.2 Lagrangian simulations

The numerical modelling of the flexible plates follows to a large extent the same approach as in Section 5.2.1. That is, the clamping frames, bolts and plate were represented using a Lagrangian discretization of the entire clamping assembly (see Figure 9.13). The plate was modelled with a mesh size of approximately 10 mm (Figures 9.13b and 9.13d) and 4-node Reissner-Mindlin shells (*Q4GS*) with 6 dofs per node and 20 Gauss integration points (5 through the thickness). The mesh size was determined based on a sensitivity study which showed that the global deformation converged at an element size of 10 mm. Moreover, the material behaviour of the plates was governed by the *VPJC* model with material and physical constants from Table 9.1 and Table 4.2. Failure was modelled using element erosion and was activated when all the integration points in the respective element reached the critical value of unity for the damage parameter in Eq. (4.36). The bolts and clamping frames were represented by 8-node brick elements (*CUB8*) with 8 Gauss points and the *VPJC* model with a high elastic limit to ensure elastic behaviour using the physical constants for steel in Table 4.2.

As in Section 5.2.1, the steel mounting frame and the bolts were modelled as one component (Figure 9.13a). The bolts were modelled as stress-free while an external pressure was applied in the contact area between the bolt head and the clamping frame to simulate the pre-tensioning of each bolt (see Figures 9.13c and 9.13d). The contact pressure was determined using the approach suggested in Ref. [157] where the pre-tensioning force $F_p = M_t/k\phi$ in each bolt was found from the applied torque ($M_t = 200$ Nm), bolt diameter ϕ, thread geometry and friction in the thread engagements and under the bolt heads. Based on the studies in Section 5.2.1, the thread geometry and friction were accounted for by setting the friction coefficient k to 0.18. The contact area was set to 1107 mm^2 which corresponded to the area in magenta at the surface of the clamping frame in Figures 9.13c and 9.13d. Dividing the pre-tensioning force ($F_p = 46.6$ kN) in each bolt by this contact area resulted in a contact pressure of 42.1

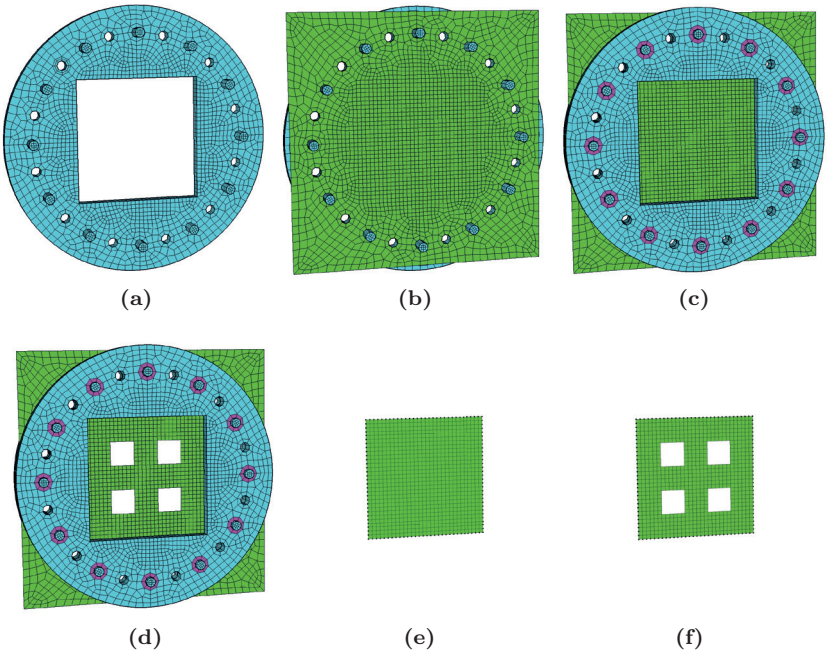

Figure 9.13: Numerical model showing (a) steel mounting frame and bolts as one component (in cyan), (b) plate specimen is added (in green), (c) complete assembly including the clamping frame (also in cyan) and contact area between bolt heads and clamping frame (in magenta) used to model the effect of the pre-tensioning of the bolts, (d) complete assembly with pre-formed holes in the plate specimen, simplified model using only the exposed area of the plate (e) without holes and (f) with pre-formed holes. The black markers in (e) and (f) illustrate the nodes fixed against translation in all directions.

MPa between the bolt head and the clamping frame. Contact between the plate, bolts and frames was modelled using a node-to-surface contact algorithm (*GLIS*) using slave nodes and master surfaces where contact was enforced by Lagrangian multipliers when a slave node penetrated a master surface. The contact then occurs along sliding surfaces, where the nodes of the plate served as the slave while the master surfaces were defined as the mounting frame and the clamping frame. An additional contact condition was also needed to avoid artificial penetration of the plate into the mounting frame. That is, a third contact condition was included where the master surface consisted of the shell elements along the perimeter of the exposed area while the slave nodes were the nodes of the mounting frame in the same area. The thickness of the plate was accounted for by applying a gap of 0.4 mm (i.e., half the plate thickness) between the plate and clamping frames to avoid initial penetrations in the contact surfaces. Friction was activated between the plate and the frames by

using the same coefficients as in Section 5.2.1, i.e., a static and dynamic friction coefficient of 0.15 and 0.10, respectively.

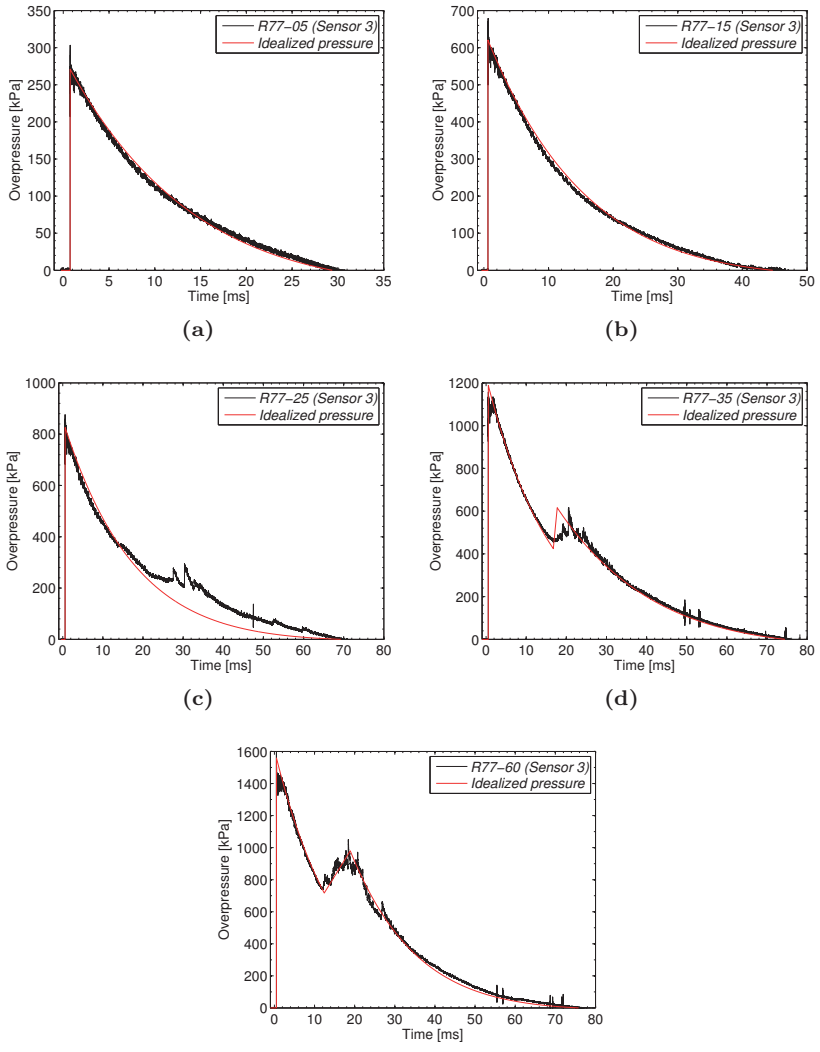

Figure 9.14: Idealized pressure histories imposed on the thin steel plates based on the massive plate tests in Section 8.3.2: (a) R77-05, (b) R77-15, (c) R77-25, (d) R77-35 and (e) R77-60. The idealized curves are found using curve-fitting of the Friedlander curve to the experimental data from Sensor 3 (see also Table 8.5).

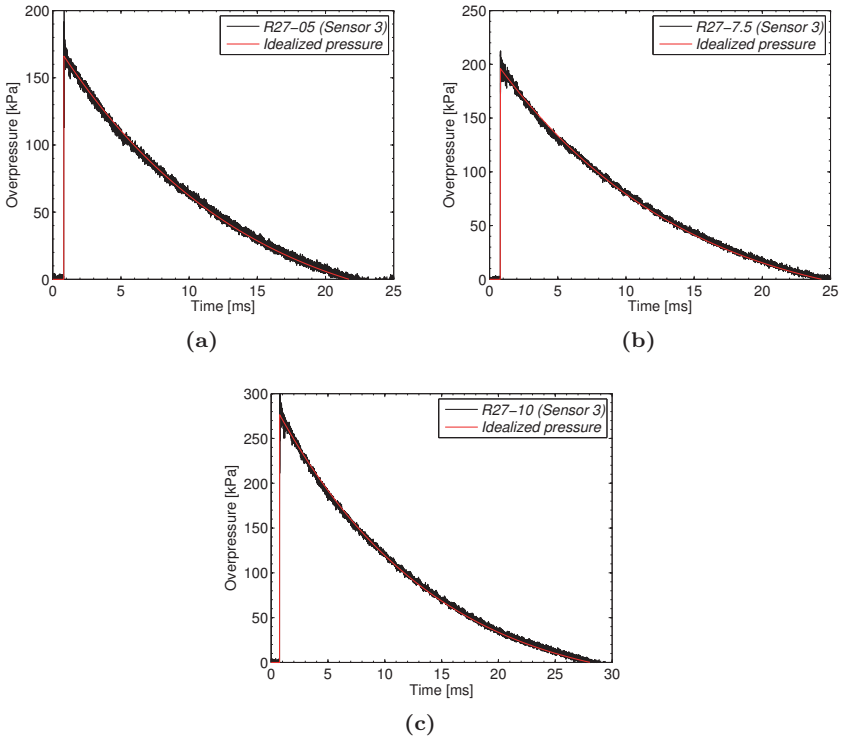

Figure 9.15: Idealized pressure histories imposed on the thin aluminium plates based on the massive plate tests in Section 8.3.2: (a) R27-05, (b) R27-7.5 and (c) R27-10. The idealized curves are found using curve-fitting of the Friedlander curve to the experimental data from Sensor 3 (see also Table 8.5).

The loading was applied using the pressure histories from the massive plate tests in Section 8.3.2 with similar blast intensities as the flexible plate tests. This was imposed as a uniformly distributed pressure on the exposed area of the plate and idealized as shown in Figures 9.14 and 9.15. Thus, these simulations make the inherent assumption that the pressure is unaltered by the plate deformation. Finally, as in Section 5.2.3, the influence of boundary conditions was also investigated by comparing the dynamic response in the clamped assembly to that in a simplified model. The simplified model contained only the exposed area of the plate where all nodes located along the perimeter were fully fixed against translation in all directions (see Figures 9.13e and 9.13f). Note that the investigations and discussions on the influence of mesh size and boundary conditions are limited to the thin steel plates in this section, since the aluminium plates contribute with limited additional information compared to the additional amount of text in describing more or less the same qualitative trends. The relevant simulations of the aluminium plates using the uncoupled

approach will therefore be presented during the investigations of FSI effects in Section 9.5.1.

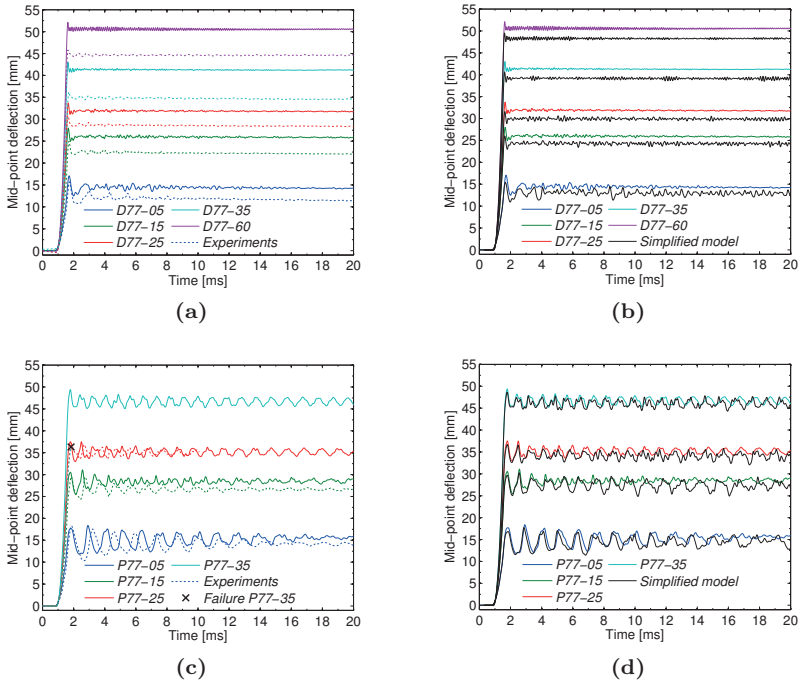

Figure 9.16: Mid-point deflection in the simulations using the uncoupled approach: (a) comparison of experimental data (dashed curves) and the clamped assembly for plates without holes, (b) clamped assembly versus simplified model, (c) comparison of experimental data and the clamped assembly for plates with pre-formed holes and (d) clamped assembly versus simplified model in simulations with pre-formed holes. The numerical results are obtained using the models presented in Figure 9.13.

The numerical results of the thin steel plates are compared to the experimental data in terms of mid-point deflection versus time in Figure 9.16, while the corresponding maximum $d_{\mathrm{z,max}}$ and permanent $d_{\mathrm{z,p}}$ mid-point deflections are summarized in Table 9.3. A negative value of $\Delta d_{\mathrm{z,max}}$ in Table 9.3 implies that $d_{\mathrm{z,max}}$ was larger in the simulation compared to the corresponding experiment. In general, the mid-point deflections are overestimated in both the clamped assembly and simplified model for the plates without holes (Figures 9.16a-b), while the plates with pre-formed holes are in better agreement with the experimental data (Figure 9.16c-d). There also seems to be a slight trend of increased deviations between the experimental and numerical results with increasing blast intensities for the simulations of plates without holes (Table 9.3). As expected, the deflections in the simplified model were slightly less

than those in the clamped assembly (Figures 9.16b and 9.16d). The simplified model also resulted in larger oscillations around the permanent equilibrium configuration after the elastic rebound (Figures 9.16b and 9.16d). It is important to emphasize that, although the simplified model is closer to the experimental data in Table 9.3, this model does not necessarily provide better predictions than the clamped assembly. This is due to the fact that the loading neglects FSI effects (Figure 9.14) and is therefore conservative. Thus, the loading may be overestimated in these simulations.

Table 9.3: Comparison of experimental and numerical results in terms of mid-point deflections.

Test	Experimental results		Numerical results					
			Clamped assembly			Simplified model		
	$d_{z,max}$ [mm]	$d_{z,p}$ [mm]	$d_{z,max}$ [mm]	$d_{z,p}$ [mm]	$\Delta d_{z,max}$ [%]	$d_{z,max}$ [mm]	$d_{z,p}$ [mm]	$\Delta d_{z,max}$ [%]
D77-05	15.7	11.4	17.1	14.3	-8.9	15.4	12.9	1.9
D77-15	25.0	22.1	28.0	25.9	-12.0	26.0	24.3	-4.0
D77-25	30.8	28.4	33.7	31.8	-9.4	31.6	29.9	-2.6
D77-35	36.2	34.6	43.0	41.2	-18.8	40.6	39.1	-12.2
D77-60	45.8	44.5	52.1	50.5	-13.8	49.5	48.3	-8.1
P77-05	18.3	14.2	18.4	15.4	-0.5	17.7	14.5	3.3
P77-15	29.5	26.6	31.1	28.5	-5.4	30.3	27.3	-2.7
P77-25	37.2	34.9	37.5	35.2	-0.8	36.7	34.1	1.3
P77-35	N/A*	N/A*	49.4	46.6	N/A*	48.7	46.0	N/A*

*Experiment resulted in complete failure along the diagonals.

The good agreement with the experimental observations for both the clamped assembly and the simplified model in the simulations of the plates with pre-formed holes, may indicate a limited effect of the boundary conditions in these tests. This observation is also supported by a visual inspection of the in-plane sliding at the support in tests D77-35 and P77-35 (see Figure 9.17), where the maximum horizontal and vertical sliding at the support are approximately 1 mm (Figures 9.17a and 9.17b) and 0.5 mm (Figures 9.17c and 9.17d) for the D77-35 and P77-35 tests, respectively. Thus, the pulling-in effect in test D77-35 is approximately twice that in test P77-35. Similar trends were also observed for the equivalent stress σ_{eq} in the clamped assembly and simplified model in test P77-35 (see Figure 9.18b), while there seems to be a more distinct difference in the distribution between the two numerical models in test D77-35 (see Figure 9.18a).

Even though the numerical results were encouraging, neither the clamped assembly or the simplified model were able to predict the failure observed in test P77-35 (Figures 9.16c and 9.16d). This is illustrated in Figure 9.19 indicating that a mesh size of 10 mm was too large to predict the same extent of localization in the extremities of the pre-formed holes as in the tests. However, it is worth noting that the simplified model (for both P77-35 and D77-35) in

Figure 9.19 predicts more or less the same damage evolution as in the exposed area of the clamped assembly. This indicates that the simplified model could be used in a qualitative study on the influence of mesh size on the failure pattern of the plates with pre-formed holes.

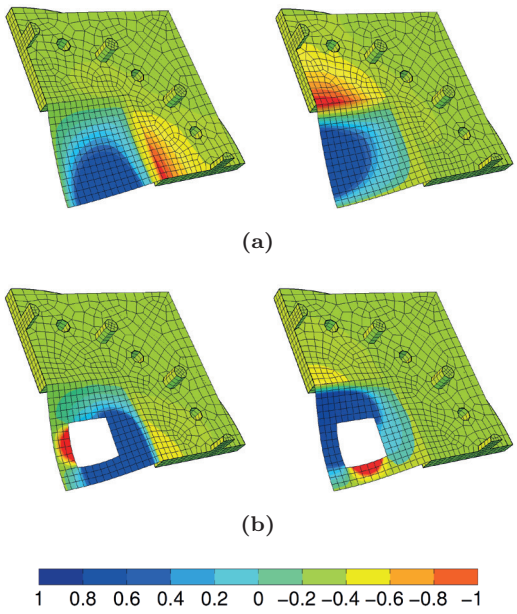

Figure 9.17: In-plane sliding in the horizontal (left) and vertical (right) directions of the clamped assembly using 1/4 of the geometry: (a) D77-35 and (b) P77-35. Fringe colors represent the in-plane displacement (in mm) at maximum deflection.

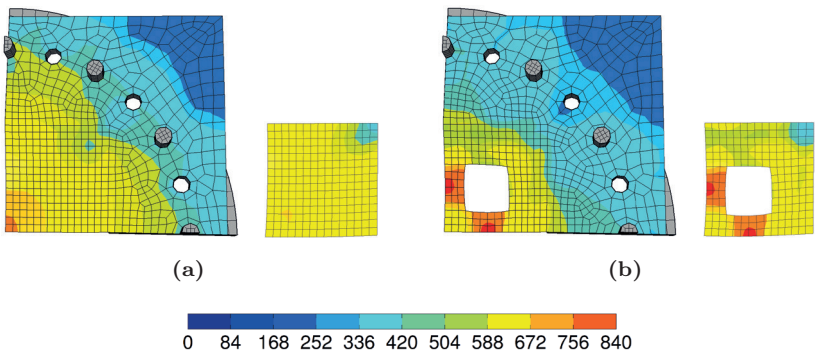

Figure 9.18: Equivalent stress σ_{eq} in the clamped assembly (left) and simplified model (right) using 1/4 of the geometry: (a) D77-35 and (b) P77-35. Fringe colors represent σ_{eq} (in MPa) at maximum deflection.

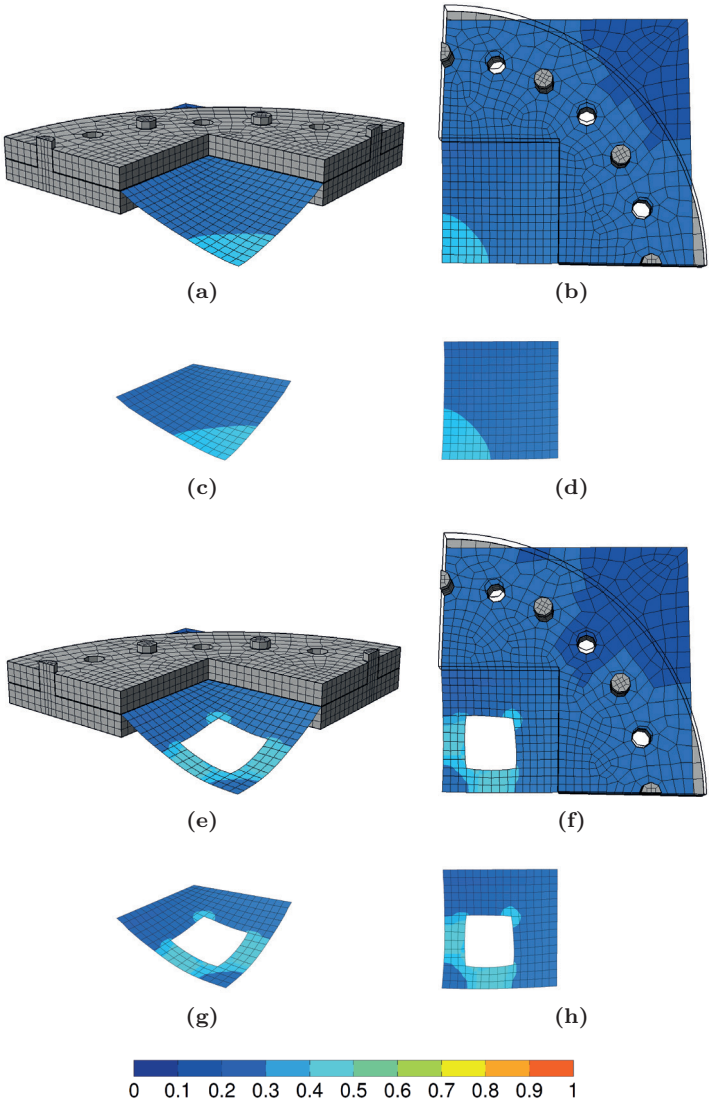

Figure 9.19: Inspection of the damage evolution using 1/4 of the model: clamped assembly in test D77-35 (a) without and (b) with transparent clamping frame, simplified model of test D77-35 in (c) perspective and (d) front view, clamped assembly in test P77-35 (e) without and (f) with transparent clamping frame, simplified model of test P77-35 in (g) perspective and (h) front view. Fringe colors represent the damage parameter in Eq. (4.36) after the permanent deflection is reached.

The influence of the mesh size on the damage evolution was therefore studied by uniformly refining the simplified model of test P77-35. Figure 9.20 shows the chosen mesh sizes of 5.0 (Figure 9.20a), 2.5 (Figure 9.20b), 1.25 (Figure

9.20c) and 0.8 mm (Figure 9.20d). A simulation with 0.8-mm mesh was also carried out for test P77-25 since this was at the limit between initiation and growth of the cracks (see Figure 8.19c). Note that the plate itself is barely visible in Figure 9.20c and 9.20d due to the dense mesh.

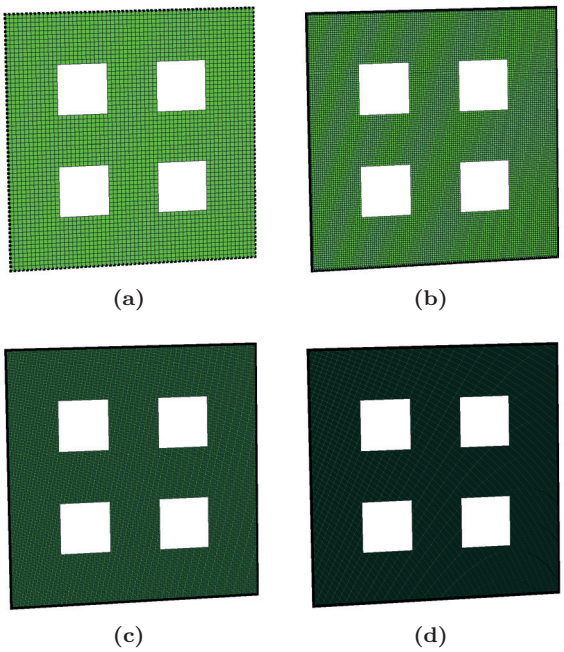

Figure 9.20: Uniform refinement of simplified model with pre-formed holes showing a mesh size of (a) 5 mm, (b) 2.5 mm, (c) 1.25 mm and (d) 0.8 mm. The black markers illustrate the nodes fixed against translation in all directions.

Figure 9.21 compares the damage evolution at 4.0 ms in test P77-35 with 5.0-mm, 2.5-mm and 1.25-mm mesh size, while Figures 9.22 and 9.23 give a more detailed presentation of the 0.8-mm mesh for tests P77-35 and P77-25, respectively. It is evident that larger elements diffuse the failure process and are not capable of predicting the localized damage in the extremities of the pre-formed holes. This is expected due to the discrete nature of the FE method. Although failure is observed at a mesh size of 1.25 mm (Figure 9.21c), a mesh size of 0.8 mm is necessary to recreate the failure patterns observed in the experiments (see Figure 9.22). In fact, compared to the experimental observations in Figures 8.19 and 8.20, the 0.8-mm mesh predicted almost exactly the same failure pattern in test P77-35 while the crack initiation in test P77-25 was slightly underestimated. It is worth noting that a 0.8-mm mesh size is at the very limit of what is recommended for shell elements when activating thinning of the element and that further refinements should be

carried out with solid elements. It should also be emphasized that the choice of the failure parameter in Section 9.2 is considered to be non-conservative, because the value of W_c was determined at the force level where failure was observed in the tension test. This is the force level where complete tearing (through-surface-crack) occurs, while failure is actually assumed to initiate inside the specimen at an earlier point in time.

Table 9.4 is included to illustrate the increased CPU time when (uniformly) refining the mesh, where the CPU costs, number of time steps and critical time step Δt_{cr} are compared after 4.0 ms. Even though the 0.8-mm mesh predicted almost exactly the same crack growth as in the experiments, the corresponding increase in CPU cost is significant and should be considered when performing fully coupled FSI simulations. The computer used to perform these simulations was a stationary PC with an Intel(R) Core(TM) i7-6700 processor and 32 GB of RAM running on the Windows 7 (64-bits) operating system. All simulations were limited to in-core single-processor calculations.

Table 9.4: Illustration of increased CPU cost (at $t = 4.0$ ms) during uniform mesh refinement of the simplified model in test P77-35.

Mesh size [mm]	CPU cost	Time steps	Δt_{cr} [μs]
10.0	40.8 s	2919	1.34
5.0	3.4 min	5861	0.67
2.5	27.2 min	11,920	0.33
1.25	3.8 h	24,188	0.16
0.8	18.8 h	36,293	0.08

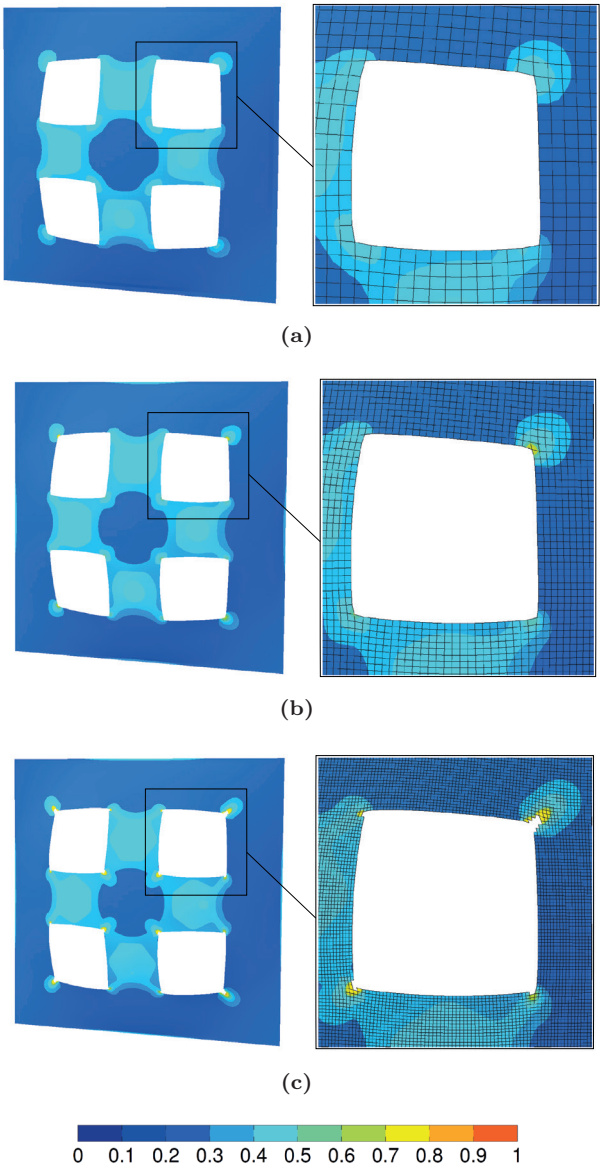

Figure 9.21: Damage evolution at t = 4.0 ms in the simplified model for test P77-35 with different mesh size: (a) 5.0-mm, (b) 2.5-mm and (c) 1.25-mm mesh. Note that the element outlines are hidden (left) to improve the visibility of the damage contours. Fringe colors represent the damage parameter in Eq. (4.36).

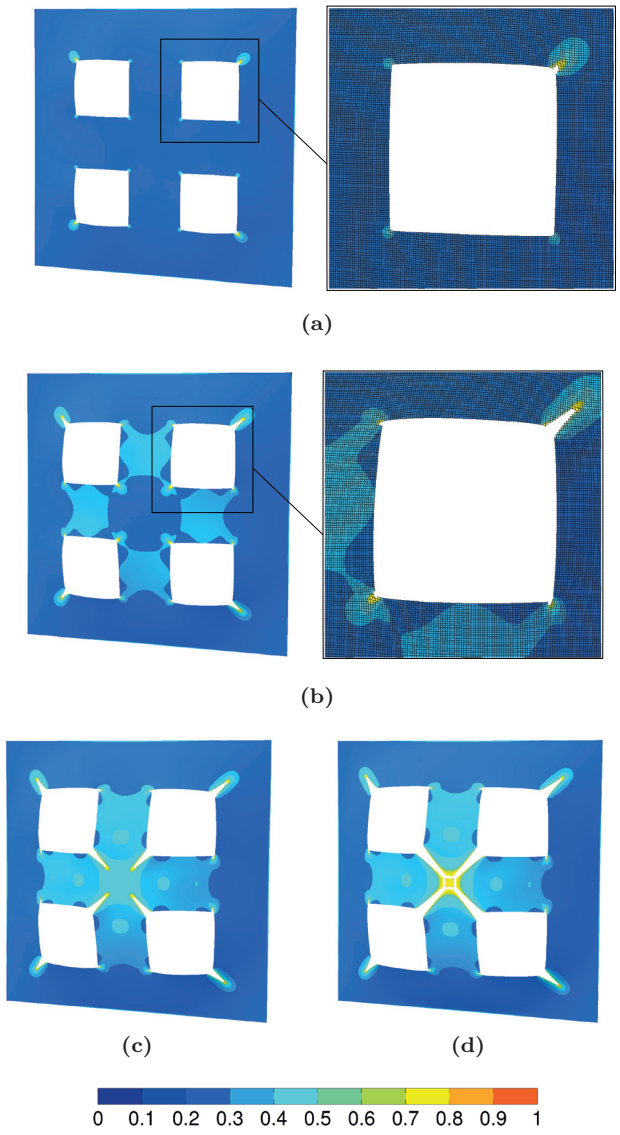

Figure 9.22: Crack growth in the simplified model for test P77-35 and 0.8-mm mesh size: (a) t = 0.98 ms, (b) t = 1.18 ms, (c) t = 1.52 ms and (d) t = 2.18 ms. Note that the element outlines are hidden (except in (a) and (b) right) to improve the visibility of the damage contours. Fringe colors represent the damage parameter in Eq. (4.36).

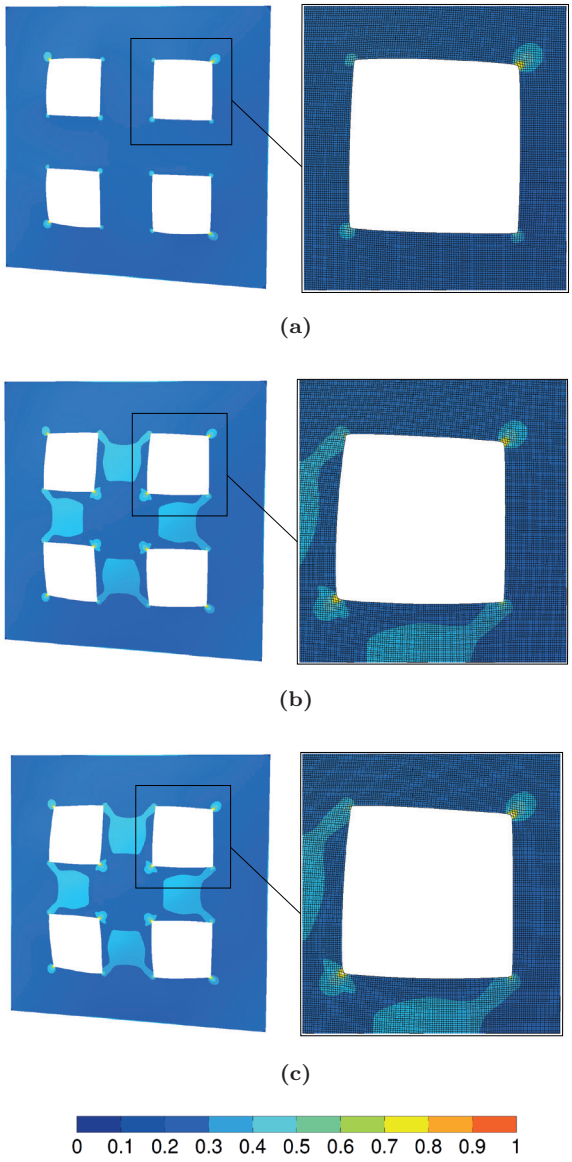

Figure 9.23: Crack growth in the simplified model for test P77-25 and 0.8-mm mesh size: (a) t = 1.18 ms, (b) t = 1.52 ms and (c) t = 4.0 ms. Note that the element outlines are hidden (left) to improve the visibility of the damage contours. Fringe colors represent the damage parameter in Eq. (4.36).

It is clear that a fine mesh size is necessary to predict the localization and crack growth observed during the tests (see Figures 9.21, 9.22 and 9.23). However, since the increase in CPU cost was significant when uniformly refining the mesh (see Table 9.4), it is desirable to evaluate the capabilities and potential reduction in CPU time when using adaptive mesh refinement (AMR) in the plate. Recent advancements in EPX [95–97] allow for AMR based on a user-defined threshold criterion, where the AMR will be driven by the damage evolution in Eq. (4.36) in the following. That is, the mesh refinement occurs at user-defined levels of the damage parameter and at successive levels of refinement within the threshold range of $D_{\min} \leq D \leq D_{\max}$. It is important to note that for this approach to be useful the mesh should be refined relatively long before the element is eroded. However, since it is unclear what is considered to be a suitable damage threshold, it was decided to perform a parametric study on the influence of the initial mesh size and the lower $D_{\min}$ and upper $D_{\max}$ threshold values in an attempt to find appropriate parameters to be used in the subsequent simulations.

A basis model was therefore defined with an initial mesh size of 10 mm, $D_{\min} = 0.005$, $D_{\max} = 0.1$ and 4 successive mesh refinements. The influence of the initial mesh size, $D_{\min}$ and $D_{\max}$ on the failure pattern in test P77-35 was then investigated by varying these parameters between 3 to 10 mm, 0.005 to 0.02, and 0.05 to 0.2, respectively. The number of successive refinements was chosen such that the refined element size was approximately equal to the plate thickness (see Table 9.5), and the elements were eroded when the damage parameter D reached unity in all integration points. The resulting failure patterns at 3.0 ms are illustrated in Figures 9.24, 9.25 and 9.26, while the corresponding CPU costs are summarized in Table 9.5. The CPU costs are compared to that in the uniformly refined 0.8-mm mesh at 3.0 ms. It should be noted that these investigations were limited to the tests experiencing complete failure, because the global response was more or less predicted by the uniform 10-mm mesh. Moreover, as for the influence of mesh size and boundary conditions presented earlier in this section, the following is limited to the thin steel plate in test P77-35 because the same findings were also obtained for the aluminium plate in test A27-10. The relevant simulations of the aluminium plates will therefore be presented during the investigations of FSI effects in Section 9.5.

Figures 9.24, 9.25 and 9.26 illustrate that the AMR technique is capable of predicting crack initiation and growth in the plate. In almost all combinations in Table 9.5, the damage localizes at the extremities of the pre-formed holes. It is also observed a significatnt reduction in the CPU cost when using AMR compared to the 0.8-mm mesh in Figure 9.20d (see Table 9.5). However, depending on the mesh size, number of refinements and damage threshold, the

Table 9.5: CPU cost in test P77-35 (at $t = 3.0$ ms) using the simplified model with AMR at the selected combinations of initial mesh size, $D_{\min}$ and $D_{\max}$.

Initial mesh [mm]	$D_{\min}$	$D_{\max}$	Refinements	Refined mesh [mm]	CPU cost	ΔCPU [%]
0.8*	N/A	N/A	N/A	0.800	14.1 h	-
10**	0.005	0.10	4	0.625	3.1 h	-78
10	0.005	0.05	4	0.625	6.3 h	-55
10	0.005	0.20	4	0.625	0.7 h	-95
10	0.010	0.10	4	0.625	2.6 h	-81
10	0.020	0.10	4	0.625	2.1 h	-85
3	0.005	0.10	2	0.750	3.3 h	-77
6	0.005	0.10	3	0.750	2.7 h	-81
3***	0.010	0.05	2	0.750	5.0 h	-65

*Uniform 0.8-mm mesh from Figure 9.20d included for comparison of CPU cost.
** Basis model for parametric study.
*** Optimized model after parametric study.

crack grows either along the diagonals (Figure 9.25b) or along the horizontals and verticals of the centre cross (Figure 9.26). Thus, it is evident that the damage threshold and initial mesh size have a significant influence on the failure pattern and to some extent the CPU cost. The value of $D_{\min}$ should be sufficiently small to predict the crack growth (Figures 9.24a and 9.24b), while a large value of $D_{\max}$ predicts only the initial crack growth in the outer corners along the diagonals (Figure 9.25c). A failure pattern similar to that in the experiment (Figure 8.20) and the simulation with a uniform 0.8-mm mesh size (Figure 9.22) was only observed for $D_{\max} = 0.05$ (Figure 9.25b). The initial mesh size was also found to have a significant influence on the damage evolution, which indicates that a fine initial mesh and a reduction in successive refinements are favourable both in terms of crack growth and CPU cost (Table 9.5 and Figure 9.26).

Finally, based on the results in the parametric study, simulations of tests P77-25 and P77-35 were carried out using the optimized parameters of 3 mm initial mesh size, $D_{\min} = 0.01$, $D_{\max} = 0.05$ and 2 successive mesh refinements. Although a $D_{\min}$ of 0.005 showed a wider crack in Figure 9.24a, this was only slightly wider than that with $D_{\min}$ equal 0.01 (Figure 9.24b). It was therefore chosen to use the largest value in an attempt to save CPU time. The results are presented in Figures 9.27 and 9.28 for tests P77-35 and P77-25, respectively. It is observed that the optimized model predicts the same crack growth as the uniformly refined mesh in Figure 9.22 for test P77-35, where the CPU cost is reduced by 65 % when using AMR (Table 9.5). The crack initiation is also captured in test P77-25 (Figure 9.28), but the initial crack growth from the experiments (see Figure 8.19c) is not predicted. Again, it is emphasized that the loading in this uncoupled approach may be overestimated but the results using AMR based on the damage parameter in Eq. (4.36) are encouraging both in terms of predicting the observed failure patterns and the reduced CPU cost.

This indicates that the simplified model with AMR could be used in further investigations on the influence of FSI effects and pre-formed holes on the failure pattern of blast-loaded plates.

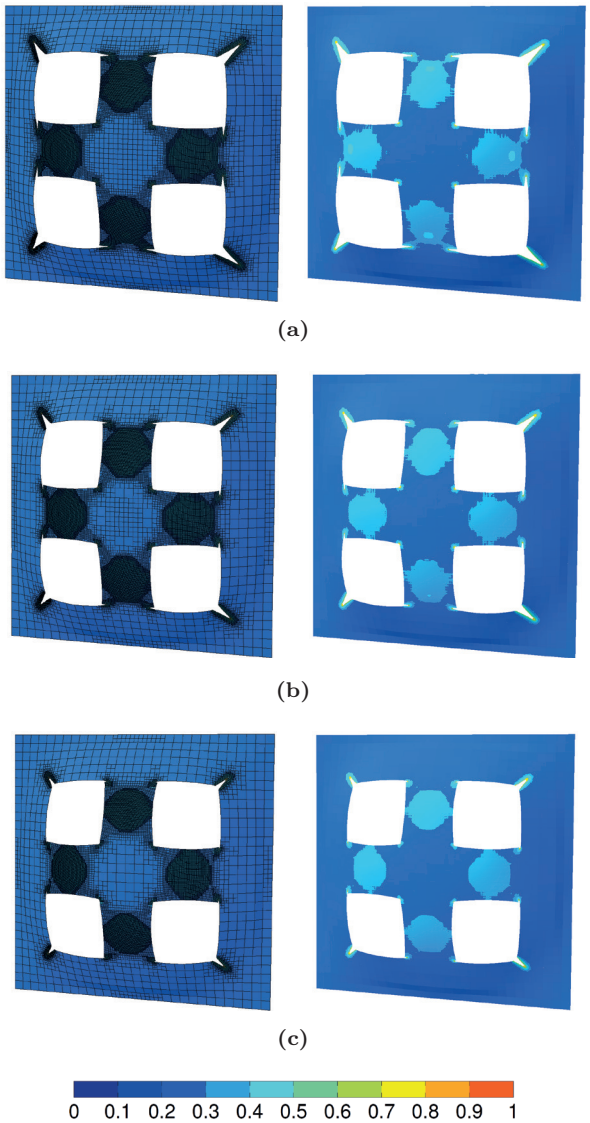

Figure 9.24: Influence of the lower threshold $D_{\min}$ on the crack growth when using AMR in the simplified model for test P77-35 with an initial mesh size of 10 mm and $D_{\max} = 0.1$: (a) basis model with $D_{\min} = 0.005$, (b) $D_{\min} = 0.01$ and (c) $D_{\min} = 0.02$. The deformed configurations are compared at $t = 3.0$ ms with (left) and without (right) mesh lines. Fringe colors represent the damage parameter in Eq. (4.36).

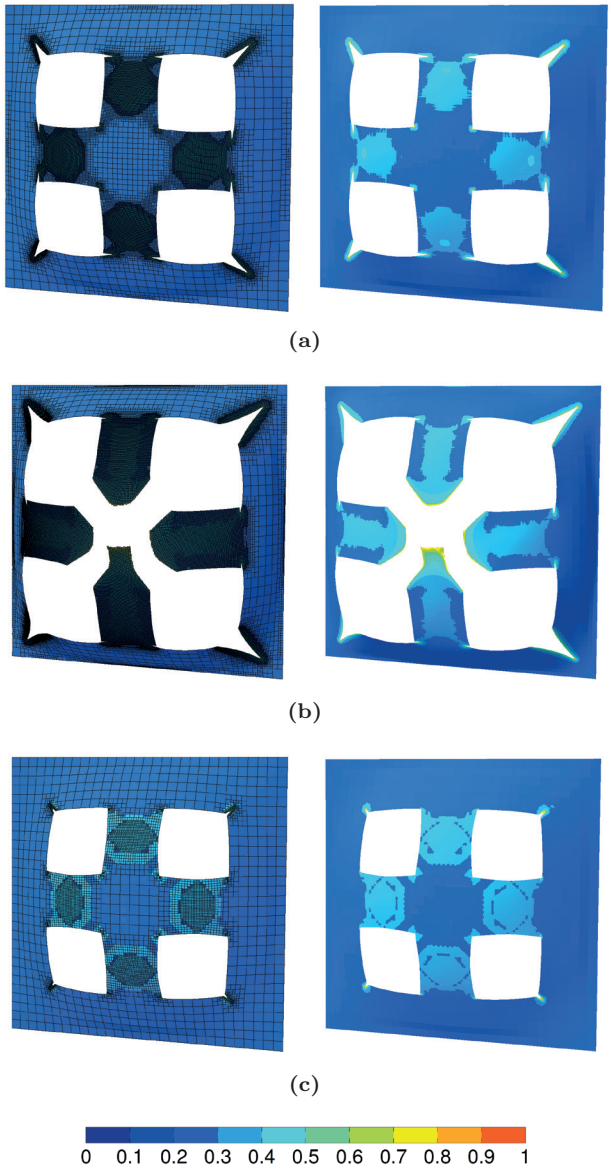

Figure 9.25: Influence of the upper threshold $D_{\max}$ on the crack growth when using AMR in the simplified model for test P77-35 with an initial mesh size of 10 mm and $D_{\min} = 0.005$: (a) basis model with $D_{\max} = 0.1$, (b) $D_{\max} = 0.05$ and (c) $D_{\max} = 0.2$. The simulations are compared at $t = 3.0$ ms where the deformed configurations are shown with (left) and without (right) mesh lines. Fringe colors represent the damage parameter in Eq. (4.36).

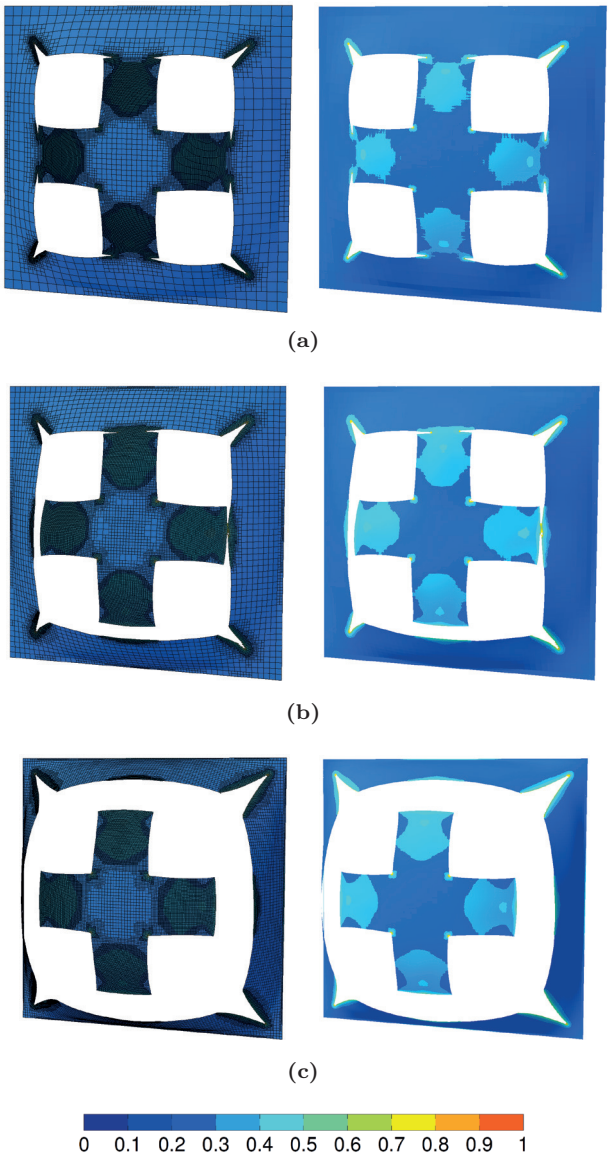

Figure 9.26: Influence of the initial mesh size on the crack growth when using AMR in the simplified model for test P77-35 with $D_{\min} = 0.005$ and $D_{\max} = 0.1$: (a) basis model with initial mesh size of 10 mm, initial mesh size of (b) 6 mm and (c) 3 mm. The simulations are compared at $t = 3.0$ ms where the deformed configurations are shown with (left) and without (right) mesh lines. Fringe colors represent the damage parameter in Eq. (4.36).

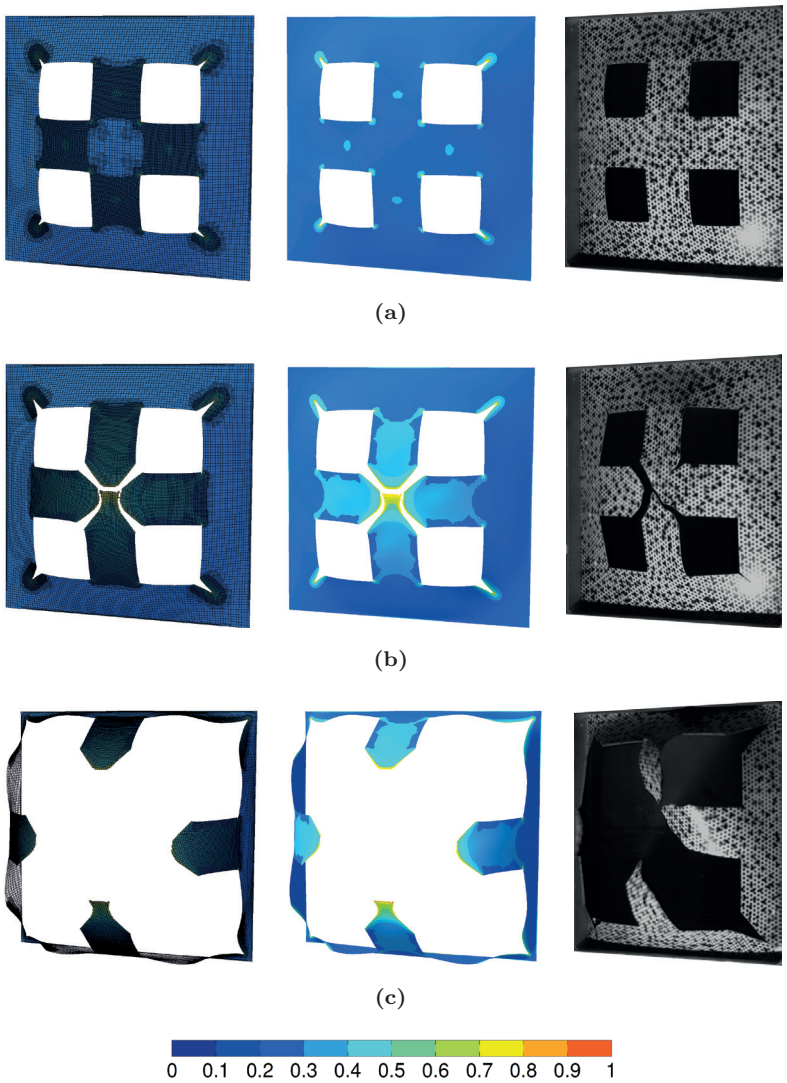

Figure 9.27: Crack growth in the simplified model for test P77-35 using AMR with an initial mesh size of 3 mm, $D_{\min} = 0.01$, $D_{\max} = 0.05$ and two successive refinements: (a) $t = 1.18$ ms, (b) $t = 1.52$ ms and (c) $t = 2.18$ ms. The deformed configurations are shown with (left) and without (middle) mesh lines, and compared to the experiment (right). Fringe colors represent the damage parameter in Eq. (4.36).

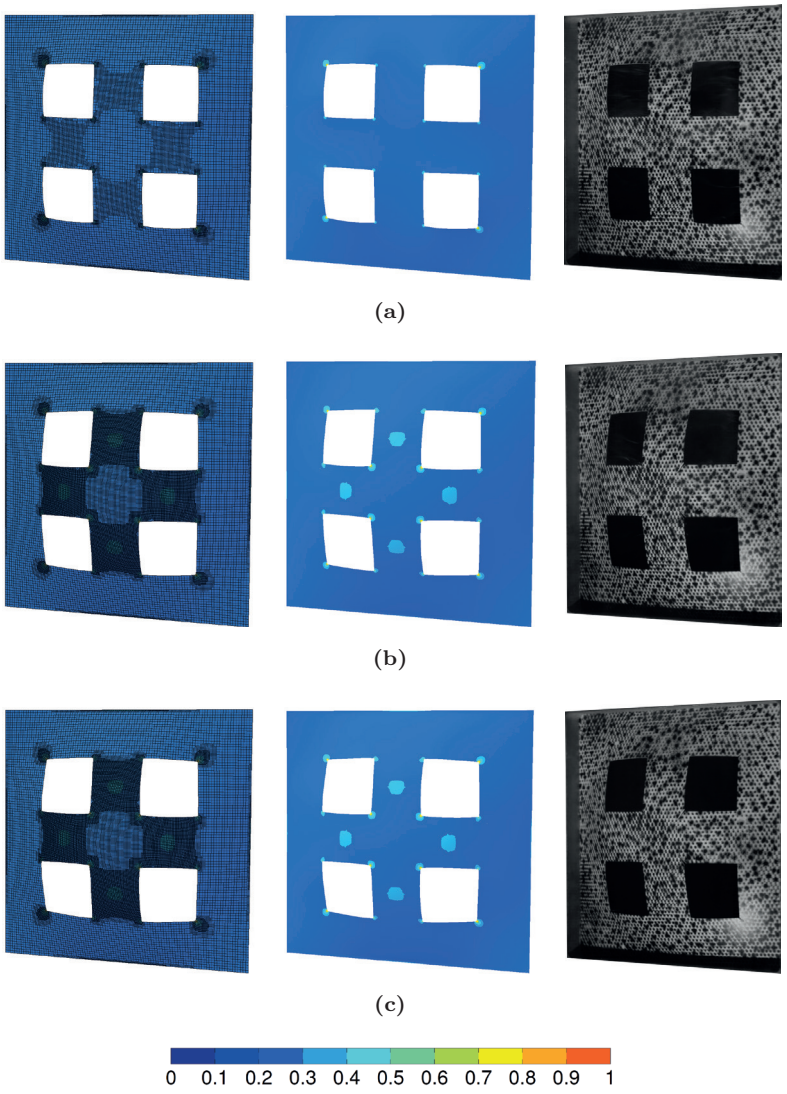

Figure 9.28: Crack growth in the simplified model for test P77-25 using AMR with an initial mesh size of 3 mm, $D_{\min} = 0.01$, $D_{\max} = 0.05$ and two successive refinements: (a) $t = 1.18$ ms, (b) $t = 1.52$ ms and (c) $t = 4.0$ ms. The deformed configurations are shown with (left) and without (middle) mesh lines, and compared to the experiment (right). Fringe colors represent the contour map of the damage parameter in Eq. (4.36).

9.5 Coupled FSI approach

Finally, fully coupled FSI simulations are performed to investigate FSI effects during the dynamic response of the flexible plates and the capabilities of recent advancements in EPX [96–98] in predicting the observed failure patterns in tests A27-10, P77-25 and P77-35. First, the shock tube experiments of the flexible plates without holes presented in Section 8.3.4 are used to study both the ALE and embedded methods presented in Section 9.3.3. Then, the experience from these simulations are used to simulate the plates with pre-formed holes. Finally, the capabilities of fully coupled simulations using adaptive mesh refinement (AMR) in predicting the observed failure patterns in the respective tests are investigated.

The coupled simulations presented herein attempt to study the influence of FSI qualitatively, since the loading was overestimated in the Eulerian simulations in Section 9.4.1. The results from the fully coupled simulations are therefore compared to the corresponding results obtained with the uncoupled approach using the loading from the Eulerian simulations in Section 9.4. The experimental results from Section 8.3.4 will also be used for comparison to the fully coupled simulations to ensure that the comparisons are reasonable.

9.5.1 Coupled simulations of flexible plates

As in the purely Eulerian simulations in Section 9.4.1, the air was modelled using the EOS of an ideal gas. The initial conditions for the fluid sub-domain were those used in Section 9.4.1, since the basis of comparison is primarily the uncoupled approach using the loading from the Eulerian simulations. That is, the initial conditions were taken from tests R27-05, R27-7.5 and R27-10 for the aluminium plates, while the initial conditions from tests R77-05, R77-15, R77-25, R77-35 and R77-60 were used for the steel plates (see Table 8.1). Rigid boundary conditions were assumed at the interior walls and rear end of the driver section. The blind flange of the tube in Section 9.4.1 was replaced by the flexible plates from Section 8.3.4 to introduce a moving boundary. The tube was also extended 0.5 m behind the test specimen to simulate the expanding volume in the tank. This is illustrated in Figure 9.29 where the green areas illustrate the absorbing (or non-reflecting) surfaces downstream the plate. Due to the square geometry of the test specimens, it was necessary to discretize the air in 3D. It was chosen to distribute the high pressure (red area in Figure 9.29) over $2 \times 2 \times 6$ CCFVs and the mesh was refined in the vicinity of the test specimen to obtain a conforming mesh of 32 x 32 elements at the F-S interface. This resembles the converged element and cell size from the mesh sensitivity studies in Sections 9.4.1 and 9.4.2 which indicated that a mesh of

approximately 10 mm was sufficient to capture both the steep pressure gradient over the shock front and also the global displacement in the blast-loaded plates. The resulting fluid mesh consisted of 116,464 8-node CCFVs (*CUVF*) where all the state variables were discretized at the centre of each computational cell. Both the ALE and the embedded method were used for the coupling at the F-S interface. The conforming fluid and plate nodes at the F-S interface were merged when using the ALE method and distinct in the simulations using the embedded method. Moreover, Giuliani's [246] mesh rezoning algorithm was used in the vicinity of the plate when the fluid sub-domain was governed by the ALE method, while the fluid sub-domain followed a purely Eulerian formulation in the embedded simulations. As in Section 9.4.1, the numerical fluxes between adjacent cells were calculated using the second order HLLC solver of the Euler equations in Eq. (9.5). The fluid and plate were coupled in all spatial directions according to Eqs. (9.10) and (9.15) (i.e., $FSCP = 1$), and the radius defining the influence domain was chosen to be barely larger than the longest diagonal of the CCFVs. Even though the simplified model seemed to slightly overestimate the axial restraint at the supports (see Figure 9.16b), the purely Lagrangian simulations in Section 9.4.2 indicated that this model captured the same trends as the clamped assembly model. It was therefore considered sufficient to use the simplified model of the plate (see Figure 9.13e) in the following for qualitative studies on the influence of FSI effects on the dynamic response of the blast-loaded plates.

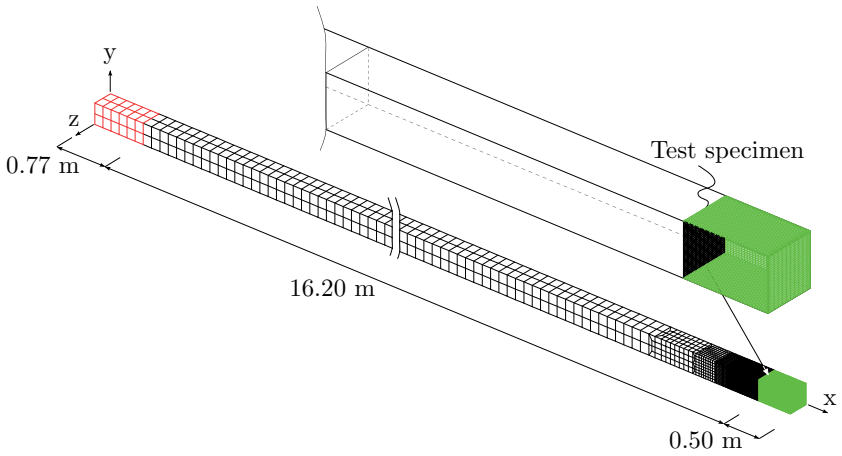

Figure 9.29: Computational mesh for the fully coupled FSI simulations of flexible plates. Absorbing (green) surfaces downstream the plate simulates the expanding volume in the tank.

Figure 9.30 compares the mid-point deflections from the ALE and embedded approaches to those in the uncoupled approaches, while Figure 9.31 contains the

corresponding pressure histories at Sensor 2. Mid-point $d_{\mathrm{z,max}}$ and permanent $d_{\mathrm{z,p}}$ deflections are summarized and compared to the uncoupled approach in Table 9.6, while the peak reflected overpressures $p_{\mathrm{r,max}}$ measured at Sensor 2 are presented in Table 9.7. Positive values of $\Delta d_{\mathrm{z,max}}$ and $\Delta p_{\mathrm{r,max}}$ imply that the values are larger in the uncoupled approach. Experimental data are also included in Tables 9.6 and 9.7 for completeness. The same results for the aluminium plates are shown in Figures 9.34 and 9.35. Note that the reflected pressures reported from the coupled simulations in Table 9.7 correspond to the first visible deviation from the nearly instantaneous rise in pressure in Figures 9.31 and 9.35. Thus, this is not the maximum pressure measured at Sensor 2. Also note that the respective tests are only denoted by their material (A, D or P) and firing overpressure in the following, because all the aluminium tests operated with a 27-cm driver while the remaining tests used a 77-cm driver.

It is observed that the ALE method predicts larger deformations than the embedded method (see Figure 9.30 and Table 9.6). Moreover, as expected, a purely numerical uncoupled approach predicts larger deformations than the corresponding fully coupled FSI simulations (Figure 9.30a and Table 9.6). This is most evident for the embedded method. The comparison against the uncoupled approach used in Section 9.4.2 (see Figure 9.30b) is somewhat misleading because the loading is overestimated in the fluid sub-domain compared to the experiments at pressures larger than approximately 800 kPa (see Section 9.4.1 and Figure 9.9). Thus, due to the significant differences in the loading, caution should be exercised when comparing the mid-point deflections in Figure 9.30b. This illustrates that a qualitative and purely numerical investigation of FSI effects is most reasonable in the following. The comparison between fully coupled simulations and experimental data in Figure 9.30c should therefore be treated with some caution and an improvement of the fluid sub-domain is necessary before quantifying FSI effects in the experiments. However, despite an almost negligible difference in the predicted loading at Sensor 2 (Figure 9.31a and Table 9.7), it is noted that the mid-point deflections obtained with the embedded method are closer to the experimental data than those in the ALE simulations (see Figure 9.30c).

As already discussed in Section 8.3.4, the influence of FSI effects can also be investigated by comparing the pressure in the vicinity of the plate. Figure 9.31a shows a reduction in the initial peak reflected overpressure in the coupled simulations, where it is observed a slight trend of an increased reduction at increasing pressure magnitudes in the steel plate tests (Table 9.7). It is important to emphasize that Sensor 2 is located upstream the test specimen (see Figure 8.1b), and that the peak pressure immediately after reflection is often assumed to be independent of the stiffness of the structure (see e.g. [72]).

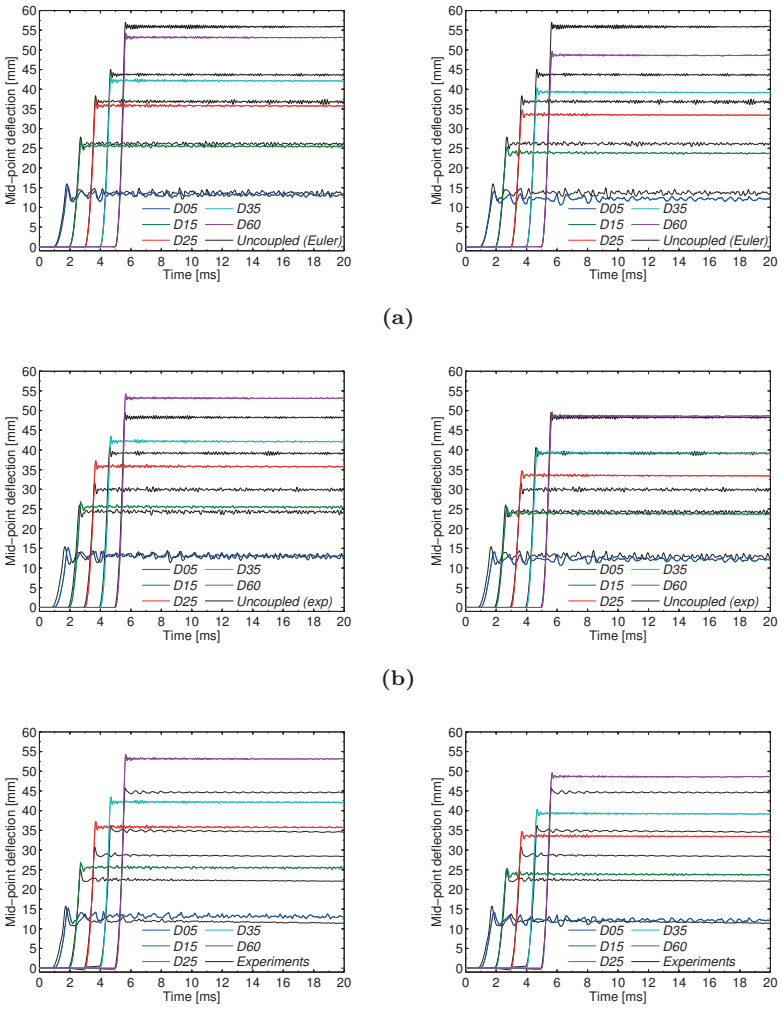

Figure 9.30: Investigation of FSI effects in terms of mid-point deflections in the fully coupled simulations of steel plates without holes. Both the ALE (left) and the embedded (right) method are compared to (a) the uncoupled approach using the loading from Eulerian simulations in Section 9.4.1, (b) the uncoupled approach from Section 9.4.2 using the loading from the experimental tests and (c) the experimental data. Note that the curves are shifted in time for improved readability.

Figure 9.31a also shows that the incident (side-on) pressures were in excellent agreement, indicating that the reduced reflected overpressure may be due to the deformation of the plates. This is also observed in previous studies which indicated that the blast mitigation could be related to the induced velocity

Table 9.6: Comparison of the mid-point deflections in the uncoupled and coupled simulations obtained from purely numerical studies. Experimental data is included for completeness.

Test	Experimental results		Numerical results							
			Uncoupled		Coupled ALE			Coupled embedded		
	$d_{z,max}$ [mm]	$d_{z,p}$ [mm]	$d_{z,max}$ [mm]	$d_{z,p}$ [mm]	$d_{z,max}$ [mm]	$d_{z,p}$ [mm]	$\Delta d_{z,max}$ [%]	$d_{z,max}$ [mm]	$d_{z,p}$ [mm]	$\Delta d_{z,max}$ [%]
D05	15.7	11.4	16.0	13.7	15.3	13.1	4.4	14.2	12.1	11.3
D15	25.0	22.1	27.9	26.1	26.8	25.5	3.9	25.4	23.7	9.0
D25	30.8	28.4	38.4	36.8	37.3	35.7	2.9	34.7	33.5	9.6
D35	36.2	34.6	45.1	43.7	43.5	42.1	3.5	40.4	39.2	10.4
D60	45.8	44.5	57.0	55.9	54.2	53.1	4.9	49.6	48.7	13.0
A05	24.3	22.7	23.6	22.3	19.3	18.0	18.2	18.0	16.6	23.7
A7.5	27.5	26.1	28.8	27.7	24.3	23.5	15.6	23.0	21.9	20.1
A10	N/A*	N/A*	37.1	36.3	31.9	31.5	N/A*	30.3	29.6	N/A*

*Experiment resulted in complete tearing along the tearing.

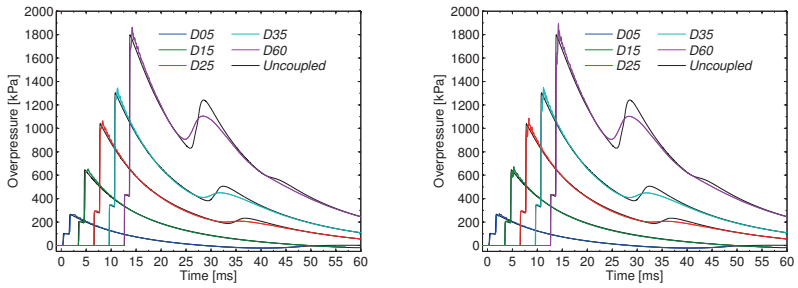

(a)

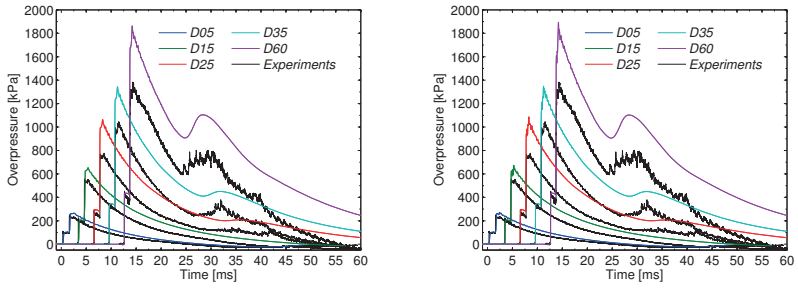

(b)

Figure 9.31: Investigation of FSI effects in terms of pressure at Sensor 2 in the fully coupled simulations of steel plates without holes. Both the ALE (left) and the embedded (right) method are compared to (a) the loading obtained from the Eulerian simulations in Section 9.4.1 and (b) the loading measured during the flexible plate tests in Section 8.3.4. Note that the curves are shifted in time for improved readability.

Table 9.7: Comparison of the reflected pressure at Sensor 2 in the uncoupled and coupled simulations obtained from purely numerical studies. Experimental data is included for completeness.

Test	Experimental results	Numerical results				
		Uncoupled	Coupled ALE		Coupled embedded	
	$p_{r,max}$ [kPa]	$p_{r,max}$ [kPa]	$p_{r,max}$ [kPa]	$\Delta p_{r,max}$ [%]	$p_{r,max}$ [kPa]	$\Delta p_{r,max}$ [%]
D05	242.6	267.2	256.7	3.9	257.6	3.6
D15	555.6	646.9	624.5	3.5	626.2	3.2
D25	767.6	1038.7	996.3	4.1	943.0	9.2
D35	992.7	1304.6	1239.5	5.0	1212.5	7.1
D60	1312.7	1796.7	1679.9	6.5	1610.0	10.4
A05	144.2	136.2	117.4	13.8	119.0	12.6
A7.5	163.6	175.0	153.8	12.1	156.0	10.9
A10	231.2	236.4	209.3	11.5	212.2	10.2

in the plate (see e.g. [72, 87, 88] and Eq. (6.99)), while Hanssen et al. [89] suggested that the reduced pressure was due to the deformed shape which resembles a global dome. Hanssen et al. [89] argued that the deformed shape will introduce a non-uniform spatial and temporal distribution of the pressure in the vicinity of the plate. The reduction in reflected pressure seems to occur before the permanent deformation is reached at approximately 1-2 ms after the initial impact. Then, a small increase in maximum pressure is observed before limited FSI effects are observed throughout the remaining part of the positive phase (Figure 9.31). This makes it natural to relate the reduction in reflected pressure to the induced velocity in the plate. A comparison of the pressure histories in the coupled approach and experiments confirms that the loading is significantly overestimated in the simulations (Figure 9.31b).

The increase in pressure after the initial reduction in the coupled simulations (see Figure 9.31) is also observed when inspecting the pressure in the vicinity of the plate. This is illustrated in Figures 9.32 and 9.33 for the coupled and uncoupled approach, respectively, for test D35. It is observed a slightly larger pressure in the uncoupled approach immediately after impact (Figures 9.32a-b and 9.33a), while the opposite occurs at the time of maximum deflection of the plate (Figures 9.32c-d and 9.33b). This indicates that the observed FSI effects may be a combination of both the induced velocity and deformed shape of the plate. That is, the initial reduction in reflected pressure is related to the induced velocity of the plate, while the subsequent increase in peak reflected pressure may be due to the deformed shape of the plate which introduces a non-uniform pressure distribution in front of the plate.

Figure 9.32 also illustrates the different treatment of FSI in the ALE and embedded methods. Both methods experience a pressure drop across the F-S interface due to the weak coupling approach when using CCFVs (see Section 9.3.3), but the ALE mesh moves with the plate (Figure 9.32c) while the plate

mesh slides through a fixed and regular fluid mesh in the embedded method (Figure 9.32d).

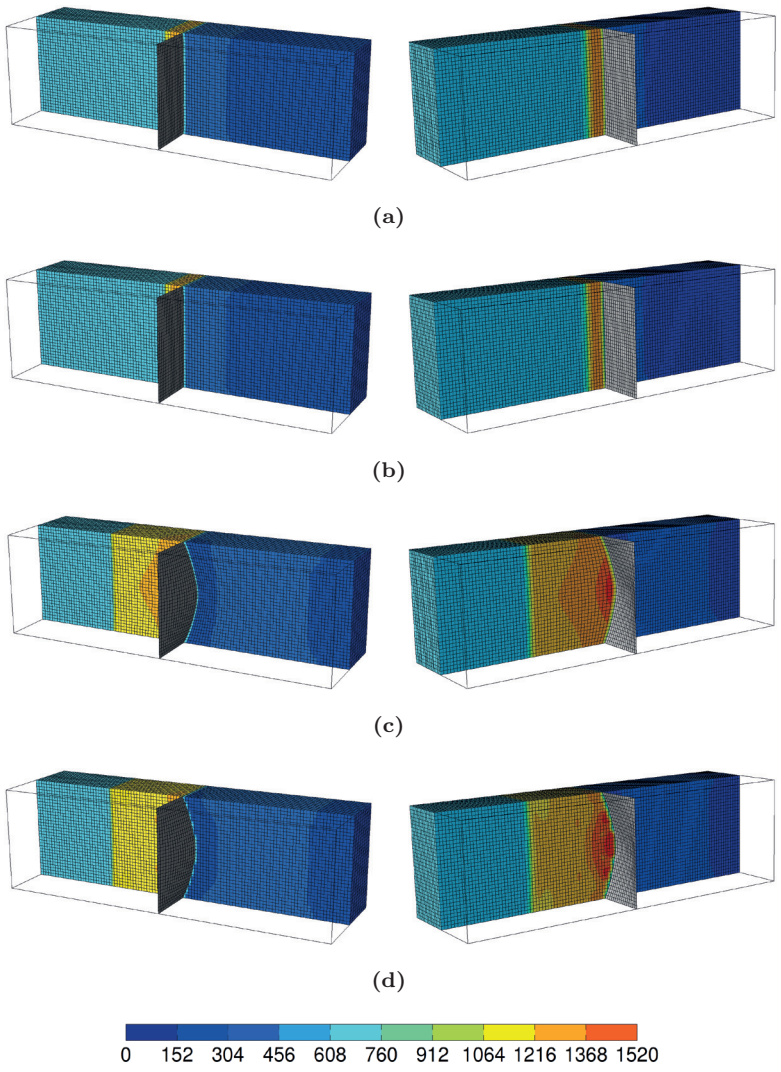

Figure 9.32: Comparison of the ALE and embedded approach in terms of pressure in the vicinity of the plate in test D35: (a) the ALE method and (b) the embedded method immediately after impact, and (c) the ALE method and (d) the embedded method at maximum deflection of the plate. Only 1/2 of the fluid mesh is shown to enable a clear view of the plate from the back (left) and front (right). Fringe colors represent the contour map of the overpressure (in kPa).

As discussed in Section 9.3.3, the accuracy of the embedded method is highly

dependent on the definition of the influence domain and may result in some leakage of the pressure through the plate if not treated properly. However, from Figure 9.32d it is evident that there is limited leakage of pressure through the plate since there are no significant build-up of overpressure or large fluid velocities in the volume behind the plate. It is noted that the choice of method affects the pressure distribution in front of the plate (Figures 9.32c-d).

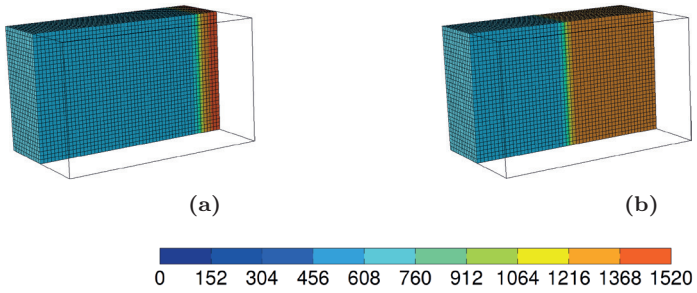

Figure 9.33: Pressure in front of the blind flange in test R35: (a) immediately after impact and (b) the time of maximum deflection of the plate in the coupled simulations in Figures 9.32c-d. Only 1/2 of the fluid mesh is shown as in Figure 9.32. Fringe colors represent the contour map of the overpressure (in kPa).

The simulations of the aluminium plates showed in general similar trends as the steel plate tests, but with some distinct differences. As for the steel plates without holes, the ALE method predicts larger deformations compared to the embedded method but the difference is less evident (see Figure 9.34 and Table 9.6). It is also observed more noticeable FSI effects in the aluminium plate tests, both in terms of mid-point deflections (Figure 9.34a and Table 9.6) and the reflected pressure measured at Sensor 2 (Figure 9.35a and Table 9.7). That is, the mid-point deflections are significantly overestimated in the uncoupled approach and the reduction in the reflected pressure is also more evident. In fact, the loading is in much better agreement between the coupled simulations and the experiments in the aluminium plate tests due to the relatively small magnitudes of the reflected overpressure (see Figure 9.35b). However, since the blast properties are somewhat underestimated in the fluid sub-domain at the driver lengths and firing pressures used in the aluminium plate tests (see Section 9.4.1 and Figure 9.9), the mid-point deflections predicted by the uncoupled approach used in Section 9.4.2 are somewhat larger (Figure 9.34b) than those obtained with the uncoupled approach using the loading from Section 9.4.1 (Figure 9.34a).

Even though the loading in the coupled simulations is in very good agreement with the experimental measurements at Sensor 2 (Figure 9.35b), the mid-

point deflections are considerably underestimated in the coupled simulations (Figure 9.34c). This may indicate that the simplified model of the plate is too constrained at the boundary.

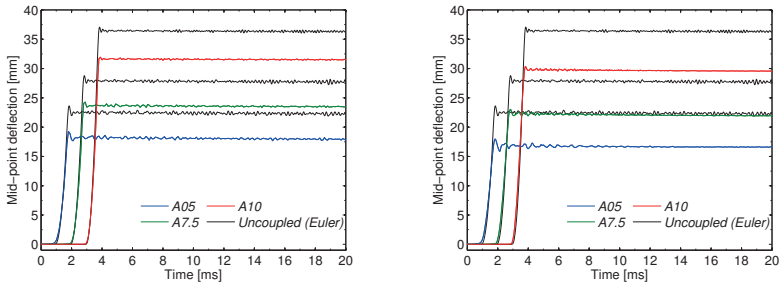

(a)

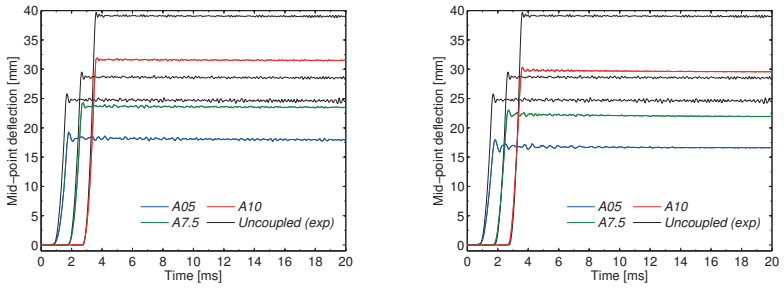

(b)

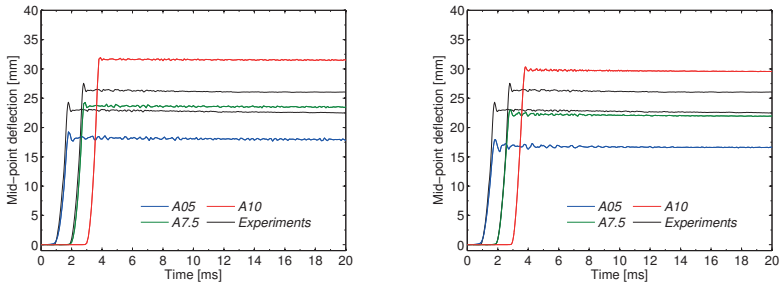

(c)

Figure 9.34: Investigation of FSI effects in terms of mid-point deflection in the fully coupled simulations of aluminium plates. Both the ALE (left) and the embedded (right) method are compared to (a) uncoupled approach using the loading from Eulerian simulations in Section 9.4.1, (b) uncoupled approach from Section 9.4.2 using the loading from the experimental tests and (c) the experimental data. Note that the curves are shifted in time for improved readability.

Based on the findings during the investigation on the influence of the boundary conditions in Section 9.4.2, it is expected that the clamped assembly in Figure 9.13c will predict mid-point deflections closer to the experimental observations (see Figure 9.16b). This illustrates that a qualitative and purely numerical investigation of FSI effects is most reasonable also for the aluminium plate tests, and that a more elaborate model of the boundary conditions is necessary before quantifying FSI effects in the experiments.

Recall that the sudden drop in pressure observed during test A10 in Figure 9.35b is due to the complete failure of the plate in this experiment. The pressure is then free to enter the expanding volume in the tank which results in a left-running rarefaction wave. This is observed as a sudden drop in pressure at Sensor 2. The element size used in these simulations were too large to predict the failure. Failure in test A10 will therefore be investigated in Section 9.5.3 by using AMR in the plate.

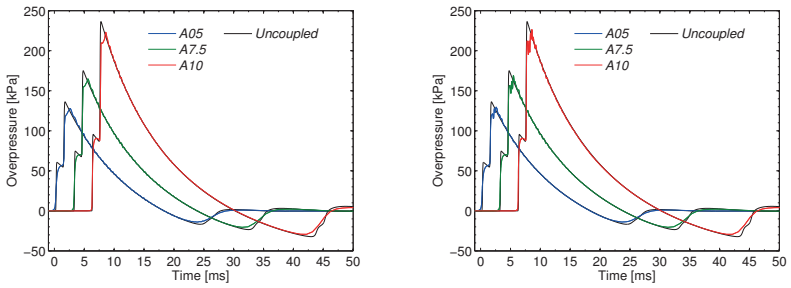

(a)

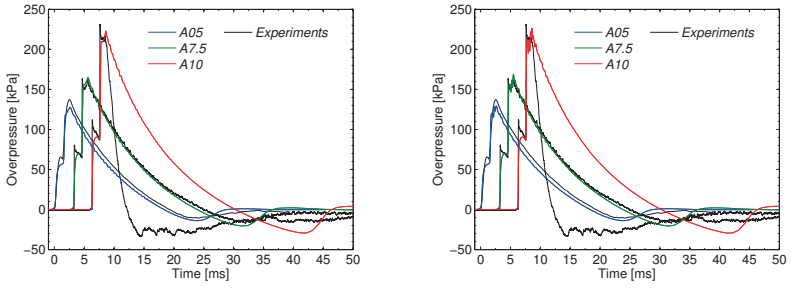

(b)

Figure 9.35: Investigation of FSI effects in terms of pressure at Sensor 2 in the fully coupled simulations of aluminium plates. Both the ALE (left) and the embedded (right) method are compared to (a) the uncoupled approach using the loading from Eulerian simulations in Section 9.4.1 and (b) the loading measured during the flexible plate tests in Section 8.3.4. Note that the curves are shifted in time for improved readability.

A plausible explanation of the increased FSI effects in the tests with aluminium plates may be found by considering the change of linear momentum during the FSI. This follows the argumentation in the early works of Taylor [74] suggesting that lightweight structures undertake less momentum compared to heavier structures when exposed to the same blast intensity. At the time of impact, the plate is exposed to a uniformly distributed pressure pulse and experiences an instantaneous development of a uniform transverse velocity field. Since the aluminium plates are approximately 1/3 of the mass of the steel plates, this will result in a relatively larger induced velocity in the aluminium plate. Eq. (6.99) then implies that the effect of reduced pressure is expected to be larger for the aluminium plates. Moreover, due to the small thickness (0.8 mm), the dynamic response of the plates is sensitive to small changes in the pressure profile. This illustrates the importance of an appropriate description of both the fluid and the structural sub-domain when studying lightweight and flexible plates subjected to blast loading.

9.5.2 Simulations of flexible plates with pre-formed holes

Special focus is now placed on the influence of pre-formed holes on the dynamic response and pressure distribution in the vicinity of the plates. The test specimen in Figure 9.29 is therefore replaced by the plate with pre-formed holes (see Figure 9.36). As in Section 9.5.1, the basis of comparison is primarily the uncoupled approach using the loading from the Eulerian simulations in Section 9.4.1. The initial conditions were therefore taken from tests R77-05, R77-15, R77-25 and R77-35 for the simulations of the steel plates with pre-formed holes (see Table 8.1). Due to the simplified boundary conditions and overestimated loading in the simulations in Section 9.5.1, it was challenging to conclude on which FSI technique (ALE or embedded) provided the best predictions. Even though the ALE method allows for failure of the plates when using CCFVs and merging the nodes at the F-S interface, the embedded method has significant advantages when it comes to larger displacements, finite rotations, failure and fragmentation of the plates. The embedded method is also considered to be the most promising and appealing technique from an engineering point of view, since the fluid and plate are meshed independently where the two meshes are simply superposed in the computational model. The simulations are therefore limited to the embedded technique in the following.

Figure 9.37 compares the mid-point deflections from the coupled approach to the uncoupled approaches, while Figure 9.38 contains the corresponding pressure histories at Sensor 2. Mid-point $d_{\mathrm{z,max}}$ and permanent $d_{\mathrm{z,p}}$ deflections are summarized and compared to the uncoupled approach in Table 9.8, while peak reflected overpressures $p_{\mathrm{r,max}}$ measured at Sensor 2 are presented in Table 9.9. As before, positive values of $\Delta d_{\mathrm{z,max}}$ and $\Delta p_{\mathrm{r,max}}$ imply that the values

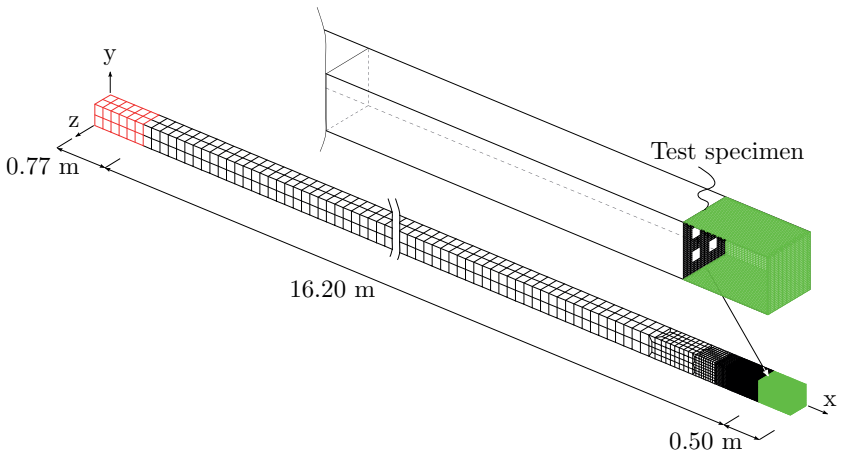

Figure 9.36: Computational mesh for the fully coupled FSI simulations of flexible plates with pre-formed holes. Absorbing (green) surfaces downstream the plate simulates the expanding volume in the tank.

are larger in the uncoupled approach. Experimental data are also included in Tables 9.8 and 9.9 for completeness.

It is observed that the simulations of the steel plates with pre-formed holes follow the same trends as the plates without holes in Section 9.5.1. That is, the mid-point deflections are overestimated in the uncoupled approach where it is observed a slight trend of increased FSI effects at larger load intensities (Figure 9.37a and Table 9.8). As in Section 9.5.1, the comparison against the uncoupled approach in Section 9.4.2 is misleading since the loading is overestimated in the fluid sub-domain. The very good agreement between the coupled simulations and the uncoupled approach in Figure 9.37b is therefore considered to be a coincidence. Recall that the pressure measurements in the massive plate tests were larger than those in the tests with pre-formed holes (see Figure 8.15). It seems that the loading is correspondingly overestimated in the coupled simulations (Figure 9.38b), resulting in the coincidental effect that these observations equalize each other in Figure 9.37b. This is not the case in test P25 where all the pressure measurements were similar in all experiments (see Figure 8.15c), which explains the deviation in mid-point deflection for this test (Figure 9.37b). The overestimated loading in the simulations (Figure 9.38b) also implies that, although the influence of boundary conditions on the dynamic response was found to be almost negligible in Section 9.4.2 and Figure 9.16d, the comparison to the experimental observations in Figure 9.37c should be treated with some caution. It is expected that an improvement of the fluid sub-domain will result in better agreement with the experimental data.

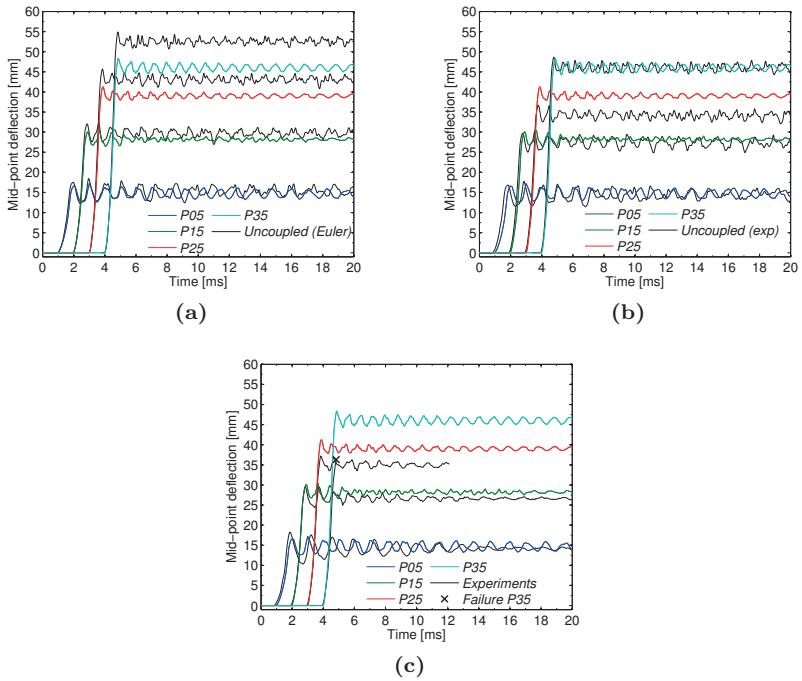

Figure 9.37: Investigation of FSI effects in terms of mid-point deflections in the fully coupled simulations of steel plates with pre-formed holes. Comparison of the coupled simulations and (a) the uncoupled approach using the loading from Eulerian simulations in Section 9.4.1, (b) the uncoupled approach from Section 9.4.2 using the loading from the experimental tests and (c) the experimental data. Note that the curves are shifted in time for improved readability.

Table 9.8: Comparison of the mid-point deflections in the uncoupled and coupled simulations obtained from numerical studies on the steel plates with pre-formed holes. Experimental data is included for completeness.

Test	Experimental results		Numerical results				
			Uncoupled		Coupled embedded		
	$d_{z,max}$ [mm]	$d_{z,p}$ [mm]	$d_{z,max}$ [mm]	$d_{z,p}$ [mm]	$d_{z,max}$ [mm]	$d_{z,p}$ [mm]	$\Delta d_{z,max}$ [%]
P05	18.3	14.2	18.5	15.3	17.2	14.6	7.0
P15	29.5	26.6	32.4	29.6	30.5	28.2	5.9
P25	37.2	34.9	45.7	43.1	41.2	39.0	9.8
P35	N/A*	N/A*	54.9	52.6	48.3	46.0	N/A*

*Experiment resulted in complete failure along the diagonals.

FSI effects are also evident in the pressure measurements at Sensor 2, which show a distinct reduction in the reflected pressure (Figure 9.38a and Table

9.9). This is expected since the loading in the uncoupled approach is obtained using a massive plate without holes. The main reduction in pressure last for approximately 1-2 ms before a minor reduction is observed throughout the entire positive phase duration (see Figure 9.38a). This was also observed in the experiments in Section 8.3.4 (Figure 8.15) and indicates a reduced pressure in the vicinity of the holes. Note that the simulations of tests P25 and P35 were aborted after approximately 30 ms due to instabilities in the fluid sub-domain (see Figure 9.38). The reason for this is not known, but since these numerical challenges occurred after the permanent deflection was reached it is considered of minor importance in this work.

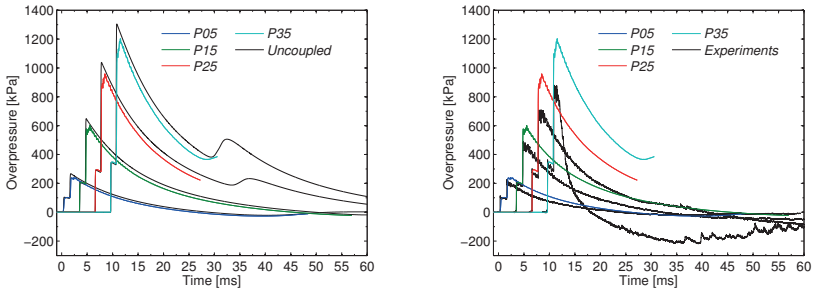

Figure 9.38: Investigation of FSI effects in terms of pressure at Sensor 2 in the fully coupled simulations of steel plates with pre-formed holes. Comparison of (a) the embedded method and uncoupled approach using the loading from Eulerian simulations in Section 9.4.1 and (b) the embedded method and loading measured during the flexible plate tests. Note that the curves are shifted in time for improved readability.

Table 9.9: Comparison of the reflected pressure at Sensor 2 in the uncoupled and coupled simulations obtained from numerical studies on the steel plates with pre-formed holes. Experimental data is included for completeness.

Test	Experimental results	Numerical results		
		Uncoupled	Coupled embedded	
	$p_{r,max}$ [kPa]	$p_{r,max}$ [kPa]	$p_{r,max}$ [kPa]	$\Delta p_{r,max}$ [%]
P05	225.9	267.2	238.4	10.8
P15	484.6	646.9	577.5	10.7
P25	716.8	1038.7	891.8	14.1
P35	849.9	1304.6	1100.9	15.6

Figure 9.39 shows the pressure distribution in the vicinity of the plate immediately after impact and at the maximum deflection of the plate in test P35. Cross-sectional views along the centre of the fluid (Figures 9.39a and 9.39c) and the pre-formed holes (Figures 9.39b and 9.39d) enable a clear view of both the pressure and the plate. The fringe colors are kept the same as in Figure

9.32 to simplify a comparison to the plates without holes.

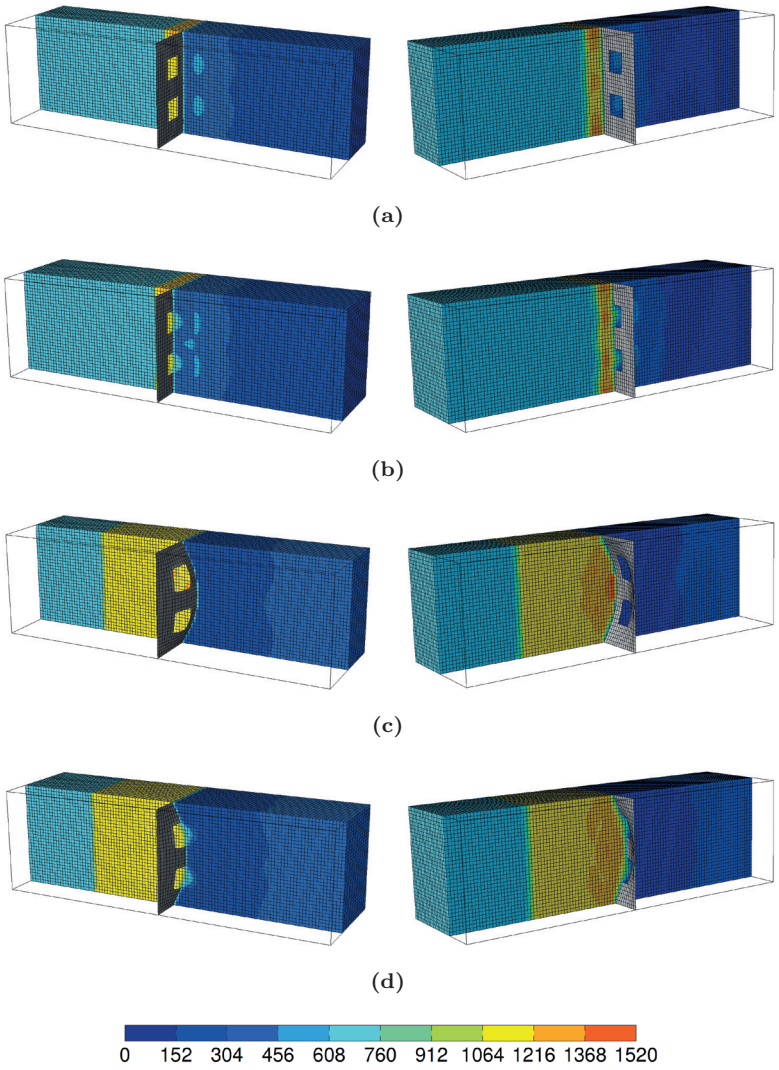

Figure 9.39: Pressure in the vicinity of the plate in test P35. Cross-sectional views along (a) the centre of the fluid and (b) the centre of the holes immediately after impact, and (c) the centre of the fluid and (d) the centre of the holes at maximum deflection of the plate. The cross-sectional views of the fluid mesh are shown to enable a clear view of the plate from the back (left) and front (right). Fringe colors represent the contour map of the overpressure (in kPa).

It is observed a slight venting of the pressure through the holes, resulting in a reduced pressure close to the holes (Figure 9.39a) and a stagnation of

the pressure in front of the holes (Figure 9.39b) immediately after impact. The stagnation in pressure in front of the holes is not that evident at the time of maximum deflection of the plate (Figure 9.39d), where the distribution resembles that in the plates without holes but with lower magnitudes of pressure (Figure 9.39c). Finally, as in the uncoupled approach in Section 9.4.2, an element size of 10 mm in the plates is too large to predict the failure observed during the P25 and P35 tests.

9.5.3 Combined fluid and structure mesh adaptivity

The Lagrangian simulations in Section 9.4.2 indicated that a mesh size equal to the plate thickness was necessary to predict the crack growth observed in the experiments, and that AMR could be used to save CPU time. This also implies that the fluid mesh needs to be refined, because the accuracy of the F-S coupling requires a sufficiently fine fluid mesh compared to that in the plate. However, the fluid sub-domain only needs to be refined in the vicinity of the plate and the remaining part can be modelled with a coarser mesh as long as it predicts the governing wave patterns. This section will therefore use recent advancements in EPX [95, 98, 225, 247], allowing for AMR both in the fluid and structural sub-domain simultaneously in the same analysis, to study the FSI effects during the failure in tests A10, P25 and P35. These features are particularly useful in combination with the embedded FSI method since the fluid and plate are discretized independently at the topological level. EPX then enables automatically refinement of the fluid mesh in the vicinity of the plate which can move and undergo large deformations (including failure and fragmentation), while the plate mesh is refined locally based on the damage evolution. This will be referred to as FSI-based and damage-based AMR, respectively, in the following.

Based on the findings in Section 9.4.2, the test specimen in Figure 9.36 is replaced by the optimized model from Table 9.5 (see Figure 9.40). That is, the plate is modelled with an initial mesh size of 0.003 m and the mesh is refined within the damage threshold $0.01 \leq D \leq 0.05$ using 2 successive refinements. The fluid sub-domain still consists of an initial element size of 0.01 m but is now also refined using one level of refinement in a region centred around the plate. This refined region was limited to a length which equals 6 times the initial cell size (i.e., 0.06 m). The refined mesh results in very small time steps in both the fluid and structural sub-domains. This will significantly increase the CPU cost and only 1/4 of the experimental geometry is modelled utilizing symmetry (see Figure 9.40). The small time steps will also slow down the initial phase of the simulation, i.e., the time from the diaphragm bursts to the shock wave impacts the plate. The approach suggested by Casadei et al. [225] is therefore used to further reduce the CPU time needed to propagate the

shock wave to the plate. This is achieved by introducing a user-defined trigger which monitors the variations in fluid pressure in a cell located 0.3 m upstream the plate (Figure 9.40). Then, the fluid is not refined until the shock wave arrives at the trigger. The critical time step of the plate is also neglected until this point in time by completely blocking the displacement of the plate (i.e., prescribing zero displacement) to avoid artificial motions due to numerical instabilities related to the large time step in the initial phase. It should also be noted that it was necessary to reduce the C_{CFL} coefficient to 0.5 to avoid numerical instabilities in the fluid sub-domain.

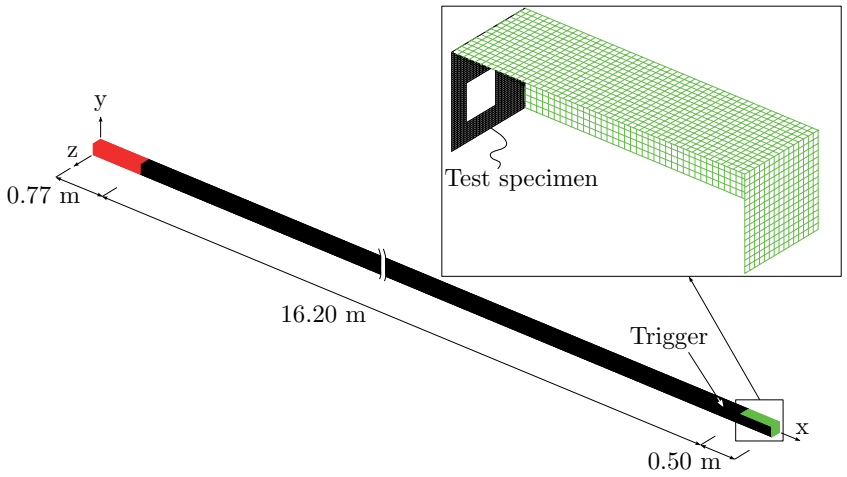

Figure 9.40: Initial computational mesh for the fully coupled FSI simulations using adaptive mesh refinement both in the plate and fluid.

As discussed in Section 9.3.3, caution should be exercised when defining the influence domain in coupled simulations. This is particularly important in simulations involving combined fluid and structural AMR. The radius R of the spheres attached to the plate nodes should always refer to the initial fluid cell size [130]. EPX will then adjust the radius automatically during the refinement of the fluid mesh. Using a regular 3D fluid mesh of cell size L_F, the radius should be slightly larger than half of the longest diagonal in each cell (i.e., $R = 1.01 \cdot \sqrt{3} L_F/2 = 0.87 L_F$). This will avoid spurious leakage of the fluid flow across the plate. The geometrical representation of the diagonals of a regular cell in 3D is illustrated in Figure 9.41. The fast search algorithm will then identify which F-S faces that are located within the influence domain of the plate (see Figure 9.6a). This is carried out using a user-defined fast search grid within the fluid sub-domain, where the fluid faces located inside the influence domain are included in the FSI. For increased CPU efficiency, the

grid should have the minimum size which ensures that all interacting faces are detected. In the particular case of combined fluid and structure AMR, this user-defined grid size should be taken as the maximum value of the refined fluid cell size and the initial plate mesh [130]. This is due to the fact that FSI-based AMR ensures that all the fluid cells in the vicinity of the plate are refined up to the user-defined level, while the refinement of the plate depends on the damage evolution. This also implies that a fine initial mesh size in the plate may be favourable in view of the CPU cost in the fast search algorithm. The refined cell size in the fluid is 0.005 m and the initial element size in the plate is 0.003 m. The radius R of the influence domain was therefore taken as 0.0087 m (based in the initial fluid cell size), while the fast search algorithm operated within a grid size ($HGRI$) of 0.0052 m which is slightly larger than the refined cell size in the fluid.

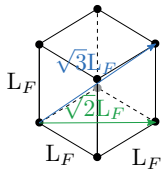

Figure 9.41: Geometrical representation of the shorter (green) and longer (blue) diagonals in a cube, where the longer diagonal is used to define the influence domain in the embedded FSI technique.

Figure 9.42 compares the mid-point deflections (Figures 9.42a and 9.42c) and overpressure at Sensor 2 (Figures 9.42b and 9.42d) in the coupled simulations with and without AMR. Experimental data are also included for completeness. It is observed that the simulations using combined fluid and structural adaptivity predicts larger mid-point deflections than the corresponding simulations without AMR (see Figures 9.42a and 9.42c). Complete failure is predicted in tests A10 and P35, where the sudden drop in pressure at Sensor 2 is evident in the simulations (Figures 9.42b and 9.42d). The increased mid-point deflections in the simulations using AMR are probably due to an improved representation of the nearly instantaneous rise in pressure over the shock wave (due to a fine cell size). This indicates that the thin aluminium and steel plates are very sensitive to small variations in the loading. In particular, the predicted mid-point deflections and pressures are in very good agreement with the experimental data for the aluminium plate tests (Figures 9.42a and 9.42b). Note that the simulations using AMR were intentionally stopped during the last part of the positive phase. This was because the dynamic response of interest was already reached at this point in time, and that the remaining part of the simulation would require a significant CPU cost due to the decrease in the critical time step during the AMR in the plate.

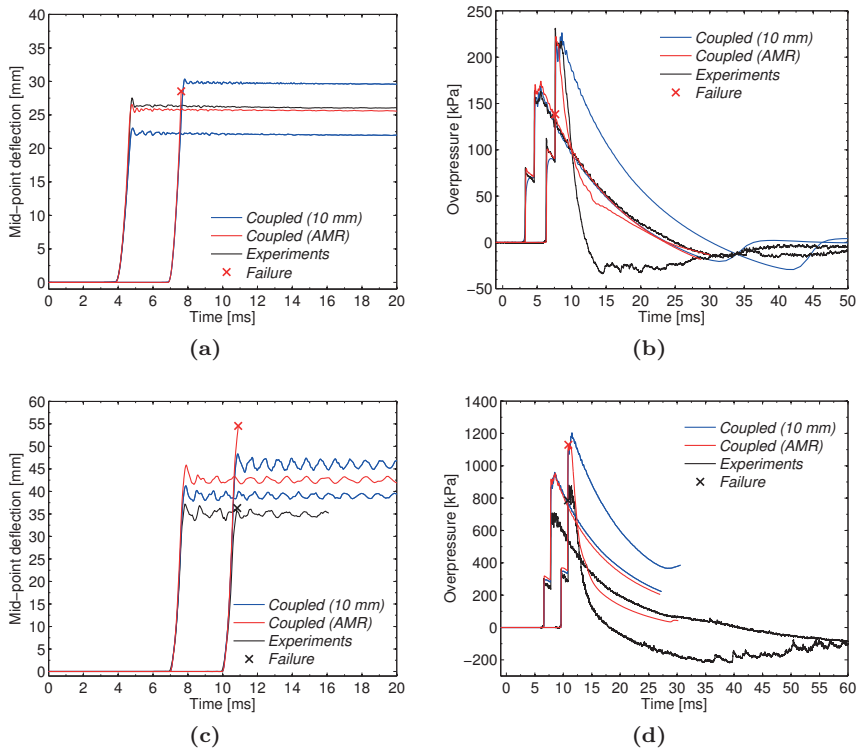

Figure 9.42: Influence of adaptive mesh refinement on the predicted mid-point deflection and pressure at Sensor 2: (a) mid-point deflection and (b) overpressures in tests A7.5 and A10, (c) mid-point deflection and (d) overpressures in tests P25 and P35. Note that the curves are shifted in time for improved readability.

Figures 9.43, 9.45, 9.47 and 9.49 contain the pressure distribution in the vicinity of the plate at characteristic times in tests A7.5, A10, P25 and P35, respectively. The corresponding damage evolution in the plates are shown in Figures 9.44, 9.46, 9.48 and 9.50. Note that the 1/4-model of the plate is mirrored along the symmetry lines to visualize the entire plate.

The results from the simulation of test A7.5 (Figures 9.43 and 9.44) are included because the uncoupled approach and AMR resulted in complete tearing along the supports for both A7.5 and A10, while the coupled approach using AMR resulted in complete tearing only in test A10 (see Figures 9.45 and 9.46). This confirms that the loading and deformations are exaggerated in the uncoupled approach (see Figures 9.34 and 9.35). Although the underlying assumption of a rigid reflection is conservative and is in general considered as safe in blast-resistant design, it may result in a significant overestimation of displacements and, consequently, the internal forces and stresses in flexible structures. As in

Section 9.5.1, it is interesting to note that the maximum pressure occurs at the plate centre during the FSI subsequent to the initial reflection (Figures 9.43c and 9.45c).

As in Section 9.5.2 and Figure 9.39, it is observed a stagnation in pressure in front of the holes and reduced pressure in the vicinity of the holes for the steel plates (Figures 9.47 and 9.49). This is most evident immediately after impact (Figures 9.47a and 9.49a). As in Section 9.4.2, the experimental observations of crack initiation and growth were predicted in tests P25 and P35 (Figures 9.48 and 9.50). Moreover, comparing Figures 9.28 and 9.48, it may seem that the coupled simulation using AMR predicts the initial crack growth from the P25 experiment. However, it is emphasized that the loading is significantly overestimated (Figure 9.42d) and the simplified boundary conditions are too restrained (Figure 9.16b).

Finally, it is noted that, although the fluid mesh is coarser than that in the plates, a qualitative evaluation indicates that the coupled simulations using AMR in both fluid and structure predict (at least to a large extent) the experimental observations. A coarser fluid mesh compared the structural mesh violates the rule of thumb presented in Section 9.3.3. That is, in simulations without AMR it is typically used larger elements in the plate than the fluid cell size. However, the good agreement with the experimental observations when using AMR are interesting from an engineering point of view since it may significantly speed up the fast search algorithm and, consequently, the CPU time.

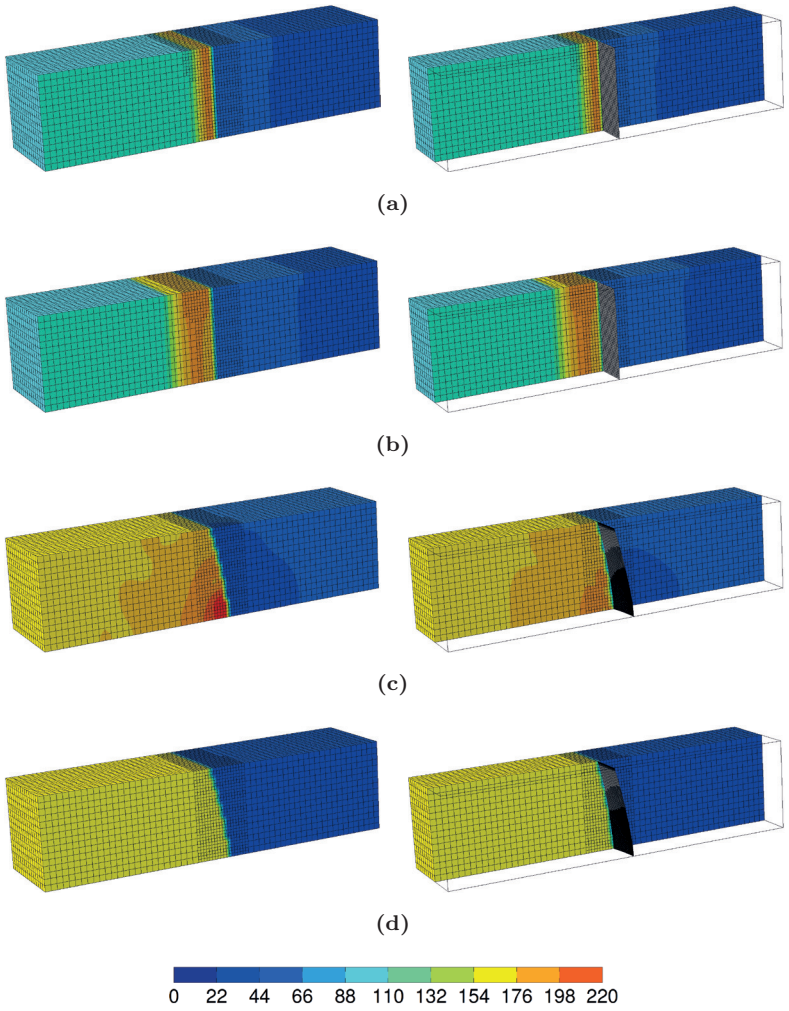

Figure 9.43: Pressure in the vicinity of the plate in test A7.5 using combined fluid and structural AMR. 1/4 of the model is used to illustrate the pressure along the centre of the fluid (left) and cross-sectional views further inside the fluid (right): (a) $t = 32.9$ ms, (b) $t = 33.0$ ms, (c) $t = 33.8$ ms and (d) $t = 36.0$ ms. Fringe colors represent the contour map of the overpressure (in kPa).

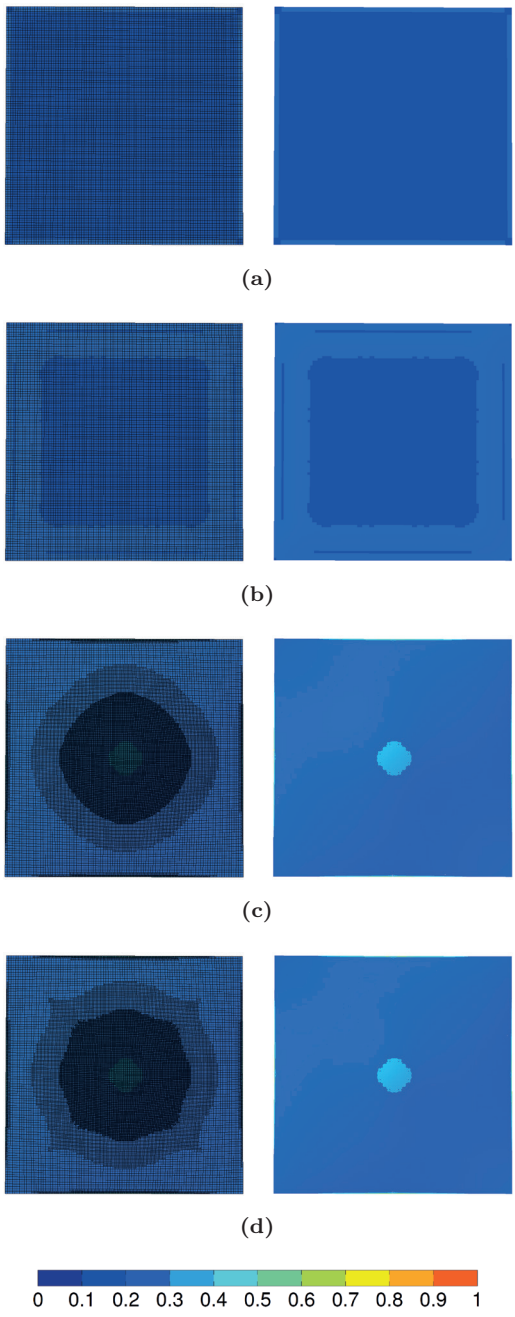

Figure 9.44: Damage evolution in the plate during the fully coupled simulations of test A7.5 using AMR: (a) $t = 32.9$ ms, (b) $t = 33.0$ ms, (c) $t = 33.8$ ms and (d) $t = 36.0$ ms. Note that the plate is shown with (left) and without (right) element outlines. Fringe colors represent the damage parameter in Eq. (4.36).

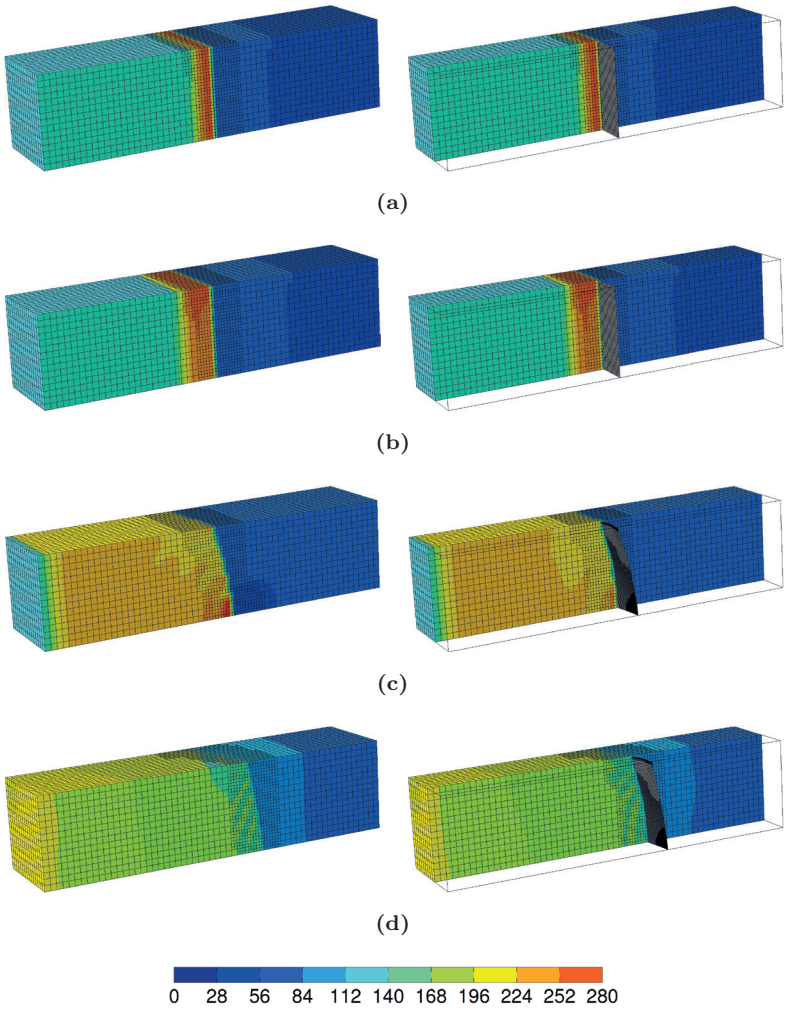

Figure 9.45: Pressure in the vicinity of the plate in test A10 using combined fluid and structural AMR. 1/4 of the model is used to illustrate the pressure along the centre of the fluid (left) and cross-sectional views further inside the fluid (right): (a) $t = 31.1$ ms, (b) $t = 31.2$ ms, (c) $t = 31.9$ ms and (d) $t = 32.8$ ms. Fringe colors represent the contour map of the overpressure (in kPa).

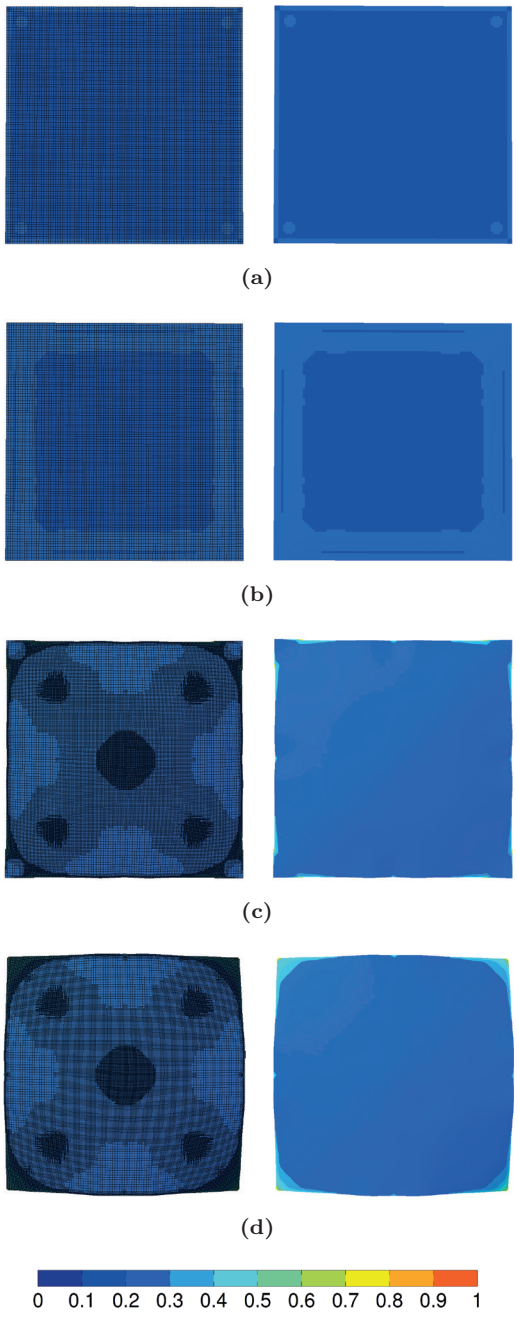

Figure 9.46: Damage evolution in the plate during the fully coupled simulations of test A10 using AMR: (a) $t = 31.1$ ms, (b) $t = 31.2$ ms, (c) $t = 31.9$ ms and (d) $t = 32.8$ ms. Note that the plate is shown with (left) and without (right) element outlines. Fringe colors represent the damage parameter in Eq. (4.36).

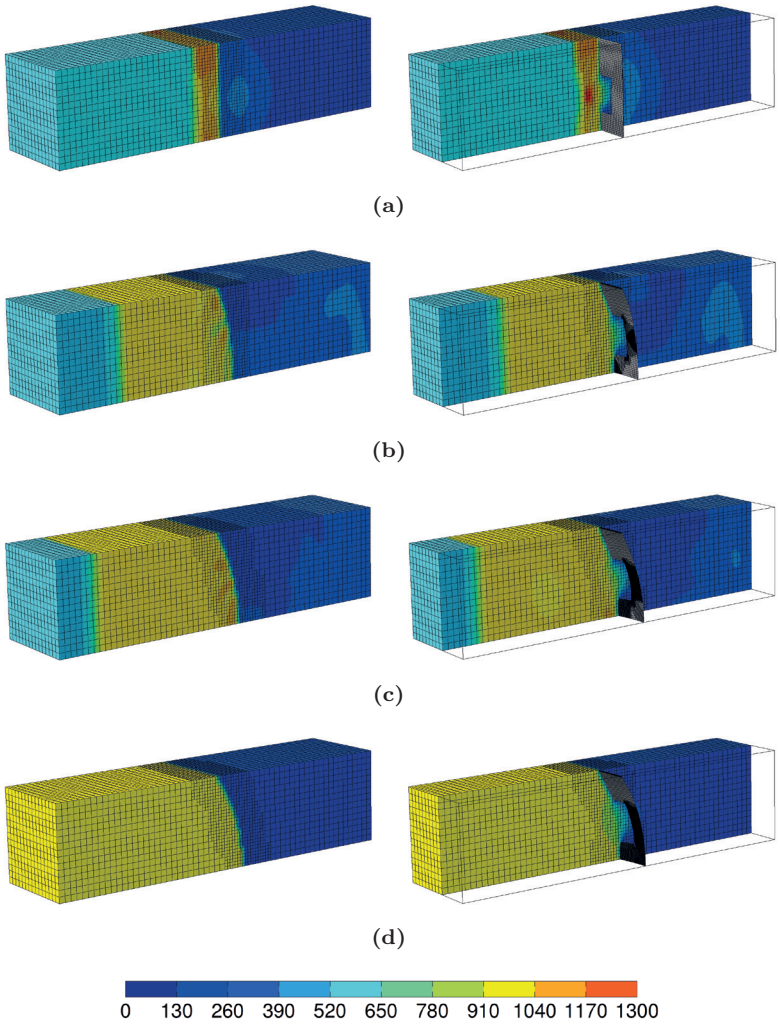

Figure 9.47: Pressure in the vicinity of the plate in test P25 using combined fluid and structural AMR. 1/4 of the model is used to illustrate the pressure along the centre of the fluid (left) and cross-sectional views along the centre of the holes (right): (a) $t = 24.3$ ms, (b) $t = 24.7$ ms, (c) $t = 24.9$ ms and (d) $t = 26.8$ ms. Fringe colors represent the contour map of the overpressure (in kPa).

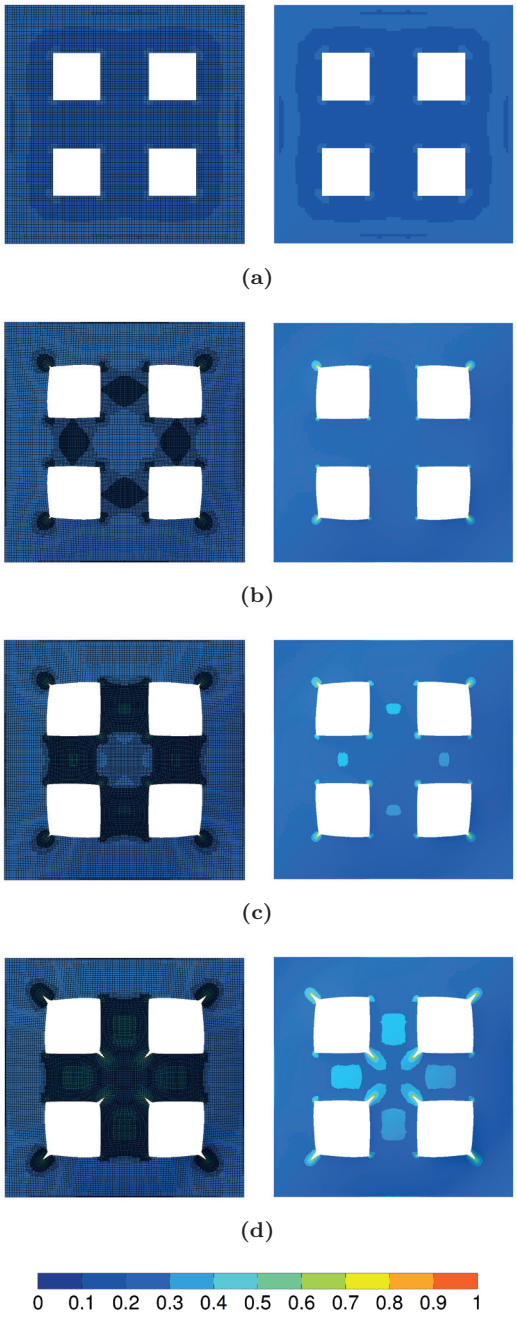

Figure 9.48: Crack growth in the plate during the fully coupled simulations of test P25 using AMR: (a) $t = 24.3$ ms, (b) $t = 24.7$ ms, (c) $t = 24.9$ ms and (d) $t = 26.8$ ms. Note that the plate is shown with (left) and without (right) element outlines. Fringe colors represent the damage parameter in Eq. (4.36).

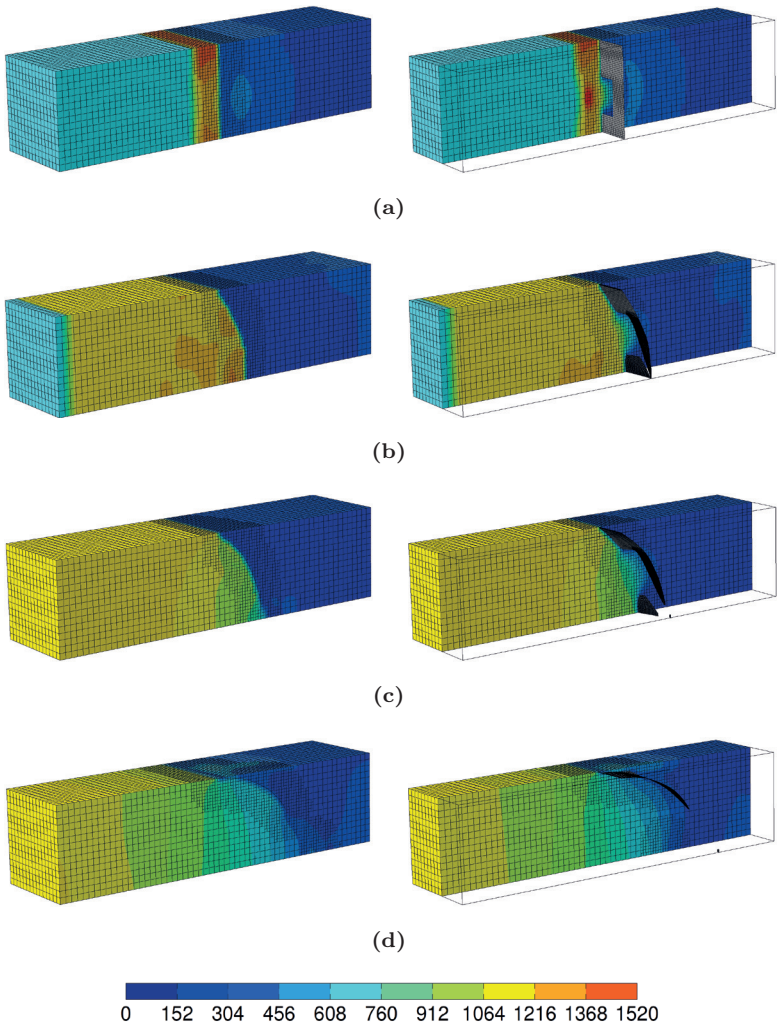

Figure 9.49: Pressure in the vicinity of the plate in test P35 using combined fluid and structural AMR. 1/4 of the model is used to illustrate the pressure along the centre of the fluid (left) and cross-sectional views along the centre of the holes (right): (a) $t = 23.1$ ms, (b) $t = 23.9$ ms, (c) $t = 24.2$ ms and (d) $t = 24.7$ ms. Fringe colors represent the contour map of the overpressure (in kPa).

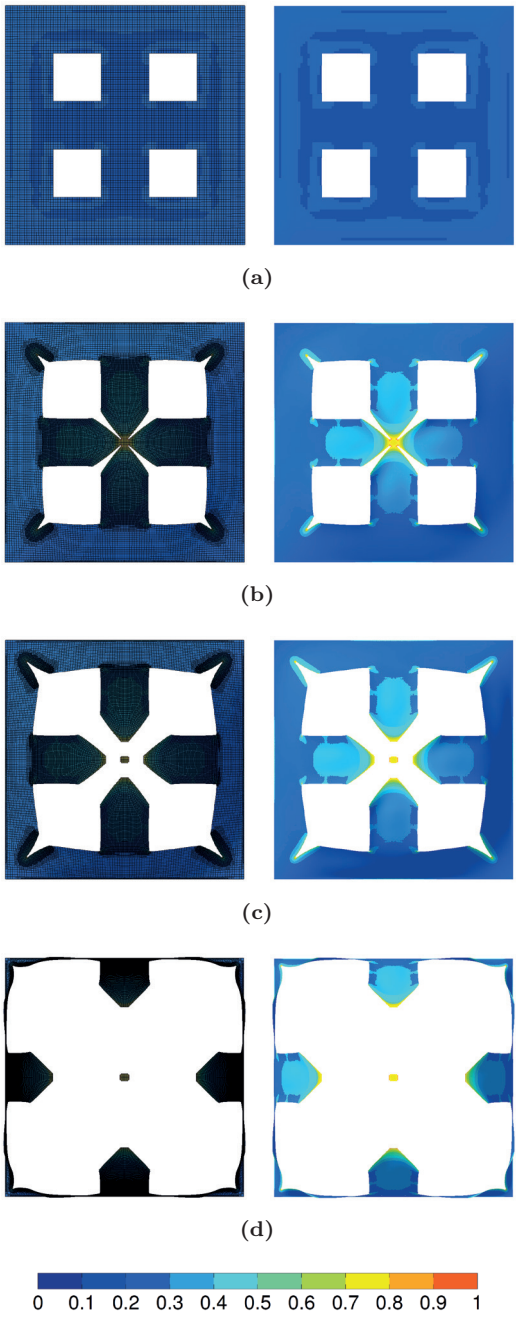

Figure 9.50: Crack growth in the plate during the fully coupled simulations of test P35 using AMR: (a) $t = 23.1$ ms, (b) $t = 23.9$ ms, (c) $t = 24.2$ ms and (d) $t = 24.7$ ms. Note that the plate is shown with (left) and without (right) element outlines. Fringe colors represent the damage parameter in Eq. (4.36).

9.6 Concluding remarks

The material parameters for the materials used in the shock tube experiments were identified, before presenting a brief overview of the governing equations in the coupled FSI simulations in EPX. Then, purely Eulerian and Lagrangian simulations were carried out to evaluate the fluid and structural sub-domains separately. The wave patterns in the Eulerian simulations were compared to the massive plate tests in Section 8.3.2. It was found that the blast properties were overestimated in the simulations for reflected pressures larger than approximately 800 kPa. Further comparisons of the wave propagation downstream the diaphragms indicated that the assumption of an instantaneous diaphragm burst overestimated the initial flow immediately downstream the diaphragm. The numerical model in the fluid sub-domain was also found to overestimate the shock velocity, and the deviation was increasing with the distance downstream the diaphragms. This may indicate that the deviation at larger reflected pressures was due to the fact that both the diaphragm opening and friction against the interior tube walls were neglected in the numerical model. However, a more detailed modelling of these effects are considered beyond the scope of this thesis.

The purely Lagrangian simulations investigated the influence of boundary conditions and mesh size on the dynamic response and failure of the plates. The loading measured during the massive plate tests in Section 8.3.2 was imposed on the exposed area of the plates in an uncoupled approach. As expected, allowing for sliding at the supports resulted in larger mid-point deflections. This was most evident for the flexible plates without holes. Failure in the plates was only predicted when using a mesh size equal to the plate thickness (i.e., 0.8 mm). However, such a uniformly refined mesh resulted in a significant increase in the CPU cost. The capabilities of damage-based adaptive mesh refinement (AMR) in the plates were therefore investigated in an attempt to reduce the CPU cost. It was found that the predicted failure patterns were highly dependent on the initial mesh size and damage threshold. Using an initial mesh size of 3 mm and two successive levels of refinement when $0.01 \leq D \leq 0.05$, the AMR model captured the same failure patterns as in the experiments with a significant reduction in CPU cost. The performance of the fluid and structural sub-domains were therefore considered sufficient for qualitative studies on the influence of FSI effects on the dynamic response of the flexible plates.

Fully coupled simulations were therefore performed based on the experience from the purely Eulerian and Lagrangian simulations. This was mainly a numerical study where the uncoupled approach served as the basis of comparison. Even

though the investigations of FSI effects were numerical, the experimental data was also included in the comparisons for completeness. As expected, the uncoupled approach predicted larger deformations due to the inherent assumption that the pressure is unaltered by the plate deformation. The coupled simulations of the steel plate tests without pre-formed holes showed a reduction in the reflected pressure (at Sensor 2) during the plate deformation, while a small increase in pressure was observed at the plate centre at the point of maximum deflection. The observed FSI effects may therefore be a combination of both the induced velocity and deformed shape of the plate, where the deformed shape introduced a non-uniform pressure distribution in front of the plate. The simulations of the aluminium plates showed in general similar trends as the steel plates, but with some distinct differences. It was observed more noticeable FSI effects in the aluminium plates, where the mid-point deflections were significantly overestimated in the uncoupled approach and the reduction in the reflected pressure was more evident in the coupled simulations. Moreover, due to the relatively small overpressures in the aluminium plate tests, the loading in the coupled simulations was in good agreement with the experimental data. However, despite this agreement, the mid-point deflections were considerably underestimated in the coupled simulations compared to the experimental observations.

The introduction of pre-formed holes in the steel plates showed a slight venting of the pressure through the holes, resulting in a reduced pressure close to the holes and a stagnation of pressure in front of the holes. As in the uncoupled approach, an element size of 10 mm was too large to predict the failure observed in the experiments. Combined fluid and structure AMR was therefore used to predict the observed failure patterns with a reasonable CPU cost. It was also observed larger mid-point deflections than in the corresponding simulations without AMR. In particular, the predicted mid-point deflections and pressures were in very good agreement with the experimental data for the aluminium plate tests. A plausible explanation for the increased mid-point deflections is an improved representation of the near instantaneous rise in pressure over the shock wave due to the fine cell size close to the plate. This indicated that thin flexible plates are very sensitive to small variations in the loading, because a minor increase in the reflected pressure resulted in a significant increase in the mid-point deflections. The observations of increasing FSI effects in blast events involving lightweight structures are also supported by the works in Refs. [70, 72, 82–85, 90, 91], where it was observed a noticeable reduction in the pressure due to the induced motion of lightweight structures.

The simulations presented in this section illustrate the complexity in coupled simulations of flexible plates exposed to blast loading, where the predicted results were found to depend on the chosen FSI technique (ALE or embedded)

and the mesh size in both the fluid and structural sub-domains. Although the results were encouraging in the coupled simulations using AMR, especially in the simulations of the aluminium plate tests, there are still several unsolved issues. In particular, the loading was overestimated in the simulations of the steel plates at increasing magnitudes of pressure and the sliding at the supports was not considered in the coupled simulations. An important step in the investigation of FSI effects during the dynamic response of thin flexible plates is a better description of the blast loading. It is therefore a need to improve the performance of the fluid sub-domain and also include more elaborate boundary conditions before quantifying the FSI effects in the experiments. These improvements are left for future work.

Part IV

Conclusions and Outlook

10

Conclusions and outlook

This thesis contributes with an improved understanding of the behaviour and modelling of flexible structures subjected to blast loading. Experimental and numerical research tools are established to study the dynamic response of flexible structures in controlled and repeatable blast environments. A better insight and new aspects of the response of blast-loaded thin aluminium and steel plates have been achieved through material and component tests in combination with numerical simulations. Special focus has been placed on material behaviour and fluid-structure interaction effects. This chapter completes the work with some final discussions, some conclusions and suggestions for further work within this topic.

10.1 Conclusions

The most important contribution from this work is presumably the establishment of experimental and computational frameworks to study the dynamic response of blast-loaded flexible structures in controlled environments. These frameworks have then been used to perform both experimental and numerical studies on the response of thin aluminium and steel plates subjected to blast loading, where the experimental data have served as a basis for evaluation of the numerical simulations. The experiments and simulations provide valuable insight to the behaviour and modelling of flexible structures in blast environments, and parameters influencing the dynamic response have been investigated and identified. The numerical simulations were mainly performed in the finite element (FE) code EUROPLEXUS. Material tests are also performed to determine the materials' behaviour at large plastic strains and for calibration of an energy-based failure criterion. In general, the response of thin aluminium and steel plates are found to be sensitive to small variations in the loading. Thus, an accurate description of the loading is necessary for quantitative investigations of the dynamic response and failure mechanisms in the plates. Depending on the blast intensity and structural properties, the response of the flexible plates may become significantly different. From a computational point of view, the simulation of blast-loaded flexible structures may be challenging since it implies the use of an appropriate constitutive relation, failure criterion and an

accurate description of the blast load. It is therefore believed that the detailed experimental data reported in this study can be used in the development and evaluation of advanced computational methods often required in blast-resistant design of flexible structures.

The experimental and numerical studies covered two distinct loading domains. First, the influence of stand-off distance on the dynamic response of thin steel and aluminium plates subjected to near-field blast loading was investigated in **Part II**. The loading was generated by detonating spherical charges of C-4 at various stand-off distances relative to the centre point of the plates, while the structural response was measured using two high-speed cameras in a stereovision setup combined with 3D-DIC analyses. The trend in all tests was that the maximum mid-point deflection was driven by the positive impulse from the airblast, since it occurred after the positive phase of the blast loading. The numerical results were generally in good agreement with the experimental data and covered the entire range of inelastic response. This included partial and complete tearing along the boundaries at the closest stand-off distances and a counter-intuitive behaviour (CIB) where the permanent deflection of the plate was in the opposite direction to the incoming blast wave due to reversed snap buckling (RSB). The influence of elastic effects and negative phase on RSB was studied numerically, and two types of CIB were identified within a narrow range of loading and structural conditions. Both types of CIB were found to depend on the timing and magnitude of the peak negative pressure relative to the dynamic response of the structure. In particular, CIB of Type III was driven by elastic effects enhanced by the negative phase during the elastic rebound, while Type III* occurred during the subsequent oscillations after the elastic rebound and was related to the timing of the peak negative pressure and the ratio between positive and negative impulses. CIB of Type III is also observed in previous studies considering projectile impacts and positive phase loading. However, to the author's best knowledge there are no previous experimental studies on metallic plates observing CIB of Type III* due to the negative phase. Thus, the blast-loaded plates experienced severe blast-structure interaction effects during the negative phase and the loading domain of thin flexible plates should not be determined solely based on the positive phase of the blast load.

Part III of this work presented the development and design of the SIMLab Shock Tube Facility (SSTF). The SSTF was found to produce controlled and repeatable blast loading in laboratory environments, where the positive phase loading was similar to that of an unconfined far-field airblast. The SSTF therefore allows for the evaluation of blast-structure interaction without the need to consider the inherent complexity in close-in and near-field detonations, and was used to study the dynamic response of blast-loaded steel and aluminium

plates. Both massive and flexible plates were mounted at the tube end during testing, where the massive plate tests serve as a basis for comparison with respect to fluid-structure interaction (FSI) effects. 3D-DIC was used to quantify the dynamic response of the flexible plates during testing, and synchronization of the 3D-DIC and pressure measurements enabled a thorough investigation of the experiments. Numerical studies, using both uncoupled and coupled approaches, were also performed in an attempt to obtain more insight into the FSI effects during the dynamic response. Special focus was placed on the influence of FSI effects during large deformations, pre-formed holes on the dynamic response and failure characteristics of the flexible plates. It was shown that the induced motion of the plate altered the pressure at its surface, where the reduced pressures were most evident in the plates with pre-formed holes. The findings in this thesis therefore supports previous observations in the literature, where FSI effects are found to mitigate the blast load acting on lightweight and flexible structures. Based on the shock tube experiments and corresponding numerical studies, the blast mitigation was related to both the induced velocity and to the deformed shape of the structure. However, the most dominating parameter in view of blast mitigation seems to be the overlapping of the dynamic response and the positive phase duration. This is interesting in view of lightweight and flexible structures. Lightweight structures will experience a higher induced velocity after impact and a reduction in the transmitted impulse, while flexible structures may experience large deformations. This implies that large deformations and energy absorption in structural members are favourable, since the blast wave is partially absorbed through various deformation mechanisms in the structure. Provided that the structural member can sustain the deformation that arise without experiencing failure, this indicates that ductile materials may be utilized in the design of flexible structures by allowing for finite deformations. The FSI may then reduce the transmitted impulse and serve as alternative load paths. However, this requires a thorough understanding of the governing physics in the problem.

The simulations of the shock tube experiments illustrate the complexity in coupled simulations of flexible plates exposed to blast loading, where the predicted results were found to depend on the chosen FSI technique and the mesh size in both the fluid and structural sub-domains. Although the results were encouraging in the coupled simulations using adaptive mesh refinement (AMR) in both sub-domains, especially in the simulations of the aluminium plate tests, there are still several unsolved issues. In particular, the loading was overestimated in the simulations of the steel plates at increasing magnitudes of pressure and the sliding at the supports was not considered in the coupled simulations. An important step in the investigation of FSI effects during the dynamic response of thin flexible plates is a better description of the blast loading. It is therefore

a need to improve the performance of the fluid sub-domain and also include more elaborate boundary conditions before quantifying the FSI effects in the experiments. The numerical simulations indicate that failure could be predicted by element erosion and a relatively simple energy-based criterion if one is able to predict the deformations, i.e., using an appropriate constitutive relation at large deformations, and an accurate description of the blast loading. Moreover, the use of damage-based AMR was promising in terms of predicting ductile failure in blast-loaded plates without too much loss of mass and at a reasonable CPU cost. This may be interesting in blast-resistant design of plated structures since these are typically made with geometries that closely resemble shell structures, i.e., one of the dimensions (typically the thickness) is significantly smaller than the others. Such structures often require a fine mesh size to represent localization of damage and crack growth. However, the predicted failure patterns with AMR were highly dependent on the initial mesh size and an appropriate damage threshold. Further investigations are therefore needed to better understand and ensure an appropriate use of damage-based AMR in engineering applications. These improvements are left for future work.

10.2 Further work

Based on the work and findings presented in this thesis, the following is suggested as further work:

- An important step in the investigation of FSI effects during the shock tube experiments is an accurate description of the blast loading. It is therefore a need to improve the performance of the fluid-subdomain in the fully coupled simulations to obtain a quantitatively agreement with the experimental data. The shock wave arrived earlier at the respective sensors in the simulations which implies that the velocity was slightly overestimated in the numerical model. A plausible explanation may be friction effects against the interior tube walls, or that the equation of state used in this work was not suitable for the largest pressures. More realistic boundary conditions for the plates should also be included in the numerical model before using the simulations to obtain a better insight into the FSI effects in the experiments. The experimental and numerical frameworks presented in this thesis could then be used to further contribute in the discussion of FSI effects during the response of flexible structures.

- The experience from the fully coupled simulations of the shock tube experiments could also be used in similar simulations of the airblast tests in **Part II**. Even though the uncoupled approach in Chapter 5 to a large extent predicted the experimental observations, it would be

interesting to study the performance of fully coupled simulations in such blast environments. These simulations would include the modelling of the explosive detonation, the 3D propagation of the blast wave through the surrounding air and the coupling at the fluid-structure interface.

- The shock tube study on the influence of pre-formed holes on the dynamic response of blast-loaded plates and reflected pressure in Chapter 8 may be extended to include slits, other geometries of the holes, various hole sizes and other plate thicknesses.

- Shock tube experiments could be used in combination with 3D-DIC measurements to determine the dynamic material properties at intermediate strain rates (10^1 s^{-1} $< \dot{\varepsilon} <$ 10^3 s^{-1}) for blast-loaded plates and under biaxial response. That is, dynamic material properties can be obtained by using the FE method and inverse modelling targeted against the experimental data. The use of the SSTF in such an approach is interesting because the flexible plates experience a non-uniform spatial and temporal strain rate distribution during the response from zero to maximum deformation. A single experiment could therefore (at least in theory) be used to identify the dynamic material properties in the actual range of strain rates.

- Although it was observed that the experimental pressure measurements and the idealized shock tube theory were in acceptable agreement, indicating that the pressure measurements reported herein are reliable, the deviations were in the order of 20 % at the largest blast intensities (see Table 8.5). An alternative approach to validate the pressure measurements against the idealized theory should therefore be considered, e.g. by producing a temporally uniform pressure pulse as a basis for evaluating the performance of the SSTF and pressure sensors.

- Since plated structures are frequently used in blast-resistant design, this motivates further studies on the performance of damage-based AMR to predict failure of coarsely meshed shell structures exposed to blast loading. This is important in practical applications and FSI simulations, because a finer mesh is often needed in the fluid compared to that in the structure to obtain an accurate pressure field.

- Other constitutive relations and failure criteria should be considered, e.g. the capabilities of stress-based instability and necking criteria in predicting failure in coarsely meshed shell structures.

- Further development of experimental measurement techniques to be used in the SSTF is also needed, e.g. the measurement of the forces transmitted to the supports during testing.

- Finally, the SSTF can be used in a wide range of applications to study blast-loaded structures within the facility's limitations in structural geometries and blast intensities. For instance, the SSTF may be used to investigate the effect of localized blast loading on larger structural components located inside the tank. The SSTF may also be used to study the flow field in the vicinity of test specimens located inside the window section.

Bibliography

[1] Global terrorism database (GTD). *National Consortium for the Study of Terrorism and Responses to Terrorism*. https://www.start.umd.edu/gtd/ [accessed 03.02.17], 2017.

[2] NOU. Norges offentlige utredninger. *NOU 2012:14, Rapport fra 22. juli-kommisjonen*, pages 411–446, 2012.

[3] W. Baker, P. Cox, P. Westine, J. Kulesz, and R. Strehlow. *Explosion Hazards and Evaluation*. Elsevier, Amsterdam, 1983.

[4] C. N. Kingery and G. Bulmash. *Airblast Parameters from TNT Spherical Air Burst and Hemispherical Surface Burst*. Defence Technical Information Center, Ballistic Research Laboratory, Aberdeen Proving Ground, Maryland, 1984.

[5] G. F. Kinney and K. J. Graham. *Explosive Shocks in Air*. Springer, Berlin, 1985.

[6] H. J. Goodman. *Compiled free-air blast data on bare spherical pentolite*. BRL Memo Rep. 1092. US Army, Ballistic Research Laboratory, Aberdeen Proving Ground, MD, 1960.

[7] C. N. Kingery. *Air blast parameters versus distance for hemispherical TNT surface bursts*. Rep. BRL 1344. US Army, Ballistic Research Laboratory, Aberdeen Proving Ground, MD, 1966.

[8] W. E. Baker. *Explosions in air*. University of Austin Press, Austin, TX, 1973.

[9] M. Swisdak. *Explosion effects and properties*. Rep. NSWC/WOL/TR 75–116. Naval Surface Weapons Center, White Oak, Silver Spring, MD, 1975.

[10] R. Reisler, B. Pettit, and L. Kennedy. *Air blast data from height-of-burst studies in Canada. Vol. I, HOB 5.4 to 71.9 feet.* BRL Memo Rep. 1950. US Army, Ballistic Research Laboratory, Aberdeen Proving Ground, MD, 1976.

[11] R. Reisler, B. Pettit, and L. Kennedy. *Air blast data from height-of-burst studies in Canada. Vol. II, HOB 45.4 to 144.5 feet*. BRL Memo Rep. 1990. US Army, Ballistic Research Laboratory, Aberdeen Proving Ground, MD, 1977.

[12] A. J. Hoffman and S. N. Mills. *Air blast measurements about explosive charges at side-on and normal incidence*. BRL Memo Rep. 988. US Army, Ballistic Research Lab, Aberdeen Proving Ground, MD, 1956.

[13] Keefer, Reisler, Giglio-Tos, and Kellner. *Airblast phenomena*. Rep. POR-3001. Ballistic Research Laboratory, Aberdeen Proving Ground, MD, 1966.

[14] W. E. Baker, P. S. Westine, and F. T. Dodge. *Similarity Methods in Engineering Dynamics: Theory and Practice of Scale Modeling*. Elsevier Science Publishers B.V., Amsterdam, Netherlands, 1991.

[15] F. P. Lees. *Loss Prevention in the Process Industries, Chapter 17 - Explosions*. Elsevier Inc., 2012.

[16] US Army Corps of Engineers (USACE). *Structures to resist the effects of accidental explosions*. UFC 3-340-02. Supersedes TM5-1300, dated November 1990. US Department of Defense, Washington DC, 2008.

[17] D. Hyde. *ConWep - Application of TM 5-855-1. Fundamentals of Protective Design for Conventional Weapons*. Structural Mechanics Division, Structures Laboratory, USACE Waterways Experiment Station, Vicksburg, MS, USA, 1992.

[18] F. G. Friedlander. The diffraction of sound pulses. I. Diffraction by a semi-infinite plane. *Proceedings of the Royal Society A: Mathematical, Physical and Engineering Science*, 186(1006):322–344, 1946.

[19] M. Larcher. *Simulation of the effects of an air blast wave, JRC Technical report, EUR 41337 EN*. Publications Office of the European Union, Luxembourg, 2007.

[20] V. Aune, T. Børvik, and M. Langseth. *Lecture Notes TKT4128 Impact Mechanics - An Introduction to Blast Mechanics*. Norwegian University of Science and Technology (NTNU), Department of Structural Engineering, SIMLab, 2015.

[21] V. Karlos, G. Solomos, and M. Larcher. Analysis of the blast wave decay coefficient using the Kingery-Bulmash data. *International Journal of Protective Structures*, 7(3):409–429, 2016.

[22] T. Krauthammer and A. Altenberg. Negative phase blast effects in glass panels. *International Journal of Impact Engineering*, 24(1):1–17, 2000.

[23] M. Larcher, G. Solomos, F. Casadei, and N. Gebbeken. Experimental and numerical investigations of laminated glass subjected to blast loading. *International Journal of Impact Engineering*, 39:42–50, 2012.

[24] C. Gantes and N. Pnevmatikos. Elastic-plastic response spectra for exponential blast loading. *International Journal of Impact Engineering*, 30(3):323–343, 2004.

[25] J. Wei and L. R. Dharani. Response of laminated architectural glazing subjected to blast loading. *International Journal of Impact Engineering*, 32(12):2032–2047, 2006.

[26] M. Teich and N. Gebbeken. The influence of the underpressure phase on the dynamic response of structures subjected to blast loads. *International Journal of Protective Structures*, 1(2):219–233, 2010.

[27] S. A. Granström. *Loading characteristics of air blasts from detonating charges*. Technical report 100, Transactions of the Royal Institute of Technology Stockholm, Sweden, 1956.

[28] NAVFAC. *Blast Resistant Structures*. Naval Facilities Engineering Command (NAVFAC), Alexandria, VA, DM 2.08, 1986.

[29] US Army Corps of Engineers (USACE). *Methodology manual for the single-degree-of-freedom blast effects design spreadsheets (SBEDS)*. USACE, ACE Protective Design Centre, USA, PDC TR-06-01 Rev 1, 2008.

[30] S. E. Rigby, A. Tyas, T. Bennett, S. D. Clarke, and S. D. Fay. The negative phase of the blast load. *International Journal of Protective Structures*, 5(1):1–20, 2014.

[31] L. M. Bryant, J. M. Erekson, and K. W. Herrle. Are you positive about negative phase? In *American Society of Civil Engineers (ASCE) Structures Congress*, pages 103–114, 2013.

[32] D. Dusenberry. *Handbook of Blast-Resistant Design of Buildings*. John Wiley & Sons, 2010.

[33] D. Bogosian, J. Ferritto, and Y. Shi. Measuring uncertainty and conservatism in simplified blast models. *30th Explosive Safety Seminar, Atlanta, USA*, pages 1–26, 2002.

[34] A. Tyas, T. Bennett, J. A. Warren, S. D. Fay, and S. E. Rigby. Clearing of blast waves on finite-sized targets - an overlooked approach. *Applied Mechanics and Materials*, 82:669–674, 2011.

[35] A. Tyas, J. A. Warren, T. Bennett, and S. D. Fay. Prediction of clearing effects in far-field blast loading of finite targets. *Shock waves*, 21:111–119, 2011.

[36] J. Shin, A. S. Whittaker, and D. Cormie. Incident and normally reflected overpressure and impulse for detonations of spherical high explosives in free air. *Journal of Structural Engineering*, 141(12):4015057, 2015.

[37] J. Shin, A. S. Whittaker, and D. Cormie. TNT equivalency for overpressure and impulse for detonations of spherical charges of high explosives. *International Journal of Protective Structures*, 6(3):567–579, 2015.

[38] J. Shin, A. S. Whittaker, D. Cormie, and W. Wilkinson. Numerical modeling of close-in detonations of high explosives. *Engineering Structures*, 81:88–97, 2014.

[39] S. E. Rigby, A. Tyas, S. D. Clarke, S. D. Fay, J. J. Reay, J. A. Warren, M. Gant, and I. Elgy. Observations from preliminary experiments on spatial and temporal pressure measurements from near-field free air explosions. *International Journal of Protective Structures*, 6(2):175–190, 2015.

[40] Z. Xue and J. W. Hutchinson. Preliminary assessment of sandwich plates subject to blast loads. *International Journal of Mechanical Science*, 45:687–705, 2003.

[41] X. Qiu, V. S. Deshpande, and N. A. Fleck. Finite element analysis of the dynamic response of clamped sandwich beams subjected to shock loading. *European Journal of Mechanics A/Solids*, 22:801–814, 2003.

[42] R. Rajendran and J. M. Lee. Blast loaded plates. *Marine Structures*, 22:99–129, 2009.

[43] G. N. Nurick and J. B. Martin. Deformation of thin plates subjected to impulsive loading - A review - Part I - Theoretical considerations. *International Journal of Impact Engineering*, 8:159–170, 1989.

[44] G. N. Nurick and J. B. Martin. Deformation of thin plates subjected to impulsive loading - A review - Part II - Experimental results. *International Journal of Impact Engineering*, 8:171–186, 1989.

[45] T. X. Yu. Chapter 9: Elastic effects in the dynamic plastic response of structures, Structural Crashworthiness and failure. In N Jones and T Wierzbicki, editors, *Proceedings of the Third International Symposium on Structural Crashworthiness*, pages 295–332. Taylor & Francis Ltd, 1991.

[46] Q. M. Li, L. M. Zhao, and G. T. Yang. Experimental results on the counter-intuitive behaviour of thin clamped beams subjected to projectile impact. *International Journal of Impact Engineering*, 11:341–348, 1991.

[47] P. S. Symonds and T. X. Yu. Counterintuitive behavior in a problem of elastic-plastic beam dynamics. *ASME Journal of Applied Mechanics*, 52:517–522, 1985.

[48] Q. M. Li, Y. M. Liu, and G. W. Ma. The anomalous region of elastic-plastic beam dynamics. *International Journal of Impact Engineering*, 32:1357–1369, 2006.

[49] Q. M. Li and Y. M. Liu. Correlation between parameter sensitivity and counter-intuitive phenomenon of elastic-plastic beam dynamics. *Computers & Structures*, 84:156–165, 2006.

[50] G. Ma, Y. Liu, and Q. M. Li. Numerical simulations of dynamic instability of elastic-plastic beams. *Journal of Engineering Mechanics ASCE*, 132:260–267, 2006.

[51] E. A. Flores-Johnson and Q. M. Li. A brief note on the counter-intuitive region of a square plate. *International Journal of Impact Engineering*, 38:136–138, 2011.

[52] P. S. Symonds, J. F. McNamara, and F. Genna. Vibrations and permanent displacements of a pin ended beam deformed plastically by short pulse excitation. *International Journal of Impact Engineering*, 4:73–82, 1986.

[53] H. Kolosky, P. Rush, and P. S. Symonds. Some experimental observations of anomalous response of fully clamped beams. *International Journal of Impact Engineering*, 11:445–456, 1991.

[54] S. U. Galiev. Experimental observations and discussion of counterintuitive behavior of plates and shallow shells subjected to blast loading. *International Journal of Impact Engineering*, 18:783–802, 1996.

[55] S. B. Menkes and H. J. Opat. Broken beams - Tearing and shear failures in explosively loaded clamped beams. *Experimental Mechanics*, 13:480–486, 1973.

[56] R. G. Teeling-Smith and G. N. Nurick. The deformation and tearing of thin circular plates subjected to impulsive loads. *International Journal of Impact Engineering*, 11:77–91, 1991.

[57] M. D. Olson, G. N. Nurick, and J. R. Fagnan. Deformation and rupture of blast loaded square plates - Predictions and experiments. *International Journal of Impact Engineering*, 13:279–291, 1993.

[58] G. N. Nurick, M. E. Gelman, and N. S. Marshall. Tearing of blast loaded plates with clamped boundary conditions. *International Journal of Impact Engineering*, 18:803–827, 1996.

[59] G. N. Nurick and G. C. Shave. The deformation and tearing of thin square plates subjected to impulsive loads - An experimental study. *International Journal of Impact Engineering*, 18:99–116, 1996.

[60] T. Wierzbicki and G. N. Nurick. Large deformation of thin plates under localized impulsive loading. *International Journal of Impact Engineering*, 18:899–918, 1996.

[61] N. Jones. *Structural Impact*. Cambridge University Press, 2nd edition, 2012.

[62] X.-S. Kong, W.-G. Wu, J. Li, P. Chen, and F. Liu. Experimental and numerical investigation on a multi-layer protective structure under the synergistic effect of blast and fragment loadings. *International Journal of Impact Engineering*, 65:146–162, 2014.

[63] G. S. Langdon, I. B. Rossiter, V. H. Balden, and G. N. Nurick. Performance of mild steel perforated plates as blast wave mitigation technique: Experimental and numerical investigation. *International Journal of Impact Engineering*, 37:1021–1036, 2010.

[64] G. S. Langdon, G. N. Nurick, and N. J. Du Plessis. The influence of separation distance on the performance of perforated plates as a blast wave shielding technique. *Engineering Structures*, 33:3537–3545, 2011.

[65] K. G. Rakvåg, N. J. Underwood, G. K. Schleyer, T. Børvik, and O. S. Hopperstad. Transient pressure loading of clamped metallic plates with pre-formed holes. *International Journal of Impact Engineering*, 53:44–55, 2013.

[66] G. K. Schleyer, N. J. Underwood, H. M. Do, J. K. Paik, and B. J. Kim. On pulse pressure loading of plates with holes. *Central European Journal of Engineering*, 2(4):496–508, 2012.

[67] R. L. Veldman, J. Ari-Gur, and C. Clum. Response of pre-pressurized reinforced plates under blast loading. *International Journal of Impact Engineering*, 35:240–250, 2008.

[68] K. P. Dharmasena, H. N. G. Wadley, K. Williams, Z. Xue, and J. W. Hutchinson. Response of metallic pyramidal lattice core sandwich panels to high intensity impulsive loading in air. *International Journal of Impact Engineering*, 38:275–289, 2011.

[69] F. Casadei, J. P. Halleux, A. Sala, and F. Chillé. Transient fluid-structure interaction algorithms for large industrial applications. *Computer Methods in Applied Mechanics and Engineering*, 190:3081–3110, 2001.

[70] N. Kambouchev, L. Noels, and R. Radovitzky. Numerical simulation of fluid-structure interaction between air blast waves and free-standing plates. *Computers & Structures*, 85(11-14):923–931, 2007.

[71] T. Børvik, A. G. Hanssen, M. Langseth, and L. Olovsson. Response of structures to planar blast loads - A finite element engineering approach. *Computers & Structures*, 87:507–520, 2009.

[72] K. V. Subramaniam, W. Nian, and Y. Andreopoulos. Blast response of an elastic structure: Evaluation of the fluid-structure interaction effects. *International Journal of Impact Engineering*, 36:965–974, 2009.

[73] M. Teich and N. Gebebeken. Analysis of FSI effects of blast loaded flexible structures. *Engineering Structures*, 55:73–79, 2011.

[74] G. I. Taylor. The pressure and impulse of submarine explosion waves on plates. *In: Batchelor, G. K. (Ed.), The Scientific Papers of Sir G. I. Taylor, Volume III, Cambridge University Press, UK*, pages 287–303, 1963.

[75] V. S. Deshpande and N. A. Fleck. One-dimensional response of sandwich plates to underwater shock loading. *Journal of the Mechanics and Physics of Solids*, 53:2347–2383, 2005.

[76] J. W. Hutchinson and Z. Xue. Metal sandwich plates optimized for pressure impulses. *International Journal of Mechanical Sciences*, 47:545–569, 2005.

[77] V. S. Deshpande, A. Heaver, and N. A. Fleck. An underwater shock simulator. *Proceedings of the Royal Society A: Mathematical, Physical and Engineering Sciences*, 462:1021–1041, 2006.

[78] L. F. Mori, S. F. Lee, Z. Y. Xue, A. Vaziri, D. T. Queheillalt, K. P. Dharmasena, H. N. G. Wadley, J. W. Hutchinson, and H. D. Espinosa. Deformation and fracture modes of sandwich structures subjected to underwater impulsive loads. *Journal of Mechanics of Materials and Structures*, 2(10):1981–2006, 2007.

[79] H. N. G. Wadley, K. Dharmasena, Y. Chen, P. Dudt, D. Knight, R. Charette, and K. Kiddy. Compressive response of multilayered pyramidal lattices during underwater shock loading. *International Journal of Impact Engineering*, 35(9):1102–1114, 2008.

[80] Z. Xue and J. W. Hutchinson. A comparative study of impulse-resistant metal sandwich plates. *International Journal of Impact Engineering*, 30:1283–1305, 2004.

[81] P. J. Tan, S. R. Reid, and J. J. Harrigan. Discussion:"The resistance of clamped sandwich beams to shock loading" (Fleck, N. A., and Deshpande, V. S., 2004, ASME J. Appl. Mech., 71, pp. 386-401). *Journal of Applied Mechanics*, 72:978–979, 2005.

[82] N. Kambouchev. *Analysis of blast mitigation strategies exploiting fluid-structure interaction*. Phd thesis, Massachusetts Institute of Technology, 2007.

[83] N. Kambouchev, L. Noels, and R. Radovitzky. Nonlinear compressibility effects in fluid-structure interaction and their implications on the air-blast loading of structures. *Journal of Applied Physics*, 100:63519, 2006.

[84] N. Kambouchev, R. Radovitzky, and L. Noels. Fluid-structure interaction effects in the dynamic response of free-standing plates to uniform shock loading. *Journal of Applied Mechanics*, 74(5):1042–1045, 2007.

[85] A. Vaziri and J. W. Hutchinson. Metal sandwich plates subjected to intense air shocks. *International Journal of Solids and Structures*, 44:2021–2035, 2007.

[86] J. W. Hutchinson. Energy and momentum transfer in air shocks. *Journal of Applied Mechanics*, 76:51307, 2009.

[87] R. Courant and K. O. Friedrichs. *Supersonic flow and shock waves*. Springer-Verlag, New York, 1976.

[88] E. F. Toro. *Riemann solvers and numerical methods for fluid dynamics*. Springer-Verlag Berlin Heidelberg, third edition, 2009.

[89] A. G. Hanssen, L. Enstock, and M. Langseth. Close-range blast loading of aluminium foam panels. *International Journal of Impact Engineering*, 27:593–618, 2002.

[90] Y. Yuan. *Blast response of structures: Limits to deformation and fluid-structure interactions*. Phd thesis, University College London, 2015.

[91] Y. Yuan and P. J. Tan. On momentum and energy transfer to clamped elasto-plastic beam in intense air blasts. In *Proceedings of the 1st International Conference on Impact Loading of Structures and Materials (ICILSM)*, page 109, 2016.

[92] D. J. Benson. Chapter 25 - Explicit Finite Element Methods for Large Deformation Problems in Solid Mechanics. *Encyclopedia of Computational Mechanics, John Wiley & Sons*, 2: Solids, 2007.

[93] F. Casadei and N. Leconte. Coupling Finite Elements and Finite Volumes by Lagrange Multipliers for Explicit Dynamic Fluid-Structure Interaction. *International Journal for Numerical Methods in Engineering*, 86(1):1–17, 2011.

[94] F. Casadei, M. Larcher, and N. Leconte. Strong and Weak Forms of a Fully Non-conforming FSI Algorithm in Fast Transient Dynamics for Blast Loading of Structures. In *Proceedings of the 3rd International Conference on Computational Methods in Structural Dynamics and Earthquake Engineering (COMPDYN 2011)*, pages 1120–1139, 2011.

[95] F. Casadei, P. Diez, and F. Verdugo. An algorithm for mesh refinement and un-refinement in fast transient dynamics. *International Journal of Computational Methods*, 10(4):1350018, 2013.

[96] F. Casadei, M. Larcher, and G. Valsamos. *Adaptivity in shell/beam/bar elements in EUROPLEXUS. JRC Technical report, EUR 26697 EN.* Publications Office of the European Union, Luxembourg, 2014.

[97] F. Casadei, M. Larcher, G. Valsamos, and V. Faucher. *Decoupled formulation of constraints on adaptive hanging nodes in EUROPLEXUS. JRC Technical report, EUR 27347 EN.* Publications Office of the European Union, Luxembourg, 2015.

[98] F. Casadei, G. Valsamos, M. Larcher, and V. Faucher. *Combined fluid and structure mesh adaptivity with fluid-structure interaction in EUROPLEXUS. JRC Technical report, EUR 27276 EN.* Publications Office of the European Union, Luxembourg, 2015.

[99] Federal Emergency Management Agency (FEMA). *Risk Assessment: Mitigate Potential Terrorist Attack Against Buildings, FEMA 452.* Federal Emergency Management Agency,Washington, D.C.: U. S. Department of Homeland Security, 2005.

[100] ISO. International Organization for Standardization. *ISO 16934, Glass in building - Explosion-resistant security glazing -Test and classification by shock-tube loading*, 2007.

[101] CEN. European Committee for Standardization. *NS-EN 13123-2: Windows, doors and shutters – Explosion resistance – Requirements and classification – Part 2: Range test*, 2001.

[102] CEN. European Commitee for Standardization. *NS-EN 13124-2: Windows, doors and shutters – Explosion resistance – Test method – Part 2: Range test*, 2001.

[103] K. Spranghers, I. Vasilakos, D. Lecompte, H. Sol, and J. Vantomme. Full-field deformation measurements of aluminum plates under free air blast loading. *Experimental Mechanics*, 52:1371–1384, 2012.

[104] S. Chung Kim Yuen, G. N. Nurick, G. S. Langdon, and Y. Iyer. Deformation of thin plates subjected to impulsive load: Part III - an update 25 years on. *International Journal of Impact Engineering*, Article in Press, 2016.

[105] S. Chung Kim Yuen and G. N. Nurick. Experimental and numerical studies on the response of quadrangular stiffened plates. Part I: Subjected to uniform blast load. *International Journal of Impact Engineering*, 31:55–83, 2005.

[106] N. Jacob, S. Chung Kim Yuen, G. N. Nurick, D. Bonorchis, S. A. Desai, and D. Tait. Scaling aspects of quadrangular plates subjected to localized blast loads - experiments and predictions. *International Journal of Impact Engineering*, 30:1179–1208, 2004.

[107] N. Jacob, G. N. Nurick, and G. S. Langdon. The effect of stand-off distance on the failure of fully clamped circular mild steel plates subjected to blast loads. *Engineering Structures*, 29:2723–2736, 2007.

[108] D. Karagiozova, G. N. Nurick, G. S. Langdon, S. Chung Kim Yuen, Y. Chi, and S. Bartle. Response of flexible sandwich-type panels to blast loading. *Composites Science and Technology*, 69(6):754–763, 2009.

[109] G. S. Langdon, D. Karagiozova, M. D. Theobald, G. N. Nurick, G. Lu, and R. P. Merrett. Fracture of aluminium foam core sacrificial cladding subjected to air-blast loading. *International Journal of Impact Engineering*, 37(6):638–651, 2010.

[110] K. P. Dharmasena, H. N. G. Wadley, Z. Xue, and J. W. Hutchinson. Mechanical response of metallic honeycomb sandwich panel structures to high-intensity dynamic loading. *International Journal of Impact Engineering*, 35(9), 2008.

[111] C. E. Needham. *Blast waves*. Springer-Verlag Berlin Heidelberg, 2010.

[112] G. K. Schleyer, S. S. Hsu, M. D. White, and R. S. Birch. Pulse pressure loading of clamped mild steel plates. *International Journal of Impact Engineering*, 28:223–247, 2003.

[113] G. Briassulis, J. H. Agui, J. Andreopoulos, and C. B. Watkins. A shock tube research facility for high-resolution measurements of compressible turbulence. *Experimental Thermal and Fluid Science*, 13:430–446, 1996.

[114] J. LeBlanc, A. Shukla, C. Rousseau, and A. Bogdanovich. Shock loading of three-dimensional woven composite materials. *Composite Structures*, 79:344–355, 2007.

[115] A. Lloyd, E. Jacques, M. Saatcioglu, D. Palermo, I. Nistor, and T. Tikka. Capabilities of a shock tube to simulate blast loading on structures. *American Concrete Institute (ACI) Special Publication*, 281:35–54, 2010.

[116] M. Colombo, M. Di Prisco, and P. Martinelli. A new shock tube facility for tunnel safety. *Experimental Mechanics*, 51(7):1143–1154, 2011.

[117] B. Justusson, M. Pankow, C. Heinrich, M. Rudolph, and A. M. Waas. Use of a shock tube to determine the bi-axial yield of an aluminium alloy under high rates. *International Journal of Impact Engineering*, 58:55–65, 2013.

[118] M. A. Louar, B. Belkassem, H. Ousji, K. Spranghers, D. Kakogiannis, L. Pyl, and J. Vantomme. Explosive driven shock tube loading of aluminium plates: Experimental study. *International Journal of Impact Engineering*, 86:111–123, 2015.

[119] R. Andreotti, M. Colombo, A. Guardone, P. Martinelli, G. Riganti, and M. Di Prisco. Performance of a shock tube facility for impact response of structures. *International Journal of Non-Linear Mechanics*, 72:53–66, 2015.

[120] A. R. K. Chennamsetty, J. LeBlanc, S. Abotula, P. N. Parrikar, and A. Shukla. Dynamic response of Hastelloy X plates under oblique shocks: Experimental and numerical studies. *International Journal of Impact Engineering*, 85:97–109, 2015.

[121] W. Nian, K. V. Subramaniam, and Y. Andreopoulos. Experimental investigation on blast response of cellular concrete. *International Journal of Impact Engineering*, 96:105–115, 2016.

[122] H. W. Liepmann and A. Roshko. *Elements of Gas Dynamics*. John Wiley & Sons, New York, 1957.

[123] I. I. Glass and J. G. Hall. *Shock tubes, Handbook of supersonic aerodynamics*. NAVORD Report 1488, Vol. 6, Section 18, U.S. Government Printing Office,Washington, DC, 1959.

[124] J. K. Wright. *Shock tubes*. John Wiley & Sons Inc., New York, 1961.

[125] A. G. Gaydon and I. R. Hurle. *The shock tube in high-temperature chemical physics*. Chapman and Hall Ltd., London, UK, 1963.

[126] V. Tiwari, M. A. Sutton, S. R. McNeill, S. Xu, X. Deng, W. L. Fourney, and D. Bretall. Application of 3D image correlation for full-field transient plate deformation measurements during blast loading. *International Journal of Impact Engineering*, 36:862–874, 2009.

[127] X. Zhao, V. Tiwari, M. A. Sutton, X. Deng, W. L. Fourney, and U. Leiste. Scaling of the deformation histories for clamped circular plates subjected to blast loading by buried charges. *International Journal of Impact Engineering*, 54:31–50, 2013.

[128] M. A. Sutton, J.-J. Orteu, and H. W. Schreier. *Image correlation for shape, motion and deformation measurements - Basic concepts, theory and applications*. Springer Science & Business Media, New York, 2012.

[129] G. Besnard, F. Hild, and S. Roux. "Finite-element" displacement fields analysis from digital images: Application to Portevin-Le Châtelier bands. *Experimental Mechanics*, 46:789–803, 2006.

[130] EUROPLEXUS. *User's manual - A computer program for the finite element simulation of fluid-structure systems under transient dynamic loading*. http://europlexus.jrc.ec.europa.eu [accessed 03.02.2017], 2016.

[131] K. H. Andersen and F. B. Hernandez. *Numerical simulations of Docol 600 DL steel plates subjected to blast loading*. Master's thesis, Norwegian University of Science and Technology, 2013.

[132] H. O. S. Eide and E. A. Melby. *Blast loaded aluminium plates - Experiments and numerical simulations*. Master's thesis, Norwegian University of Science and Technology, 2013.

[133] T. A. Hustad and A. L. Lindland. *Aluminium structures exposed to blast loading*. Master's thesis, Norwegian University of Science and Technology, 2014.

[134] S. Heggelund. *Docol 600 DL steel plates subjected to blast loading*. Master's thesis, Norwegian University of Science and Technology, 2014.

[135] C. Baglo and T. M. Dybvik. *Experimental and numerical study on plated structures subjected to blast loading - Numerical simulations and experimental validation*. Master's thesis, Norwegian University of Science and Technology, 2015.

[136] T. Tielemans. *Experimental and numerical study on plated structures subjected to blast loading*. Project thesis, Norwegian University of Science and Technology, 2015.

[137] H. M. Granum and L. M. Løken. *Experimental and numerical study on perforated steel plates subjected to blast loading*. Master's thesis, Norwegian University of Science and Technology, 2016.

[138] CEN. European Commitee for Standardization. *NS-EN 13123-1: Windows, doors and shutters – Explosion resistance – Requirements and classification – Part 1: Shock tube*, 2001.

[139] CEN. European Commitee for Standardization. *NS-EN 13124-1: Windows, doors and shutters – Explosion resistance – Test method – Part 1: Shock tube*, 2001.

[140] CEN. European Committee for Standardization. *NS-EN 13541: Glass in building – Security glazing – Test and classification by shock-tube loading*, 2012.

[141] P. W. Cooper. *Explosive Engineering*. Wiley-VCH, Inc., 1996.

[142] T. Krauthammer. *Modern Protective Structures*. CRC Press, Taylor & Francis Group, 2001.

[143] D. Cormie, G. Mays, and P. Smith. *Blast effects on buildings*. Thomas Telford, London, UK, second edition, 2012.

[144] E. J. Conrath, T. Krauthammer, K. A. Marchand, and P. F. Mlakar. *Structural design for physical security - State of the Practice*. American Society of Civil Engineers, 1999.

[145] J. M. Dewey. The Rankine-Hugoniot Equations: Their extensions and inversions related to blast waves. In *19th International Symposium on Military Aspects of Blast and Shock (MABS)*, 2006.

[146] W. J. M. Rankine. On the thermodynamic theory of waves of finite longitudinal disturbance. *Philosophical Transactions of the Royal Society London*, 160:277–286, 1870.

[147] W. J. M. Rankine. On the thermodynamic theory of waves of finite longitudinal disturbance. *Philosophical Transactions of the Royal Society London*, 160:287–288, 1870.

[148] P. H. Hugoniot. Mémoire sur la propagation du mouvement dans les corps et ples spécialement dans les gaz parfaits. *1 e Partie, Journal de l'École Polytechnique, Paris*, 57:3–97, 1887.

[149] P. H. Hugoniot. Mémoire sur la propagation du mouvement dans les corps et plus spécialement dans les gaz parfaits. *2 e Partie, Journal de l'École Polytechnique, Paris*, 57:1–125, 1889.

[150] US Army Material Command (AMC). *Engineering design handbook. Explosions in air. Part one. AD/A-003 817.* U.S. Army Material Command, Alexandria, Virginia, 1974.

[151] V. Karlos and G. Solomos. *Calculation of blast loads for application to structural components, JRC Technical report, EUR 26456 EN.* Publications Office of the European Union, Luxembourg, 2013.

[152] United Nations (UN). *International Ammunition Technical Guideline (ITAG), Formulae for ammunition management 01.80.* United Nations, 2011.

[153] VAPO. *Vulnerability Assessment and Protection Option (VAPO) Software.* https://www.ara.com/projects/vulnerability-assessment-and-protection-option-vapo [accessed 03.02.2017], 2017.

[154] J. F. Nichols and G. Doyle. Current Engineering Models and Capabilities in the Vulnerability Assessment and Protection Option (VAPO) Software. *Structures Congress, ASCE*, pages 176–187, 2014.

[155] S. E. Rigby, A. Tyas, and T. Bennett. Elastic-plastic response of plates subjected to cleared blast loads. *International Journal of Impact Engineering*, 66:37–47, 2014.

[156] V. Aune, E. Fagerholt, K. O. Hauge, M. Langseth, and T. Børvik. Experimental study on the response of thin aluminium and steel plates subjected to airblast loading. *International Journal of Impact Engineering*, 90:106–121, 2016.

[157] CEN. European Committee for Standardization. *NS-EN 1090-2:2008+A1:2011, Execution of steel structures and aluminium structures - Part 2: Technical requirements for steel structures*, 2008.

[158] Kistler Instrument Corp. *Piezoelectric Pressure Sensor, Type 603B.* http://www.kistler.com [accessed 03.02.17], 2016.

[159] Swedish Steel AB (SSAB). *Docol DP/DL Cold reduced dual phase steels.* SSAB Swedish Steel Ltd, http://www.ssab.com [accessed 03.02.17], 2017.

[160] G. Gruben, E. Fagerholt, O. S. Hopperstad, and T. Børvik. Fracture characteristics of a cold-rolled dual-phase steel. *European Journal of Mechanics A/Solids*, 30:204–218, 2011.

[161] G. Gruben, O. S. Hopperstad, and T. Børvik. Evaluation of uncoupled ductile fracture criteria for the dual-phase steel Docol 600DL. *International Journal of Mechanical Sciences*, 62:133–146, 2012.

[162] J. K. Holmen, O. S. Hopperstad, and T. Børvik. Low velocity impact on multi-layered dual-phase steel plates. *International Journal of Impact Engineering*, 78:161–177, 2015.

[163] CEN. European Committee for Standardization. *NS-EN 515 Aluminium and aluminium alloys - Wrought products - Temper designations*, 1993.

[164] J. A. Zukas, T. Nicholas, H. F. Swift, L. B. Greszczuk, and D. R. Curran. *Impact Dynamics*. Wiley & Sons, New York, USA, 1982.

[165] J. D. Campbell. Dynamic plasticity: macroscopic and microscopic aspects. *Materials Science and Engineering*, 12(1):3–21, 1973.

[166] N. Jones. The credibility of predictions for structural designs subjected to large dynamic loadings causing inelastic behaviour. *International Journal of Impact Engineering*, 53:106–114, 2013.

[167] D. K. Christoulis, S. Guetta, V. Guipont, and M. Jeandin. The influence of the substracte on the deposition of cold-sprayed titanium: An experimental and numerical study. *Journal of Thermal Spray Technology*, 20:523–533, 2011.

[168] E. Fagerholt. *Field measurements in mechanical testing using close-range photogrammetry and digital image analysis*. Phd thesis, Norwegian University of Science and Technology, 2012.

[169] E. Fagerholt, T. Børvik, and O. S. Hopperstad. Measuring discontinuous displacement fields in cracked specimens using Digital Image Correlation with mesh adaptation and crack-path optimization. *Optics and Lasers in Engineering*, 51:299–310, 2013.

[170] D. Bonorchis and G. N. Nurick. The influence of boundary conditions on the loading of rectangular plates subjected to localised blast loading - Importance in numerical simulations. *International Journal of Impact Engineering*, 36:40–52, 2009.

[171] T. Belytschko, W. Liu, and B. Moran. *Nonlinear Finite Elements for Continua and Structures*. John Wiley & Sons, Ltd., Chichester, UK, 2000.

[172] M. Ortiz and J. Simo. An analysis of a new class of integration algorithms for elastoplastic relations. *International Journal of Numerical Methods in Engineering*, 23:353–366, 1986.

[173] G. R. Johnson and W. H. Cook. A Constitutive Model and Data for Metals Subjected to Large Strains, High Strain Rates and High Temperatures. In *Proceedings of the 7th International Symposium on Ballistics, Hague*, pages 541–547, 1983.

[174] M. G. Cockcroft and D. J. Latham. Ductility and the workability of metals. *Journal of the Institute of Metals*, 96:33–39, 1968.

[175] V. Aune, F. Casadei, G. Valsamos, and T. Børvik. *Formulation and implementation of the VPJC material model in EUROPLEXUS*. JRC Technical Reports, EUR 27982 EN, Publications Office of the European Union, Luxembourg, 2016.

[176] O. S. Hopperstad and T. Børvik. *Lecture Notes KT8306 Plasticity Theory*. Norwegian University of Science and Technology (NTNU), Department of Structural Engineering, SIMLab, 2013.

[177] S. A. Khan and S. Huang. *Continuum Theory of Plasticity*. Wiley-Interscience, 1995.

[178] E. A. de Souza Neto, D. Peric, and D. R. J. Owen. *Computational methods for plasticity : theory and applications*. Wiley, UK, 2008.

[179] F. Irgens. *Continuum Mechanics*. Springer-Verlag Berlin Heidelberg, 2008.

[180] M. Ortiz and G. T. Camacho. Adaptive Lagrangian modelling of ballistic penetration metallic targets. *Computer Methods in Applied Mechanics and Engineering*, 142:269–301, 1997.

[181] T. Børvik, O. S. Hopperstad, T. Berstad, and M. Langseth. A computational model of viscoplasticity and ductile damage for impact and penetration. *European Journal of Mechanics A/Solids*, 20:685–712, 2001.

[182] E. Voce. The relationship between stress and strain for homogenous deformation. *Journal of the Institute of Metals*, 74:536–562, 1948.

[183] T. L. Anderson. Fracture Mechanics - Fundamentals and Applications. *Taylor and Francis Group, third edition*, 2005.

[184] G. S. Langdon, W. C. Lee, and L. A. Louca. The influence of material type on the structural response of plates to air-blast loading. *International Journal of Impact Engineering*, 78:150–160, 2015.

[185] T. Børvik, S. Dey, and A. H. Clausen. Perforation resistance of five different high-strength plates subjected to small-arms projectiles. *International Journal of Impact Engineering*, 36:948–964, 2009.

[186] A. Kane, T. Børvik, A. Benallal, and O. S. Hopperstad. Failure criteria with unilateral conditions for simulation of plate perforation. *European Journal of Mechanics - A/Solids*, 30:468–476, 2011.

[187] S. Dey, T. Børvik, O. S. Hopperstad, and M. Langseth. On the influence of fracture criterion in projectile impact of steel plates. *Computational Materials Science*, 38:176–191, 2006.

[188] J. K. Holmen, J. Johnsen, O. S. Hopperstad, and T. Børvik. Influence of fragmentation on the capacity of aluminium alloy plates subjected to ballistic impact. *European Journal of Mechanics A/Solids*, 55:221–233, 2016.

[189] M. L. Wilkins. Calculation of elastic-plastic flow. *Technical report UCRL-7322, Lawrence radiation Laboratory, University of California. Livermore, California*, April 19, 1963.

[190] R. D. Krieg and D. B. Krieg. Accuracies of numerical solution methods for elastic-perfectly plastic model. *ASME Journal of Pressure Vessel Technology*, 99(4):510–515, 1977.

[191] J. Simo and R. L. Taylor. Consistent tangent operators for rate-independent elastoplasticity. *Computer Methods in Applied Mechanics and Engineering*, 48(3):101–118, 1985.

[192] R. P. R. Cardoso and J. W. Yoon. Stress integration method for a nonlinear kinematic/isotropic hardening model and its characterization based on polycrystal plasticity. *International Journal of Plasticity*, 25:1684–1710, 2009.

[193] R. de Borst and P. H. Feenstra. Studies in anisotropic plasticity with reference to the Hill criterion. *International Journal for Numerical Methods in Engineering*, 29:315–336, 1990.

[194] F. Casadei, V. Aune, G. Valsamos, and M. Larcher. *Testing of the Johnson-Cook material model VPJC in EUROPLEXUS*. JRC Technical Reports, EUR 27594 EN, Publications Office of the European Union, Luxembourg, 2015.

[195] J. K. Holmen, J. Johnsen, J. Jupp, O. S. Hopperstad, and T. Børvik. Effects of heat treatment on the ballistic properties of AA6070 aluminium alloy. *International Journal of Impact Engineering*, 57:119–133, 2013.

[196] LSTC. *Livermore Software Technology Corporation (LSTC)*. http://www.lstc.com [accessed 03.02.17], 2016.

[197] V. Aune, G. Valsamos, F. Casadei, M. Larcher, M. Langseth, and T. Børvik. Numerical study on the structural response of blast-loaded thin aluminium and steel plates. *International Journal of Impact Engineering*, 99:131–144, 2017.

[198] C. Ruggieri, T. L. Panontin, and R. H. Dodds Jr. Numerical modelling of ductile crack growth in 3-D using computational cell elements. *International Journal of Fracture*, 18(1):99–116, 1996.

[199] M. P. Vieille. Sur les discontinuities par la détente brusque de gaz comprimés. *Comptes Rendus de l'Académie des Sciences*, 129:1228–1230, 1899.

[200] R. J. LeVeque. *Finite-volume methods for hyperbolic problems*. Cambridge University Press, first edition, 2004.

[201] J. D. Anderson. *Fundamentals of Aerodynamics*. McGraw-Hill, third edition, 2001.

[202] J. D. Anderson. *Modern Compressible Flow*. McGraw-Hill, third edition, 2004.

[203] S. J. Hiermaier. *Structures Under Crash and Impact - Continuum Mechanics, Discretization and Experimental Characterization*. Springer, 2008.

[204] H. J. Pain and E. W. E. Rogers. Shock waves in gases. *Reports on Progress in Physics*, 25:287–336, 1962.

[205] J. A. Zukas. *Introduction to hydrocodes*. Elsevier, 2004.

[206] S. Downes, A. Knott, and I. Robinsion. Towards a shock tube method for the dynamic calibration of pressure sensors. *Philosophical Transactions of the Royal Society London A*, 372(2023):299–316, 2014.

[207] C. Hirsch. *Numerical Computation of Internal and External Flows*. Elsevier Ltd., second edition, 2007.

[208] I. Danaila, P. Joly, S. M. Kaber, and M. Postel. *An Introduction to Scientific Computing*. Springer Science and Business Media, LLC, first edition, 2007.

[209] V. Aune, E. Fagerholt, M. Langseth, and T. Børvik. A shock tube facility to generate blast loading on structures. *International Journal of Protective Structures*, 7(3):340–366, 2016.

[210] CEN. European Committee for Standardization. *NS-EN 13445: Unfired Pressure Vessels*, 2014.

[211] P. Kumar and A. Shukla. Dynamic response of glass panels subjected to shock loading. *Journal of Non-Crystalline Solids*, 357:3917–3923, 2011.

[212] B. Zakrisson, B. Wikman, and H. Häggblad. Numerical simulations of blast loads and structural deformation from near-field explosions in air. *International Journal of Impact Engineering*, 38:597–612, 2011.

[213] N. N. Kleinschmit. *A Shock tube technique for blast wave simulation and studies of flow structure interactions in shock tube blast experiments.* Master's thesis, Univeristy of Nebraska-Lincoln, 2011.

[214] ISO. International Organization for Standardization. *ISO 2768-1, General tolerances - Part 1: Tolerances for linear and angular dimensions without individual tolerance indications*, 1989.

[215] C. Harris and M. Stevens. A combined corner and edge detector. In *Proceedings of the 4th Alvey Vision Conference*, pages 189–192, Manchester, UK, 1988.

[216] J. Heikkilä. *Accurate camera calibration and feature based 3-D reconstruction from monocular image sequences.* Phd thesis, University of Oulo, Finland, 1997.

[217] P. Sturm and S. Maybank. On plane-based camera calibration: A general algorithm, singularities, applications. In *Proceedings of the IEEE Conference on Computer Vision and Pattern Recognition*, pages 432–437, Colorado, US, 1999.

[218] F. Hild, B. Raka, M. Baudequin, S. Roux, and F. Cantelaube. Multiscale displacement field measurements of compressed mineral wool samples by digital image correlation. *Applied Optics*, 41:6815–6828, 2002.

[219] G. Gruben, M. Langseth, E. Fagerholt, and O. S. Hopperstad. Low-velocity impact on high-strength steel sheets: An experimental and numerical study. *International Journal of Impact Engineering*, 88:153–171, 2016.

[220] W. Riedel, C. Mayrhofer, K. Thoma, and A. Stoltz. Engineering and numerical tools for explosion protection of reinforced concrete. *International Journal of Protective Structures*, 1(1):85–101, 2010.

[221] R. G. Little. Cost-effective strategies to address urban terrorism: a risk management approach. In H. W. Richardson, P. Gordon, and J. E. I. I. Moore, editors, *The Economic Costs and Consequences of Terrorism*, pages 98–115. Edward Elgar Publishing Ltd, 2007.

[222] K. A. Brekken and P. T. Ingier. *Modelling of window glasses exposed to blast loading.* Master's thesis, Norwegian University of Science and Technology, 2016.

[223] S. R. Haug and K. Osnes. *Submerged floating tunnels subjected to internal blast loading.* Master's thesis, Norwegian University of Science and Technology, 2015.

[224] E. Hillestad and J. E. Pettersen. *Experimental and numerical studies of plain and reinforced concrete plates subjected to blast loading.* Master's thesis, Norwegian University of Science and Technology, 2016.

[225] F. Casadei, V. Aune, F. Daude, P. Galon, G. Valsamos, and M. Larcher. *Shock tube tests with coupled 1D-3D models in EUROPLEXUS. JRC Technical report, EUR 27890 EN.* Publications Office of the European Union, Luxembourg, 2016.

[226] M. Larcher and F. Casadei. Explosions in complex geometries - a comparison of several approaches. *International Journal of Protective Structures*, 1(2):169–196, 2010.

[227] J. Donea, A. Huerta, and J.-Ph. Ponthot. Chapter 14 - Arbitrary Lagrangian-Eulerian Methods. *Encyclopedia of Computational Mechanics, Vol. 1: Fundamentals, John Wiley & Sons, Ltd*, 2004.

[228] W. A. Wall, A. Gerstenberger, P. Gamnitzer, C. Förster, and E. Ramm. Large deformation fluid-structure interaction - Advances in ALE methods and new fixed grid approaches. *Lecture Notes in Computational Science and Engineering. Springer, Berlin*, 53:195–232, 2006.

[229] G. Hou, J. Wang, and A. Layton. Numerical methods for fluid-structure interaction - A review. *Communications in Computational Physics*, 12:337–377, 2012.

[230] T. Belytschko and J. Kennedy. Computer models for subassembly simulation. *Nuclear Engineering and Design*, 49:17–38, 1978.

[231] T. Belytschko, J. Kennedy, and D. Schoeberle. Quasi-Eulerian finite element formulation for fluid structure interaction. *Journal of Pressure Vessel Technology*, 102:62–69, 1980.

[232] J. Donea, P. Fasoli-Stella, and P. Giuliani. Lagrangian and eulerian finite element techniques for transient fluid-structure interaction problems. *In: Transactions of the 4th International Conference on Structural Mechanics in Reactor Technology*, 1977.

[233] C. Hirth, A. Amsden, and J. Cook. An Arbitrary Lagrangian-Eulerian computing method for all flow speeds. *Journal of Computational Physics*, 14:227–253, 1974.

[234] T. Hughes, W. Liu, and T. Zimmermann. Lagrangian-Eulerian finite element formulation for incompressible viscous flows. *Computer Methods in Applied Mechanics and Engineering*, 29:329–349, 1981.

[235] W. Noh. CEL: A time-dependent two-space-dimensional coupled Eulerian-Lagrangian code. *In Alder, B., Fernbach, S., Rotenberg, M., eds.: Methods in Computational Physics. Volume 3., Academic Press: New York*, pages 117–179, 1964.

[236] R. Deiterding and S. Wood. Parallel adaptive fluid-structure interaction simulation of explosions impacting on building structures. *Computers & Fluids*, 88:719–729, 2013.

[237] C. Peskin. The immersed boundary method. *Acta Numerica*, 1:479–517, 2002.

[238] R. Mittal and G. Iaccarino. Immersed boundary methods. *Annual Review of Fluid Mechanics*, 37:239–261, 2005.

[239] M. A. Puso, J. Sanders, R. Settgast, and B. Liu. An embedded mesh method in a multiple material ALE. *Computer Methods in Applied Mechanics and Engineering*, 245-246:273–289, 2012.

[240] F. Cirak, R. Deiterding, and S. Mauch. Large-scale fluid-structure interaction simulation of viscoplastic and fracturing thin-shells subjected to shocks and detonations. *Computers & Structures*, 85:1049–1065, 2007.

[241] M. Vanella, P. Rabenold, and E. Balaras. A direct-forcing embedded-boundary method with adaptive mesh refinement for fluid-structure interaction problems. *Journal of Computational Physics*, 229:6427–6449, 2010.

[242] R. van Loon, P. Anderson, F. van de Vosse, and S. Sherwin. Comparison of various fluid-structure interaction methods for deformable bodies. *Computers & Structures*, 85:833–843, 2007.

[243] J. W. Banks, W. D. Henshaw, and D. W. Schwendeman. Deforming composite grids for solving fluid structure problems. *Journal of Computational Physics*, 231:3518–3547, 2012.

[244] A. Chorin and J. E. Marsden. *A mathematical introduction to fluid mechanics*. Springer-Verlag Publishing Company, Inc., 2000.

[245] F. Casadei and S. Potapov. Permanent fluid-structure interaction in explicit transient dynamics. *Computer Methods in Applied Mechanics and Engineering*, 193:4157–4194, 2004.

[246] S. Giuliani. An algorithm for continuous rezoning of the hydrodynamics grid in Arbitrary Lagrangian Eulerian computer codes. *Nuclear Engineering and Design*, 72:205–212, 1982.

[247] F. Casadei, V. Aune, G. Valsamos, and M. Larcher. *Generalization of the pinball contact/impact model for use with mesh adaptivity and element erosion in EUROPLEXUS. JRC Technical report, EUR 27888 EN.* Publications Office of the European Union, Luxembourg, 2016.

DEPARTMENT OF STRUCTURAL ENGINEERING
NORWEGIAN UNIVERSITY OF SCIENCE AND TECHNOLOGY

N–7491 TRONDHEIM, NORWAY
Telephone: +47 73 59 47 00 Telefax: +47 73 59 47 01

"Reliability Analysis of Structural Systems using Nonlinear Finite Element Methods",
C. A. Holm, 1990:23, ISBN 82-7119-178-0.

"Uniform Stratified Flow Interaction with a Submerged Horizontal Cylinder",
Ø. Arntsen, 1990:32, ISBN 82-7119-188-8.

"Large Displacement Analysis of Flexible and Rigid Systems Considering
Displacement-Dependent Loads and Nonlinear Constraints",
K. M. Mathisen, 1990:33, ISBN 82-7119-189-6.

"Solid Mechanics and Material Models including Large Deformations",
E. Levold, 1990:56, ISBN 82-7119-214-0, ISSN 0802-3271.

"Inelastic Deformation Capacity of Flexurally-Loaded Aluminium Alloy Structures",
T. Welo, 1990:62, ISBN 82-7119-220-5, ISSN 0802-3271.

"Visualization of Results from Mechanical Engineering Analysis",
K. Aamnes, 1990:63, ISBN 82-7119-221-3, ISSN 0802-3271.

"Object-Oriented Product Modeling for Structural Design",
S. I. Dale, 1991:6, ISBN 82-7119-258-2, ISSN 0802-3271.

"Parallel Techniques for Solving Finite Element Problems on Transputer Networks",
T. H. Hansen, 1991:19, ISBN 82-7119-273-6, ISSN 0802-3271.

"Statistical Description and Estimation of Ocean Drift Ice Environments",
R. Korsnes, 1991:24, ISBN 82-7119-278-7, ISSN 0802-3271.

“Properties of concrete related to fatigue damage: with emphasis on high strength
concrete”,
G. Petkovic, 1991:35, ISBN 82-7119-290-6, ISSN 0802-3271.

"Turbidity Current Modelling",
B. Brørs, 1991:38, ISBN 82-7119-293-0, ISSN 0802-3271.

"Zero-Slump Concrete: Rheology, Degree of Compaction and Strength. Effects of
Fillers as Part Cement-Replacement",
C. Sørensen, 1992:8, ISBN 82-7119-357-0, ISSN 0802-3271.

"Nonlinear Analysis of Reinforced Concrete Structures Exposed to Transient Loading",
K. V. Høiseth, 1992:15, ISBN 82-7119-364-3, ISSN 0802-3271.

"Finite Element Formulations and Solution Algorithms for Buckling and Collapse Analysis of Thin Shells",
R. O. Bjærum, 1992:30, ISBN 82-7119-380-5, ISSN 0802-3271.

"Response Statistics of Nonlinear Dynamic Systems",
J. M. Johnsen, 1992:42, ISBN 82-7119-393-7, ISSN 0802-3271.

"Digital Models in Engineering. A Study on why and how engineers build and operate digital models for decisison support",
J. Høyte, 1992:75, ISBN 82-7119-429-1, ISSN 0802-3271.

"Sparse Solution of Finite Element Equations",
A. C. Damhaug, 1992:76, ISBN 82-7119-430-5, ISSN 0802-3271.

"Some Aspects of Floating Ice Related to Sea Surface Operations in the Barents Sea",
S. Løset, 1992:95, ISBN 82-7119-452-6, ISSN 0802-3271.

"Modelling of Cyclic Plasticity with Application to Steel and Aluminium Structures",
O. S. Hopperstad, 1993:7, ISBN 82-7119-461-5, ISSN 0802-3271.

"The Free Formulation: Linear Theory and Extensions with Applications to Tetrahedral Elements
with Rotational Freedoms",
G. Skeie, 1993:17, ISBN 82-7119-472-0, ISSN 0802-3271.

"Høyfast betongs motstand mot piggdekkslitasje. Analyse av resultater fra prøving i Veisliter'n",
T. Tveter, 1993:62, ISBN 82-7119-522-0, ISSN 0802-3271.

"A Nonlinear Finite Element Based on Free Formulation Theory for Analysis of Sandwich Structures",
O. Aamlid, 1993:72, ISBN 82-7119-534-4, ISSN 0802-3271.

"The Effect of Curing Temperature and Silica Fume on Chloride Migration and Pore Structure of High Strength Concrete",
C. J. Hauck, 1993:90, ISBN 82-7119-553-0, ISSN 0802-3271.

"Failure of Concrete under Compressive Strain Gradients",
G. Markeset, 1993:110, ISBN 82-7119-575-1, ISSN 0802-3271.

"An experimental study of internal tidal amphidromes in Vestfjorden",
J. H. Nilsen, 1994:39, ISBN 82-7119-640-5, ISSN 0802-3271.

"Structural analysis of oil wells with emphasis on conductor design",
H. Larsen, 1994:46, ISBN 82-7119-648-0, ISSN 0802-3271.

"Adaptive methods for non-linear finite element analysis of shell structures",
K. M. Okstad, 1994:66, ISBN 82-7119-670-7, ISSN 0802-3271.

"On constitutive modelling in nonlinear analysis of concrete structures",
O. Fyrileiv, 1994:115, ISBN 82-7119-725-8, ISSN 0802-3271.

"Fluctuating wind load and response of a line-like engineering structure with emphasis on motion-induced wind forces",
J. Bogunovic Jakobsen, 1995:62, ISBN 82-7119-809-2, ISSN 0802-3271.

"An experimental study of beam-columns subjected to combined torsion, bending and axial actions",
A. Aalberg, 1995:66, ISBN 82-7119-813-0, ISSN 0802-3271.

"Scaling and cracking in unsealed freeze/thaw testing of Portland cement and silica fume concretes",
S. Jacobsen, 1995:101, ISBN 82-7119-851-3, ISSN 0802-3271.

"Damping of water waves by submerged vegetation. A case study of laminaria hyperborea",
A. M. Dubi, 1995:108, ISBN 82-7119-859-9, ISSN 0802-3271.

"The dynamics of a slope current in the Barents Sea",
Sheng Li, 1995:109, ISBN 82-7119-860-2, ISSN 0802-3271.

"Modellering av delmaterialenes betydning for betongens konsistens",
Ernst Mørtsell, 1996:12, ISBN 82-7119-894-7, ISSN 0802-3271.

"Bending of thin-walled aluminium extrusions",
Birgit Søvik Opheim, 1996:60, ISBN 82-7119-947-1, ISSN 0802-3271.

"Material modelling of aluminium for crashworthiness analysis",
Torodd Berstad, 1996:89, ISBN 82-7119-980-3, ISSN 0802-3271.

"Estimation of structural parameters from response measurements on submerged floating tunnels",
Rolf Magne Larssen, 1996:119, ISBN 82-471-0014-2, ISSN 0802-3271.

“Numerical modelling of plain and reinforced concrete by damage mechanics”,
Mario A. Polanco-Loria, 1997:20, ISBN 82-471-0049-5, ISSN 0802-3271.

“Nonlinear random vibrations - numerical analysis by path integration methods”,
Vibeke Moe, 1997:26, ISBN 82-471-0056-8, ISSN 0802-3271.

"Numerical prediction of vortex-induced vibration by the finite element method",
Joar Martin Dalheim, 1997:63, ISBN 82-471-0096-7, ISSN 0802-3271.

"Time domain calculations of buffeting response for wind sensitive structures",
Ketil Aas-Jakobsen, 1997:148, ISBN 82-471-0189-0, ISSN 0802-3271.

"A numerical study of flow about fixed and flexibly mounted circular cylinders",
Trond Stokka Meling, 1998:48, ISBN 82-471-0244-7, ISSN 0802-3271.

"Estimation of chloride penetration into concrete bridges in coastal areas",
Per Egil Steen, 1998:89, ISBN 82-471-0290-0, ISSN 0802-3271.

"Stress-resultant material models for reinforced concrete plates and shells",
Jan Arve Øverli, 1998:95, ISBN 82-471-0297-8, ISSN 0802-3271.

"Chloride binding in concrete. Effect of surrounding environment and concrete composition",
Claus Kenneth Larsen, 1998:101, ISBN 82-471-0337-0, ISSN 0802-3271.

"Rotational capacity of aluminium alloy beams",
Lars A. Moen, 1999:1, ISBN 82-471-0365-6, ISSN 0802-3271.

"Stretch Bending of Aluminium Extrusions",
Arild H. Clausen, 1999:29, ISBN 82-471-0396-6, ISSN 0802-3271.

"Aluminium and Steel Beams under Concentrated Loading",
Tore Tryland, 1999:30, ISBN 82-471-0397-4, ISSN 0802-3271.

"Engineering Models of Elastoplasticity and Fracture for Aluminium Alloys",
Odd-Geir Lademo, 1999:39, ISBN 82-471-0406-7, ISSN 0802-3271.

"Kapasitet og duktilitet av dybelforbindelser i trekonstruksjoner",
Jan Siem, 1999:46, ISBN 82-471-0414-8, ISSN 0802-3271.

"Etablering av distribuert ingeniørarbeid; Teknologiske og organisatoriske erfaringer fra en norsk ingeniørbedrift",
Lars Line, 1999:52, ISBN 82-471-0420-2, ISSN 0802-3271.

"Estimation of Earthquake-Induced Response",
Símon Ólafsson, 1999:73, ISBN 82-471-0443-1, ISSN 0802-3271.

"Coastal Concrete Bridges: Moisture State, Chloride Permeability and Aging Effects"
Ragnhild Holen Relling, 1999:74, ISBN 82-471-0445-8, ISSN 0802-3271.

"Capacity Assessment of Titanium Pipes Subjected to Bending and External Pressure",
Arve Bjørset, 1999:100, ISBN 82-471-0473-3, ISSN 0802-3271.

“Validation of Numerical Collapse Behaviour of Thin-Walled Corrugated Panels”,
Håvar Ilstad, 1999:101, ISBN 82-471-0474-1, ISSN 0802-3271.

“Strength and Ductility of Welded Structures in Aluminium Alloys”,
Miroslaw Matusiak, 1999:113, ISBN 82-471-0487-3, ISSN 0802-3271.

“Thermal Dilation and Autogenous Deformation as Driving Forces to Self-Induced Stresses in High Performance Concrete”,
Øyvind Bjøntegaard, 1999:121, ISBN 82-7984-002-8, ISSN 0802-3271.

“Some Aspects of Ski Base Sliding Friction and Ski Base Structure”,
Dag Anders Moldestad, 1999:137, ISBN 82-7984-019-2, ISSN 0802-3271.

"Electrode reactions and corrosion resistance for steel in mortar and concrete",
Roy Antonsen, 2000:10, ISBN 82-7984-030-3, ISSN 0802-3271.

"Hydro-Physical Conditions in Kelp Forests and the Effect on Wave Damping and Dune Erosion. A case study on Laminaria Hyperborea",
Stig Magnar Løvås, 2000:28, ISBN 82-7984-050-8, ISSN 0802-3271.

"Random Vibration and the Path Integral Method",
Christian Skaug, 2000:39, ISBN 82-7984-061-3, ISSN 0802-3271.

"Buckling and geometrical nonlinear beam-type analyses of timber structures",
Trond Even Eggen, 2000:56, ISBN 82-7984-081-8, ISSN 0802-3271.

”Structural Crashworthiness of Aluminium Foam-Based Components”,
Arve Grønsund Hanssen, 2000:76, ISBN 82-7984-102-4, ISSN 0809-103X.

“Measurements and simulations of the consolidation in first-year sea ice ridges, and some aspects of mechanical behaviour”,
Knut V. Høyland, 2000:94, ISBN 82-7984-121-0, ISSN 0809-103X.

”Kinematics in Regular and Irregular Waves based on a Lagrangian Formulation”,
Svein Helge Gjøsund, 2000-86, ISBN 82-7984-112-1, ISSN 0809-103X.

”Self-Induced Cracking Problems in Hardening Concrete Structures”,
Daniela Bosnjak, 2000-121, ISBN 82-7984-151-2, ISSN 0809-103X.

"Ballistic Penetration and Perforation of Steel Plates",
Tore Børvik, 2000:124, ISBN 82-7984-154-7, ISSN 0809-103X.

"Freeze-Thaw resistance of Concrete. Effect of: Curing Conditions, Moisture Exchange and Materials",
Terje Finnerup Rønning, 2001:14, ISBN 82-7984-165-2, ISSN 0809-103X

"Structural behaviour of post tensioned concrete structures. Flat slab. Slabs on ground",
Steinar Trygstad, 2001:52, ISBN 82-471-5314-9, ISSN 0809-103X.

"Slipforming of Vertical Concrete Structures. Friction between concrete and slipform panel",
Kjell Tore Fosså, 2001:61, ISBN 82-471-5325-4, ISSN 0809-103X.

"Some numerical methods for the simulation of laminar and turbulent incompressible flows",
Jens Holmen, 2002:6, ISBN 82-471-5396-3, ISSN 0809-103X.

“Improved Fatigue Performance of Threaded Drillstring Connections by Cold Rolling”,
Steinar Kristoffersen, 2002:11, ISBN: 82-421-5402-1, ISSN 0809-103X.

"Deformations in Concrete Cantilever Bridges: Observations and Theoretical Modelling",
Peter F. Takâcs, 2002:23, ISBN 82-471-5415-3, ISSN 0809-103X.

"Stiffened aluminium plates subjected to impact loading",
Hilde Giæver Hildrum, 2002:69, ISBN 82-471-5467-6, ISSN 0809-103X.

"Full- and model scale study of wind effects on a medium-rise building in a built up area",
Jónas Thór Snæbjørnsson, 2002:95, ISBN82-471-5495-1, ISSN 0809-103X.

“Evaluation of Concepts for Loading of Hydrocarbons in Ice-infested water”,
Arnor Jensen, 2002:114, ISBN 82-417-5506-0, ISSN 0809-103X.

”Numerical and Physical Modelling of Oil Spreading in Broken Ice”,
Janne K. Økland Gjøsteen, 2002:130, ISBN 82-471-5523-0, ISSN 0809-103X.

”Diagnosis and protection of corroding steel in concrete”,
Franz Pruckner, 20002:140, ISBN 82-471-5555-4, ISSN 0809-103X.

“Tensile and Compressive Creep of Young Concrete: Testing and Modelling”,
Dawood Atrushi, 2003:17, ISBN 82-471-5565-6, ISSN 0809-103X.

“Rheology of Particle Suspensions. Fresh Concrete, Mortar and Cement Paste with Various Types of Lignosulfonates”,
Jon Elvar Wallevik, 2003:18, ISBN 82-471-5566-4, ISSN 0809-103X.

“Oblique Loading of Aluminium Crash Components”,
Aase Reyes, 2003:15, ISBN 82-471-5562-1, ISSN 0809-103X.

“Utilization of Ethiopian Natural Pozzolans”,
Surafel Ketema Desta, 2003:26, ISSN 82-471-5574-5, ISSN:0809-103X.

“Behaviour and strength prediction of reinforced concrete structures with discontinuity regions”, Helge Brå, 2004:11, ISBN 82-471-6222-9, ISSN 1503-8181.

“High-strength steel plates subjected to projectile impact. An experimental and numerical study”, Sumita Dey, 2004:38, ISBN 82-471-6282-2 (printed version), ISBN 82-471-6281-4 (electronic version), ISSN 1503-8181.

“Alkali-reactive and inert fillers in concrete. Rheology of fresh mixtures and expansive reactions.”
Bård M. Pedersen, 2004:92, ISBN 82-471-6401-9 (printed version), ISBN 82-471-6400-0 (electronic version), ISSN 1503-8181.

“On the Shear Capacity of Steel Girders with Large Web Openings”.
Nils Christian Hagen, 2005:9 ISBN 82-471-6878-2 (printed version), ISBN 82-471-6877-4 (electronic version), ISSN 1503-8181.

”Behaviour of aluminium extrusions subjected to axial loading”.
Østen Jensen, 2005:7, ISBN 82-471-6873-1 (printed version), ISBN 82-471-6872-3 (electronic version), ISSN 1503-8181.

”Thermal Aspects of corrosion of Steel in Concrete”.
Jan-Magnus Østvik, 2005:5, ISBN 82-471-6869-3 (printed version), ISBN 82-471-6868 (electronic version), ISSN 1503-8181.

”Mechanical and adaptive behaviour of bone in relation to hip replacement.” A study of bone remodelling and bone grafting.
Sébastien Muller, 2005:34, ISBN 82-471-6933-9 (printed version), ISBN 82-471-6932-0 (electronic version), ISSN 1503-8181.

“Analysis of geometrical nonlinearities with applications to timber structures”.
Lars Wollebæk, 2005:74, ISBN 82-471-7050-5 (printed version), ISBN 82-471-7019-1 (electronic version), ISSN 1503-8181.

“Pedestrian induced lateral vibrations of slender footbridges”,
Anders Rönnquist, 2005:102, ISBN 82-471-7082-5 (printed version), ISBN 82-471-7081-7 (electronic version), ISSN 1503-8181.

“Initial Strength Development of Fly Ash and Limestone Blended Cements at Various Temperatures Predicted by Ultrasonic Pulse Velocity”,
Tom Ivar Fredvik, 2005:112, ISBN 82-471-7105-8 (printed version), ISBN 82-471-7103-1 (electronic version), ISSN 1503-8181.

“Behaviour and modelling of thin-walled cast components”,
Cato Dørum, 2005:128, ISBN 82-471-7140-6 (printed version), ISBN 82-471-7139-2 (electronic version), ISSN 1503-8181.

“Behaviour and modelling of selfpiercing riveted connections”,
Raffaele Porcaro, 2005:165, ISBN 82-471-7219-4 (printed version), ISBN 82-471-7218-6 (electronic version), ISSN 1503-8181.

”Behaviour and Modelling og Aluminium Plates subjected to Compressive Load”,
Lars Rønning, 2005:154, ISBN 82-471-7169-1 (printed version), ISBN 82-471-7195-3 (electronic version), ISSN 1503-8181.

”Bumper beam-longitudinal system subjected to offset impact loading”,
Satyanarayana Kokkula, 2005:193, ISBN 82-471-7280-1 (printed version), ISBN 82-471-7279-8 (electronic version), ISSN 1503-8181.

“Control of Chloride Penetration into Concrete Structures at Early Age”,
Guofei Liu, 2006:46, ISBN 82-471-7838-9 (printed version), ISBN 82-471-7837-0 (electronic version), ISSN 1503-8181.

“Modelling of Welded Thin-Walled Aluminium Structures”,
Ting Wang, 2006:78, ISBN 82-471-7907-5 (printed version), ISBN 82-471-7906-7 (electronic version), ISSN 1503-8181.

”Time-variant reliability of dynamic systems by importance sampling and probabilistic analysis of ice loads”,
Anna Ivanova Olsen, 2006:139, ISBN 82-471-8041-3 (printed version), ISBN 82-471-8040-5 (electronic version), ISSN 1503-8181.

“Fatigue life prediction of an aluminium alloy automotive component using finite element analysis of surface topography”.
Sigmund Kyrre Ås, 2006:25, ISBN 82-471-7791-9 (printed version), ISBN 82-471-7791-9 (electronic version), ISSN 1503-8181.

”Constitutive models of elastoplasticity and fracture for aluminium alloys under strain path change”,
Dasharatha Achani, 2006:76, ISBN 82-471-7903-2 (printed version), ISBN 82-471-7902-4 (electronic version), ISSN 1503-8181.

“Simulations of 2D dynamic brittle fracture by the Element-free Galerkin method and linear fracture mechanics”,
Tommy Karlsson, 2006:125, ISBN 82-471-8011-1 (printed version), ISBN 82-471-8010-3 (electronic version), ISSN 1503-8181.

“Penetration and Perforation of Granite Targets by Hard Projectiles”,
Chong Chiang Seah, 2006:188, ISBN 82-471-8150-9 (printed version), ISBN 82-471-8149-5 (electronic version), ISSN 1503-8181.

"Deformations, strain capacity and cracking of concrete in plastic and early hardening phases",
Tor Arne Hammer, 2007:234, ISBN 978-82-471-5191-4 (printed version), ISBN 978-82-471-5207-2 (electronic version), ISSN 1503-8181.

"Crashworthiness of dual-phase high-strength steel: Material and Component behaviour", Venkatapathi Tarigopula, 2007:230, ISBN 82-471-5076-4 (printed version), ISBN 82-471-5093-1 (electronic version), ISSN 1503-8181.

"Fibre reinforcement in load carrying concrete structures",
Åse Lyslo Døssland, 2008:50, ISBN 978-82-471-6910-0 (printed version), ISBN 978-82-471-6924-7 (electronic version), ISSN 1503-8181.

"Low-velocity penetration of aluminium plates",
Frode Grytten, 2008:46, ISBN 978-82-471-6826-4 (printed version), ISBN 978-82-471-6843-1 (electronic version), ISSN 1503-8181.

"Robustness studies of structures subjected to large deformations",
Ørjan Fyllingen, 2008:24, ISBN 978-82-471-6339-9 (printed version), ISBN 978-82-471-6342-9 (electronic version), ISSN 1503-8181.

"Constitutive modelling of morsellised bone",
Knut Birger Lunde, 2008:92, ISBN 978-82-471-7829-4 (printed version), ISBN 978-82-471-7832-4 (electronic version), ISSN 1503-8181.

"Experimental Investigations of Wind Loading on a Suspension Bridge Girder",
Bjørn Isaksen, 2008:131, ISBN 978-82-471-8656-5 (printed version), ISBN 978-82-471-8673-2 (electronic version), ISSN 1503-8181.

"Cracking Risk of Concrete Structures in The Hardening Phase",
Guomin Ji, 2008:198, ISBN 978-82-471-1079-9 (printed version), ISBN 978-82-471-1080-5 (electronic version), ISSN 1503-8181.

"Modelling and numerical analysis of the porcine and human mitral apparatus",
Victorien Emile Prot, 2008:249, ISBN 978-82-471-1192-5 (printed version), ISBN 978-82-471-1193-2 (electronic version), ISSN 1503-8181.

"Strength analysis of net structures",
Heidi Moe, 2009:48, ISBN 978-82-471-1468-1 (printed version), ISBN 978-82-471-1469-8 (electronic version), ISSN1503-8181.

"Numerical analysis of ductile fracture in surface cracked shells",
Espen Berg, 2009:80, ISBN 978-82-471-1537-4 (printed version), ISBN 978-82-471-1538-1 (electronic version), ISSN 1503-8181.

"Subject specific finite element analysis of bone – for evaluation of the healing of a leg lengthening and evaluation of femoral stem design",
Sune Hansborg Pettersen, 2009:99, ISBN 978-82-471-1579-4 (printed version), ISBN 978-82-471-1580-0 (electronic version), ISSN 1503-8181.

"Evaluation of fracture parameters for notched multi-layered structures",
Lingyun Shang, 2009:137, ISBN 978-82-471-1662-3 (printed version), ISBN 978-82-471-1663-0 (electronic version), ISSN 1503-8181.

"Modelling of Dynamic Material Behaviour and Fracture of Aluminium Alloys for Structural Applications"
Yan Chen, 2009:69, ISBN 978-82-471-1515-2 (printed version), ISBN 978-82 471-1516-9 (electronic version), ISSN 1503-8181.

"Nanomechanics of polymer and composite particles"
Jianying He 2009:213, ISBN 978-82-471-1828-3 (printed version), ISBN 978-82-471-1829-0 (electronic version), ISSN 1503-8181.

"Mechanical properties of clear wood from Norway spruce"
Kristian Berbom Dahl 2009:250, ISBN 978-82-471-1911-2 (printed version) ISBN 978-82-471-1912-9 (electronic version), ISSN 1503-8181.

"Modeling of the degradation of TiB_2 mechanical properties by residual stresses and liquid Al penetration along grain boundaries"
Micol Pezzotta 2009:254, ISBN 978-82-471-1923-5 (printed version) ISBN 978-82-471-1924-2 (electronic version) ISSN 1503-8181.

"Effect of welding residual stress on fracture"
Xiabo Ren 2010:77, ISBN 978-82-471-2115-3 (printed version) ISBN 978-82-471-2116-0 (electronic version), ISSN 1503-8181.

"Pan-based carbon fiber as anode material in cathodic protection system for concrete structures"
Mahdi Chini 2010:122, ISBN 978-82-471-2210-5 (printed version) ISBN 978-82-471-2213-6 (electronic version), ISSN 1503-8181.

"Structural Behaviour of deteriorated and retrofitted concrete structures"
Irina Vasililjeva Sæther 2010:171, ISBN 978-82-471-2315-7 (printed version) ISBN 978-82-471-2316-4 (electronic version) ISSN 1503-8181.

"Prediction of local snow loads on roofs"
Vivian Meløysund 2010:247, ISBN 978-82-471-2490-1 (printed version) ISBN 978-82-471-2491-8 (electronic version) ISSN 1503-8181.

"Behaviour and modelling of polymers for crash applications"
Virgile Delhaye 2010:251, ISBN 978-82-471-2501-4 (printed version) ISBN 978-82-471-2502-1 (electronic version) ISSN 1503-8181.

"Blended cement with reducted CO_2 emission – Utilizing the Fly Ash-Limestone Synergy",
Klaartje De Weerdt 2011:32, ISBN 978-82-471-2584-7 (printed version) ISBN 978-82-471-2584-4 (electronic version) ISSN 1503-8181.

"Chloride induced reinforcement corrosion in concrete" Concept of critical chloride content – methods and mechanisms.
Ueli Angst 2011:113, ISBN 978-82-471-2769-9 (printed version) ISBN 978-82-471-2763-6 (electronic version) ISSN 1503-8181.

"A thermo-electric-Mechanical study of the carbon anode and contact interface for Energy savings in the production of aluminium".
Dag Herman Andersen 2011:157, ISBN 978-82-471-2859-6 (printed version) ISBN 978-82-471-2860-2 (electronic version) ISSN 1503-8181.

"Structural Capacity of Anchorage Ties in Masonry Veneer Walls Subjected to Earthquake". The implications of Eurocode 8 and Eurocode 6 on a typical Norwegain veneer wall.
Ahmed Mohamed Yousry Hamed 2011:181, ISBN 978-82-471-2911-1 (printed version) ISBN 978-82-471-2912-8 (electronic ver.) ISSN 1503-8181.

"Work-hardening behaviour in age-hardenable Al-Zn-Mg(-Cu) alloys".
Ida Westermann , 2011:247, ISBN 978-82-471-3056-8 (printed ver.) ISBN 978-82-471-3057-5 (electronic ver.) ISSN 1503-8181.

"Behaviour and modelling of selfpiercing riveted connections using aluminium rivets".
Nguyen-Hieu Hoang, 2011:266, ISBN 978-82-471-3097-1 (printed ver.) ISBN 978-82-471-3099-5 (electronic ver.) ISSN 1503-8181.

"Fibre reinforced concrete".
Sindre Sandbakk, 2011:297, ISBN 978-82-471-3167-1 (printed ver.) ISBN 978-82-471-3168-8 (electronic ver) ISSN 1503:8181.

"Dynamic behaviour of cablesupported bridges subjected to strong natural wind".
Ole Andre Øiseth, 2011:315, ISBN 978-82-471-3209-8 (printed ver.) ISBN 978-82-471-3210-4 (electronic ver.) ISSN 1503-8181.

"Constitutive modeling of solargrade silicon materials"
Julien Cochard, 2011:307, ISBN 978-82-471-3189-3 (printed ver). ISBN 978-82-471-3190-9 (electronic ver.) ISSN 1503-8181.

"Constitutive behavior and fracture of shape memory alloys"
Jim Stian Olsen, 2012:57, ISBN 978-82-471-3382-8 (printed ver.) ISBN 978-82-471-3383-5 (electronic ver.) ISSN 1503-8181.

“Field measurements in mechanical testing using close-range photogrammetry and digital image analysis”
Egil Fagerholt, 2012:95, ISBN 978-82-471-3466-5 (printed ver.) ISBN 978-82-471-3467-2 (electronic ver.) ISSN 1503-8181.

“Towards a better under standing of the ultimate behaviour of lightweight aggregate concrete in compression and bending”,
Håvard Nedrelid, 2012:123, ISBN 978-82-471-3527-3 (printed ver.) ISBN 978-82-471-3528-0 (electronic ver.) ISSN 1503-8181.

“Numerical simulations of blood flow in the left side of the heart”
Sigrid Kaarstad Dahl, 2012:135, ISBN 978-82-471-3553-2 (printed ver.) ISBN 978-82-471-3555-6 (electronic ver.) ISSN 1503-8181.

“Moisture induced stresses in glulam”
Vanessa Angst-Nicollier, 2012:139, ISBN 978-82-471-3562-4 (printed ver.) ISBN 978-82-471-3563-1 (electronic ver.) ISSN 1503-8181.

“Biomechanical aspects of distraction osteogensis”
Valentina La Russa, 2012:250, ISBN 978-82-471-3807-6 (printed ver.) ISBN 978-82-471-3808-3 (electronic ver.) ISSN 1503-8181.

“Ductile fracture in dual-phase steel. Theoretical, experimental and numerical study”
Gaute Gruben, 2012:257, ISBN 978-82-471-3822-9 (printed ver.) ISBN 978-82-471-3823-6 (electronic ver.) ISSN 1503-8181.

“Damping in Timber Structures”
Nathalie Labonnote, 2012:263, ISBN 978-82-471-3836-6 (printed ver.) ISBN 978-82-471-3837-3 (electronic ver.) ISSN 1503-8181.

“Biomechanical modeling of fetal veins: The umbilical vein and ductus venosus bifurcation”
Paul Roger Leinan, 2012:299, ISBN 978-82-471-3915-8 (printed ver.) ISBN 978-82-471-3916-5 (electronic ver.) ISSN 1503-8181.

“Large-Deformation behaviour of thermoplastics at various stress states”
Anne Serine Ognedal, 2012:298, ISBN 978-82-471-3913-4 (printed ver.) ISBN 978-82-471-3914-1 (electronic ver.) ISSN 1503-8181.

“Hardening accelerator for fly ash blended cement”
Kien Dinh Hoang, 2012:366, ISBN 978-82-471-4063-5 (printed ver.) ISBN 978-82-471-4064-2 (electronic ver.) ISSN 1503-8181.

“From molecular structure to mechanical properties”
Jianyang Wu, 2013:186, ISBN 978-82-471-4485-5 (printed ver.) ISBN 978-82-471-4486-2 (electronic ver.) ISSN 1503-8181.

“Experimental and numerical study of hybrid concrete structures”
Linn Grepstad Nes, 2013:259, ISBN 978-82-471-4644-6 (printed ver.) ISBN 978-82-471-4645-3 (electronic ver.) ISSN 1503-8181.

“Mechanics of ultra-thin multi crystalline silicon wafers”
Saber Saffar, 2013:199, ISBN 978-82-471-4511-1 (printed ver.) ISBN 978-82-471-4513-5 (electronic ver). ISSN 1503-8181.

“Through process modelling of welded aluminium structures”
Anizahyati Alisibramulisi, 2013:325, ISBN 978-82-471-4788-7 (printed ver.) ISBN 978-82-471-4789-4 (electronic ver.) ISSN 1503-8181.

“Combined blast and fragment loading on steel plates”
Knut Gaarder Rakvåg, 2013:361, ISBN978-82-471-4872-3 (printed ver.) ISBN 978-82-4873-0 (electronic ver.). ISSN 1503-8181.

“Characterization and modelling of the anisotropic behaviour of high-strength aluminium alloy”
Marion Fourmeau, 2014:37, ISBN 978-82-326-0008-3 (printed ver.) ISBN 978-82-326-0009-0 (electronic ver.) ISSN 1503-8181.

“Behaviour of threated steel fasteners at elevated deformation rates”
Henning Fransplass, 2014:65, ISBN 978-82-326-0054-0 (printed ver.) ISBN 978-82-326-0055-7 (electronic ver.) ISSN 1503-8181.

“Sedimentation and Bleeding”
Ya Peng, 2014:89, ISBN 978-82-326-0102-8 (printed ver.) ISBN 978-82-326-0103-5 (electric ver.) ISSN 1503-8181.

“Impact against X65 offshore pipelines”
Martin Kristoffersen, 2014:362, ISBN 978-82-326-0636-8 (printed ver.) ISBN 978-82-326-0637-5 (electronic ver.) ISSN 1503-8181.

“Formability of aluminium alloy subjected to prestrain by rolling”
Dmitry Vysochinskiy, 2014:363,, ISBN 978-82-326-0638-2 (printed ver.) ISBN 978-82-326-0639-9 (electronic ver.) ISSN 1503-8181.

“Experimental and numerical study of Yielding, Work-Hardening and anisotropy in textured AA6xxx alloys using crystal plasticity models”
Mikhail Khadyko, 2015:28, ISBN 978-82-326-0724-2 (printed ver.) ISBN 978-82-326-0725-9 (electronic ver.) ISSN 1503-8181.

“Behaviour and Modelling of AA6xxx Aluminium Alloys Under a Wide Range of Temperatures and Strain Rates”
Vincent Vilamosa, 2015:63, ISBN 978-82-326-0786-0 (printed ver.) ISBN 978-82-326-0787-7 (electronic ver.) ISSN 1503-8181.

“A Probabilistic Approach in Failure Modelling of Aluminium High Pressure Die-Castings”
Octavian Knoll, 2015:137, ISBN 978-82-326-0930-7 (printed ver.) ISBN 978-82-326-0931-4 (electronic ver.) ISSN 1503-8181.

“Ice Abrasion on Marine Concrete Structures”
Egil Møen, 2015:189, ISBN 978-82-326-1034-1 (printed ver.) ISBN 978-82-326-1035-8 (electronic ver.) ISSN 1503-8181.

“Fibre Orientation in Steel-Fibre-Reinforced Concrete”
Giedrius Zirgulis, 2015:229, ISBN 978-82-326-1114-0 (printed ver.) ISBN 978-82-326-1115-7 (electronic ver.) ISSN 1503-8181.

“Effect of spatial variation and possible interference of localised corrosion on the residual capacity of a reinforced concrete beam”
Mohammad Mahdi Kioumarsi, 2015:282, ISBN 978-82-326-1220-8 (printed ver.) ISBN 978-82-1221-5 (electronic ver.) ISSN 1503-8181.

“The role of concrete resistivity in chloride-induced macro-cell corrosion”
Karla Horbostel, 2015:324, ISBN 978-82-326-1304-5 (printed ver.) ISBN 978-82-326-1305-2 (electonic ver.) ISSN 1503-8181.

“Flowable fibre-reinforced concrete for structural applications”
Elena Vidal Sarmiento, 2015-335, ISBN 978-82-326-1324-3 (printed ver.) ISBN 978-82-326-1325-0 (electronic ver.) ISSN 1503-8181.

“Development of chushed sand for concrete production with microproportioning”
Rolands Cepuritis, 2016:19, ISBN 978-82-326-1382-3 (printed ver.) ISBN 978-82-326-1383-0 (electronic ver.) ISSN 1503-8181.

“Withdrawal properties of threaded rods embedded in glued-laminated timer elements”
Haris Stamatopoulos, 2016:48, ISBN 978-82-326-1436-3 (printed ver.) ISBN 978-82-326-1437-0 (electronic ver.) ISSN 1503-8181.

“An Experimental and numerical study of thermoplastics at large deformation”
Marius Andersen, 2016:191, ISBN 978-82-326-1720-3 (printed ver.) ISBN 978-82-326-1721-0 (electronic ver.) ISSN 1503-8181.

“Modeling and Simulation of Ballistic Impact”
Jens Kristian Holmen, 2016:240, ISBN 978-82-326-1818-7 (printed ver). ISBN 978-82-326-1819-4 (electronic ver.) ISSN 1503-8181.

“Early age crack assessment of concrete structures”
Anja B. Estensen Klausen, 2016:256, ISBN 978-82-326-1850-7 (printed ver). ISBN 978-82-326-1851-4 (electronic ver.) ISSN 1503-8181.

“Uncertainty quantification and sensitivity analysis for cardiovascular models”
Vinzenz Gregor Eck, 2016:234, ISBN 978-82-326-1806-4 (printed ver.) ISBN 978-82-326-1807-1 (electronic ver.) ISSN 1503-8181.

“Dynamic behaviour of existing and new railway catenary systems under Norwegain conditions”
Petter Røe Nåvik, 2016:298, ISBN 978-82-326-1935-1 (printed ver.) ISBN 978-82-326-1934-4 (electronic ver.) ISSN 1503-8181.

“Mechanical behaviour of particle-filled elastomers at various temperatures”
Arne Ilseng, 2016-295, ISBN978-82-326-1928-3 (printed ver.) ISBN 978-82-326-1929-0 (electronic ver.) ISSN 1503-8181.

“Nanotechnology for Anti-Icing Application”
Zhiwei He, 2016:348, ISBN 978-82-326-2038-8 (printed ver.) ISBN 978-82-326-2019-5 (electronic ver.) ISSN 1503-8181.

“Conduction Mechanisms in Conductive Adhesives with Metal-Coated Polyer Spheres”
Sigurd Rolland Pettersen, 2016:349, ISBN 978-326-2040-1 (printed ver,) ISBN 978-82-326-2041-8 (electronic ver.) ISSN 1503-8181.

“The interaction between calcium lignosulfonate and cement”
Alessia Colombo, 2017:20, ISBN 978-82-326-2122-4 (printed ver.) ISBN 978-82-326-2123-1 (electronic ver.) ISSN 1503-8181